الجمهورية الجزائرية الديمقراطية الشعبية
People's Democratic Republic of Algeria
وزارة التعليم العالي و البحث العلمي
Ministry of Higher Education and Scientific Research

جامعة ابي بكر بلقايد - تلمسان
Abou Bekr Belkaid University – Tlemcen
كلية التكنولوجيا
Faculty of Technology

**THESIS**

Presented for the **degree** of **Doctorate 3rd Cycle**

**In** : Electronic

**Specialty** : Electronic Instrumentation

***By*** *:* Hichem ROUIGUEB

***Topic***

# Study, design and modelling of advanced solar cells

*Defended publicly on 06/06/2026 , before the examination committee composed of :*

| | | | |
|---|---|---|---|
| Mr. Ahmed Nassim MOULAI KHATIR | -Associate Professor | -Univ. of Tlemcen | -President |
| Mr. Salim KERAI | -Professor | -Univ. of Tlemcen | -Director |
| Mr. Mohammed KHAOUANI | -Associate Professor | -Univ. of Ain Temouchent | -Co-Director |
| Mr. Oussama ZEGGAI | -Associate Professor | -Univ. of Chlef | -Examiner |
| Ms. Fatima Zohra RAHOU | -Associate Professor | -Univ. of Tlemcen | -Examiner |
| Mr. Abderrahmane Zakarya DJENNATI | -Associate Professor | -Univ. of Tlemcen | -Guest |

Academic Year : 2025/2026

# ACKNOWLEDGMENTS

First and foremost, I express my deepest gratitude to **Allah, the Almighty**, for granting me the strength, patience, perseverance, and wisdom necessary to complete this doctoral research.

I would like to extend my sincere and profound appreciation to my supervisors, **Prof. Salim KERAI** and **Dr. Mohammed KHAOUANI**, for their invaluable guidance, unwavering support, insightful advice, and continuous encouragement throughout the course of this work. Their expertise, scientific rigor, and constructive criticism have played a fundamental role in the successful completion of this thesis.

I would also like to express my sincere gratitude to **Dr. Abderrahmane Zakarya DJENNATI** for his constant support, availability, valuable discussions, and precious assistance during the different stages of this research.

My sincere thanks are extended to **Dr. Ahmed Nassim MOULAI KHATIR**, President of the jury, for the honor of chairing my thesis defense. I am equally grateful to the distinguished members of the jury, **Dr. Oussama ZEGGAI** and **Dr. Fatima Zohra RAHOU**, for accepting to evaluate this work and for their valuable comments, constructive suggestions, and insightful observations that have contributed to improving the quality of this thesis.

I would also like to thank all the faculty members and staff of the **Faculty of Technology, Abou Bekr Belkaid University of Tlemcen**, whose dedication to teaching, scientific excellence, and commitment to research have greatly contributed to my academic and professional development.

Finally, I would like to express my heartfelt gratitude to my family, friends, and all those who have supported me, directly or indirectly, throughout this journey. Their encouragement, understanding, and confidence in me have been a constant source of motivation and inspiration.

To all of them, I offer my sincere thanks and deepest appreciation.

# DEDICATION

“



***.... I dedicate this work to:***

*TO my dear father* ***Mohammed****,*

*TO my beloved mother* ***Nouara****,*

*Who have never stopped praying for me, supporting me, and encouraging me to reach my goals.*

*TO my dear brother* ***Karime*** *and my dear sister* ***Karima****,*

*TO my beloved sister* ***Farah****, her husband* ***Ilyes****, and their little princesses* ***Houda****,* ***Hadil*** *and* ***Nada****,*

*May* ***God*** *bless you with health, happiness, and success.*

*TO my dear friends* ***B. Anes*** *and* ***A. Oussama****,*

*For their friendship, help, and support during difficult times.*

*TO all those who are dear to me — to all of you, thank you.*

★★★

”

***- Hichem***

# Contents

**Acknowledgments** . . . . . **I**

**Dedication** . . . . . **II**

**List of Figures** . . . . . **XI**

**List of Tables** . . . . . **XIII**

**List of Listings** . . . . . **XIV**

**List of Acronyms** . . . . . **XV**

**Abstract** . . . . . **XVIII**

**الملخص** . . . . . **XX**

**Résumé** . . . . . **XXI**

**General Introduction** . . . . . **1**

**1 Global Energy Challenges and the Basics of Photovoltaics** . . . . . **5**

1.1 Introduction . . . . . 6

1.2 Brief history of energy research and developments in photovoltaics . . . . . 6

1.3 Solar radiation and the solar constant . . . . . 8

1.4 Semiconductor materials in photovoltaics . . . . . 10

1.4.1 Energy band structure of semiconductors . . . . . 10

1.4.2 Semiconductor materials and optimal band gap . . . . . 10

1.5 The physics of photovoltaics: concept and operation . . . . . 12

1.5.1 Photovoltaic effect . . . . . 12

1.5.2 Equivalent Electrical Model and Characteristic Parameters of a Solar Cell . . . . . 14

1.5.2.1 Short-circuit current ($J_{sc}$) . . . . . 15

1.5.2.2 Open-circuit voltage ($V_{oc}$) . . . . . 16

1.5.2.3 Fill factor (FF) . . . . . 16

1.5.2.4 Power Conversion Efficiency (PCE) . . . . . 16

1.5.2.5 Quantum efficiency . . . . . 16

1.6 Structure and architecture of photovoltaic cells . . . . . 17

1.6.1 Substrate . . . . . 17

1.6.2 Absorbing layer . . . . . 18

1.6.3 Charge transport layers . . . 18
1.6.4 Anti-reflective coating (ARC) . . . 18
1.6.5 Metal contacts . . . 19
1.6.6 Surface and interface passivation . . . 19
1.7 Loss mechanisms and performance limitations . . . 19
1.7.1 Optical losses . . . 19
1.7.2 Thermal losses . . . 19
1.7.3 Electronic losses . . . 20
1.7.3.1 Radiative recombination . . . 20
1.7.3.2 Non-radiative recombination (Shockley–Read–Hall, SRH) 21
1.7.3.3 Auger recombination . . . 21
1.7.4 Technological losses . . . 21
1.8 Classification of photovoltaic cell generations . . . 22
1.8.1 First generation: Crystalline silicon . . . 24
1.8.1.1 Silicon proprieties . . . 24
1.8.1.2 Manufacturing process . . . 24
1.8.1.3 Advantages and limitations . . . 25
1.8.2 Second generation: Thin films . . . 26
1.8.2.1 Amorphous silicon (a-Si) cells . . . 27
1.8.2.2 Cadmium telluride (CdTe) cells . . . 27
1.8.2.3 Copper–Indium–Gallium–Selenide (CIGS) cells . . . 28
1.8.2.4 III–V material-based solar cells . . . 28
1.8.3 Third generation . . . 29
1.8.3.1 Organic photovoltaic cells (OPV) . . . 30
1.8.3.2 Quantum dot photovoltaic cells . . . 31
1.8.3.3 Dye-sensitised solar cells (DSSCs) . . . 31
1.9 Current applications and prospects . . . 32
1.10 Conclusion . . . 33

**2 Perovskite solar cells and tandem structures . . . 34**
2.1 Introduction . . . 35
2.2 Perovskite materials . . . 35
2.2.1 History and emergence of perovskites in photovoltaics . . . 35
2.2.2 $ABX_3$ formula and classification . . . 37
2.2.3 Advantages of perovskites . . . 38
2.2.4 Initial limitations and challenges for the industry . . . 39
2.3 Crystallography and properties of perovskites . . . 40
2.3.1 Crystallographic phases and phase transitions . . . 40
2.3.2 Electronic structure and optoelectronic properties . . . 42
2.3.3 Microstructure and structure–property relationships . . . 44
2.3.4 Defects and recombination traps . . . 44
2.4 Advanced materials and composition engineering of perovskites . . . 45
2.4.1 Metal halide perovskites . . . 45
2.4.2 Mixed cation perovskites . . . 46
2.4.3 Low-lead and lead-free alternatives . . . 46
2.4.4 2D/3D heterostructures and perovskite nanocrystals . . . 48

2.4.5 Compositional engineering and additives . . . 48
2.5 Manufacture and deposition of perovskite films . . . 49
2.5.1 Solution deposition methods . . . 49
2.5.2 Vacuum deposition methods . . . 51
2.5.3 Post-treatment and maturation . . . 51
2.5.4 Encapsulation and protection against moisture and oxygen . . . 52
2.6 Design and operating principles of perovskite cells . . . 54
2.6.1 Materials and structures of PSCs . . . 55
2.6.1.1 Materials used in PSCs . . . 55
2.6.1.2 Architectures of PSCs . . . 56
2.6.2 Operating principle of PSCs . . . 59
2.6.3 Hysteresis and ion migration in PSCs . . . 60
2.7 Performance and Technological Challenges . . . 61
2.7.1 Efficiency Under Controlled Conditions . . . 61
2.7.2 Stability and Degradation Mechanisms . . . 61
2.7.2.1 Extrinsic Degradation . . . 61
2.7.2.2 Intrinsic Degradation . . . 62
2.7.3 Challenges for Industrialisation and Upscaling . . . 62
2.8 Tandem Solar Cells (TSCs) . . . 63
2.8.1 Principles and Advantages of Tandem Structures . . . 63
2.8.2 Architectures and monolithic integration . . . 65
2.8.2.1 Two-Terminal Architecture (2T) . . . 65
2.8.2.2 Interconnecting Layers (ICL) . . . 66
2.8.2.3 Four-Terminal Architecture (4T) . . . 66
2.8.3 Possible combinations . . . 67
2.8.3.1 All-perovskite tandems . . . 67
2.8.3.2 Perovskite / CIGS . . . 69
2.8.3.3 Perovskite / Silicon . . . 70
2.9 Conclusion . . . 72

**3 Analytical modelling of perovskite and tandem solar cells . . . 74**
3.1 Introduction . . . 75
3.2 Analytical modelling of a perovskite solar cell (n-i-p) . . . 75
3.2.1 Device modelling . . . 76
3.2.2 Development of the analytical model . . . 76
3.2.3 Analytical results and validation . . . 89
3.2.3.1 Comparison and validation with experimental results . . . 89
3.2.3.2 Analysis of external and internal quantum efficiencies (EQE and IQE) . . . 91
3.2.3.3 Influence of the thickness of the absorbing layer on performance . . . 92
3.2.3.4 Influence of ETL ($TiO_2$) doping on photovoltaic performance . . . 94
3.3 Extension to analytical modelling of tandem cells . . . 95
3.3.1 Analytical model of perovskite/silicon tandem cells . . . 95
3.3.2 Analytical results for the tandem cell . . . 100

3.3.2.1 Comparison of J–V characteristics and photovoltaic parameters . . . 100
3.3.2.2 Influence of the thickness of the intrinsic silicon layer . . . 101
3.3.2.3 Optimisation of the perovskite layer thickness . . . 102
3.3.2.4 Current Matching and Performance Analysis of the Tandem Cell . . . 104
3.4 Conclusion . . . 105

**4 Numerical simulation using Silvaco software and analysis of results . . 106**
4.1 Introduction . . . 107
4.2 Overview of Silvaco Software . . . 107
4.2.1 Introduction and operating principle of the software . . . 107
4.2.2 Modules and tools in Silvaco TCAD . . . 108
4.2.3 Cell construction using Silvaco . . . 110
4.2.4 General simulation methodology and configuration steps . . . 110
4.3 Simulation and optimisation of single-junction PSC . . . 116
4.3.1 Verification of cell operation . . . 116
4.3.1.1 Thermodynamic equilibrium (0 V, darkness) . . . 116
4.3.1.2 Forward bias under illumination . . . 117
4.3.1.3 Reverse bias under illumination . . . 117
4.3.1.4 General interpretation . . . 119
4.3.2 Cross-validation of results . . . 119
4.3.2.1 Analysis of current–voltage characteristics (J–V) . . . 119
4.3.2.2 Optical study: absorption and transmission spectra . . . 120
4.3.2.3 Comparative analysis of EQE and IQE between numerical simulation (Silvaco) and analytical model . . . 122
4.3.3 Parametric analysis of the impact of materials on the performance of PSC . . . 124
4.3.3.1 Impact of Absorbing Material on the Performance of PSC 124
4.3.3.2 Influence of Hole Transport Layer (HTL) Doping . . . 126
4.4 Simulation of the Perovskite/Silicon Heterojunction (HJT) Tandem Cell . 136
4.4.1 Selection of the Highest Performing Perovskite Subcell . . . 136
4.4.2 Tandem Architecture Design . . . 136
4.4.3 Comparative Analysis of Photovoltaic Performance: Optimised Perovskite Cell and Perovskite/Silicon HJT Tandem Cell . . . 138
4.4.3.1 Analysis of J–V Curves . . . 138
4.4.3.2 Spectral Analysis: Absorption, Transmission and Optical Losses . . . 139
4.4.3.3 Study of external quantum efficiency and internal quantum efficiency . . . 141
4.4.3.4 Influence of temperature on the performance of tandem photovoltaic cells . . . 143
4.4.4 Prospects for optimisation . . . 145
4.5 Conclusion . . . 146

**General Conclusion . . . 147**

**Bibliography** . . . . . **150**

**Appendices** . . . . . **198**

# List of Figures


1.1 Chronological Timeline of Major Milestones in Energy Development and Photovoltaic Research. . . . . 7
1.2 Global Installed Solar Photovoltaic Capacity, 2015–2035 . . . . . 8
1.3 Representation of the three illumination constants: AM0 (extraterrestrial), AM1 (zenith), and AM1.5 (standard terrestrial reference condition) . . . . 9
1.4 Solar spectrum reaching Earth's surface, showing the relative contributions of UV (5%), visible (43%), and IR (52%) bands . . . . . 9
1.5 Energy diagram of the SC. . . . . 10
1.6 Schematic diagram of the PN junction . . . . . 12
1.7 Generation of charge carriers through photon absorption . . . . . 13
1.8 Functional diagram of a PN junction photovoltaic cell . . . . . 14
1.9 Simplified equivalent electrical model of a photovoltaic cell. . . . . 15
1.10 Typical current-voltage (J-V) characteristic and related parameters of a solar cell . . . . . 15
1.11 Quantum efficiency of an ideal solar cell as a function of the incident photon wavelength . . . . . 17
1.12 Functional layer architecture of a single-junction photovoltaic cell. . . . . 18
1.13 Radiative, non-radiative, and Auger recombination mechanisms in photovoltaic cells. . . . . 20
1.14 Classification of solar photovoltaic cell technologies. . . . . 22
1.15 Solar cell efficiency evolution over generations . . . . . 23
1.16 The different stages in the manufacturing process for crystalline silicon photovoltaic modules . . . . . 25
1.17 Typical architectures of second-generation thin-film photovoltaic cells: CIGS, CdTe and amorphous/microcrystalline silicon (a-Si/$\mu$c-Si . . . . . 26
1.18 Schematic comparison of the different forms of silicon: monocrystalline, polycrystalline, and amorphous. . . . . 27
1.19 Architecture of OPV cells. . . . . 30

2.1 Illustration of the perovskite mineral with the formula $CaTiO_3$ . . . . . 36
2.2 Timeline of the history and development of perovskite solar cells. . . . . 36
2.3 Schematic diagram of the cubic crystal structure $ABX_3$, extended lattice view and elementary cell. . . . . 37
2.4 Main advantages of perovskites for photovoltaic applications. . . . . 39
2.5 Diagram of the different crystalline phases of perovskites: (a) cubic, (b) tetragonal, and (c) orthorhombic. . . . . 40
2.6 Band structure of $APbX_3$, showing the unique inverse electronic arrangement revealed by bonding in isolated $[PbI_6]^{4-}$ octahedra. . . . . 43

2.7 Comparative absorption characteristics of $MAPbI_3$ perovskite thin film and standard photovoltaic absorbers . . . 43
2.8 Overview of microstructural disorders in perovskite thin films: grain boundaries, heterointerfaces, and intra-crystalline disorders . . . 44
2.9 Comparison of photovoltaic efficiencies (PCE) of perovskites based on lead (Pb), tin (Sn) and germanium (Ge), illustrating the potential and relative lag of low-lead and lead-free alternatives . . . 47
2.10 Modulation of the crystal structure of $MAPbBr_3$ perovskite by sequential addition of MABr and CsBr additives, leading to a mixed $MA_{1-x}Cs_xPbBr_3$ perovskite with reduced vacancies and structural homogenisation . . . 49
2.11 Diagram of single-step and two-step spin coating procedures for the formation of $CH_3NH_3PbI_3$ . . . 50
2.12 Hot-casting method used to deposit and form a uniform perovskite thin film 51
2.13 Main vacuum deposition methods for perovskite films. (a) Co-evaporation, (b) Single-source evaporation, (c) Sequential deposition. . . . 52
2.14 Diagram illustrating the growth of perovskite grains induced by post-treatments . . . 53
2.15 Diagram illustrating the protection of perovskite materials against environmental stresses (humidity, oxygen, high temperature, UV radiation) through encapsulation . . . 54
2.16 Schematic representation of the main structures of PSCs: (a) mesoporous n–i–p, (b) planar n–i–p, (c) planar p–i–n, and (d) mesoporous p–i–n. . . . 57
2.17 Impact of defective ions and recombination on J–V hysteresis. (a) Simulated J–V hysteresis with and without ions and recombination (Rec); (b, c) Hysteresis loops for different combinations of bulk ($R_{bulk}$) and interfacial ($R_{ETL}$, $R_{HTL}$) recombination processes . . . 60
2.18 Record efficiencies of single-junction solar cells as a function of their bandgap, compared to the Shockley–Queisser theoretical limit . . . 64
2.19 Theoretical efficiency limit of two-terminal tandem solar cells as a function of the bandgaps of the top and bottom sub-cells . . . 64
2.20 Comparative diagrams of tandem solar cell architectures: (a) monolithic 2T architecture with tunnel junction, (b) 4T architecture with electrically independent subcells. . . . 66
2.21 (a) Schematic of a 2T all-perovskite tandem solar cell with wide and narrow bandgap sub-cells. (b) Theoretical efficiency map as a function of top and bottom bandgaps. (c) Typical energy-level alignment enabling efficient charge extraction . . . 68
2.22 (a) Schematic diagram of a perovskite/CIGS tandem, illustrating the device configuration and energy levels of (b) the top subcell and (c) the bottom subcell. . . . 69
2.23 Representative schematics of main monolithic perovskite/silicon tandem solar cell architectures: (a) working principle, (b) structure with nc-Si recombination layer, (c) SHJ cell in p–i–n configuration with SnO buffer, (d) n-type homo-junction Si cell with metal/ITO recombination, (e) SHJ cell in n–i–p configuration with MoOx buffer. . . . 71

3.1 Device structure of a $MAPbI_3$-based PSC. . . . . 77
3.2 Energy diagram displaying perovskite thickness $t_p$ and built-in potential $V_{bi}$. 80
3.3 Flow chart of MATLAB code used. . . . . 89
3.4 $J$–$V$ curves comparison showing the experimental data validating the analytical model of the PSC. . . . . 90
3.5 External quantum efficiency (EQE) and internal quantum efficiency (IQE) curves derived from the analytical model for the n-i-p perovskite cell. . . . 91
3.6 $J$–$V$ curves from the analytical model for different thicknesses of the $MAPbI_3$ perovskite layer (0.26 µm to 0.35 µm). . . . . 93
3.7 Influence of ETL ($TiO_2$) doping on device parameters. . . . . 94
3.8 Perovskite/Silicon tandem solar cell device schematic. . . . . 96
3.9 J–V characteristics for the perovskite top-cell, silicon bottom-cell, and perovskite/silicon tandem cell. . . . . 101
3.10 Efficiency of the tandem cell as a function of the thickness of the intrinsic silicon layer. . . . . 102
3.11 Short-circuit current of the top and bottom subcells as a function of perovskite layer thickness. . . . . 103
3.12 Overall efficiency of the tandem cell as a function of perovskite layer thickness. 103
3.13 J–V curves in current-matched mode for the perovskite subcell, silicon subcell, and the optimised tandem cell. . . . . 104

4.1 Silvaco simulation workflow displaying ATLAS inputs and outputs . . . . . 109
4.2 Modular organization of command groups in the ATLAS software. . . . . 111
4.3 Visualisation of the automatic meshing of the simulated structure. . . . . 112
4.4 (a) Schematic representation of the regions of the perovskite solar cell defined in ATLAS; (b) Doping profile associated with the different regions. 113
4.5 Diagram of the simulated perovskite cell structure, showing the position of the electrodes (cathode at the top on the FTO layer, anode at the bottom in rear contact). . . . . 114
4.6 Band diagram of the cell at thermodynamic equilibrium (0 V, darkness). . 117
4.7 Band diagram under forward bias and illumination. . . . . 118
4.8 Band diagram under reverse bias and illumination. . . . . 118
4.9 Comparative J–V curves between simulation, modelling, and experiments for the FTO/$TiO_2$/$MAPbI_3$/HTM PSC. . . . . 119
4.10 Spectral absorption and transmission curves as a function of optical wavelength for a PSC. . . . . 121
4.11 EQE of Silvaco simulation and analytical modelling for PSC. . . . . 122
4.12 IQE of Silvaco simulation and analytical modelling for PSC. . . . . 123
4.13 Simulated J–V curves obtained by varying the perovskite material in the reference cell FTO/$TiO_2$/Perovskite/Spiro-OMeTAD. . . . . 125
4.14 Simulated J–V curves of the PSC with Spiro-OMeTAD as the HTL at different doping concentrations. . . . . 127
4.15 Simulated J–V curves of the PSC with PTAA as the HTL at different doping concentrations. . . . . 129
4.16 Simulated J–V curves of the PSC with PolyTPD as the HTL at different doping concentrations. . . . . 130

4.17 Simulated J–V curves of the PSC with P3HT as the HTL at different doping concentrations. . . . 132
4.18 Simulated J–V curves of the PSC with PEDOT:PSS as the HTL at different doping concentrations. . . . 133
4.19 Simulated J–V curves of the PSC with CuSCN (a) and $NiO_x$ (b) as the HTL at different doping concentrations. . . . 135
4.20 Device structure of the tandem Perovskite/Si HJT solar cell. . . . 137
4.21 Simulated J–V curves of the optimised PSC and the perovskite/silicon heterojunction (HJT) tandem cell. . . . 139
4.22 Absorption and transmission profiles of the optimised perovskite device and the perovskite/silicon tandem device. . . . 140
4.23 EQE spectra of the optimized perovskite device and the perovskite/silicon tandem device. . . . 141
4.24 IQE spectra of the optimized perovskite device and the perovskite/silicon tandem device. . . . 142
4.25 Simulated J–V curves of the perovskite/silicon HJT tandem cell across the temperature range from 265 K to 360 K. . . . 143
4.26 Temperature dependence of the $J_{sc}$, $V_{oc}$, FF, and PCE of the perovskite/silicon HJT tandem cell. . . . 144

# List of Tables


1.1 Classification of semiconductor materials used in photovoltaics . . . . . 12
1.2 Comparison of the three generations of photovoltaic cells . . . . . 23

2.1 Comparison of crystalline phases, optoelectronic properties, and their impact on perovskite performance . . . . . 41
2.2 Impact of different cation combinations on the stability and optoelectronic properties of perovskites . . . . . 47
2.3 Summary of reported performance for two-terminal perovskite/silicon tandem cells . . . . . 72

3.1 Main photovoltaic parameters extracted from the analytical model and experimental measurements. . . . . 91
3.2 Photovoltaic parameters derived from the analytical model as a function of the thickness of the $MAPbI_3$ layer. . . . . 92
3.3 Performance parameters for sub-cells and tandem cells. . . . . 100
3.4 Performance parameters of the perovskite and silicon subcells and the perovskite/silicon tandem cell under current-matched conditions. . . . . 105

4.1 Physical and technological parameters of the PSC simulated in Silvaco ATLAS . . . . . 110
4.2 Physical and electrical parameters of simulated hybrid perovskite layers. . 124
4.3 Electrical parameters extracted from simulated J–V curves for different perovskite materials in the FTO/$TiO_2$/Perovskite/Spiro-OMeTAD cell. . . 125
4.4 Physical and electrical parameters of alternative HTLs. . . . . 126
4.5 Photovoltaic parameters extracted from the simulated J–V curves for each Spiro-OMeTAD doping concentration. . . . . 127
4.6 Photovoltaic parameters extracted from the simulated J–V curves for each PTAA doping concentration. . . . . 129
4.7 Photovoltaic parameters extracted from the simulated J–V curves for each PolyTPD doping concentration. . . . . 130
4.8 Photovoltaic parameters extracted from the simulated J–V curves for each P3HT doping concentration. . . . . 131
4.9 Photovoltaic parameters extracted from the simulated J–V curves for each PEDOT:PSS doping concentration. . . . . 133
4.10 Photovoltaic parameters extracted from the simulated J–V curves for each CuSCN and $NiO_x$ doping concentration. . . . . 135
4.11 Physical and electrical parameters for ZnO and Si HJT cell layers. . . . . 138
4.12 Electrical parameters extracted from the J–V characteristics of the optimized perovskite cell and perovskite/silicon HJT tandem cell. . . . . 138

4.13 Photovoltaic performance metrics of the perovskite/silicon HJT tandem cell at different operating temperatures. . . . . 144

# LISTINGS

4.1 Definition of regions and doping in ATLAS. . . . . 112
4.2 Definition of electrodes in ATLAS. . . . . 113
4.3 Definition of material parameters in ATLAS. . . . . 115
4.4 Activation of physical models in ATLAS. . . . . 115
4.5 Definition of numerical methods in ATLAS. . . . . 115

# LIST OF ACRONYMS

| | |
|---|---|
| **$ABX_3$** | Perovskite formula |
| **a-Si** | Amorphous silicon |
| **AM0** | Air mass 0 |
| **AM1** | Air mass 1 |
| **AM1.5** | Standard solar reference condition |
| **ARC** | Anti-reflective coating |
| **CdTe** | Cadmium telluride |
| **CIGS** | Copper indium gallium selenide |
| **DSSCs** | Dye-sensitized solar cells |
| **EQE** | External quantum efficiency |
| **ETL** | Electron transport layer |
| **FF** | Fill factor |
| **FTO** | Fluorine-doped tin oxide |
| **Ge** | Germanium |
| **HJT** | Heterojunction |
| **HTL** | Hole transport layer |
| **ICL** | Interconnecting layer |
| **IQE** | Internal quantum efficiency |

| | |
|---|---|
| **Jsc** | Short-circuit current density |
| **JV** | Current-voltage |
| **$MAPbI_3$** | Methylammonium lead iodide |
| **MAPI** | $CH_3NH_3PbI_3$ |
| **MPP** | Maximum power point |
| **NiOx** | Nickel oxide |
| **OPV** | Organic photovoltaic |
| **P3HT** | Poly(3-hexylthiophene) |
| **PCE** | Power conversion efficiency |
| **PCBM** | Phenyl-$C_{61}$-butyric acid methyl ester |
| **PSC** | Perovskite solar cell |
| **PSCs** | Perovskite solar cells |
| **PV** | Photovoltaic |
| **PVD** | Physical vapor deposition |
| **RP** | Ruddlesden–Popper |
| **SAED** | Selected area electron diffraction |
| **SC** | Solar cell |
| **SHJ** | Silicon heterojunction |
| **Si** | Silicon |
| **$SiO_2$** | Silicon dioxide |
| **$Si_3N_4$** | Silicon nitride |
| **$SnO_2$** | Tin dioxide |
| **Spiro-OMeTAD** | Spiro-linked hole transport material |
| **SRH** | Shockley–Read–Hall |
| **SQ** | Shockley–Queisser |
| **TCAD** | Technology computer-aided design |
| **TCO** | Transparent conductive oxide |
| **TSCs** | Tandem solar cells |

| | |
|---|---|
| **TOPCon** | Tunnel oxide passivated contact |
| **UV** | Ultraviolet |
| **Voc** | Open-circuit voltage |
| **ZnO** | Zinc oxide |

# ABSTRACT

This thesis is part of the development of new-generation photovoltaic technologies capable of meeting global energy and environmental challenges. Faced with the structural and efficiency limitations of silicon solar cells, perovskite-based materials have emerged as a promising alternative thanks to their remarkable optoelectronic properties, low manufacturing cost and flexibility of integration. The main objective of this work is to study, design, and model advanced perovskite-based solar cells, as well as perovskite/silicon tandem architectures, using analytical approaches and numerical simulations, and to validate the obtained results by comparison with a experimental study. First, a rigorous analytical model was developed to describe the electrical behaviour of a single-junction n–i–p perovskite cell. This model is based on the coupled solution of the continuity and Poisson equations, integrating optical generation and the internal electric field in the absorbing layer. The analytical expressions obtained were used to plot the current-voltage (J–V) characteristics and extract the essential photovoltaic parameters, revealing a power conversion efficiency (PCE) of 12.8%, very close to the experimental value of 13.15% reported in the literature. Parametric analysis showed that the thickness of the perovskite layer directly influences the overall efficiency, while the doping of the electron transport layer ($TiO_2$) plays a decisive role in charge extraction efficiency. Extending the model to a perovskite/silicon (n–i–p) tandem architecture demonstrated the superiority of this configuration, achieving efficiencies greater than 26%, while validating the relevance of the proposed analytical model.

In a second step, numerical simulations were performed using Silvaco TCAD software to confirm the validity of the model and study the effects of physical and technological parameters on performance. The reference structure FTO/$TiO_2$/$MAPbI_3$/Spiro-OMeTAD was first simulated, then optimised by introducing Ruddlesden–Popper-type 2D/3D hybrid materials, which improved efficiency from 12.69% ($MAPbI_3$) to 18.32%, representing a significant gain in performance while enhancing the stability of the device. Comparative analysis of hole transport layers (HTL) showed that the PolyTPD compound offers the best compromise between efficiency and durability. On this basis, a perovskite/silicon HJT tandem cell was designed, demonstrating excellent spectral complementarity and efficiencies exceeding 30%. Finally, a complementary thermal study highlighted the sensitivity of performance to temperature variations, confirming the need for optimised thermal management to ensure long-term stability. This work makes an original contribution to the understanding and modelling of perovskite-based solar cells by establishing a direct correlation between fundamental carrier physics, analytical modelling and numeri-

cal simulation. The results obtained pave the way for the rational design of more efficient, stable and industrialisable photovoltaic devices, actively contributing to the advent of a new generation of sustainable solar technologies.

**Keywords:** solar cells, perovskite, tandem architecture, analytical modelling, numerical simulation, photovoltaic efficiency, thermal stability, 2D/3D hybrid materials, charge transport layer.

# الملخص


تندرج هذه الأطروحة في إطار تطوير تقنيات الخلايا الكهروضوئية من الجيل الجديد القادرة على مواجهة التحديات الطاقوية والبيئية العالمية. ونظرًا للقيود البنيوية ومحدودية الكفاءة التي تعاني منها الخلايا الشمسية المصنوعة من السيليكون، برزت المواد القائمة على البيروفسكايت كبديل واعد بفضل خصبخصائصها البصرية والإلكترونية المتميزة، وتكلفتها المنخفضة في التصنيع، ومرونتها العالية في التكامل ضمن مختلف البنى الهندسية. الهدف الرئيسي من هذا العمل هو دراسة وتصميم ونمذجة خلايا شمسية متقدمة تعتمد على البيروفسكايت، إضافةً إلى بنى هجينة من نوع بيروفسكايت/سيليكون، وذلك من خلال الجمع بين النمذجة التحليلية والمحاكاة العددية، والتحقق من النتائج عبر المقارنة مع دراسة تجريبية .

في المرحلة الأولى، تم تطوير نموذج تحليلي دقيق لوصف السلوك الكهربائي لخلية بيروفسكايت ذات وصلة بسيطة من نوع n–i–p. يعتمد هذا النموذج على الحل المزدوج لمعادلات الاستمرارية وبواسون، مع الأخذ في الاعتبار توليد الضوء والمجال الكهربائي الداخلي في طبقة الامتصاص. وقد مكنت المعادلات التحليلية المستخلصة من رسم خصائص التيار–الجهد (J–V) واستخلاص أهم المعلمات الكهروضوئية، حيث أظهرت كفاءة تحويل (PCE) قدرها 12.8%، وهي قريبة جدًا من القيمة التجريبية البالغة 13.15% المذكورة في الأدبيات. وأظهرت الدراسة البارامترية أن سماكة طبقة البيروفسكايت تؤثر مباشرة على الكفاءة الإجمالية، في حين أن تركيز التطعيم في طبقة نقل الإلكترونات ($TiO_2$) يلعب دورًا حاسمًا في فعالية استخلاص الشحنات. كما أظهر توسيع النموذج إلى بنية خلية هجينة بيروفسكايت/سيليكون تفوقًا واضحًا لهذه البنية، حيث وصلت الكفاءة إلى أكثر من 26%، مما يؤكد صحة النموذج المقترح.

في المرحلة الثانية، أُجريت محاكاة عددية باستخدام برنامج Silvaco TCAD للتحقق من صحة النموذج ودراسة تأثير المعلمات الفيزيائية والتكنولوجية على أداء الخلية. تم أولاً محاكاة البنية المرجعية FTO/$TiO_2$/$MAPbI_3$/Spiro-OMeTAD، ثم تحسينها بإدخال مواد هجينة ثنائية وثلاثية الأبعاد من نوع Ruddlesden–Popper، مما أدى إلى رفع الكفاءة من 12.69% (في $MAPbI_3$) إلى 18.32%، مع تعزيز ملحوظ في الاستقرار الحراري. وأظهرت المقارنة بين طبقات نقل الفجوات (HTL) أن مادة PolyTPD تمثل أفضل توازن بين الكفاءة والمتانة. بناءً على ذلك، تم تصميم خلية هجينة بيروفسكايت/سيليكون HJT أظهرت تكاملاً طيفيًا ممتازًا وكفاءات تجاوزت 30%. وأخيرًا، أبرزت دراسة حرارية إضافية حساسية أداء الخلايا تجاه تغيرات درجة الحرارة، مؤكدةً ضرورة إدارة حرارية مثالية لضمان الاستقرار على المدى الطويل.

تقدم هذه الأطروحة مساهمة أصلية في فهم ونمذجة الخلايا الشمسية المعتمدة على البيروفسكايت، من خلال الربط بين الفيزياء الأساسية لحركة الحوامل، والنمذجة التحليلية، والمحاكاة العددية. كما تمهد النتائج المتحصل عليها الطريق نحو تصميم عقلاني لخلايا شمسية أكثر كفاءة واستقرارًا وقابلة للتصنيع الصناعي، مما يسهم بفاعلية في بزوغ جيل جديد من التقنيات الشمسية المستدامة.



**الكلمات المفتاحية:** الخلايا الشمسية، البيروفسكايت، البنى الهجينة (Tandem)، النمذجة التحليلية، المحاكاة العددية، كفاءة التحويل الضوئي، الاستقرار الحراري، المواد الهجينة 2D/3D، طبقة نقل الشحنات.

# RÉSUMÉ

Cette thèse s'inscrit dans le cadre du développement de technologies photovoltaïques de nouvelle génération capables de répondre aux défis énergétiques et environnementaux mondiaux. Face aux limites structurelles et d'efficacité des cellules solaires au silicium, les matériaux à base de pérovskites se sont imposés comme une alternative prometteuse grâce à leurs propriétés optoélectroniques remarquables, leur faible coût de fabrication et leur flexibilité d'intégration. L'objectif principal de ce travail est d'étudier, de concevoir et de modéliser des cellules solaires avancées à base de pérovskites, ainsi que leurs architectures tandem pérovskite/silicium, en combinant une approche analytique, des simulations numériques et une validation par comparaison avec une étude expérimentale. Dans un premier temps, un modèle analytique rigoureux a été développé afin de décrire le comportement électrique d'une cellule pérovskite simple jonction de type n–i–p. Ce modèle repose sur la résolution couplée des équations de continuité et de Poisson, en intégrant la génération optique et le champ électrique interne dans la couche absorbante. Les expressions analytiques obtenues ont permis de tracer les caractéristiques courant-tension (J–V) et d'extraire les paramètres photovoltaïques essentiels, révélant une efficacité de conversion (PCE) de 12,8 %, très proche de la valeur expérimentale de 13,15 % rapportée dans la littérature. L'analyse paramétrique a montré que l'épaisseur de la couche pérovskite influence directement le rendement global, tandis que le dopage de la couche de transport électronique ($TiO_2$) joue un rôle déterminant dans l'efficacité d'extraction des charges. L'extension du modèle à une architecture tandem pérovskite/silicium (n–i–p) a permis de démontrer la supériorité de cette configuration, atteignant des rendements supérieurs à 26 %, tout en validant la pertinence du modèle analytique proposé.

Dans un second temps, des simulations numériques ont été réalisées à l'aide du logiciel Silvaco TCAD afin de confirmer la validité du modèle et d'étudier les effets des paramètres physiques et technologiques sur les performances. La structure de référence FTO/$TiO_2$/$MAPbI_3$/Spiro-OMeTAD a d'abord été simulée, puis optimisée en introduisant des matériaux hybrides 2D/3D de type Ruddlesden–Popper, qui ont permis d'améliorer l'efficacité de 12,69 % ($MAPbI_3$) jusqu'à 18,32 %, traduisant un gain notable en performance tout en renforçant la stabilité du dispositif. L'analyse comparative des couches de transport de trous (HTL) a montré que le composé PolyTPD offre le meilleur compromis entre rendement et durabilité. Sur cette base, une cellule tandem pérovskite/silicium HJT a été conçue, démontrant une excellente complémentarité spectrale et des rendements dépassant 30 %. Enfin, une étude thermique complémentaire

a mis en évidence la sensibilité des performances aux variations de température, confirmant la nécessité d'une gestion thermique optimisée pour assurer la stabilité à long terme. Ce travail apporte une contribution originale à la compréhension et à la modélisation des cellules solaires à base de pérovskite, en établissant une corrélation directe entre la physique fondamentale des porteurs, la modélisation analytique et la simulation numérique. Les résultats obtenus ouvrent la voie à la conception rationnelle de dispositifs photovoltaïques plus efficaces, stables et industrialisables, participant activement à l'avènement d'une nouvelle génération de technologies solaires durables.

**Mots clés :** cellules solaires, pérovskite, architecture tandem, modélisation analytique, simulation numérique, efficacité photovoltaïque, stabilité thermique, matériaux hybrides 2D/3D, couche de transport de charges.

# GENERAL INTRODUCTION

Humanity is currently at a decisive turning point in terms of energy. The gradual depletion of fossil fuel resources, combined with the constant increase in global energy demand and the worsening of climate change, requires the urgent implementation of sustainable, carbon-free and accessible energy systems. In this context, renewable energies appear to be an essential solution to these global challenges. Among them, solar energy occupies a prominent place thanks to its universal availability, its inexhaustible nature and its ability to produce clean electricity without direct greenhouse gas emissions.For several decades, the photovoltaic conversion of solar energy into electricity has been a major area of research. Crystalline silicon-based solar cells have dominated the photovoltaic industry thanks to their technological maturity, stability and respectable efficiency. However, despite decades of optimisation, these devices are now reaching their fundamental limits, notably the Shockley–Queisser limit, which restricts the maximum theoretical efficiency of single-junction cells to around 29%. In addition, the cost of production, mechanical rigidity and low absorption of silicon for certain wavelengths impose constraints on new applications.

These limitations have motivated the search for alternative materials capable of offering higher efficiencies, simple and inexpensive manufacturing processes, and great flexibility of integration. Second-generation solar cells, based on thin films (CIGS, CdTe, a-Si), have enabled lower production costs and greater flexibility, but at the expense of moderate efficiency and environmental issues related to certain toxic materials. More recently, third-generation solar cells have opened up new prospects by combining high efficiency, low cost and simple manufacturing processes. Among these, cells based on hybrid perovskite materials have emerged as a revolutionary advance, transforming the global photovoltaic landscape.

These materials have remarkable optoelectronic properties, an adjustable band gap, high absorption coefficient, long charge carrier lifetime, balanced electron and hole mobility, and the possibility of low-temperature deposition. These exceptional characteristics explain the spectacular increase in the efficiency of perovskite-based solar cells, which has risen from 3.8% in 2009 to over 26% today. However, despite these impressive performances, several challenges remain and are limiting the large-scale commercialisation of these devices, the chemical and thermal stability of the perovskite layer, sensitivity to

humidity, degradation under prolonged illumination, and losses related to recombination at interfaces. A thorough understanding of the physical mechanisms governing carrier transport and recombination is therefore essential to improve the reliability and performance of these devices. At the same time, the rise of tandem architectures has opened up new possibilities for overcoming the limitations of single-junction cells. The principle is based on the superimposition of two complementary photovoltaic cells, a top cell with a wide bandgap (often perovskite) absorbing high-energy photons, and a bottom cell with a narrower bandgap capturing lower-energy photons. This spectral coupling allows for more efficient use of the solar spectrum and theoretically leads to efficiencies exceeding 30%. Perovskite/silicon tandem structures, particularly those based on heterojunction silicon (HJT) cells, are currently one of the most promising avenues for the next generation of high-efficiency photovoltaic devices.

This thesis entitled *Study, design and modelling of advanced solar cells* is part of a scientific approach aimed at exploring, understanding and optimising the performance of new-generation solar cells, with a particular focus on perovskite-based devices and perovskite/silicon tandem structures. The approach adopted combines analytical modelling, numerical simulation, and comparison with experimental data. enabling a comprehensive and hierarchical understanding of the behaviour of these devices. More specifically, this work aims to:

- Present the theoretical and technological foundations essential to semiconductors and the physical principles of photovoltaic conversion.
- Conduct an in-depth analysis of perovskite materials, their optoelectronic properties, cell architectures and technological constraints, with a focus on the factors influencing their stability and efficiency.
- Develop a rigorous analytical model describing the electrical and optical phenomena in single-junction perovskite cells, then extend this model to tandem structures.
- Perform accurate numerical simulations with Silvaco TCAD software on a single-junction perovskite cell, enabling rigorous cross-validation between the analytical model and experimental data. Subsequently, extend this simulation to tandem architectures in order to evaluate their behaviour and performance.
- Explore strategies for optimising transport layers, absorbing materials (particularly 2D/3D Ruddlesden–Popper-type perovskites) and interfaces, studying their influence on thermal stability and overall performance.

The thesis is structured into four main chapters, organised coherently to follow the scientific progression of the work:

The first chapter begins with an in-depth analysis of the global energy context, highlighting humanity's continuing dependence on fossil fuels, their environmental consequences and the need for a transition to renewable, clean and sustainable energy sources. This reflection naturally leads to a focus on solar energy, an inexhaustible and accessible resource whose potential offers a credible alternative to conventional energies. With this

in mind, a section is devoted to solar radiation and the solar constant, which are essential for understanding the amount of energy received by the Earth and the parameters influencing photovoltaic conversion. The concepts of solar spectrum, irradiance, inclination and geographical position are presented in order to establish the physical basis for the conversion of light energy into electrical energy. On this basis, the chapter introduces the fundamental properties of semiconductor materials, the pillars of photovoltaic devices. It details band structure, the concept of band gap, doping, charge carrier mobility, enabling an understanding of the phenomena of charge absorption and transport. These concepts lead to the study of the principles of photovoltaics, through a description of how the p–n junction works, the process of charge carrier generation under illumination, and the phenomena of recombination and transport. Finally, the chapter concludes with a classification of solar cells according to their generations, from crystalline silicon-based technologies (first generation) to thin films (second generation), to innovative third-generation devices. This progression highlights the successive advances in the quest for superior performance, reduced costs and increased durability.

The second chapter is devoted to an in-depth study of perovskite materials and their integration into third-generation solar cells. It begins with a presentation of the historical context and rapid progress of halogen-hybrid perovskite materials, followed by a detailed analysis of their crystallographic structure, optoelectronic properties, and composition engineering strategies aimed at improving their stability and performance. Various families of perovskites are discussed, including conventional 3D structures, mixed cation or halide perovskites, and Ruddlesden–Popper-type 2D/3D hybrid architectures, providing a comprehensive overview of recent advances in this field. The chapter then focuses on the manufacturing and deposition processes for perovskite layers. A comprehensive analysis of the design and operation of perovskite-based solar cells is also developed, including the mechanisms of carrier generation, transport and recombination, as well as the main challenges related to stability and industrial scaling. Finally, the last part of the chapter deals with tandem solar cells, presenting their physical principles, integration architectures and possible material combinations, in order to highlight their potential to exceed the efficiency limits of single-junction cells.

The third chapter focuses on the development of a rigorous analytical model of perovskite-based solar cells and its extension to perovskite/silicon tandem architectures. First, a theoretical framework based on continuity and carrier transport equations is established, allowing for a precise description of the physical processes of generation, diffusion and recombination within a single-junction perovskite cell. The analytical relationships obtained between current and voltage make it possible to plot J–V characteristics and extract essential photovoltaic parameters such as short-circuit current, open-circuit voltage, fill factor and overall efficiency. In a second step, this model is generalised to a monolithic two-terminal tandem architecture, integrating a top perovskite subcell and a lower silicon subcell. The analysis highlights the electrical interactions between the two subcells, in particular the condition of current continuity and voltage summation, while emphasizing the importance of optimising the absorbing thicknesses for optimal current matching. The results obtained demonstrate the major advantage of the tandem configuration, which is capable of overcoming the efficiency limits imposed on single-junction cells.

The fourth chapter is devoted to an in-depth numerical study aimed at validating and consolidating the analytical model previously developed for perovskite-based solar cells. Using Silvaco TCAD simulation software, a single-junction perovskite cell was simulated by incorporating realistic physical parameters such as interfacial recombination, spectral dependence of absorption and carrier transport properties. Cross-validation between analytical and numerical results and experimental data from the literature was used to assess the accuracy and robustness of the model. The subsequent parametric study focused on the influence of the absorbing material, comparing a reference three-dimensional (3D) perovskite with a Ruddlesden–Popper-type 2D/3D hybrid structure, as well as on the role of the hole transport layer (HTL) through the analysis of different organic and inorganic materials. The most efficient configuration obtained was then used as the basis for the design of a perovskite/silicon heterojunction (HJT) tandem cell, highlighting the significant gains in efficiency and stability offered by this advanced architecture. Finally, a thermal analysis was performed to evaluate the stability of the device and the evolution of its performance under different temperature and illumination conditions.

In conclusion, this thesis is part of an integrated and progressive approach, ranging from the physical fundamentals of photovoltaics to the design of advanced devices based on perovskite materials and tandem structures. It combines analytical modelling and numerical simulation, together with comparison with experimental data, in a coherent approach aimed at linking fundamental phenomena to the actual performance of solar cells. The results obtained make original contributions to the understanding of transport, recombination and functional layer optimisation mechanisms, while demonstrating the potential of tandem architectures to overcome the limitations of single-junction cells. This work thus opens up promising prospects for the rational design of high-efficiency, stable and economically competitive photovoltaic technologies, actively contributing to the sustainable energy transition of the future.

CHAPTER

# 1

# GLOBAL ENERGY CHALLENGES AND THE BASICS OF PHOTOVOLTAICS

## 1.1 Introduction

The planet is currently facing an energy crisis of unprecedented proportions, characterised by the gradual depletion of fossil fuel resources, sustained growth in global energy demand and the worsening effects of climate change. This combination of challenges requires a rapid and profound transition to sustainable, decarbonised and accessible energy systems that are capable of meeting growing needs while limiting the environmental footprint. In this context, solar energy occupies a central place among renewable solutions. Photovoltaic conversion has established itself as one of the key technologies thanks to spectacular advances in efficiency, reliability and cost reduction, paving the way for increasing competitiveness with conventional sources.

The aim of this first chapter is to provide the theoretical, scientific, and technological foundations necessary for understanding photovoltaics. After a historical and conceptual overview, we will present the physical principles of solar conversion, then propose a structured classification of the different generations of solar cells, detailing their constituent materials, architectures, manufacturing processes, performance, and limitations. We will also examine the main trends in innovation and the prospects for the sectors development.

Finally, this analysis will serve as a natural transition to the following chapters, which focus on emerging materials such as perovskites and advanced architectures such as tandem structures, which are now positioned as major candidates for pushing the limits of photovoltaic conversion and paving the way for the next energy revolution.

## 1.2 Brief history of energy research and developments in photovoltaics

The evolution of energy sources has accompanied human progress, from the use of muscle power and the discovery of fire to the exploitation of fossil fuels with the industrial revolution [1], [2]. Coal, then oil and gas, were the pillars of industrialisation in the 19th and 20th centuries, but their growing environmental impact has driven research towards cleaner and more sustainable alternatives, such as renewable energies in particular: hydroelectricity, wind power, biomass, geothermal energy, and solar energy [3]–[5].

Solar energy, specifically, is now at the heart of the energy transition. Abundant, free, and universally available, it offers immense potential [6]–[9]. In 1839, Edmond Becquerel discovered the photovoltaic effect, the ability of certain materials to generate an electric current when exposed to light [10], [11]. This discovery marked the beginning of research into solar energy, but it was not until 1954 that photovoltaic technology became truly viable, with the creation of the first silicon solar cells by Bell Laboratories, with an efficiency of 6% [12]–[14]. From that point on, progress has been spectacular, efficiency has continued to increase, reaching over 26% today, and technological advances have led to a significant reduction in the production costs of solar panels [15], [16]. Figure 1.1 illustrates the major historical milestones in energy development, with particular emphasis on photovoltaic research and solar energy integration into global strategies.

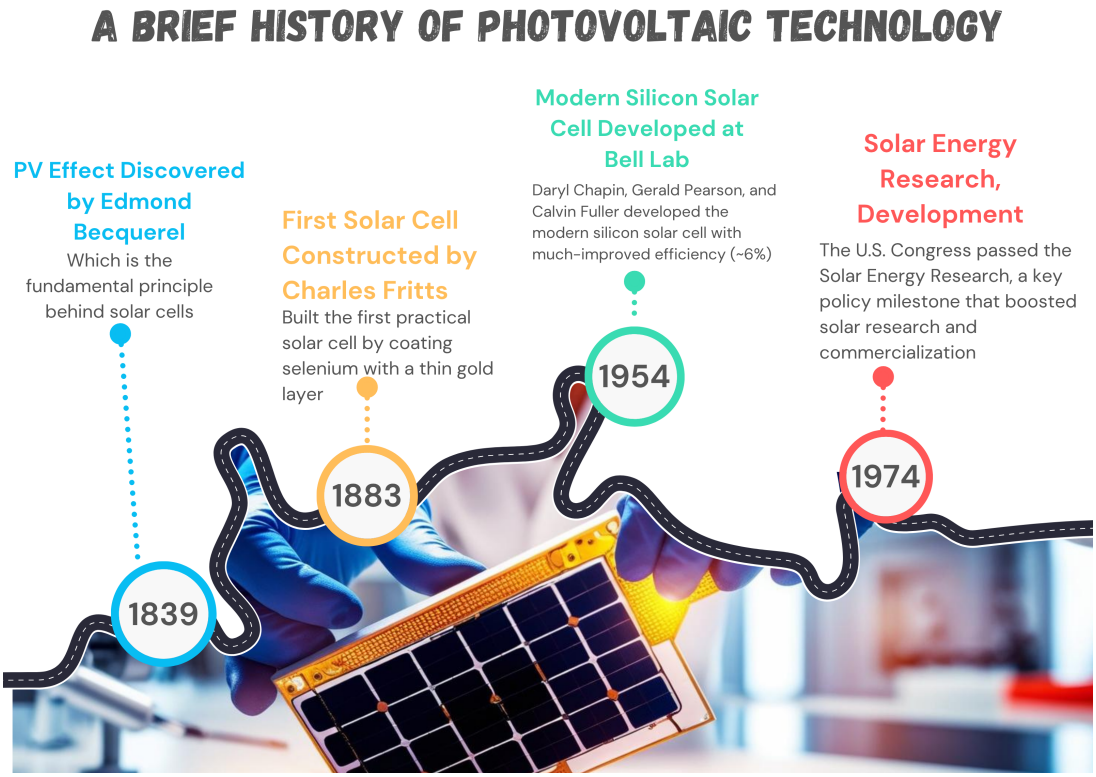



Figure 1.1: Chronological Timeline of Major Milestones in Energy Development and Photovoltaic Research.

The first practical solar cell, made by Charles Fritts in 1883, combined a thin layer of gold and selenium, but its low efficiency (around 1%) prevented large-scale commercial adoption [11], [17]. However, it marked a key milestone in the development of this technology. Today, installed photovoltaic capacity exceeds 2,200 GW (2.2 terawatts) worldwide, with rapid growth in installations around the world, supported by falling costs and continuous improvements in efficiency [18]–[20]. Figure 1.2 illustrates the historic and projected global installed photovoltaic capacity from 2015 to 2035, highlighting solar accelerating growth trend.

Solar photovoltaic energy is now a pillar of clean electricity generation, not only because of its abundance, but also because of its modularity and its ability to be integrated into various sectors such as industry, residential, and transportation [21]–[23]. Recent innovations, such as perovskite solar cells, which have seen their efficiency increase from 3.8% to over 25% in a decade, open up new prospects for the future of solar energy [24]–[27]. These advances are likely to further strengthen the role of solar energy in the global energy mix. Thanks to its availability, modularity, and integrability, solar photovoltaic energy is positioned as a key lever in the global energy transition, with a growing role in the electrification of the industrial, residential, and transportation sectors in the coming decades [28]. Today, solar photovoltaic energy accounts for around 3% of global electricity production, a rapidly growing share, and is expected to continue to play a major role in meeting the growing demand for clean electricity worldwide [29], [30].

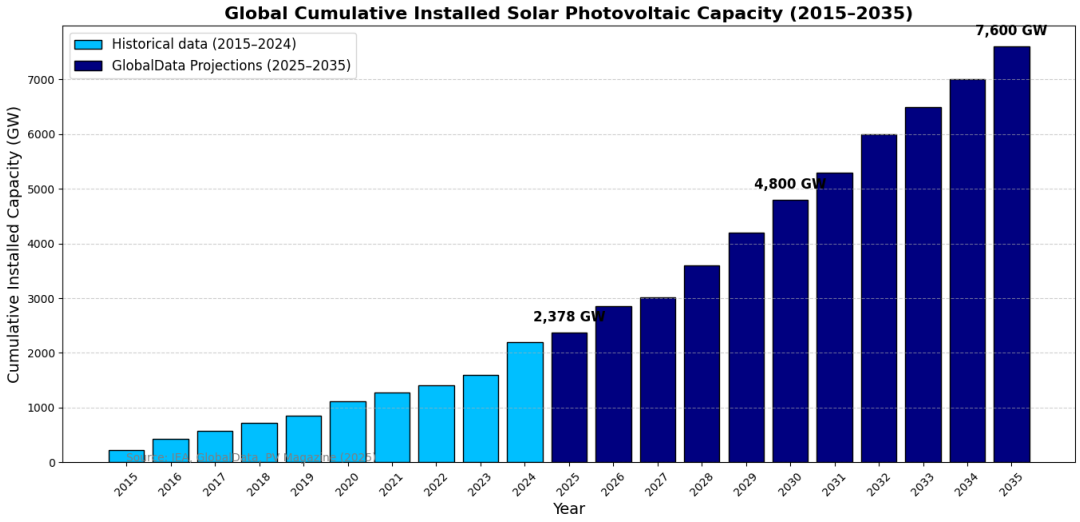



Figure 1.2: Global Installed Solar Photovoltaic Capacity, 2015–2035 [18].

## 1.3 Solar radiation and the solar constant

The Sun is the main source of radiant energy for the Earth, emitting a continuous spectrum of electromagnetic radiation covering a wide range of wavelengths, from ultraviolet to near infrared. Incident radiation plays a fundamental role in photovoltaic conversion, as it provides the energy base to be converted into electricity [31], [32].

The average intensity of solar radiation measured above the Earth's atmosphere is called the solar constant. Its standardized value is approximately 1361 W/m$^2$, corresponding to the power received per unit area perpendicular to the sun rays in a vacuum, at the average distance between the Earth and the Sun [33]. When it passes through the atmosphere, solar radiation is attenuated and modified by several phenomena such as:

- Absorption by atmospheric gases (ozone, water vapor, carbon dioxide).
- Molecular (Rayleigh) and particle (Mie) scattering.
- Reflection by clouds and aerosols.

These interactions reduce the light intensity and alter the spectral composition compared to the initial radiation. In order to qualify and standardize the performance of photovoltaic cells under terrestrial conditions, standard spectra known as Air Mass (AM) are defined [34].

Air Mass represents the relative optical distance traveled by sunlight in the atmosphere, normalized to the trajectory when the Sun is at its zenith (perpendicular to the ground, AM = 1) [35]. Mathematically, it can be expressed by the following relationship [34]:

$$AM = \frac{1}{\cos\theta} \tag{1.1}$$

Where $\theta$ is the angle of solar elevation relative to the vertical.

As illustrated in Figure 1.3, three main constants are generally considered [32]:

- AM0, corresponding to radiation measured outside the atmosphere, used mainly for space applications and fundamental research.
- AM1, which corresponds to zenith sunlight, when the Sun rays strike the Earth's surface perpendicularly (zero angle of incidence).
- AM1.5, corresponding to refracted solar radiation passing through an air mass 1.5 times that at the zenith (approximately a solar angle of 48°), considered the standard terrestrial reference for testing photovoltaic cells. There are two variants, AM1.5D (direct sunlight only) and AM1.5G (global, direct plus diffuse).

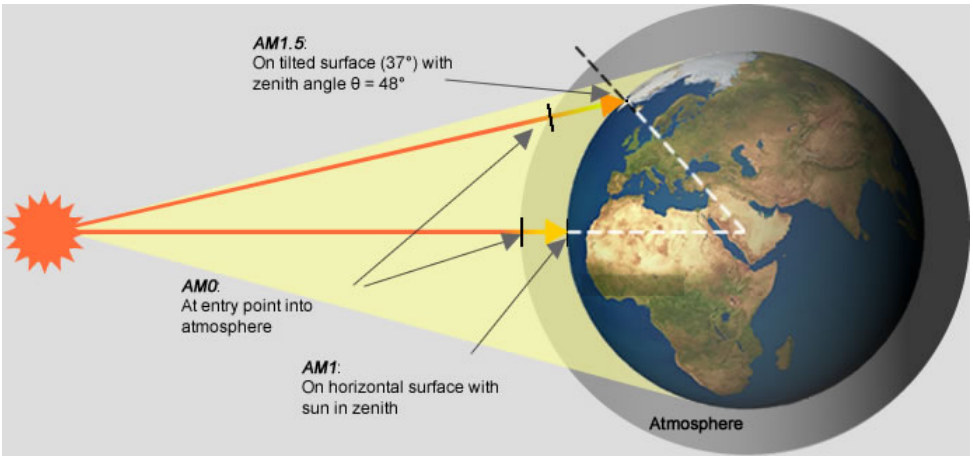



Figure 1.3: Representation of the three illumination constants: AM0 (extraterrestrial), AM1 (zenith), and AM1.5 (standard terrestrial reference condition) [36].

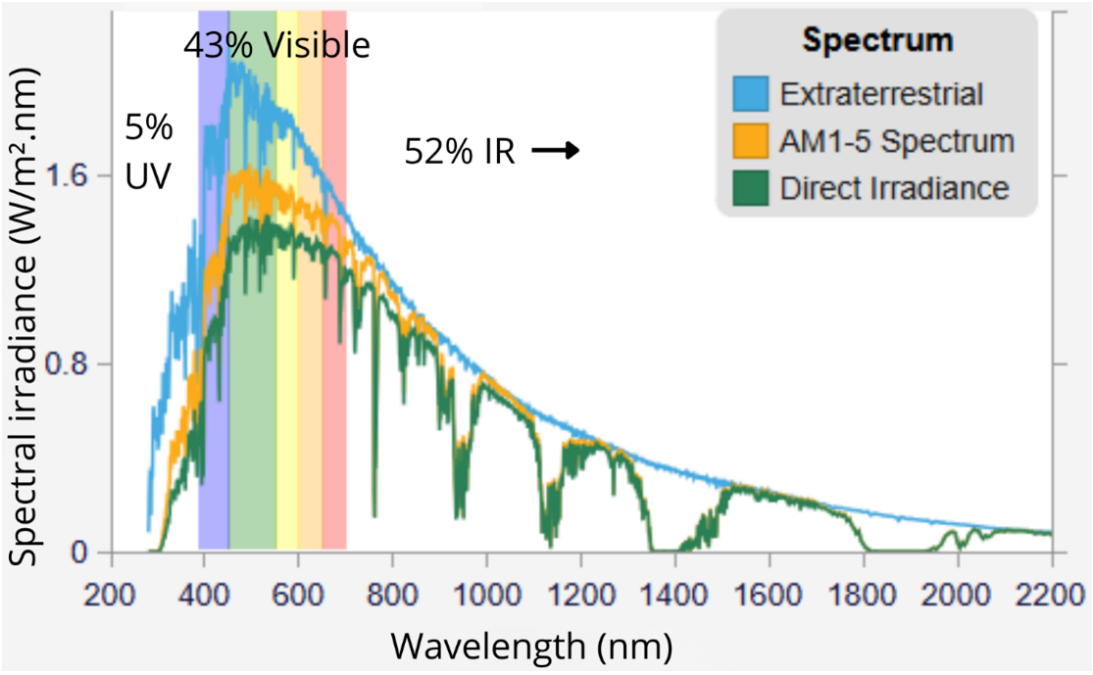



Figure 1.4: Solar spectrum reaching Earth's surface, showing the relative contributions of UV (5%), visible (43%), and IR (52%) bands [36].

The AM1.5 spectrum has a power of approximately 1000 W/m² on a surface perpendicular to the sun rays and distributes energy as follows, approximately 5% in ultraviolet (UV), 43% in visible, and 52% in near infrared (IR) [37], [38], as illustrated in Figure 1.4. This distribution strongly influences the choice and optimization of semiconductor materials capable of efficiently absorbing this energy and maximizing photon-electron conversion [39].

A thorough understanding of the solar spectrum is crucial, not only for characterizing photovoltaic cell performance in laboratory conditions according to international standards, but also for accurately sizing solar systems and reliably estimating their efficiency across different geographical and climatic environments [40], [41].

## 1.4 Semiconductor materials in photovoltaics

### 1.4.1 Energy band structure of semiconductors

The core of photovoltaic devices is made up of semiconductors, which convert light energy directly into electrical energy. Semiconductors are materials whose electrical properties are situated between those of conductors and insulators, enabling controlled conductivity that is essential for the photovoltaic effect. Their operation is based on an electronic structure based on energy bands, which determine the ability to absorb light and conduct charges, and therefore their electrical and optical properties. A SC is characterised by a valence band, filled with electrons, and a conduction band, initially empty. These two bands are separated by an energy band gap $E_g$, in which no electronic state is available without external excitation [42]–[44]. At 0 K, the conduction band is empty while the valence band is full, as the temperature increases, $E_g$ decreases, allowing some valence electrons to migrate into the conduction band, thereby increasing conductivity. Figure 1.5 illustrates the fundamental energy band structure of a semiconductor, showing the valence band, conduction band, and the band gap.

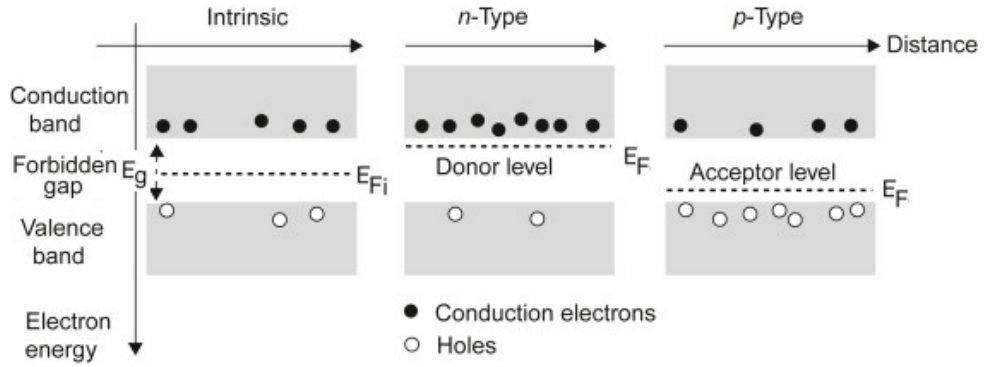



Figure 1.5: Energy diagram of the semiconductor [42].

### 1.4.2 Semiconductor materials and optimal band gap

Semiconductors can be simple elements such as silicon (Si, $E_g \approx 1.12$ eV at 300 K) or germanium (Ge, $E_g \approx 0.66$ eV), binary compounds such as indium phosphide (InP,

$E_g \approx 1.34$ eV), gallium arsenide (GaAs, $E_g \approx 1.42$ eV) or cadmium telluride (CdTe, $E_g \approx 1.45$ eV), as well as ternary alloys such as aluminum gallium arsenide ($Al_xGa_{1-x}As$, tunable $E_g$ between ∼1.4 and 2.2 eV) or silicon germanium ($Si_xGe_{1-x}$, $E_g$ between ∼0.66 and 1.12 eV depending on composition). These materials are generally characterised by a crystalline structure where tetravalent atoms form covalent bonds; for example, the crystal structure of silicon organises atoms into a lattice where each atom shares four valence electrons with its neighbours, thereby completing their outer shells.

For optimal photovoltaic efficiency, $E_g$ should ideally be between 1.1 eV and 1.6 eV, ensuring a good compromise between absorption of the solar spectrum and generation of electrical voltage. A small gap increases thermal losses, while a large gap limits absorption and therefore the current generated. The theoretical maximum efficiency is therefore constrained by this value, according to the Shockley-Queisser limit [45]–[47]. The position of the donor and acceptor levels in the bandgap close to conduction and valence, respectively, minimises the energy required to release carriers, thereby optimising the spectral response around the bandgap. While the band gap $E_g$ determines the fundamental ability of a semiconductor to absorb light and generate electron–hole pairs, the overall conversion efficiency of a photovoltaic cell also depends on the fate of these carriers once generated. Efficient devices require not only optimal absorption but also the generation, separation, and collection of photogenerated carriers. This in turn involves high carrier mobilities, which enable rapid transport, and long carrier lifetimes, which limit recombination before extraction. Both parameters are strongly affected by crystalline purity and defect density, and can be improved by strategies such as surface passivation or the incorporation of dedicated transport layers that suppress recombination. For example, state-of-the-art high-efficiency cells typically require mobilities exceeding 1000 $cm^2/V \cdot s$ and carrier lifetimes longer than 1 ms, values that are achievable only with high-quality crystalline semiconductors and effective passivation treatments.

Semiconductors can be classified as intrinsic, consisting of pure materials with low conductivity, or extrinsic, obtained by doping with impurities to significantly enhance conductivity [44], [48]. Doping with pentavalent atoms such as phosphorus or arsenic introduces free electrons (n-type), while trivalent dopants such as boron or aluminum create holes (p-type). This controlled doping enables the formation of the PN junction, a fundamental building block of photovoltaic devices. At the interface between p- and n-type regions, a depletion region is created with an internal electric field that drives the separation and transport of photogenerated electron–hole pairs, thereby enabling current generation [49], [50]. The equilibrium potential barrier ($V_{bi}$) is typically around 0.7 V for Si and 0.3 V for Ge at 300 K. Figure 1.6 illustrates the PN junction, highlighting the depletion layer, the built-in electric field, and the distribution of majority and minority carriers that underpin photovoltaic operation.

The SC materials used in PV are classified essentially according to their crystalline structure (crystalline or amorphous) and their chemical nature (inorganic, organic or hybrid). Each of these categories exhibits distinct electronic, optical and technological properties, which determine the conversion efficiency, long-term stability and manufacturing and integration possibilities of solar cells [43]. Table 1.1 summarises these categories, with representative examples and their main characteristics, illustrating their relevance for various photovoltaic applications.

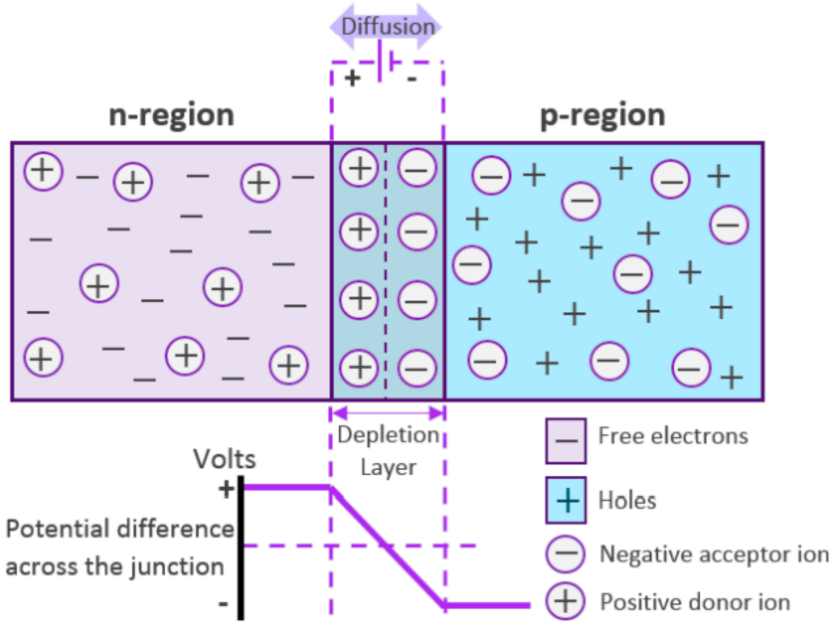



Figure 1.6: Schematic diagram of the PN junction [49].

Table 1.1: Classification of semiconductor materials used in photovoltaics [51]–[54].

| **Crystalline structure** | **Chemical nature** | **Examples** | **Notes** |
|---|---|---|---|
| Crystalline | Inorganic | Monocrystalline Si, Polycrystalline Si, GaAs | High stability and carrier mobility (>1000 $cm^2/V \cdot s$ for c-Si), but high cost for GaAs (used in concentrator cells). |
| Crystalline | Hybrid | Halide perovskites (e.g., $CH_3NH_3PbI_3$) | Tunable bandgap ( 1.2–1.6 eV), low-cost fabrication (solution process), but limited stability under humidity. |
| Amorphous | Inorganic | Amorphous Si (a-Si) | Low cost, flexible, thin-film compatible, but poor durability (Staebler–Wronski effect). |
| Crystalline or amorphous | Organic | Polymer semiconductors (P3HT:PCBM) | Lightweight, printable (flexible electronics), but lower durability and photo-oxidative stability. |

## 1.5 The physics of photovoltaics: concept and operation

### 1.5.1 Photovoltaic effect

The photovoltaic effect refers to the fundamental physical phenomenon that causes the direct conversion of light energy into electrical energy in photovoltaic devices. It occurs in certain semiconductor materials when they are exposed to light radiation, such as sunlight [55]–[57].

When a photon, an elementary particle of light with energy $E = h\nu$ (where $h$ is Planck

constant and $\nu$ is the frequency of the radiation), strikes a semiconductor, it can be absorbed if its energy is greater than or equal to the band gap ($E_g$) of the material, defined as $E_g = E_c - E_v$, where $E_c$ and $E_v$ are the energies of the conduction and valence bands, respectively [58]. This absorption excites an electron from the valence band (initial level $E_i$) to the conduction band (final level $E_t$), according to the relationship $h\nu = E_t - E_i$, creating an electron-hole pair. If $E > E_g$, the excess energy is dissipated by thermalization, resulting in energy losses, as shown in Figure 1.7. The electron then becomes a mobile negative charge carrier, while the hole acts as a positive charge carrier [59], [60].

To exploit this generation of carriers and produce an electric current, the photovoltaic cell relies on a specific architecture, mainly a PN junction [61]. This architecture consists of two regions of the same semiconductor doped differently, an n-type region (enriched in electrons) and a p-type region (enriched in holes). At the interface between these two zones, the initial diffusion of majority carriers leads to their partial recombination, forming a depletion zone where a permanent internal electric field emerges [62], [63].

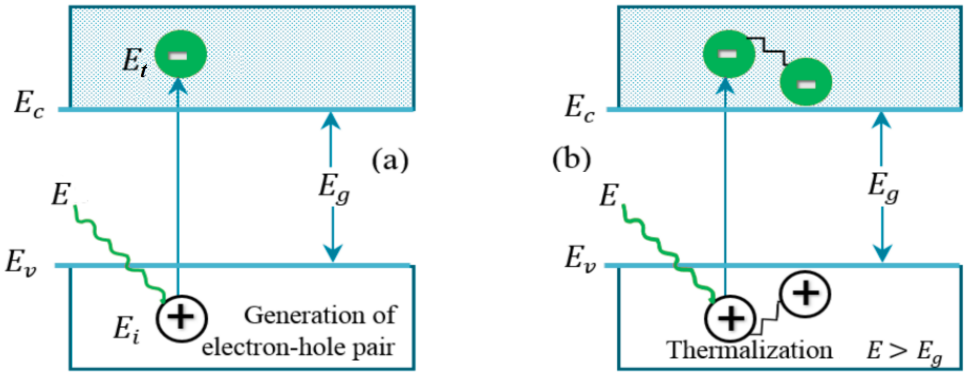



Figure 1.7: Generation of charge carriers through photon absorption [49].

This electric field plays a crucial role; it effectively separates the photogenerated carriers by forcing the electrons to migrate to the n-type region and the holes to the p-type region, preventing their immediate recombination. When metal contacts are placed at the ends of the cell and an external circuit is connected, the separation of charges leads to the orderly flow of a direct electric current. The voltage across the junction, coupled with this current, then provides usable electrical power [64]–[66]. The diagram shown in Figure 1.8 illustrates the principle of operation of the PV effect, detailing the generation of electron-hole pairs, their separation by the internal electric field, and the flow of current in an external circuit.

The efficiency of this process depends on several key physical parameters, including:

- The band gap width $E_g$, which sets the photon absorption threshold. For example, silicon, with a gap of approximately 1.12 eV, efficiently absorbs a large part of the solar spectrum, contributing to its industrial success [68].

- The crystalline quality and electronic properties of the material, which influence the lifetime, carrier mobility and recombination rate, directly impacting conversion efficiency [69].

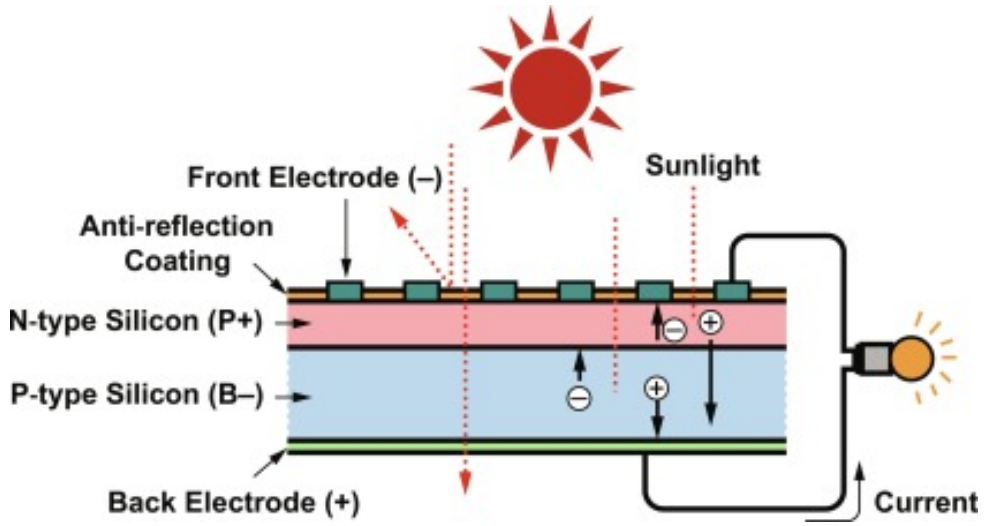



Figure 1.8: Functional diagram of a PN junction photovoltaic cell [67].

- Cell design and engineering, including the optimisation of anti-reflective layers, metal contacts and the thickness of the active layer, in order to maximise carrier collection and minimise resistive losses [70].
- The depth of light penetration, which must correspond to the active zone of efficient carrier generation to optimise photon absorption [71].
- Losses due to thermalisation (excess photonic energy) and recombination (radiative or non-radiative), which reduce energy efficiency, particularly in materials with a short carrier lifetime.

It is also important to note that the current generated by the photovoltaic effect is proportional to the incident light intensity. This phenomenon enables clean, silent and renewable conversion of solar energy into electricity, without polluting emissions, making photovoltaic technology a central pillar of the sustainable energy transition [72], [73].

### 1.5.2 Equivalent Electrical Model and Characteristic Parameters of a Solar Cell

The solar cell can be modeled by an equivalent electrical circuit, as illustrated in Figure 1.9, consisting mainly of a light-generated current source $J_{ph}$, connected in parallel with a PN junction modeled by a diode. Two parasitic resistances are taken into account, a series resistance $R_s$, representing ohmic losses (in metal contacts, electrodes, charge transport layers), and a parallel resistance $R_{sh}$, reflecting leakage currents or shunts internal to the junction. This modelling enables us to quantitatively address the actual electrical response of the cell under different illumination and load conditions [74].

The current-voltage characteristic of a cell is then described by the following equation [39]:

$$J(V) = J_{ph} - J_0 \left( e^{\frac{q(V+JR_s)}{nkT}} - 1 \right) - \frac{V + JR_s}{R_{sh}} \tag{1.2}$$

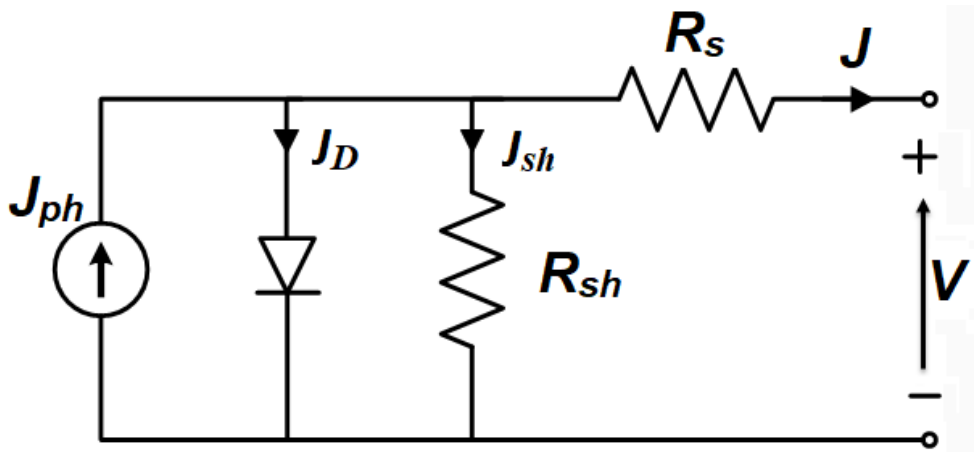



Figure 1.9: Simplified equivalent electrical model of a photovoltaic cell.

Where $J$ is the output current, $J_{ph}$ the light-generated photocurrent (proportional to irradiance and slightly temperature-dependent), $J_0$ the diode saturation current, $V$ the cell terminal voltage, $R_s$ the series resistance, $R_{sh}$ the shunt resistance, $q$ the elementary charge, $n$ the ideality factor of the diode, $k$ the Boltzmann constant and $T$ the absolute temperature [75]. The characterization of a photovoltaic cell electrical performance is based on several essential parameters [35], [76]. These parameters are extracted from the J-V curve illustrated in Figure 1.10, which is obtained under standard illumination. These quantities enable us to assess actual performance and identify the intrinsic and technological limitations influencing its operation.

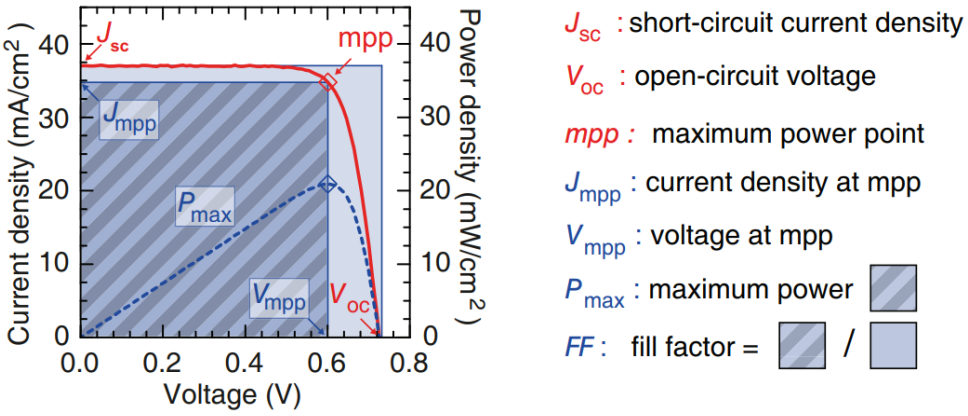



Figure 1.10: Typical current-voltage (J-V) characteristic and related parameters of a solar cell [76].

### 1.5.2.1 Short-circuit current ($J_{sc}$)

The short-circuit current ($J_{sc}$) is the current generated by the cell when the terminal voltage is zero (V = 0), i.e., under short-circuit conditions. It reflects the cell ability to generate and collect charge carriers induced by photon absorption. $J_{sc}$ depends on optical absorption (related to the bandgap of the material) and collection efficiency (influenced by carrier mobility and passivation). For example, $J_{sc}$ reaches 40 mA/cm² for monocrystalline silicon and 25-30 mA/cm² for perovskites due to their different absorption spectra.

#### 1.5.2.2 Open-circuit voltage ($V_{oc}$)

This is the maximum voltage delivered by the cell when no current is drawn (open circuit (J=0)). It expresses the difference in electrical potential generated by the separation of charges at the PN junction. $V_{\text{oc}}$ is limited by the bandgap of the material and non-radiative recombination. For example, perovskite cells have a $V_{\text{oc}}$ of 1.0-1.2 V, while perovskite-silicon tandem cells exceed 1.8 V thanks to better loss management.

#### 1.5.2.3 Fill factor (FF)

Quantifies the quality of the current-voltage curve, it is the ratio between the maximum power actually extracted and the theoretical power ideally available (product of the short-circuit current and the open-circuit voltage). Formally, it is expressed as:

$$FF = \frac{P_{\max}}{J_{sc} \times V_{oc}} = \frac{J_{mpp} \times V_{mpp}}{J_{sc} \times V_{oc}} \tag{1.3}$$

Where Impp and Vmpp are respectively the current and voltage at the maximum power point (MPP). A high FF ($> 80\%$) indicates low resistive and recombination losses, as in silicon heterojunctions (FF 85%) or tandem cells (FF $> 80\%$).

#### 1.5.2.4 Power Conversion Efficiency (PCE)

Efficiency is the fundamental indicator of the overall performance of a photovoltaic cell. It expresses the ability to convert incident light power ($P_{\text{in}}$) into maximum useful electrical power extracted ($P_{\max}$). Mathematically, it is expressed as:

$$PCE = \frac{P_{\max}}{P_{\text{in}}} = \frac{J_{mpp} \times V_{mpp}}{P_{\text{in}}} = \frac{J_{sc} \times V_{oc} \times FF}{P_{\text{in}}} \tag{1.4}$$

#### 1.5.2.5 Quantum efficiency

External Quantum Efficiency (EQE) and Internal Quantum Efficiency (IQE) are fundamental spectroscopic quantities for evaluating the performance of a photovoltaic cell as a function of wavelength. EQE represents the fraction of Incident photons at a given wavelength that are converted into electrons collected in the cell's structure. This parameter includes not only the absorption of photons and the generation of charge carriers, but also the optical losses associated with reflection and transmission, as well as the recombination that occur before the charges are actually collected. In contrast, IQE measures the fraction of photons actually absorbed by the cell that generate charge carriers, thus excluding optical losses at the surface such as reflection and transmission. This distinction makes it possible to isolate purely electronic and recombination effects within the material [77]–[79]. Comparative analysis of the EQE and IQE curves as a function of wavelength exhibits a detailed view of the mechanisms involved in efficiency losses. It enables phenomena such as interface defects, surface and volume recombination and absorption inefficiency in certain spectral ranges to be identified and quantified with precision. This detailed understanding is essential for guiding both optical and electronic optimisation strategies

in the design of photovoltaic devices [80]. The spectral profile of quantum yields, exhibited in Figure 1.11, is therefore an essential analytical tool for improving the design and technological performance of solar cells.

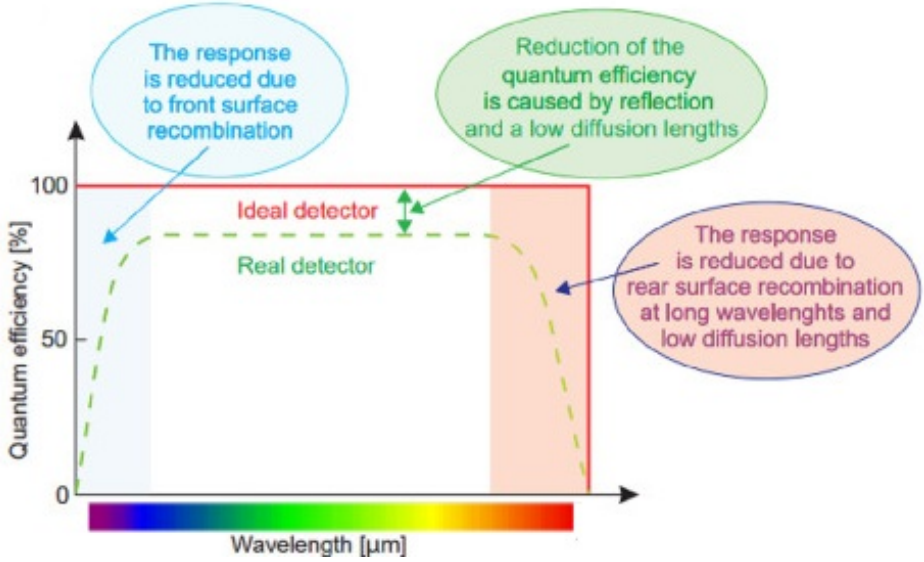



Figure 1.11: Quantum efficiency of an ideal solar cell as a function of the incident photon wavelength [81].

## 1.6 Structure and architecture of photovoltaic cells

The performance of a PV cell depends essentially on the quality of its multilayer architecture, optimised to maximise the conversion of light energy into electrical energy. This conversion is based on the precise organisation of complementary functional layers, each playing a specific role in the generation, separation and collection of electronic charge carriers. An optimised design of these layers, adapted to the properties of the materials (e.g., silicon, perovskites), is crucial to achieve high efficiencies, often exceeding 25% for advanced technologies such as heterojunctions or tandem cells. Controlling the structure and architecture of these layers is therefore essential for optimising the performance and durability of photovoltaic devices [82]. Figure 1.12 shows a diagram of the different functional layers that make up a single-junction photovoltaic cell. The components of a typical photovoltaic cell are as follows [83]–[85]:

### 1.6.1 Substrate

This is the main mechanical support for the device, ensuring rigidity and integrity. Depending on the application, glass (industrial standard), polymer or metal substrates may be used, particularly for flexible cells or those integrated into buildings. In perovskite solar cells, flexible substrates such as Polyethylene Terephthalate (PET) are frequently used to reduce manufacturing costs, lighten the structure and enable portable or curved surface applications [86].

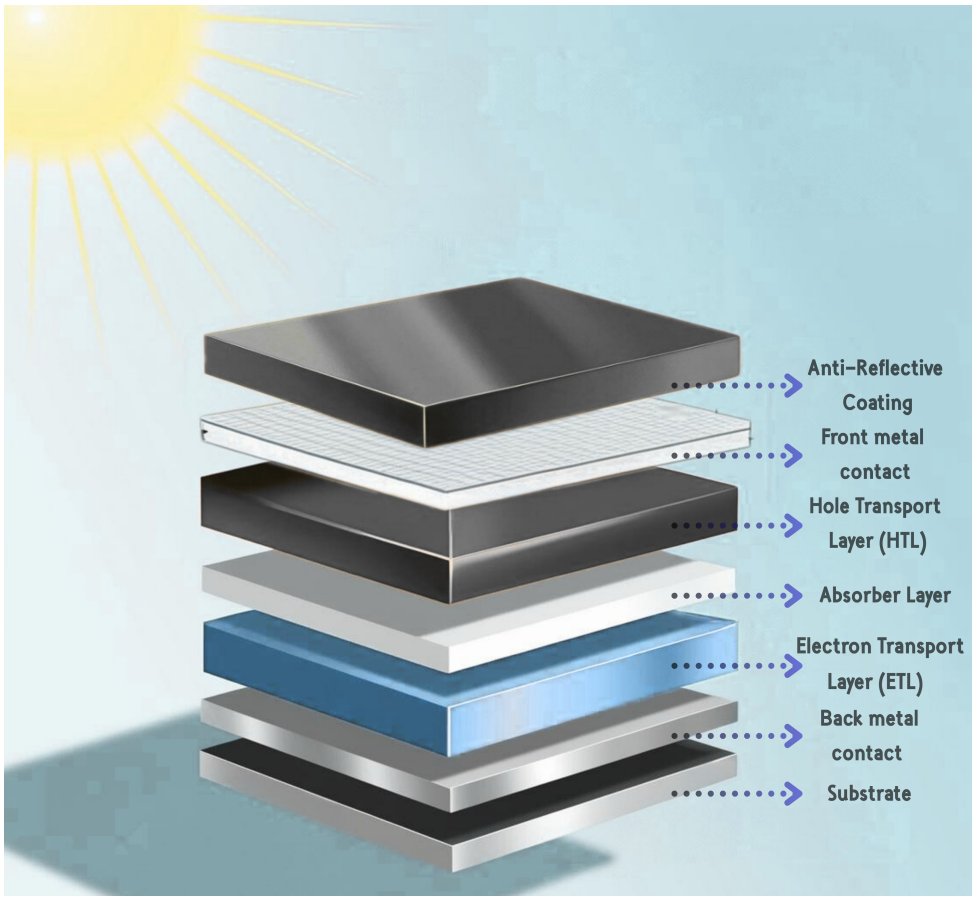



Figure 1.12: Functional layer architecture of a single-junction photovoltaic cell.

### 1.6.2 Absorbing layer

The active core of the device, this layer is responsible for absorbing solar photons and generating electron-hole pairs. It is made from semiconductor materials such as silicon (monocrystalline or polycrystalline), perovskites or other composites suitable for the targeted spectral absorption. The choice of material depends on the target solar spectrum (AM1.5) and efficiency requirements, with perovskites achieving efficiencies above 25% in 2025 thanks to their tunable bandgap.

### 1.6.3 Charge transport layers

These thin semiconductor layers, placed between the absorbing layer and the electrodes, ensure selective carrier transport. The electron transport layer (ETL, e.g., $TiO_2$ or $SnO_2$ in perovskite cells) directs electrons to the cathode, while the hole transport layer (HTL, e.g., spiro-OMeTAD or $NiO_x$) guides holes to the anode. In perovskite-silicon tandem cells, intermediate layers such as ITO optimise intercellular recombination.

### 1.6.4 Anti-reflective coating (ARC)

This layer, usually deposited on the surface, often made of materials such as $SiO_2$ or $Si_3N_4$, reduces the reflection of incident light, lowering optical losses from 10–15% to less than

5% in modern cells. This maximises photon absorption in the active layer. In bifacial cells, ARC is optimised for both sides, increasing overall efficiency.

### 1.6.5 Metal contacts

The metal contacts, in the form of a thin front grid and a continuous rear contact, collect and transfer electrical current. They must combine high conductivity (e.g., silver or aluminum) and low shading (optical transparency >90% for the front grid), so as not to block incident light. Recent technologies, such as TCO (transparent conductive oxide) contacts, improve collection in semi-transparent cells.

### 1.6.6 Surface and interface passivation

Passivation involves covering critical interfaces with thin protective layers (e.g., $Al_2O_3$ or $SiN_x$ for silicon, organic layers for perovskites), reducing surface defects and non-radiative recombination that degrade performance. It is a major lever for improving the electrical quality of cells.

## 1.7 Loss mechanisms and performance limitations

The performance of photovoltaic cells is inherently limited by various loss mechanisms that operate at several physical and technological levels, reducing the overall efficiency of converting sunlight into electricity [87]. These losses can be grouped into four main categories: optical, thermal, electronic, and technological [88], [89].

### 1.7.1 Optical losses

Optical losses occur even before the actual generation of electrical charges [90]. They mainly include:

- The reflection of light at the surface of the cell, which reduces the quantity of photons penetrating the absorbing layer, despite the frequent use of anti-reflective coatings (ARC).
- Unabsorbed photons that pass through the active layer without generating charge carriers, particularly those whose energy is lower than the band gap of the semiconductor material.

These phenomena limit effective photon absorption and therefore the initial generation of electron-hole pairs [32].

### 1.7.2 Thermal losses

Thermal losses refer to the irreversible conversion of part of the light energy into heat.

- Thermalisation, corresponds to the dissipation of excess photon energy—energy above the band gap of the semiconductor—in the form of heat, reducing the maximum electrical voltage that a cell can supply.
- The rise in cell temperature, caused by various factors (absorption, limited heat dissipation), degrades electrical performance, particularly by reducing the open-circuit voltage and maximum power.

These cumulative thermal effects are a significant factor in the intrinsic limitation of efficiency [91].

### 1.7.3 Electronic losses

Electronic losses are a major source of efficiency limitations in photovoltaic cells. They result mainly from the unwanted recombination of charge carriers (electrons and holes) generated by photon absorption, which are therefore unable to be collected to contribute to the electrical current [44]. This recombination reduces both the effective lifetime and diffusion length of minority carriers, leading to a reduction in extractable current and, consequently, in the overall conversion efficiency [92], [93]. Recombination mechanisms can be grouped into three broad categories, illustrated in Figure 1.13.

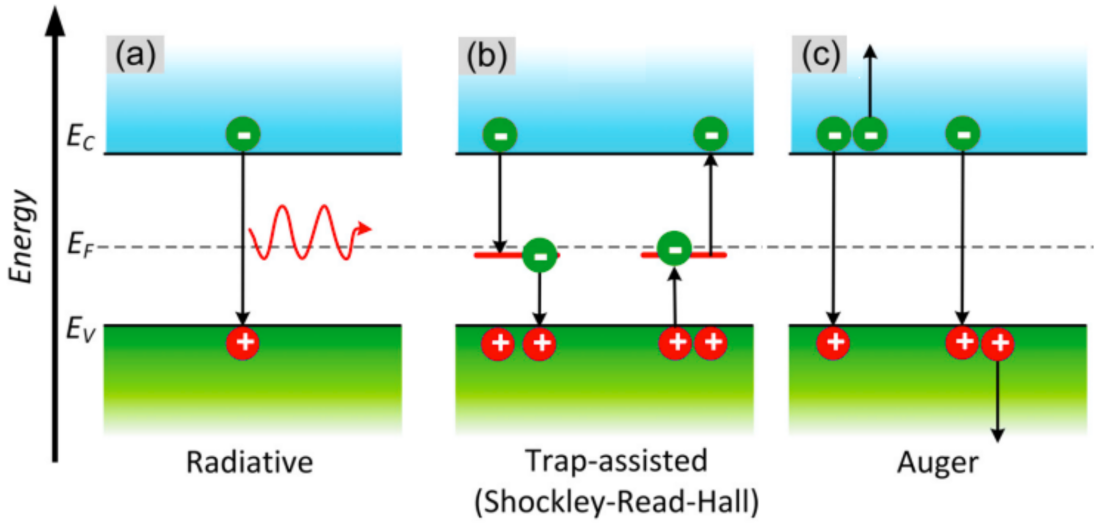



Figure 1.13: Radiative, non-radiative, and Auger recombination mechanisms in photovoltaic cells.

#### 1.7.3.1 Radiative recombination

Radiative recombination is a process in which an electron recombines with a hole by emitting a photon whose energy is close to the band gap of the semiconductor, as depicted in Figure 1.13(a). This mechanism is essentially an inverse process of photon absorption, corresponding to spontaneous emission of light (luminescence). This recombination is known as "band-to-band" and is dominant in direct bandgap semiconductors. It is an intrinsic performance limitation because it corresponds to an energy loss resulting in a photon emitted to the outside, not captured for electrical generation. However, its rate

is generally lower than non-radiative recombination in commercial-grade materials [92], [94].

#### 1.7.3.2 Non-radiative recombination (Shockley–Read–Hall, SRH)

The mechanism of non-radiative recombination is mainly mediated by defects in the semiconductor material, such as impurities, gaps, or trap states within the bulk or at the interfaces. This process, described by the SRH model, leads to the annihilation of carriers without light emission, with the energy dissipated as heat (phonons), as illustrated in Figure 1.13(b). This recombination is particularly important in semiconductors with indirect band gaps, such as crystalline silicon, and in materials exhibiting structural defects or poor surface passivation. It significantly reduces the lifetime and diffusion length of minority carriers, having a negative impact on the collected current and final yield [92], [95].

The SRH recombination rate, which represents the dominant non-radiative recombination mechanism in real semiconductors in the presence of traps, is expressed as follows [96], [97]:

$$R_{\mathrm{SRH}} = \frac{np - n_i^2}{(n + n_t)\tau_{p0} + (p + p_t)\tau_{n0}} \tag{1.5}$$

where $n$ and $p$ are the electron and hole concentrations, $n_i$ is the intrinsic carrier concentration, $\tau_{n0}$ and $\tau_{p0}$ are the minority carrier lifetimes (for electrons and holes, respectively), while $n_t$ and $p_t$ represent the effective carrier densities in the trap state.

#### 1.7.3.3 Auger recombination

Auger recombination is a non-radiative process involving three charge carriers, where the energy released by electron–hole recombination is transferred to a third carrier (electron or hole), excited to a higher energy level in the conduction or valence band. This excited carrier then relaxes by inelastic collisions, resulting in energy loss in the form of heat, as shown in Figure 1.13(c). This mechanism becomes particularly significant at high carrier densities, especially under strong illumination or in heavily doped materials. Auger recombination is a major limitation in high-performance devices, particularly when other recombination mechanisms are effectively controlled [92], [98].

### 1.7.4 Technological losses

Technological losses relate to material and structural imperfections associated with the manufacture and assembly of cells:

- Surface or volume defects, as well as poor-quality interfaces, which increase recombination and degrade performance.
- Resistive effects, such as series and parallel (shunt) resistances due to faulty contacts and interconnections, resulting in power losses caused by the Joule effect.

- Shading of the front metal contacts, particularly the busbar, which reduces the active surface area exposed to light and decreases the generated current.

These factors can also influence the longevity and reliability of photovoltaic modules [32].

## 1.8 Classification of photovoltaic cell generations

Photovoltaic cells are classified into three technological generations based on the active materials used, their architecture, their energy efficiency, and their manufacturing method, as shown in Figure 1.14. This classification reflects the gradual evolution of performance, production costs, and research priorities in the solar field. Each generation meets specific needs such as improving efficiency, reducing costs, integrating new media, or environmental sustainability [61], [99].

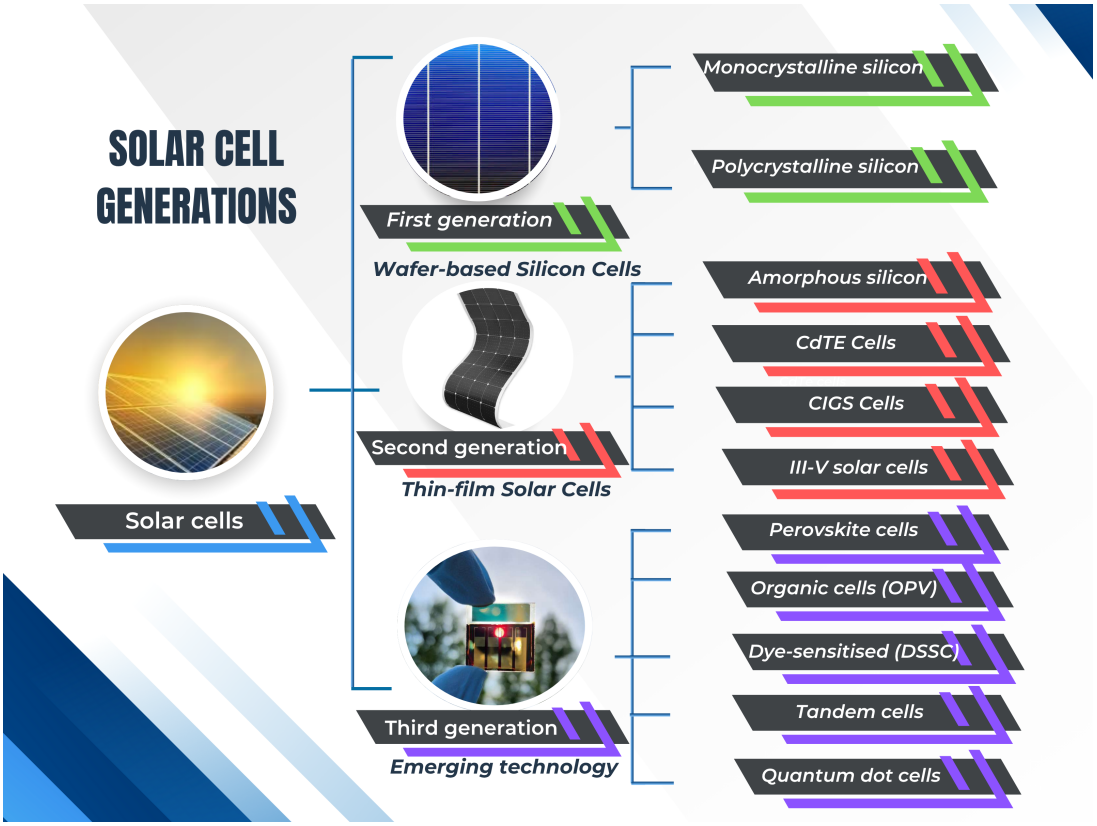



Figure 1.14: Classification of solar photovoltaic cell technologies.

The first generation includes traditional crystalline silicon-based technologies (monocrystalline or polycrystalline), which dominate the market thanks to their high efficiency, reliability, and longevity. The second generation includes thin-film cells, such as CdTe, CIGS, or amorphous silicon, developed to reduce costs and material consumption while offering greater mechanical flexibility, facilitating their integration on a variety of surfaces.

Finally, the third generation brings together emerging technologies based on innovative materials and concepts, such as organic cells, dye-sensitized cells (DSSC), perovskites, and multi-junction structures [100]–[102]. These devices aim to exceed the theoretical limits of

conventional cells while addressing the challenges of sustainability, lightness, and low-cost manufacturing.

Figure 1.15 illustrates the efficiency levels attained by various generations of solar cells based on their specific technologies. To date, the highest efficiency has been achieved by a III–V four-junction concentrating photovoltaic cell, which exhibits a power conversion efficiency (PCE) of 47.6%. Table 1.2 presents a comparative summary of the three generations in terms of materials, efficiency, and cost.

Table 1.2: Comparison of the three generations of photovoltaic cells [51], [103]–[105].

| **Generation** | **First generation** | **Second generation** | **Third generation** |
|---|---|---|---|
| Materials used | Monocrystalline Si, Polycrystalline Si | a-Si, CdTe, CIGS, III–V materials | Perovskites, organics, DSSC, etc. |
| Efficiency range | 6–25% | 10–15% | >25% |
| Advantages | Mature technology, increasing efficiency | Flexible, lightweight, roll-to-roll production, cost-effective | Low-cost materials, high efficiency potential, emerging R&D focus |
| Limitations | High material cost, temperature sensitivity | Moderate efficiency, stability issues | Still under development, stability challenges |
| Manufacturing process | Wafer-based | Roll-to-roll | Various (solution or vapor-based) |
| Applications | Residential, commercial, utility | BIPV, portable devices, small projects | Large-scale systems, consumer electronics, off-grid |
| Durability | Good | Moderate | Material-dependent |
| Stability | Good | Moderate | Material-dependent |

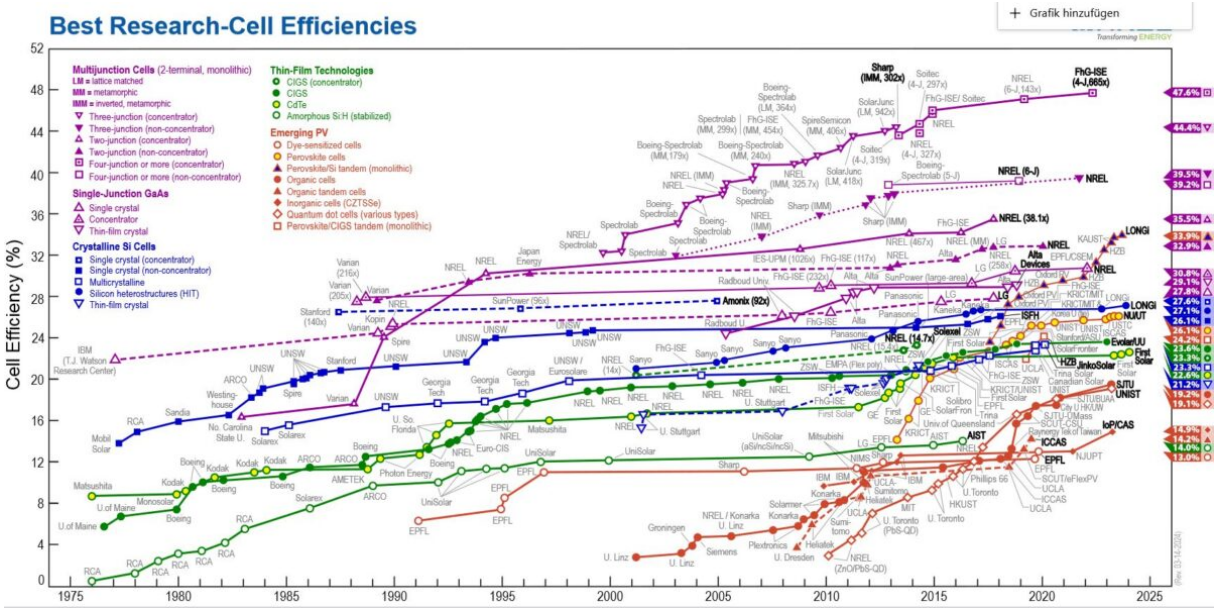



Figure 1.15: Solar cell efficiency evolution over generations [106].

## 1.8.1 First generation: Crystalline silicon

### 1.8.1.1 Silicon proprieties

First-generation photovoltaic cells are mainly based on crystalline silicon, which has been the most mature and widespread technology in the solar industry for several decades. This generation has contributed significantly to the massive development of photovoltaic energy thanks to its robustness, reliability, and relatively stable performance over time [102], [107]. Silicon (Si), the benchmark semiconductor material for this generation, owes its predominance to a combination of optimal electronic, structural, and physicochemical properties. An element in group IV of the periodic table, it has a diamond-type tetrahedral crystal structure, which gives the lattice great stability. At room temperature, it has an indirect band gap ($E_g$) of approximately 1.1 eV, which is an ideal compromise, low enough to allow the absorption of a large portion of the solar spectrum (particularly in the near infrared), but high enough to generate a useful output voltage, reducing thermal losses. Derived from abundant natural resources such as quartz ($SiO_2$) or sand, silicon must be purified using complex industrial processes notably the Siemens process, to achieve the ultra-high purity required to minimize crystal defects and reduce non-radiative recombination. It is then recrystallized to produce monocrystalline lingots or polycrystalline ingots, depending on the desired architecture [52], [108].

Silicon, classified as a metalloid, has several key advantages for photovoltaic applications. Its abundance in the Earth's crust, where it is the second most abundant element, ensures a stable resource for large-scale industrial production [109]. It is also distinguished by its non-toxicity, environmental compatibility, high thermal stability, and corrosion resistance, ensuring the durability of modules even in extreme climatic environments. In addition, its seamless integration into existing microelectronic processes facilitates industrialization, performance reproducibility, and cost control [110], [111].

### 1.8.1.2 Manufacturing process

These cells are manufactured from wafers cut from monocrystalline or polycrystalline silicon ingots. The quality of the silicon used is crucial; monocrystalline silicon has a homogeneous crystalline structure and few defects, which promotes high electron mobility and limits charge recombination, leading to typical efficiencies of between 18% and 24% under standard conditions [112], [113]. In contrast, polycrystalline silicon consists of multiple crystalline grains oriented in different directions, creating more recombination sites and slightly lower performance, typically between 15% and 20%, but its production cost is lower [114].

The operation of first-generation cells is based primarily on a conventional p–n junction, which creates an internal electric field that ensures the efficient separation of photogenerated charge carriers. This fundamental mechanism enables the conversion of light energy into electrical energy, but limits the theoretical maximum efficiency to around 29%, according to the Shockley–Queisser limit for a single bandgap junction [113]. From an industrial standpoint, these technologies offer proven maturity and reliability, with module lifespans often exceeding 25 or even 30 years and low annual degradation [115], [116]. How-

ever, their manufacture remains energy-intensive and costly, requiring a complex process of silicon purification, the growth of monocrystalline ingots using the Czochralski method (the Cz method, named after Jan Czochralski, is the most common method of producing mono-Si), and the precise cutting of wafers [117]–[119]. These steps also involve a significant carbon footprint and high resource consumption. In order to better understand the industrial constraints and levers for optimizing crystalline silicon cells, it is important to briefly describe the main steps in the photovoltaic module manufacturing process. This industrial process comprises several key phases, ranging from the purification of metallic silicon to the assembly and final encapsulation of the modules, and largely determines the quality, cost, and environmental impact of the finished products [120]. These different stages are illustrated in Figure 1.16.

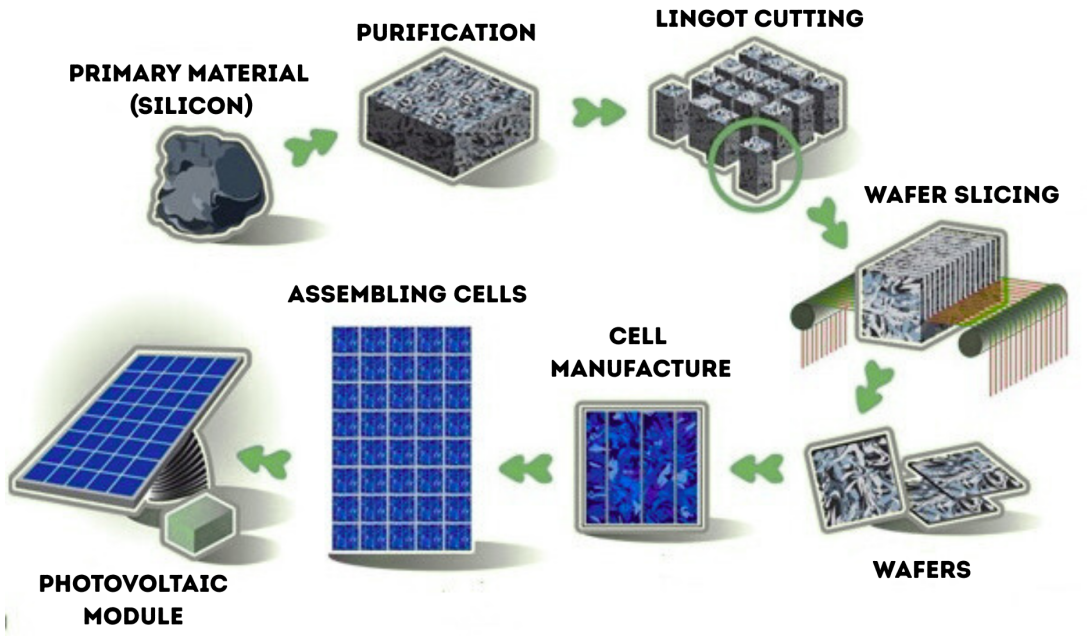



Figure 1.16: The different stages in the manufacturing process for crystalline silicon photovoltaic modules [121].

#### 1.8.1.3 Advantages and limitations

To overcome some of these limitations, various improvements are now being implemented, including advanced surface passivation, which reduces recombination at interfaces, and optimization of metal contacts to minimize resistive losses and shading [120]. In addition, the development of hybrid structures, such as multiple (tandem) junctions incorporating complementary materials, aims to overcome the efficiency barriers imposed by the physics of single junctions [52], [122]. In summary, despite the rise of second- and third-generation technologies, crystalline silicon cells remain a fundamental pillar of industrial photovoltaics, offering a proven compromise between efficiency, durability, and reliability. Their widespread adoption in the global market underscores their continued importance in the solar energy mix [123].

### 1.8.2 Second generation: Thin films

Second-generation photovoltaic technologies rely on the use of semiconductor materials deposited in thin layers on rigid or flexible substrates, unlike the thick wafers characteristic of the first generation [124], [125]. This approach reduces the amount of semiconductor material used, significantly lowers production costs, and offers possibilities for integration on a variety of surfaces thanks to the potential flexibility of the films [126]. The thickness of the active layers is generally between a few hundred nanometers and a few micrometers.

Thin-film cells mainly use three semiconductor materials: amorphous silicon (a-Si), cadmium telluride (CdTe), and multi-element compounds such as copper-indium-gallium-selenide (CIGS) [127]. Figure 1.17 displays the comparative architectures of the main second-generation thin-film photovoltaic cells (CIGS, CdTe, and a-Si/$\mu$c-Si), exhibiting the constituent materials and typical thicknesses of their different layers. These technologies are distinguished by a compromise between efficiency, cost, stability, and environmental impact. Typical commercial efficiencies range from 10% to 16%, with laboratory performance reaching significantly higher values. However, their durability and stability generally remain inferior to those of crystalline silicon cells, representing a major technological challenge [16], [128], [129].

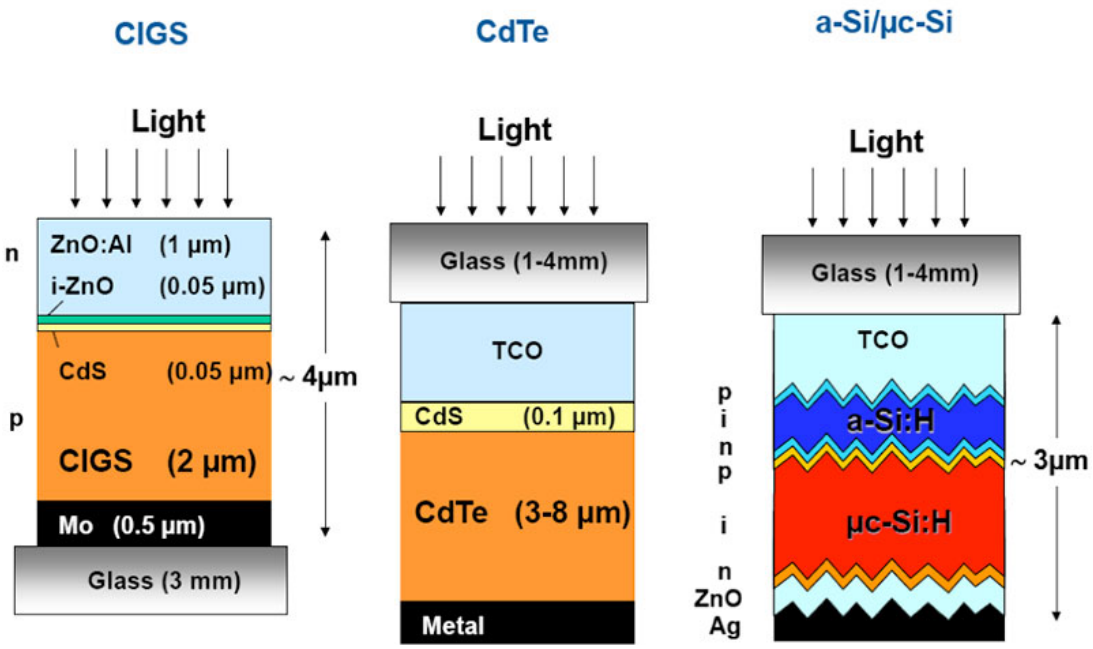



Figure 1.17: Typical architectures of second-generation thin-film photovoltaic cells: CIGS, CdTe and amorphous/microcrystalline silicon (a-Si/$\mu$c-Si) [130].

In terms of challenges, second-generation cells enable a significant reduction in active thickness, which reduces the amount of raw material used, improves substrate flexibility and opens the way to integrated applications such as building-integrated photovoltaics (BIPV) or curved surfaces [131], [132]. However, these technologies face major challenges, including the scarcity of certain critical materials, the toxicity of components such as cadmium or arsenic, and the difficulty of achieving efficiency levels as high as those of first- or third-generation cells [133]. In addition, the long-term stability and degradation of thin films still raise questions that have not been fully resolved, particularly in extreme

climatic conditions [134]. Finally, deposition processes require precise control and sometimes significant technological investments, which hinders the economic competitiveness of some of these technologies [135].

#### 1.8.2.1 Amorphous silicon (a-Si) cells

Hydrogenated amorphous silicon differs from crystalline silicon in that it has a disordered atomic structure, in which the atoms are not organized in a periodic lattice [61], [136]. This fundamental difference in structure is illustrated in Figure 1.18, which compares the main allotropic forms of silicon used in photovoltaics. This disorder generates a high density of localized states in the band gap, which hinders the mobility of charge carriers. To mitigate these electronic defects, the material is passivated by incorporating hydrogen, hence the name a-Si:H. This material is generally deposited by plasma-enhanced chemical vapor deposition (PECVD) at moderate temperatures of around 200°C [137], [138]. This characteristic allows the use of flexible substrates such as heat-resistant polymers, paving the way for portable, foldable, or textile-integrated applications [139]–[141].

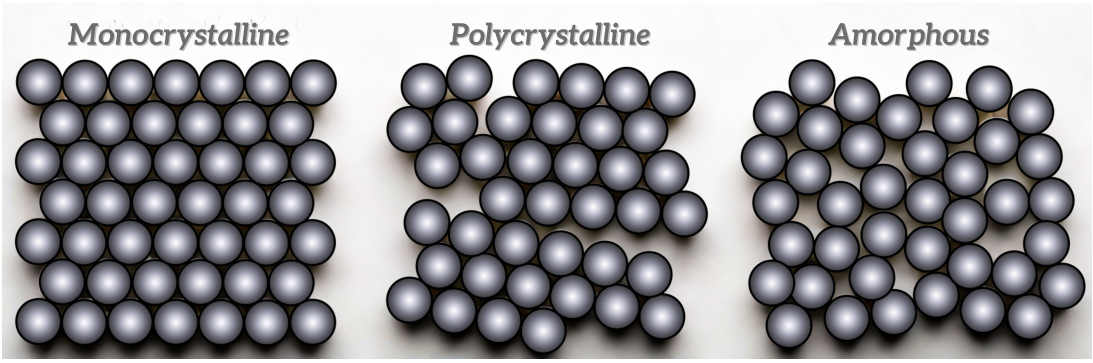



Figure 1.18: Schematic comparison of the different forms of silicon: monocrystalline, polycrystalline, and amorphous.

The classic architecture of a-Si cells is based on a p-i-n type superimposed layer structure, where the intrinsic layer acts as the absorbing material [136], [142]. The transparent electrodes are often made of indium tin oxide (ITO), while the rear electrode is made of reflective metal [143], [144]. Despite its low active thickness (approximately 300 to 500 nm), the high absorption coefficient of a-Si allows for efficient light collection. However, performance remains limited to typical efficiencies of 6–9% for single cells, due to low carrier mobility and the presence of defects [145]. Tandem structures, combining a-Si and microcrystalline ($\mu$c-Si), can achieve efficiencies of up to 12%. One of the major challenges is the Staebler–Wronski effect, a photo-induced degradation that reduces efficiency after prolonged exposure to light [128].

#### 1.8.2.2 Cadmium telluride (CdTe) cells

Among thin-film technologies, CdTe cells stand out for their industrial maturity and simplicity of manufacture, located in the elements of groups II and VI of the periodic table [146]. Cadmium telluride is a direct bandgap semiconductor with a bandgap of

1.45 eV, very close to the optimal value for photovoltaic conversion. This allows for efficient absorption of sunlight in an active layer of only 2–3 µm [147], [148]. The most common deposition processes include sputtering, thermal evaporation, or chemical vapor deposition (CVD) [149].

The standard architecture comprises a transparent conductive layer (usually ITO or $SnO_2$), a cadmium sulfide (CdS) buffer layer, then the active CdTe layer, followed by a metal back contact, often based on graphite, copper, or specific alloys. The CdS forms a heterojunction with the CdTe, allowing for good charge separation [150]. This structure has excellent tolerance to crystalline defects, high thermal stability, and an operational life exceeding 25 years. Industrial yields currently reach 18–19%, while laboratory cells exceed 22% [151]. However, the presence of cadmium, a toxic heavy metal, is raising growing environmental concerns. In addition, tellurium is a relatively rare element, which could limit the global expansion of this technology in the long term [136], [152].

#### 1.8.2.3 Copper–Indium–Gallium–Selenide (CIGS) cells

CIGS technology is the most efficient second-generation option in terms of yield, while exhibiting great flexibility of application [153]. The active material, $Cu(In,Ga)Se_2$, is a direct bandgap semiconductor whose energy gap can be adjusted between 1.0 eV and 1.7 eV by modulating the proportion of gallium. This band engineering capability allows for optimised absorption across the entire solar spectrum, and therefore high energy efficiency [154]. The active layer is typically deposited by vacuum co-evaporation or sputtering followed by annealing in a selenium atmosphere, which requires precise control of the composition [155], [156].

The structure of a CIGS cell comprises a glass or steel substrate covered with a layer of molybdenum acting as a rear contact, followed by the CIGS layer itself, a CdS buffer layer, and then a transparent conductive oxide such as ZnO [156]. In the latest devices, CdS tends to be replaced by more environmentally friendly materials, such as ZnS or $In_2S_3$, to meet environmental requirements. Production yields range from 13–16%, while laboratory records reach over 23% [157]. CIGS modules maintain good performance even in low sunlight or partial shade. However, the scarcity of indium and gallium, as well as the complexity of the deposition processes, are obstacles to mass industrialisation. Research is underway to develop more sustainable alternatives to these critical materials [16].

#### 1.8.2.4 III–V material-based solar cells

III–V material-based solar cells, such as gallium arsenide (GaAs), gallium indium phosphide (GaInP) or indium gallium arsenide (InGaAs), mainly belong to the second generation of photovoltaic cells, due to their manufacture in the form of thin layers using epitaxial processes. Derived from elements in groups III (gallium, indium) and V (arsenic, phosphorus) of the periodic table, they are characterised by a direct band gap, a high optical absorption coefficient and a low recombination rate, enabling efficiencies of over 25% to be achieved for a single GaAs junction [158], and up to 28–30% under optimal conditions [159].

Due to their excellent performance under high irradiation and their resistance to radiation, these cells are particularly suited to demanding environments such as satellites or concentrated photovoltaic (CPV) systems. Their high-quality crystalline structure, obtained by metal organic chemical vapor deposition (MOCVD) or molecular beam epitaxy (MBE), ensures efficient collection of charge carriers. However, the scarcity of the materials used and the complexity of manufacturing result in high costs, limiting their large-scale deployment for conventional terrestrial applications [160], [161].

III–V materials also play a central role in the design of multi-junction or tandem cells, typical of the third generation, where several layers with different band gaps are superimposed in order to capture a larger portion of the solar spectrum and exceed the theoretical efficiency limit of single junctions. For example, a GaInP/GaAs/InGaAs triple-junction cell can achieve efficiencies of over 40% under high concentration [162]. Current research aims to reduce costs through the use of reusable substrates, the optimisation of interfaces to limit recombination losses, and the development of hybrid architectures combining III–V with low-cost materials such as silicon or quantum dots [163].

### 1.8.3 Third generation

The third generation of PVs represents an ambitious effort in contemporary research to overcome the technological and economic constraints of previous generations. While the first generation, mainly based on crystalline silicon, has reached a solid industrial maturity and the second generation, based on thin films, has enabled a significant reduction in material and manufacturing costs, the third generation aims to combine high efficiency, low production costs, mechanical flexibility and greater environmental friendliness [105], [133].

These emerging technologies are based on innovative concepts of light absorption and conversion, often inspired by advances in nanotechnology and complex materials chemistry. They aim not only to exceed the theoretical Shockley-Queisser limit applicable to simple junctions, but also to exhibit new functionalities such as semi-transparency, harmonious integration into architecture, and the ability to operate efficiently under low light conditions [164], [165].

A major characteristic of this generation is the wide variety of materials used, which differ greatly from conventional semiconductors. Absorbers are often organic, organic-inorganic hybrids or composed of quantum nanostructures, capable of finely modulating electronic and optical properties at the nanometer scale [166], [167]. In addition, manufacturing processes favor low-temperature techniques that are compatible with flexible substrates, paving the way for a variety of applications, from portable electronics to energy integration in street furniture. These technologies include perovskite solar cells, organic photovoltaic cells (OPV), quantum dot cells and dye-sensitised solar cells (DSSC) [108], [132], [164]. Each of these approaches has specific conversion mechanisms, distinct advantages and technical challenges to overcome, paving the way for new opportunities for the photovoltaic industry of tomorrow. PSC, in particular, are attracting growing scientific interest due to their remarkable performance and adaptability, making them a priority area of research in our work.

#### 1.8.3.1 Organic photovoltaic cells (OPV)

Organic photovoltaic cells (OPV) represent an innovative technology that uses carbon-based organic materials, such as polymers and small molecules, to convert sunlight into electricity [168]–[170]. Unlike traditional inorganic semiconductors, their compounds exhibit lightness, flexibility and low-cost manufacturing capabilities, due in particular to low-temperature processes compatible with flexible substrates [171]–[173]. This opens up applications in a variety of fields, such as portable devices, smart textiles and architectural integration.

The typical structure of OPVs comprises several layers deposited on a transparent substrate (often glass or flexible plastic), with an active layer combining an electron donor and an electron acceptor. This system forms an essential interface called a heterojunction, where the excitons created by the absorption of photons are dissociated into free charges that are then collected within the device, generating an electric current [174]–[176]. This multilayer organisation is illustrated in Figure 1.19, which exhibits the typical structure of an organic photovoltaic cell. The efficiency of this conversion depends heavily on the quality of the morphology and the optimisation of the materials used.

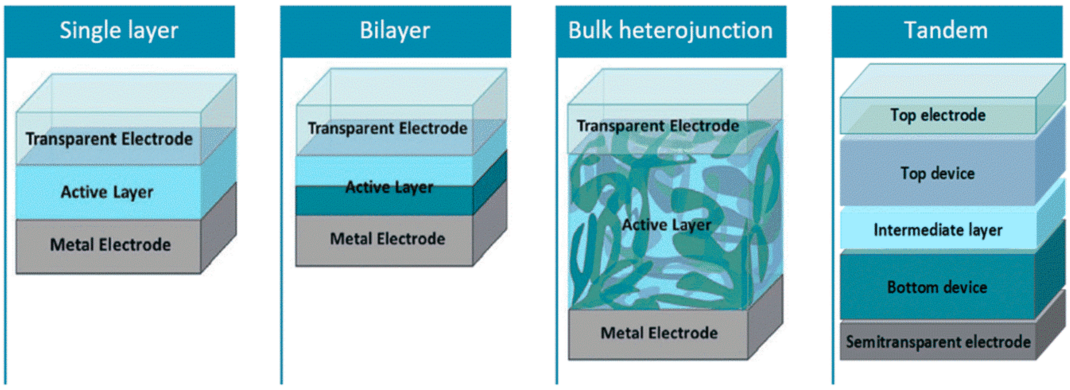



Figure 1.19: Architecture of OPV cells.

Among their main advantages are their light weight and mechanical flexibility, as well as their low manufacturing cost thanks to printing methods such as roll-to-roll. These characteristics facilitate aesthetic and functional integration into a variety of media, favoring, for example, the production of semi-transparent panels for buildings [177]–[180]. However, this technology still suffers from lower efficiency than inorganic cells, typically around 10 to 15% under commercial conditions, due in particular to the low mobility of charge carriers and losses related to the short lifetime of excitons [181]–[184].

One of the major challenges is also durability, as organic materials degrade relatively quickly under the effects of light, oxygen and humidity, which limits their longevity. To overcome these weaknesses, researchers are working on new acceptance materials, tandem architectures and advanced encapsulation systems to improve stability over time. These combined efforts pave the way for significant industrialisation potential, with promising applications in portable electronics, photovoltaic lighting and smart homes [185], [186].

#### 1.8.3.2 Quantum dot photovoltaic cells

Quantum dot photovoltaic cells use nanometric semiconductor nanoparticles, whose optical and electronic properties can be modulated with great precision thanks to the quantum confinement effect [187]. This phenomenon makes it possible to adjust the size of the nanocrystals to effectively modulate the band gap, thereby optimising the absorbed spectral range. This unique capability allows solar conversion over a wider range than traditional photovoltaic technologies, potentially improving solar energy capture [188]–[190]. These quantum dots are generally made of various materials such as cadmium selenide (CdSe), lead sulphide (PbS) or ternary compounds such as copper-indium-selenium ($CuInS_2$) [191]–[193]. They are manufactured using sophisticated chemical or physical processes and then deposited on different types of substrates, both rigid and flexible. This manufacturing flexibility, combined with the thinness of the active layers, promotes low-cost industrial potential. The high light absorption capacity of quantum dots and their ability to integrate tandem architectures reinforce their attractiveness for improving photovoltaic efficiency [194]–[196].

Beyond these properties, quantum dots exhibit a remarkable ability to generate multiple electron-hole pairs from a single photon, a phenomenon called exciton multiplicity. This ability paves the way for an increase in maximum efficiency beyond the classic Shockley-Queisser limit, positioning this technology as one of the most promising for the future of photovoltaics [197], [198]. Nevertheless, this technology still faces major challenges. Long-term stability remains limited, particularly due to the degradation of nanoparticles and interfaces under real-world operating conditions [199]. In addition, the toxicity of certain materials used, particularly those based on cadmium or lead, raises significant environmental concerns. These constraints are driving active research into more environmentally friendly alternative materials and improved processes to ensure greater sustainability [200], [201].

#### 1.8.3.3 Dye-sensitised solar cells (DSSCs)

Dye-sensitised solar cells, also known as DSSCs or Grätzel cells, represent an innovative and relatively low-cost photovoltaic technology based on a photoelectrochemical conversion mechanism [202], [203]. The typical structure of a DSSC comprises a wide bandgap semiconductor layer, usually consisting of a nanostructured film of titanium dioxide ($TiO_2$), onto which photosensitive molecules (dyes) are grafted. These dyes play an essential role in absorbing sunlight [204]. When a photon strikes the dye, it excites an electron in the molecule, which is then injected into the conduction band of the $TiO_2$. This electron then flows through the semiconductor to a transparent electrode, generating an electric current. At the same time, the oxidised dye is regenerated by an electrolyte, which transports the charges to the counter electrode, thus closing the electrical circuit [64], [205].

This architecture is notable for its low potential manufacturing cost, relative simplicity and ability to be integrated into flexible or transparent substrates, making it an attractive solution for building-integrated photovoltaics (building facades, semi-transparent windows), portable electronics and off-grid applications. The commercial efficiencies of

DSSCs generally range between 11% and 13%, while laboratories achieve nearly 14%, demonstrating a promising balance between performance and cost [206]. However, a major weakness remains stability over time, mainly due to the degradation of dyes under prolonged exposure to light and the volatility of traditional liquid electrolytes, which affect the durability of the devices. To overcome these limitations, research is focusing on the development of solid or semi-solid electrolytes, as well as more resistant dyes and modular architectures that improve operational robustness [207]–[209]. Overall, DSSCs exhibit a versatile and eco-efficient alternative to conventional photovoltaic technologies, particularly suited to applications requiring lightness, flexibility and aesthetic integration, while continuing to address the challenge of their durability for wider industrial deployment [210], [211].

## 1.9 Current applications and prospects

Today, photovoltaic energy has established itself as one of the main renewable sources exploited worldwide, with diverse uses ranging from residential to industrial. In the residential sector, rooftop or facade installations enable individuals to reduce their dependence on the electricity grid while contributing to the energy transition [212], [213]. The industrial sector, meanwhile, favors large-scale solar power plants capable of powering heavy infrastructure and contributing significantly to national electricity production. Off-grid systems, which are independent of the grid, are essential in isolated or developing areas, offering a sustainable alternative to thermal generators [22]. In addition, the integration of photovoltaics into mobility is experiencing remarkable growth, with panels installed on electric vehicles, boats, and even solar drones. Agriculture also benefits from this technology through agro-photovoltaic solutions, which allow energy production and crop cultivation to coexist on the same land [214].

Recent innovations are further expanding the range of applications. The development of BIPV (Building Integrated Photovoltaics) transforms solar panels into architectural elements, integrated directly into facades, roofs, or glazing, combining aesthetics and energy performance [132]. The flexibility of the modules, made possible by the use of organic, hybrid, or composite materials, paves the way for new applications on curved or moving surfaces. New high-efficiency materials, such as perovskites or nanostructure-based composites, make it possible to envisage lighter, more transparent devices that are better suited to discreet integration into the urban environment [16]. Architectural integration is thus becoming a major lever for the democratization of photovoltaics, making this technology more visually and functionally acceptable in the built landscape.

The prospects for technological and scientific development are particularly promising. Research is focusing on increasing efficiency through multi-junction or tandem approaches, reducing production costs through large-scale printing processes, and improving the durability of materials in extreme weather conditions [73], [215]. The exploitation of new concepts, such as the recovery of residual thermal energy or the use of semi-transparent photovoltaic devices for indoor applications, is opening up new avenues [216]. In the longer term, combining photovoltaics with advanced storage systems and smart grids could enable optimal management of the energy produced, strengthening the energy independence of buildings and communities. All of these developments point to a central

role for photovoltaics in the future global energy mix, with ever greater integration into our everyday environment [217], [218].

## 1.10 Conclusion

This first chapter has laid the essential foundations for understanding photovoltaic technologies, covering their historical development, operating principles and the diversity of existing generations and architectures. We have seen how technological advances, combined with environmental imperatives, have led to constant improvements in efficiency and reductions in costs, making this energy source competitive with conventional sources. The classification of the different generations of solar cells, from the first based on crystalline silicon to third-generation devices incorporating innovative concepts, provides a clear overview of the scientific and industrial challenges driving the sector. Analysis of current applications and future prospects has also highlighted the growing role of photovoltaics in the global energy transition, as well as the opportunities offered by architectural integration, material flexibility and the rise of new design approaches.

This summary naturally paves the way for the developments that will be discussed in the following chapters. The next chapter will focus on perovskite photovoltaic cells, an emerging technology that is attracting growing interest due to its exceptional performance and high flexibility of integration. We will analyze in detail the perovskite material, its optoelectronic properties, the different manufacturing methods and the materials associated with the functional layers. Finally, we will examine tandem structures, which combine perovskite with other photovoltaic technologies to exceed current efficiency limits and pave the way for a new generation of high-performance devices.

CHAPTER

# 2

# PEROVSKITE SOLAR CELLS AND TANDEM STRUCTURES

## 2.1 Introduction

The previous chapter presented the fundamentals of the photovoltaic effect, its historical evolution, and the three generations of solar cells, highlighting the innovative potential of the third generation. Among these emerging technologies, perovskite-based solar cells and tandem architectures stand out for their exceptional performance and their ability to transform next-generation photovoltaics. Perovskites offer efficiencies exceeding 25 % in the laboratory thanks to their high light absorption, excellent charge carrier mobility and adjustable bandgap, while enabling simple and economically competitive manufacturing processes. As for tandem structures, they combine perovskites with complementary materials, such as silicon or other perovskites, to exploit a broader solar spectrum and achieve experimental efficiencies exceeding 30 %, thus overcoming the inherent limitations of single-junction cells.

This chapter is devoted to an in-depth study of perovskite cells and tandem architectures. We will first examine the fundamental properties and manufacturing techniques of perovskite materials. We will then analyse the different architectures of these cells, discussing their operating principles and the main technical challenges, particularly in terms of stability and industrial scaling. Finally, we will explore tandem structures, their configurations and their potential for maximising photovoltaic conversion. This analysis will provide the scientific basis for the modelling and simulation work that will be covered in the following chapters.

## 2.2 Perovskite materials

Perovskite materials have emerged as a disruptive innovation in the field of photovoltaics, offering a unique balance between high efficiency, low production costs and design flexibility [219]. Their rapid emergence over the past fifteen years has profoundly changed the technological landscape, positioning this family of materials as a pillar of third-generation solar cells [220], [221].

### 2.2.1 History and emergence of perovskites in photovoltaics

The discovery of perovskite materials dates back to the 19th century, with the initial identification of a mineral with a perovskite structure ($CaTiO_3$) in the Ural Mountains in 1839 by mineralogist Gustav Rose, named in honor of Count Lev Aleksevich Perovski [219], [222]. This first perovskite is a mineral with a cubic morphology and a metallic grey appearance, as depicted in Figure 2.1. The first metal halide perovskites, which form the basis of modern solar cells, were synthesised about 50 years later, in the 1890s by H. L. Wells, but their photovoltaic potential was not explored until much later [223].

In the 20th century, advances in solid-state physics, such as X-ray crystallography, revolutionised the study of perovskites, revealing their unique electronic and luminescent properties. In the 1950s, applications in capacitors and electrochemical transducers emerged at Philips and Western Electric [224], [225]. In 1978, Dieter Weber synthesised the first organic-inorganic hybrid perovskites (HOIP), replacing caesium with methy-

lammonium ions [226]. David Mitzi and his colleagues at IBM in the 1990s and 2000s developed synthesis approaches and explored their optoelectronic properties, including light-emitting devices [227]–[229].



Figure 2.1: Illustration of the perovskite mineral with the formula $CaTiO_3$ [225].

The emergence of perovskite solar cells (PSCs) as a viable technology truly began in 2009, when Akihiro Kojima and his colleagues reported the first use of hybrid halide perovskites ($MAPbI_3$ and $MAPbBr_3$) as sensitizers in dye-sensitised solar cells (DSSCs), achieving an initial power conversion efficiency (PCE) of 3.8% [230]. In 2011, Nam-Gyu Park improved this to 6.5% by optimising deposition on nanocrystalline $TiO_2$ [231]. This pioneering breakthrough paved the way for exponential progress. In 2012, efficiencies of 9–10% were achieved with solid configurations, replacing the liquid electrolyte with a solid HTL such as spiro-OMeTAD, by the group of M. M. Lee and Henry Snaith [232]. In 2013, an explosion of interest led to PCEs exceeding 15% thanks to optimisations in morphology and interfaces [233]. Figure 2.2 outlines the timeline and key milestones in the history and development of perovskite solar cells, highlighting major advances from early discoveries to recent improvements in efficiency.

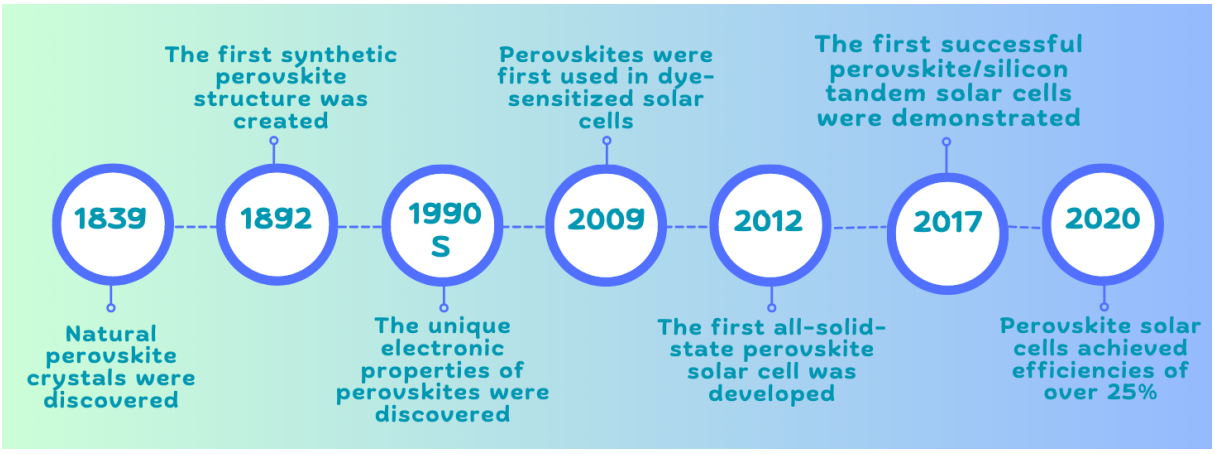



Figure 2.2: Timeline of the history and development of perovskite solar cells.

Over the years, PSCs have undergone unprecedented evolution, becoming the fastest-growing solar technology in history. In 2016, Michael Grätzel demonstrated 21.1% efficiency with triple-cation compositions [234]. Recognition came in 2013 when *Science* included perovskites in its Top 10 breakthroughs. By 2025, single-junction cells had surpassed 26.7% PCE, while perovskite-silicon tandems had reached over 33%, and all-perovskite tandems had exceeded 30% in some cases [235], [236]. This acceleration is attributed to advances in materials engineering, such as the use of mixed cations and controlled deposition techniques, positioning perovskites as a promising alternative to silicon-based cells for sustainable and economical solar production. The impact of these developments is such that commercialisation initiatives are underway, with prototypes demonstrating increasing industrial viability, including flexible modules and megawatt-scale pilot lines.

### 2.2.2 $ABX_3$ formula and classification

Photovoltaic perovskites generally adopt a cubic or pseudo-cubic crystal structure described by the general formula $ABX_3$. In this configuration, the A-site is occupied by a monovalent cation, either organic, such as methylammonium ($MA^+ = CH_3NH_3^+$) or formamidinium ($FA^+ = CH(NH_2)_2^+$), or inorganic, such as cesium ($Cs^+$) or rubidium ($Rb^+$). Site B corresponds to a divalent metal cation, most often lead ($Pb^{2+}$), but which can also be replaced by tin ($Sn^{2+}$) or germanium ($Ge^{2+}$) in research aimed at reducing toxicity. Finally, site X is a halide anion, such as iodide ($I^-$), bromide ($Br^-$) or chloride ($Cl^-$) [237]. This configuration forms a cubic or pseudo-cubic network in which cation B is at the center of an octahedron formed by six anions X (coordination 6), while cation A occupies the interstitial cubo-octahedral cavities, surrounded by approximately 12 anions X, thus ensuring the stability of the three-dimensional structure. Figure 2.3 shows two views of the perovskite $ABX_3$ structure. The first part displays the cation A located in the cavities formed by $BX_6$ octahedra, while the second part shows the unit cell with the cation B at the center of the octahedron surrounded by anions X, and the cations A at interstitial sites.

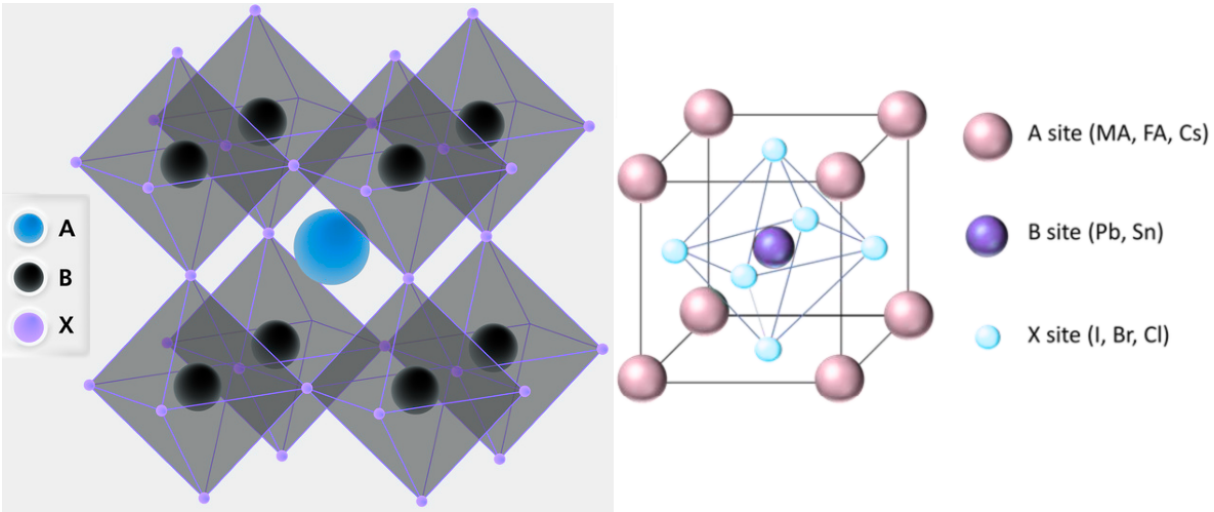



Figure 2.3: Schematic diagram of the cubic crystal structure $ABX_3$, extended lattice view and elementary cell.

The stability of the perovskite structure is governed by the Goldschmidt tolerance factor [238], defined by:

$$t = \frac{r_A + r_X}{\sqrt{2}\,(r_B + r_X)} \tag{2.1}$$

where $r$ denotes the ionic rays. The perovskite structure remains stable when the tolerance factor lies between 0.8 and 1. Values greater than 1 generally lead to a non-photoactive hexagonal structure ($\delta$-phase), while values less than 0.8 favor the appearance of non-perovskite or orthorhombic phases. However, among common compositions, only $MAPbI_3$ falls within this range. $FAPbI_3$ has a tolerance factor exceeding 1, while $CsPbI_3$ tolerance factor is below 0.8. As a result, both $FAPbI_3$ and $CsPbI_3$ exhibit poor structural stability and tend to decompose easily at room temperature [238], [239].

Depending on their composition and dimensionality, perovskites are classified into several categories. Three-dimensional (3D) organic–inorganic hybrid perovskites, such as $MAPbI_3$ or $FAPbI_3$, have broad spectral absorption and high structural flexibility, but can suffer from thermal instability [240]. Fully inorganic variants, such as $CsPbI_3$, offer better thermal and environmental stability, at the cost of a wider bandgap (approximately 1.7 eV), limiting absorption in the near infrared [241]. Mixed compositions, for example $APb(I_{1-y}Br_y)_3$ or double/triple cation formulations (MA/FA/Cs), allow for optimisation of crystalline quality, stability and photoactivity [242]. In terms of dimensionality, three-dimensional (3D) structures dominate in terms of performance, but two-dimensional (2D) perovskites, such as those incorporating long alkylammonium chains (e.g., $(BA)_2PbI_4$), or 2D/3D heterostructures, improve resistance to moisture and degradation by forming hydrophobic barriers. 2D/3D heterostructures combine these advantages, while derivatives such as $A_2BX_6$ (e.g., $Cs_2SnI_6$) or $ABBX_3$ (e.g., $CsSnPbI_3$) further expand the range of exploitable optoelectronic properties [243]. These classifications allow for fine-tuning of properties, which is essential for tandem cell applications where a variable bandgap is crucial for complementary absorption [244].

### 2.2.3 Advantages of perovskites

The enthusiasm for perovskites can be explained by a number of advantages that make them one of the most promising materials for photovoltaic conversion, as illustrated in Figure 2.4, which highlights their many benefits. Their high absorption coefficient allows for the creation of ultra-thin active layers, on the order of a few hundred nanometers, while efficiently capturing sunlight. They also have high charge carrier mobility and long carrier lifetimes, which minimises non-radiative recombination and optimises charge extraction, thus contributing to high conversion efficiency.

A major advantage is their adjustable bandgap, which can be modified simply by changing the ionic composition, offering the flexibility to optimise spectral absorption and design high-performance tandem architectures [245]. Beyond these optoelectronic properties, perovskites stand out for their durability and positive environmental impact; they are recyclable, sustainable and made from abundant, low-cost materials, promoting eco-responsible production [246]. Their low weight and transparency open the door to innovative applications, such as integration into windows or curved surfaces. In addition, their compatibility with simple, low-energy manufacturing processes, such as solu-

tion deposition or co-evaporation, enables large-scale, low-cost production that is easy to implement and offers a high return on investment [247]. Finally, their adaptability to flexible form factors broadens their scope of application, from traditional solar panels to portable devices or those integrated into architectural structures, thereby reinforcing their potential for an accessible and efficient energy transition [248].

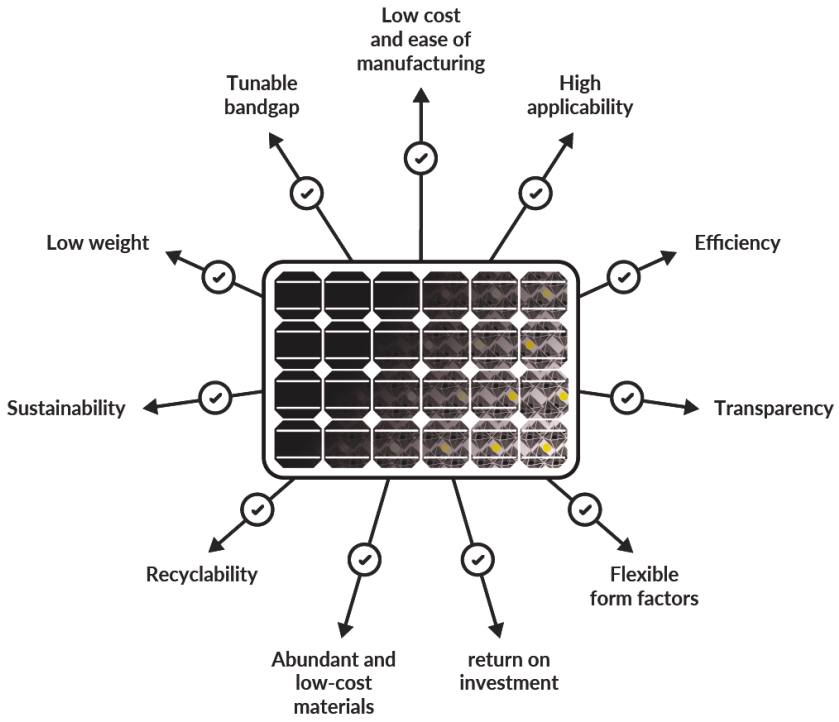



Figure 2.4: Main advantages of perovskites for photovoltaic applications.

### 2.2.4 Initial limitations and challenges for the industry

Despite their remarkable performance, perovskites must overcome several major obstacles before they can be adopted on a large scale by industry. The main challenge remains their stability, as organic-inorganic hybrid perovskites are sensitive to moisture (decomposition into $PbI_2$ and volatile compounds), heat (phase transitions above 85°C), oxygen and UV rays, which significantly reduces their lifetime in real-world conditions [249], [250].

In addition, the toxicity associated with lead, which is widely used in high-efficiency compositions, also raises environmental and regulatory issues, particularly due to its solubility in water, which promotes leaching. Lead-free alternatives, particularly those based on tin (e.g., $MASnI_3$, $FASnI_3$), have achieved PCE values above 17% in 2025, but remain limited by the oxidation of $Sn^{2+}$ to $Sn^{4+}$ and lower stability [251]. Finally, the transition to industrial production is another key challenge. Maintaining uniformity, crystallinity, and reproducibility over large areas (>100 $cm^2$) remains complex, with efficiency losses of 20–30% compared to laboratory cells. These limitations, although initial, are already the subject of intensive research aimed at ensuring a successful transition from the laboratory to the market, while ensuring compliance with regulatory and environmental requirements [252].

## 2.3 Crystallography and properties of perovskites

The crystallography of perovskites plays a decisive role in their photovoltaic performance. Their atomic structure, phase transitions and microstructure directly determine their optoelectronic properties, efficiency and long-term stability [253].

### 2.3.1 Crystallographic phases and phase transitions

Halide perovskites exhibit great structural flexibility, adopting different crystalline phases depending on temperature and composition [254], [255]. In the cubic phase (shown in Figure 2.5a), the [$BX_6$] octahedra are perfectly aligned with a B–X–B angle of 180°, and the lattice parameters verify $a = b = c$. This configuration, typically observed at high temperatures but also present in certain compounds such as $MAPbBr_3$ at room temperature (with a tolerance factor $t \approx 0.927$), offers optimal crystalline symmetry for photovoltaic applications. It promotes isotropic light absorption and efficient charge carrier transport, while maximising the coherence of the electronic orbitals, which helps to reduce non-radiative recombination and improve the overall performance of the devices [256].

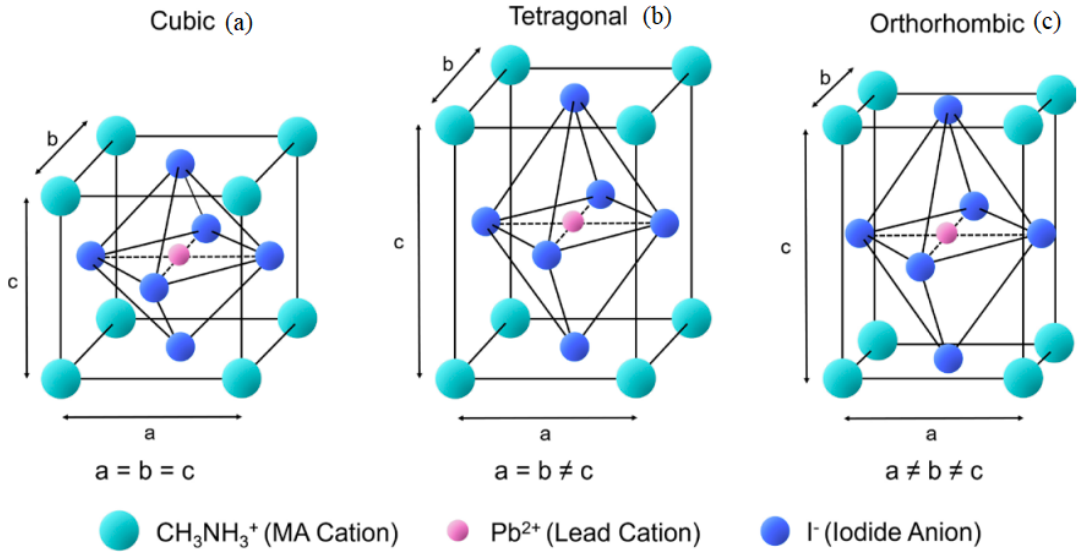



Figure 2.5: Diagram of the different crystalline phases of perovskites: (a) cubic, (b) tetragonal, and (c) orthorhombic.

When the temperature is lowered, perovskites undergo structural distortions of the [$BX_6$] octahedra, leading successively to transitions to the tetragonal phase (Figure 2.5b) and then the orthorhombic phase (Figure 2.5c). In the tetragonal phase, typically observed for slightly lower tolerance factors, such as $MAPbI_3$ ($t \approx 0.912$), the rotations or inclinations of the octahedra described by Glazer notation slightly reduce the symmetry. These distortions modify the bandgap width ($\approx 1.55$ eV versus 1.50 eV in the cubic phase), while maintaining good photoactivity. This tetragonal structure is often stabilised by stronger A–X interactions than B–X interactions, influencing carrier mobility and dynamics [257]. At even lower temperatures, or for tolerance factors below 0.8 (e.g., $CsPbI_3$ with $t \approx 0.807$), the structure adopts an orthorhombic phase, marked by octahedral distortions in several directions [258]. This phase often leads to a non-photoactive $\delta$ form,

characterised by a wider bandgap ($\approx$ 2.82 eV for $\delta$-$CsPbI_3$) and reduced absorption in the visible range, which greatly limits its photovoltaic interest. Each crystalline phase of perovskites has distinct characteristics that directly influence photovoltaic performance [258], [259]. Table 2.1 summarises a comparison of the main phases (cubic, tetragonal and orthorhombic), their structural parameters, optoelectronic properties and impact on device efficiency.

Table 2.1: Comparison of crystalline phases, optoelectronic properties, and their impact on perovskite performance [260]–[263].

| **Crystalline phase** | **Example** | **Bandgap (eV)** | **Optoelectronic properties** | **Impact on performance** |
|---|---|---|---|---|
| Cubic | $MAPbBr_3$ | 2.3 | • Isotropic absorption ($> 10^5$ $cm^{-1}$, 400–600 nm)<br>• High carrier mobility ($> 200$ $cm^2/V \cdot s$)<br>• Strong photoluminescence ($> 90\%$) | • High $J_{sc}$ (20–22 $mA/cm^2$)<br>• Stable $V_{oc}$ ($\sim$1.5 V)<br>• Ideal for tandem solar cells |
| Tetragonal | $MAPbI_3$ | 1.55 | • Slightly anisotropic absorption ($10^5$ $cm^{-1}$, 600–800 nm)<br>• Moderate mobility ($\sim$100 $cm^2/V \cdot s$)<br>• Reduced photoluminescence ($\sim$80%) | • Moderate $J_{sc}$ (18–20 $mA/cm^2$)<br>• $V_{oc}$ affected by hysteresis ($\sim$–50 mV)<br>• Maintained photoactivity |
| Orthorhombic | $CsPbI_3$ | 2.82 | • Limited absorption ($< 10^4$ $cm^{-1}$, >700 nm)<br>• Low carrier mobility (<50 $cm^2/V \cdot s$)<br>• Weak photoluminescence (<50%) | • Low $J_{sc}$ (<10 $mA/cm^2$)<br>• Non-photoactive, inefficient<br>• Requires stabilization ($Cs^+$, $Br^-$) |

These phase transitions, although often reversible, can induce structural defects that reduce the stability and lifetime of devices. For example, $FAPbI_3$ transitions from the photoactive cubic phase ($\alpha$-$FAPbI_3$, 1.48 eV) to a non-photoactive hexagonal $\delta$ phase (2.4 eV) at room temperature, but this instability can be corrected by adding $Cs^+$ or $Br^-$. Similarly, $MAPbI_3$ undergoes a tetragonal to orthorhombic transition at around 160 K, changing its bandgap (1.55 to 1.65 eV) and inducing defects that reduce the $V_{oc}$ of the devices. Thus, mixed compositions (e.g., triple cations Cs/MA/FA) and additives ($SnF_2$, fullerenes, etc.) are now key strategies for stabilising photoactive phases and limiting hysteresis in devices [264].

The stability of perovskite photovoltaics is closely linked to their crystallinity. A well-ordered cubic structure provides isotropic transport and low recombination, while tetragonal or orthorhombic distortions introduce defects that weaken the material. Phase transitions can cause mechanical stresses and structural defects, reducing the lifetime of the devices. Current strategies aim to stabilise the photoactive phases (cubic or tetragonal) through composition engineering (multi-cation or multi-anion alloys) and by optimising growth processes in order to obtain highly crystalline, homogeneous films that are resistant to ambient conditions [265].

### 2.3.2 Electronic structure and optoelectronic properties

The electronic structure of halide perovskites is dominated by [$BX_6$] octahedra, which determine both their energy gap and their optoelectronic performance. The valence band maximum (VBM) primarily arises from the hybridisation of halogen $p$ orbitals (I, Br, Cl) with the $6s$ orbital of the metal cation ($Pb^{2+}$, $Sn^{2+}$), while the conduction band minimum (CBM) originates from the $6p$ orbitals of lead or tin [266]–[268]. This specific orbital contribution results in an "inverse" band structure and is the fundamental reason for the material's high defect tolerance [269].

This configuration confers a direct bandgap, generally between 1.5 and 2.3 eV (e.g., 1.55 eV for $MAPbI_3$, 2.3 eV for $MAPbBr_3$), which can be modulated by anion substitution (Cl > Br > I) or cation substitution ($FA^+ > MA^+ > Cs^+$), as well as by composition engineering [270]. For example, $MAPb(I_{1-x}Br_x)_3$ adjusts the gap from 1.55 eV ($x = 0$) to 2.3 eV ($x = 1$), while $Cs_xFA_{1-x}PbI_3$ reduces the gap to ∼1.48 eV for $x = 0.1$. The bandgap can thus be optimised between 1.2 and 3.6 eV, adapted to single-junction cells (∼1.3 eV, close to the Shockley–Queisser optimum) or tandem cells (∼1.7 eV with silicon). The crystalline phase also influences the gap, with cubic symmetry favouring a narrower bandgap than the tetragonal phase. Figure 2.6 illustrates the electronic band structure of $APbX_3$, highlighting the characteristic inverse electronic arrangement resulting from the bonds in the isolated $[PbI_6]^{4-}$ octahedra.

In terms of optoelectronic performance, halide perovskites exhibit an exceptionally high absorption coefficient ($> 10^5$ $cm^{-1}$) [271], surpassing that of crystalline Si or GaAs, as shown in Figure 2.7. This ensures efficient capture of the solar spectrum with thin layers (300–500 nm). The dominant halogen-$p$ to metal-$p$ optical transition promotes abrupt absorption and intense photoluminescence (internal quantum yield >90% in high-quality films), indicating low losses due to non-radiative recombination.

In terms of transport, perovskites exhibit ambipolar behaviour with low effective masses and reduced exciton binding energy, facilitating the spontaneous dissociation of excitons into free carriers at room temperature. Electrons and holes have balanced mobilities (7–12 $cm^2/V \cdot s$ for polycrystals, up to 60 $cm^2/V \cdot s$ for single-crystal $MAPbI_3$) and long diffusion lengths (100 nm to >1 µm), significantly higher than those of organic semiconductors.

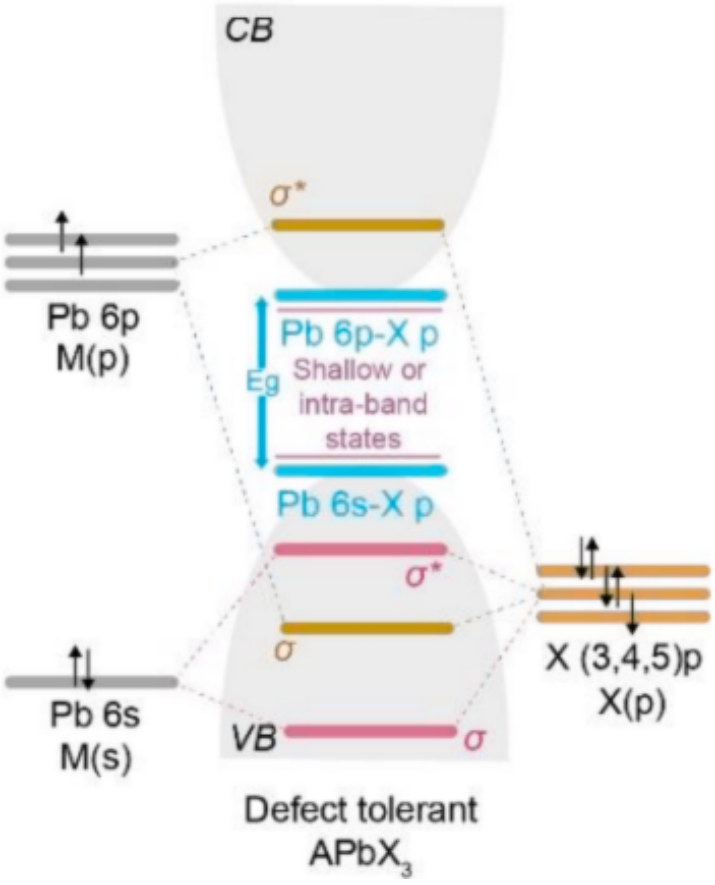



Figure 2.6: Band structure of $APbX_3$, showing the unique inverse electronic arrangement revealed by bonding in isolated $[PbI_6]^{4-}$ octahedra.

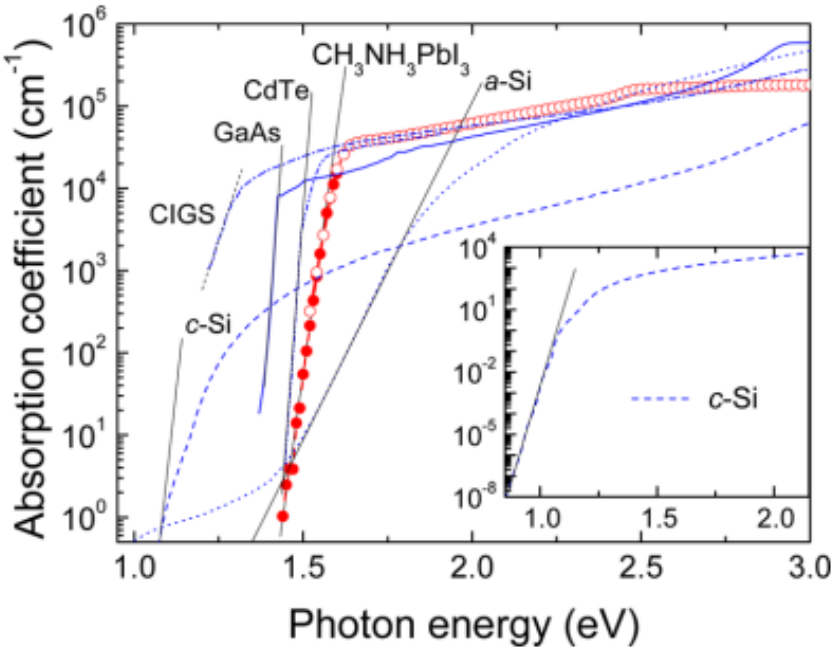



Figure 2.7: Comparative absorption characteristics of $MAPbI_3$ perovskite thin film and standard photovoltaic absorbers [272].

### 2.3.3 Microstructure and structure–property relationships

The microstructure of perovskite layers, as crystalline materials, is characterised by disorder extending across several scales, from local atomic distortions to large-scale structural heterogeneity [273], [274]. This microstructural disorder strongly influences the optoelectronic properties and stability of perovskite solar cells (PSCs). Polycrystalline films, which are fundamental to PSC architectures, typically exhibit microstructural features such as grain boundaries (GBs) [275], [276], heterointerfaces [277], [278], and intra-crystalline disorder (ICDs) [279], as illustrated in Figure 2.8. Grain boundaries have long been considered critical regions due to their high defect density, which promotes non-radiative recombination and reduces carrier lifetime, thereby limiting device efficiency [280]. However, under certain growth conditions or through targeted passivation strategies, these GBs can become electrically benign or even beneficial, facilitating charge separation and improving local photovoltage [281].

Despite these advances, grain boundaries remain preferred pathways for ion migration, causing compositional inhomogeneities, parasitic reactions with metal electrodes (such as silver), and accelerated degradation under operational or thermal conditions [282]. This explains why they are often initiation sites for material degradation. Heterointerfaces, which are often vulnerable to intergranular cracking and delamination under mechanical stress, also negatively impact charge separation and extraction [283], [284]. Recent engineering advances, including chemical treatments and the use of intermediate layers, have reduced ion migration, improved energy alignment, and increased the chemical and mechanical stability of devices. Finally, intra-crystalline disorders, which are localised but omnipresent within grains, remain poorly explored due to limitations in characterisation techniques. They play an important role in charge transport and recombination, affecting overall performance and durability [285].

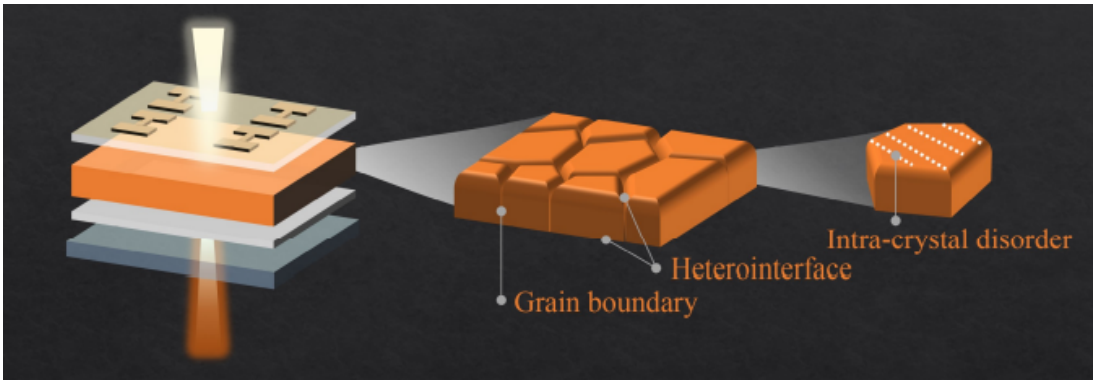



Figure 2.8: Overview of microstructural disorders in perovskite thin films: grain boundaries, heterointerfaces, and intra-crystalline disorders [286].

### 2.3.4 Defects and recombination traps

The performance of PSCs depends heavily on the presence of structural defects in the active layer. These imperfections—including halogen vacancies ($I^-$, $Br^-$), cation interstitials ($MA^+$, $Pb^{2+}$), and interface disorders between layers—create electronic states within the bandgap. These states, known as traps, disrupt the optoelectronic equilibrium of the

material and directly influence the lifetime and mobility of charge carriers. The presence of such traps promotes non-radiative recombination, a process in which the energy of photogenerated electrons and holes is dissipated as heat instead of being converted into electrical current [287], [288]. This undesirable recombination shortens carrier lifetime and limits the energy conversion efficiency of the device. Furthermore, structural and interfacial defects do not merely reduce instantaneous performance: they also play a critical role in accelerated degradation mechanisms, promoting ion migration, chemical instability and reactivity with moisture, temperature, or light [289].

Although the defect density in perovskites generally remains lower than that in amorphous or organic semiconductors, controlling it remains a crucial challenge for ensuring long-term stability and reliability. Indeed, the presence of deep or poorly controlled defects can constitute initiation points for degradation, leading to gradual performance loss [290]. To meet this challenge, several approaches are being developed. Chemical passivation—introducing molecules or additives capable of neutralising charge traps—is particularly effective in reducing non-radiative recombination. Similarly, engineering the interfaces between the perovskite layer and charge transport materials can mitigate the energy and structural discontinuities responsible for recombination at heterocontacts. Finally, optimising deposition and crystallisation processes aims to limit defect formation by controlling stoichiometry, purity and morphology of films. Thus, understanding and controlling defects—whether point, structural, or interfacial—is now an essential research area for simultaneously improving the efficiency and stability of perovskite solar cells, with a view to large-scale industrialisation [291].

## 2.4 Advanced materials and composition engineering of perovskites

### 2.4.1 Metal halide perovskites

Metal halide perovskites, mainly lead (Pb)-based, are the benchmark for high-efficiency photovoltaic materials thanks to their exceptional optoelectronic properties. Their three-dimensional structure provides highly efficient solar absorption and ambipolar charge transport, promoting rapid carrier extraction and high electrical performance [292]. Despite these advantages, several limitations hinder their practical deployment. The toxicity of lead remains a major environmental and regulatory obstacle, while the intrinsic stability of the material is compromised by humidity, heat and light exposure, leading to rapid performance degradation. Furthermore, controlling the deposition of uniform, high-quality films remains complex, and variations in morphology and crystallinity can reduce reproducibility on an industrial scale [246].

To overcome these constraints, advanced strategies have been developed. Partial substitution of A or X ions allows the energy gap to be adjusted and temperature-sensitive phases to be stabilised, thereby reducing performance degradation. Passivation of surface defects and grain boundaries extends the lifetime of carriers and limits non-radiative recombination, resulting in increased short-circuit current ($J_{sc}$) and open-circuit voltage ($V_{oc}$) [291]. Furthermore, engineering interfaces with electron and hole carriers improves

charge extraction and device stability. Finally, the development of hybrid or multi-cationic structures and integration into tandem architectures simultaneously optimises efficiency and durability, paving the way for competitive and more reliable devices on an industrial scale. Among these metal halide materials, $MAPbI_3$ and $FAPbI_3$ are organo-inorganic perovskites, while $CsPbBr_3$ (caesium lead bromide) and $CsPbI_3$ (caesium lead iodide) are inorganic variants offering increased thermal stability. In addition, $MAPbBr_3$ and $FAPbBr_3$, with wider energy gaps (∼2.3 eV), as well as $MAPbCl_3$, used in mixtures to modulate the gap between 1.6 and 3.0 eV, expand the possibilities for application in wide-bandgap or multi-layer tandem devices [240].

### 2.4.2 Mixed cation perovskites

The integration of multiple cations at site A, such as $FA^+$, $MA^+$, $Cs^+$ or $Rb^+$, is a key strategy for stabilising the crystal lattice of perovskites and improving their photovoltaic performance. Mixed compositions, such as $(FAPbI_3)_{1-x}(CsPbI_3)_x$ or $Cs_x(MA_{0.17}FA_{0.83})_{1-x}Pb(I_{0.83}Br_{0.17})_3$, allow precise adjustment of the bandgap between 1.6 and 1.7 eV, suitable for tandem devices, while reducing hysteresis in $J$–$V$ curves [293], [294]. The incorporation of several cations significantly improves thermal and environmental stability, stabilising the photoactive phase at high temperatures (>150 °C) and limiting sensitivity to humidity. These materials exhibit superior crystallinity, more uniform grains and better passivation of defects at grain boundaries, reducing non-radiative recombination and extending carrier lifetime [295]. The addition of bromide ($Br^-$) also enhances resistance to thermal cycling, contributing to the robustness of the material. Thanks to this fine engineering of the cationic composition, mixed-cation perovskites achieve efficiencies exceeding 26% in optimised configurations and durability extended beyond 3,000 hours under encapsulation, paving the way for large-scale production of reliable and reproducible perovskite modules [296], [297]. Table 2.2 summarises the impact of different cation combinations on the stability and optoelectronic properties of perovskites, highlighting the crucial role of cation engineering in simultaneously improving durability and photovoltaic performance.

### 2.4.3 Low-lead and lead-free alternatives

In response to environmental concerns about lead toxicity, alternatives based on tin ($Sn^{2+}$) and germanium ($Ge^{2+}$) have been explored. Compounds such as $FASnI_3$ or $CsGeI_3$ have reduced bandgaps (∼1.2–1.4 eV), close to the theoretical optimum for photovoltaic conversion and suitable for tandem architectures, while offering good carrier mobility. However, their development remains limited by significant chemical instability, linked in particular to the rapid oxidation of $Sn^{2+}$ to $Sn^{4+}$ and the volatility of Ge-based precursors, leading to increased recombination, lower conductivity and accelerated degradation [299].

To mitigate these problems, various strategies are being implemented, such as the addition of reducing additives such as $SnF_2$, hydrophobic encapsulants that extend stability to ∼1000 h, or partial Pb/Sn and Pb/Ge substitutions that reconcile stability, environmental safety and photovoltaic efficiency. These improvements have enabled some recent prototypes to achieve efficiencies of around 15–18% PCE [300]. Figure 2.9 presents a comparison of the efficiencies (PCE) of perovskite cells based on lead, tin, and germanium.

Table 2.2: Impact of different cation combinations on the stability and optoelectronic properties of perovskites [298].

| **Combination of cations (site A)** | **Example composition** | **Effect on stability** | **Optoelectronic impact** |
|---|---|---|---|
| FA + Cs | $(FAPbI_3)_{1-x}$ $(CsPbI_3)_x$ (x = 0, 1) | Improves thermal stability and reduces transition to non-photoactive $\delta$-$FAPbI_3$ phase | Bandgap adjustment (1.55–1.65 eV), improved efficiency |
| MA + FA | $MA_{0.25}FA_{0.75}PbI_3$ | Reduces hysteresis and improves crystallinity | Modulated bandgap (∼1.55 eV), better charge extraction |
| MA + Cs | $(MA_{0.8}Cs_{0.2})$ $Pb(I_{0.8}Br_{0.2})_3$ | Enhances moisture tolerance and structural stability | Increases open-circuit voltage (Voc) |
| FA + Rb | $FA_{0.85}Rb_{0.15}$ $Pb(I_{0.9}Br_{0.1})_3$ | Stabilizes the photoactive phase at high temperatures | Improved efficiency, better defect passivation |
| Triple cation (MA + FA + Cs) | $Cs_{0.05}FA_{0.85}MA_{0.10}$ $Pb(I_{0.85}Br_{0.15})_3$ | Significantly increases thermal and environmental stability (>3000 hours under encapsulation) | Efficiency >26%, adjusted bandgap (1.6–1.7 eV), low hysteresis |

It clearly illustrates that, despite lagging behind lead-based compounds in terms of performance, low-lead and lead-free solutions are progressing towards promising efficiencies, confirming their potential as environmentally friendly alternatives for sustainable photovoltaic devices. So, although low-lead or lead-free perovskites remain less efficient than their lead-based counterparts, they represent a promising avenue for ecological transition, reconciling environmental constraints with the potential for application in sustainable photovoltaic devices.

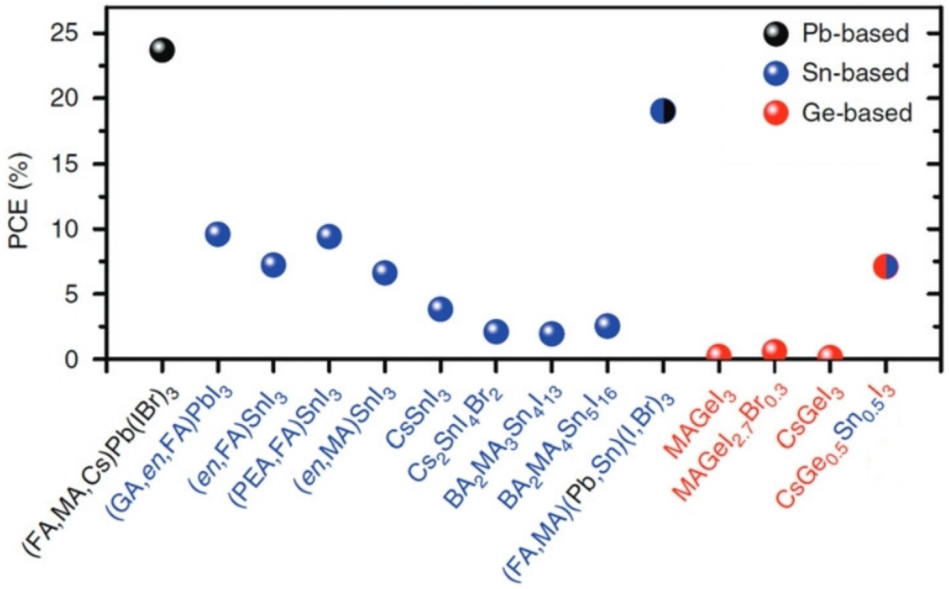



Figure 2.9: Comparison of photovoltaic efficiencies (PCE) of perovskites based on lead (Pb), tin (Sn) and germanium (Ge), illustrating the potential and relative lag of low-lead and lead-free alternatives [300].

### 2.4.4 2D/3D heterostructures and perovskite nanocrystals

The dimensional engineering of perovskites, through 2D/3D heterostructures and nanocrystals, is a key strategy for reconciling stability and high performance in photovoltaic devices. 2D/3D heterostructures combine a high-efficiency three-dimensional (3D) core with a protective two-dimensional (2D) layer formed by bulky organic cations [301]. This hydrophobic architecture greatly reduces moisture-induced degradation and improves passivation of surface defects while maintaining efficient carrier transport. These structures, often based on compositions such as $(BA)_2(MA)_{n-1}Pb_nI_{3n+1}$ (BA = butylammonium, MA = methylammonium) or $(PEA)_2(MA)_3Pb_4I_{13}$ (where PEA is phenylethylammonium), exhibit high efficiencies (22–24%), durability exceeding 4000 hours under ambient conditions, and thermal stability up to 200 °C. Their bandgap, adjustable between 1.6 and 2.0 eV depending on the number of layers ($n$), makes them particularly suitable for tandem cells and compatible with flexible substrates, paving the way for lightweight and robust solar panels [302], [303].

At the same time, perovskite nanocrystals (typically 5–20 nm), such as $CsPbBr_3$, $CsPbI_3$ or $MAPbBr_3$, exploit the quantum confinement effect, which allows the bandgap and emission colour (from green to near infrared) to be finely modulated. They are characterised by intense photoluminescence, adjustable emission and high compatibility with optoelectronic devices. They have demonstrated potential >25% in laboratory tandem configurations. The combined integration of 2D/3D heterostructures and nanocrystals demonstrates advanced perovskite engineering, combining environmental robustness with cutting-edge optoelectronic performance, and positions these materials among the most promising candidates for next-generation photovoltaic and optoelectronic technologies [304].

### 2.4.5 Compositional engineering and additives

Compositional engineering and the use of additives are key strategies for optimising both performance and durability of perovskite cells, beyond simple ion substitution. Modulation of sites A (e.g., $Cs^+$, $MA^+$), B (e.g., $Pb^{2+}$, $Sn^{2+}$) and X (e.g., $I^-$, $Br^-$, $Cl^-$) allows advanced customisation of properties. The partial introduction of $Sn^{2+}$ into mixed Pb/Sn compositions lowers the bandgap to approximately 1.25–1.3 eV, optimising spectral absorption for single or tandem architectures. The incorporation of $Cl^-$ improves crystallinity and provides better thermal stability, while cations such as $K^+$ or $Rb^+$ promote a more homogeneous structure and reduce defect formation [305]. For example, the addition of additives such as methylammonium bromide (MABr) and caesium bromide (CsBr) allows gradual modulation of the crystal structure, promoting the transition from $MAPbBr_3$ to a mixed composition $MA_{1-x}Cs_xPbBr_3$ characterised by improved homogeneity and reduced vacancies, as illustrated in Figure 2.10.

At the same time, additives such as MACl, quaternary ammonium salts or certain organic ligands (e.g., thiocyanates) promote large grain growth (>1.5 µm), limit non-radiative recombination and effectively passivate interfacial defects, thereby reducing trap density. These advances contribute to high performance, with conversion efficiencies exceeding 26–27% for latest-generation perovskite cells, and operational stability beyond

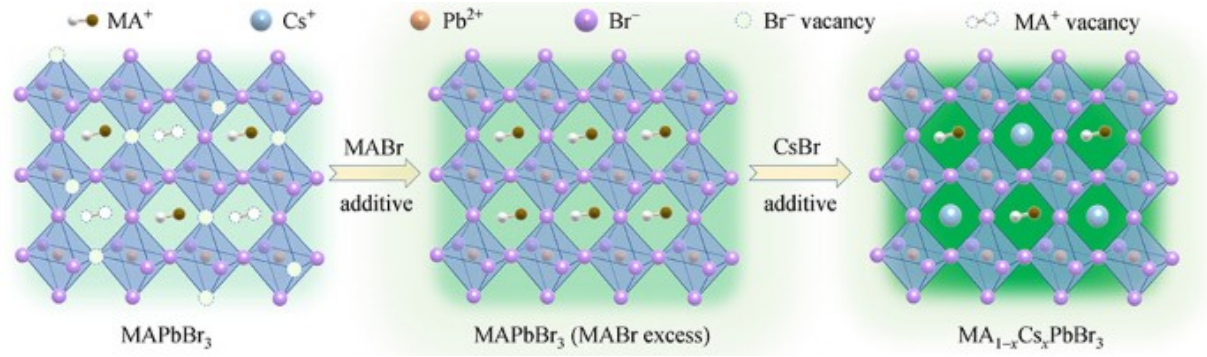



Figure 2.10: Modulation of the crystal structure of $MAPbBr_3$ perovskite by sequential addition of MABr and CsBr additives, leading to a mixed $MA_{1-x}Cs_xPbBr_3$ perovskite with reduced vacancies and structural homogenisation [305].

3,500 hours under encapsulationThis integrated chemical engineering approach improves layer homogeneity, enhances resistance to moisture, light and heat, and positions perovskites among the most promising materials for high-efficiency, long-life photovoltaic technologies. [306], [307].

## 2.5 Manufacture and deposition of perovskite films

The manufacture of perovskite films is a critical step in optimising solar cell performance. The quality of the active layer, determined by its morphology, crystallinity, grain size and uniformity, has a direct impact on charge carrier generation and transport. Obtaining a thick, homogeneous and defect-free layer requires strict control of the composition of the chemical precursors, the deposition conditions and the manufacturing environment. Deposition methods fall into two main categories; solution processes, which are valued for their simplicity, low cost and adaptability to large surfaces, and vacuum techniques, which offer precise control of film thickness and purity, essential for reproducibility and industrial scalability [308]. Beyond these approaches, current research focuses on controlling morphology, reducing defects and ensuring compatibility with large-scale industrial processes. These strategies aim not only to improve photovoltaic efficiency, but also to guarantee the stability and reliability of devices, in line with recent technological advances in the field of perovskite solar cells [309], [310].

### 2.5.1 Solution deposition methods

Solution processes are the most widely used method due to their simplicity, low cost and compatibility with a variety of substrates. These techniques are particularly suitable for mesoporous architectures, as they allow the precursor solution to penetrate the pores of the $TiO_2$ layer. The most common method is spin coating [219], [311].

In the case of single-step spin coating, organic and inorganic precursors (e.g., $PbI_2$ (lead iodide) and MAI (methylammonium iodide)/FAI (formamidinium iodide)) are dissolved in polar solvents such as DMF (dimethylformamide), DMSO (dimethyl sulfoxide) or GBL (gamma-butyrolactone), then deposited onto the rotating substrate. Partial evap-

oration of the solvent causes supersaturation, triggering perovskite crystallisation. Moderate annealing (often <100°C) is then applied to complete crystallisation and obtain a polycrystalline texture. Although this approach allows thin layers (<1 µm) to be formed, it suffers from defects such as holes and significant surface roughness. The addition of a secondary polar solvent or antisolvent, such as toluene, improves nucleation and leads to more homogeneous and transparent films [312]–[314].

Two-step spin coating, widely adopted to overcome these limitations, involves first depositing a layer of $PbI_2$, followed by treatment with a solution of the organic cation (MAI, FAI) dissolved in anhydrous isopropanol (IPA), leading to *in situ* conversion to perovskite ($MAPbI_3$). This method produces dense, homogeneous films with low roughness and better surface coverage [315]. The two spin coating approaches are illustrated in Figure 2.11, which compares the one-step and two-step processes for forming $MAPbI_3$ perovskite films.

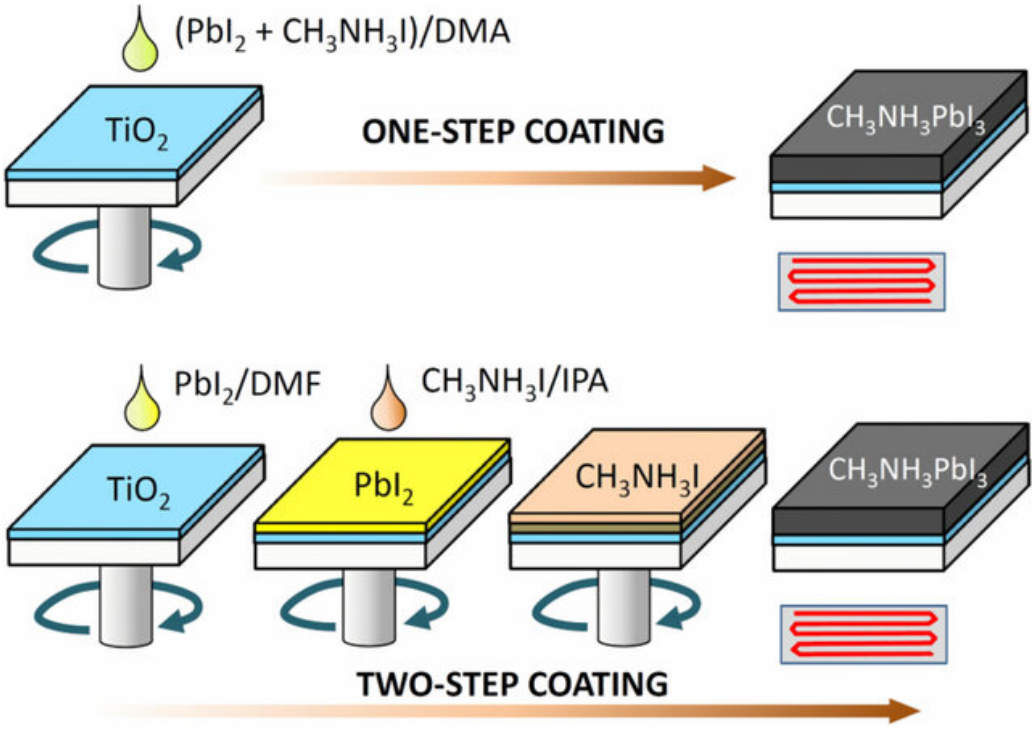



Figure 2.11: Diagram of single-step and two-step spin coating procedures for the formation of $CH_3NH_3PbI_3$ [315].

Other solution-based techniques, such as dip coating, involve immersing a $PbI_2$-coated substrate in an organic halide solution, followed by annealing. This method produces smooth, uniform films but can lead to incomplete conversion due to the formation of a dense surface layer that limits the penetration of the organic cation [316], [317].

Finally, the innovative hot casting technique involves depositing precursors onto a heated substrate (up to 190°C). This promotes almost instantaneous crystallisation, resulting in millimetre-sized grains and a dense layer with high crystallinity. This approach improves carrier mobility but remains more difficult to control [318], [319]. The principle of this process is shown in Figure 2.12. For scale-up, methods such as spray coating, doctor blade coating and slot-die coating offer high reproducibility over large areas and

pave the way for roll-to-roll industrial processes. However, controlling parameters such as substrate temperature and crystallisation processes remains a major challenge in ensuring layer qua

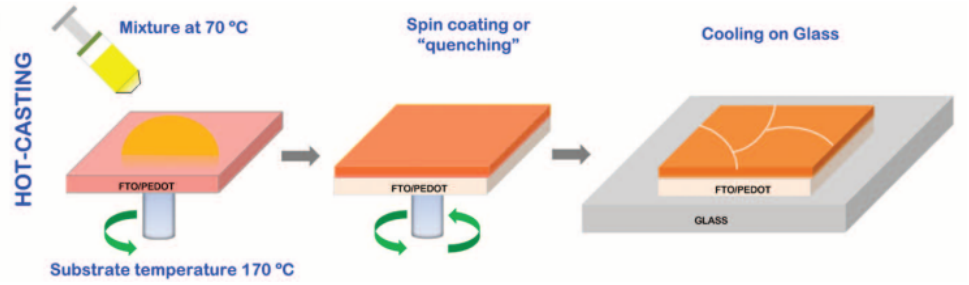



Figure 2.12: Hot-casting method used to deposit and form a uniform perovskite thin film [319].

### 2.5.2 Vacuum deposition methods

Vacuum processes, such as thermal evaporation and co-evaporation, allow precise control of film thickness, uniformity and stoichiometry. They produce compact, continuous and reproducible layers, which are essential for high-performance devices, particularly perovskite/silicon tandem cells [320]. Thermal evaporation under vacuum involves separately heating organic and inorganic precursors (MAI and $PbI_2$) in a vacuum chamber ($10^{-5}$–$10^{-6}$ mbar), allowing them to condense simultaneously on the substrate [321]. This process generates homogeneous films with low roughness and well-defined grains, with excellent thickness control. However, it requires high temperatures (∼350°C) and remains costly, which limits its large-scale industrial adoption [322].

Co-evaporation further improves composition accuracy by simultaneously evaporating the different precursors, forming the perovskite phase directly on the substrate. Although effective, this technique requires rigorous calibration of the flows and remains complex [323], [324]. Hybrid processes, combining spin coating and vapour phase treatment, have also been developed [325]. For example, an initial deposition of $PbI_2$ can be followed by exposure to MAI vapour, leading to efficient conversion to perovskite, while reducing costs compared to pure co-evaporation. These hybrid approaches represent an interesting compromise between quality and cost. Figure 2.13 schematically illustrates the main vacuum deposition methods for perovskite films, including simultaneous co-evaporation of precursors, single-source evaporation, and hybrid sequential deposition.

### 2.5.3 Post-treatment and maturation

Regardless of the deposition method, post-treatment is essential to improve the crystallinity, stability and performance of perovskite films. Thermal annealing (often between 80 and 120°C for several minutes) promotes grain growth, reduces the density of crystalline defects and improves film uniformity. The use of antisolvents (e.g., chlorobenzene, toluene), applied during or after deposition, controls nucleation and produces denser, smoother layers, while reducing residual electron traps. These processes contribute to better charge carrier extraction and greater photovoltaic efficiency. Other innovative approaches include the use of chemical treatments, plasmas, or halogenated vapours (e.g.,

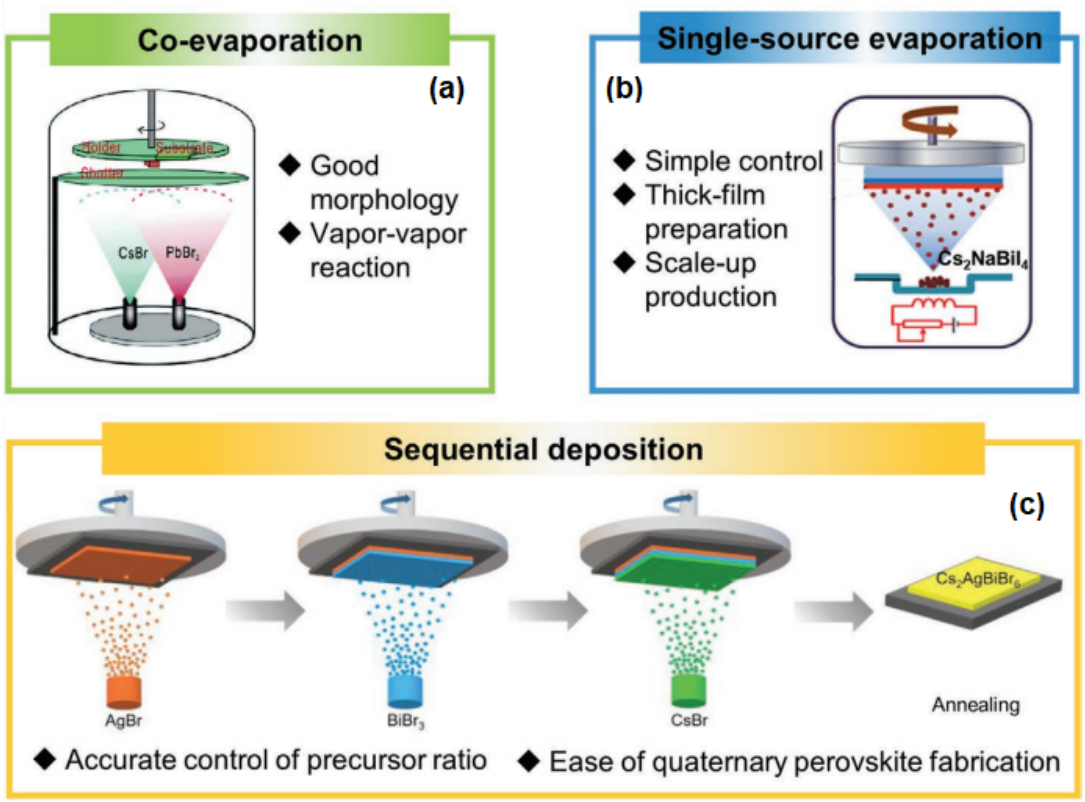



Figure 2.13: Main vacuum deposition methods for perovskite films [322]. (a) Co-evaporation, (b) Single-source evaporation, (c) Sequential deposition.

MAI vapour treatment), which promote the passivation of surface defects and the stabilisation of interfaces [323].

Furthermore, post-treatment also plays a crucial role in optimising heterointerfaces, where specific techniques can be used to reduce interfacial recombination, passivate trap states and adjust band shifts. Recent work has shown that the introduction of 2D/3D heterostructures, such as the $MAPbI_3$–$PEA_2PbI_4$ system, promotes the formation of an energy band gradient at the perovskite–ETL interface, thereby improving charge extraction and long-term stability. Another key area of research concerns the improvement of grain boundaries, which represent a major pathway for non-radiative recombination. By reducing the density of defects at these boundaries through optimised annealing strategies, selective doping or passivation treatments, it is possible to increase grain size and limit performance losses. As illustrated in Figure 2.14, these approaches induce more uniform perovskite grain growth, significantly reducing unwanted recombination and enhancing the overall stability of the devices. Therefore, whether it is a question of optimising interfaces or controlling grain boundaries, post-treatments are now an essential lever for simultaneously improving the efficiency and durability of perovskite solar cells [326].

### 2.5.4 Encapsulation and protection against moisture and oxygen

Encapsulation is a crucial step in ensuring the durability and industrial reliability of perovskite solar cells, whose stability is severely compromised by moisture, oxygen, UV

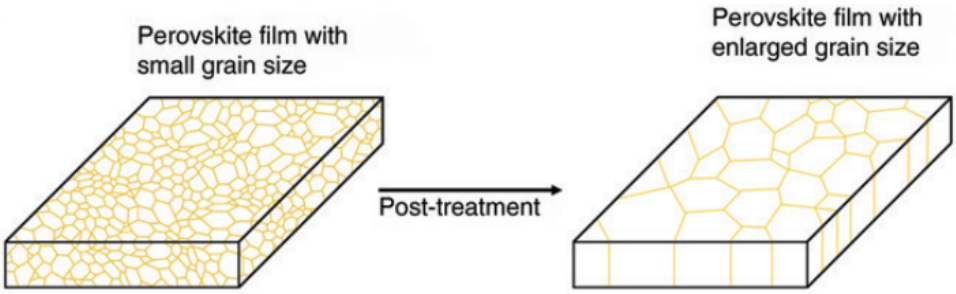



Figure 2.14: Diagram illustrating the growth of perovskite grains induced by post-treatments [326].

radiation and thermal stress. To meet commercialisation requirements, the encapsulation material must be virtually impermeable to diffuse species, prevent the evaporation of organic or halogenated compounds and the possible release of toxic lead-based by-products, while maintaining high optical transparency so as not to impair the efficiency of the devices. It must also remain chemically inert with respect to the active layers and mechanically robust to withstand abrasion, thermal cycling and harsh environmental conditions. Two key parameters, water vapour transmission rate (WVTR) and oxygen transmission rate (OTR), are used to qualify the effectiveness of an encapsulant: values below $10^{-3}$–$10^{-6}$ g·m$^{-2}$·day$^{-1}$ (WVTR) and $10^{-4}$–$10^{-6}$ cm$^3$·m$^{-2}$·day$^{-1}$·atm$^{-1}$ (OTR) are considered necessary for effective protection [327].

Various encapsulation strategies have been developed to meet these requirements simultaneously. The traditional glass-to-glass approach involves sealing the device between two glass plates using resin, ensuring excellent sealing but at the expense of flexibility. Polymer encapsulants, such as EVA (ethylene vinyl acetate), parylene or certain hydrophobic polyurethanes, offer a lighter and more flexible solution that is compatible with flexible devices, but their long-term resistance to gas permeation remains limited. Thin inorganic films deposited by ALD (atomic layer deposition) or CVD (chemical vapour deposition) ($Al_2O_3$, $SiO_2$, $SiN_x$) provide an extremely effective barrier to moisture and oxygen penetration, but at the cost of mechanical fragility and higher cost. Finally, hybrid systems combining organic and inorganic layers in multilayer structures combine transparency, flexibility and impermeability, and are currently one of the most promising avenues for next-generation perovskite modules [327], [328].

The results reported in the literature illustrate the significant advances achieved through these processes, with lifespans exceeding 5000 hours under ambient conditions, more than 95% of initial efficiency retained after 2000 hours of accelerated ageing tests (85°C, 85% relative humidity), and photovoltaic performance exceeding 25% after optimised encapsulation. In addition, some encapsulants also provide protection against UV and thermal stress, limiting photo-instability and delaying accelerated degradation. In this way, encapsulation can no longer be considered as simple protective packaging, but as a key technological element determining the environmental stability, operational life and industrial viability of perovskite solar cells [327], [329]. The importance of this role is summarised in Figure 2.15, which illustrates the protective mechanisms implemented against external degradation agents.

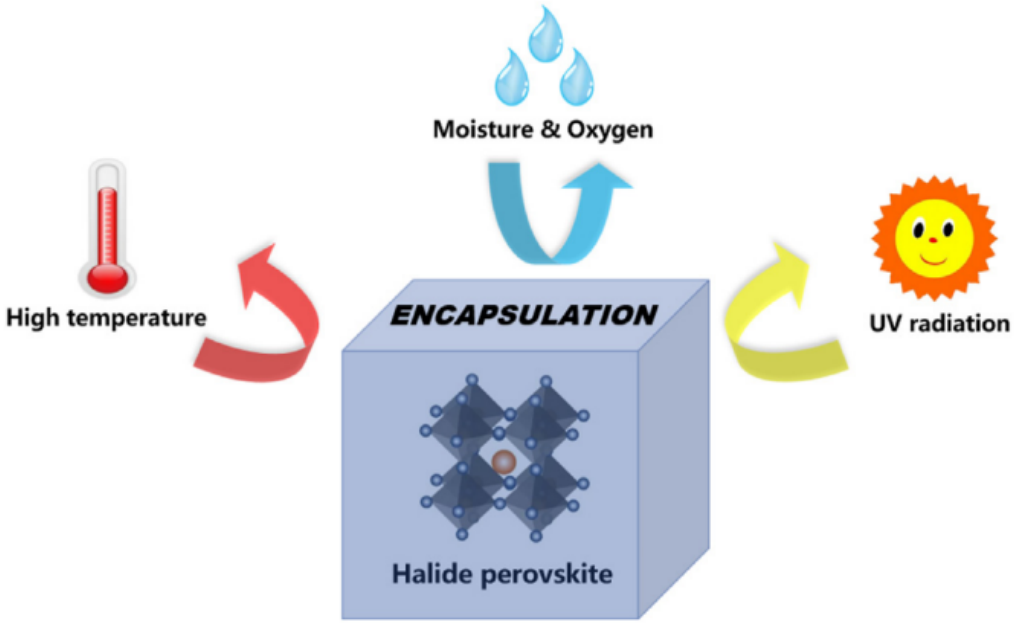



Figure 2.15: Diagram illustrating the protection of perovskite materials against environmental stresses (humidity, oxygen, high temperature, UV radiation) through encapsulation [329].

## 2.6 Design and operating principles of perovskite cells

The remarkable success of perovskite solar cells (PSCs) is based on the unique combination of an absorber with exceptional optoelectronic properties and sophisticated engineering of architectures and functional layers. The efficiency, stability and reproducibility of these devices depend as much on the configuration adopted as on the quality of the interfaces and the energy alignment between the different layers. The rapid progress made over the last decade demonstrates that mastering these parameters is essential not only to achieve high efficiencies, but also to ensure the durability of the devices [330], [331].

In this context, studying the architectures helps us understand how the stacking and organisation of the layers directly influence the collection and separation of photogenerated charges. The attention paid to the materials constituting the functional layers (absorber, ETL, HTL, electrodes) is crucial, since each interface must ensure selective transport while minimising parasitic recombination. Similarly, understanding the operating principle, based on the generation, separation and extraction of charge carriers, is an essential step in optimising overall performance [332]. Finally, despite their yields now exceeding 26% in single junction and more than 33% in tandem, perovskite cells still present specific challenges. Among these, hysteresis in J–V curves [333], [334] and internal ion migration are key phenomena that limit operational stability and require special attention in the design of architectures [335].

## 2.6.1 Materials and structures of PSCs

### 2.6.1.1 Materials used in PSCs

The phenomenal success of PSCs is based not only on the originality of their architecture, but above all on the wide variety of materials that can be used for each of their constituent layers. Unlike conventional photovoltaic technologies, where the choices are relatively fixed (crystalline silicon, thin layers based on CdTe or CIGS), perovskite cells offer unprecedented flexibility, allowing the materials to be adapted to performance, stability or production cost requirements. The perovskite absorber layer at the heart of solar cells converts solar photons into electrical charges. It consists of either organo-inorganic hybrid halide perovskites (e.g. $MAPbI_3$, $FAPbI_3$) or entirely inorganic perovskites (e.g. $CsPbI_3$). Its main role is the efficient generation of electron-hole pairs thanks to excellent absorptivity and good film quality, which largely determines the overall performance of the device [336], [337].

In a PSC, transport layers play a central role in the selectivity and efficiency of charge extraction [338]. The ETL is responsible for collecting and transferring photogenerated electrons to the transparent electrode while blocking holes in order to limit recombination. Historically, titanium dioxide ($TiO_2$) has been the inorganic material of choice due to its good band alignment and high optical transparency [339]. However, it has two major drawbacks, instability under UV illumination and the need for high-temperature processing, which limits its integration into low-temperature processes and on flexible substrates. Inorganic alternatives such as tin oxide ($SnO_2$), zinc oxide (ZnO), indium oxide ($In_2O_3$), tungsten oxide ($WO_x$) and cerium oxide ($CeO_x$) have therefore been developed, as these materials offer higher electron mobility, increased transparency and compatibility with low-temperature deposition processes [340], [341]. In inverted (p–i–n) architectures, n-type organic materials such as fullerenes and their derivatives, such as PCBM and ICBA, have also shown remarkable efficiency, particularly thanks to their excellent energy alignment and simple implementation in solution. However, their stability remains limited, which hinders their use in long-life devices [342].

In terms of hole transport layers (HTL), one of the most widely used materials remains 2,1,7,7-tetrakis(N,N-di-p-methoxyphenylamine)-9,9 -spirobifluorene (Spiro-OMeTAD), which is highly valued for its ability to efficiently extract holes [343], [344]. However, its main drawback is the need to add dopants such as lithium bis(trifluoromethanesulfonyl)imide (Li-TFSI) and 4-tert-butylpyridine (tBP), which compromise long-term stability. Other organic materials, such as PTAA or conductive polymers (PEDOT:PSS, PolyTPD), offer interesting alternatives, particularly due to their low cost and solution deposition [345], [346]. However, the acidic and hygroscopic nature of PEDOT:PSS, for example, limits its durability [347]. Given these constraints, inorganic materials such as $NiO_x$, CuSCN and CuI are attracting growing interest. They offer excellent chemical stability, good energy alignment and compatibility with industrial processes, making them among the most promising candidates for large-scale applications [348].

Electrodes are another critical component. The front electrode is generally made of transparent conductive oxides such as ITO or FTO, which combine high electrical conductivity with transparency greater than 80%. However, their high cost and rigidity limit

their industrial adoption, particularly for flexible applications. Alternatives such as doped oxides (AZO, IZO), ultra-thin metal grids and graphene films are therefore being actively researched [349]. The rear electrode is most often composed of noble metals such as gold or silver, which ensure excellent charge extraction, but their high cost and tendency to ion migration raise durability issues [350]. More economical and stable options, such as copper, aluminum or printable carbon electrodes, are increasingly being explored [351]. Beyond these essential components, interface engineering and passivation strategies play a decisive role in improving contact selectivity and limiting non-radiative recombination. The introduction of ultra-thin oxide layers ($Al_2O_3$), self-assembled monolayers or functional additives reduces crystalline defects and increases operational stability in the face of degradation factors such as humidity, oxygen or heat [352].

#### 2.6.1.2 Architectures of PSCs

PSCs can adopt several architectures, which largely determine the dynamics of charge transport, the quality of interfaces and, therefore, overall photovoltaic performance. Among these, two main families dominate research and development, mesoporous structures, derived from dye-sensitised cells, and planar architectures, inspired by organic photovoltaic cells. The planar structures can be divided into two sub-categories, the direct n–i–p configuration, where light first passes through the ETL, and the inverted p–i–n configuration, in which light first interacts with the HTL [353]. These different configurations are shown in Figure 2.16, which also highlights the materials generally used for each layer.

*i.* **Mesoporous structures**

Mesoporous architectures are one of the first approaches adopted for the development of PSCs. They are based on the infiltration of the active perovskite layer into a nanoporous metal oxide matrix, usually $TiO_2$ or, more rarely, $Al_2O_3$. This three-dimensional structure provides a large contact surface between the perovskite and the electron transport layer (ETL), facilitating the separation and extraction of photogenerated charges. The mesoporous scaffold acts as an electronic guide while providing mechanical support for the perovskite deposit, promoting homogeneous crystallisation and better surface coverage. There are two main variants of this architecture, the most common mesoporous n–i–p configuration, where the ETL is placed under the perovskite and the HTL above, and the less common mesoporous p–i–n configuration, which reverses this order. Both exploit the advantages of the nanoporous skeleton, but differ in the charge collection sequence and performance optimisation depending on the materials used [354], [355]. This type of architecture has contributed significantly to the rapid improvement in PSC performance over the last decade. It offers several advantages [356], including:

- An extended interface between the perovskite and the mesoporous oxide, which promotes efficient electron transfer,
- A reduction in volume recombination, thanks to the immediate proximity of the transport interfaces,
- Controlled perovskite morphology, with the mesoporous network serving as a natural template during crystallisation.

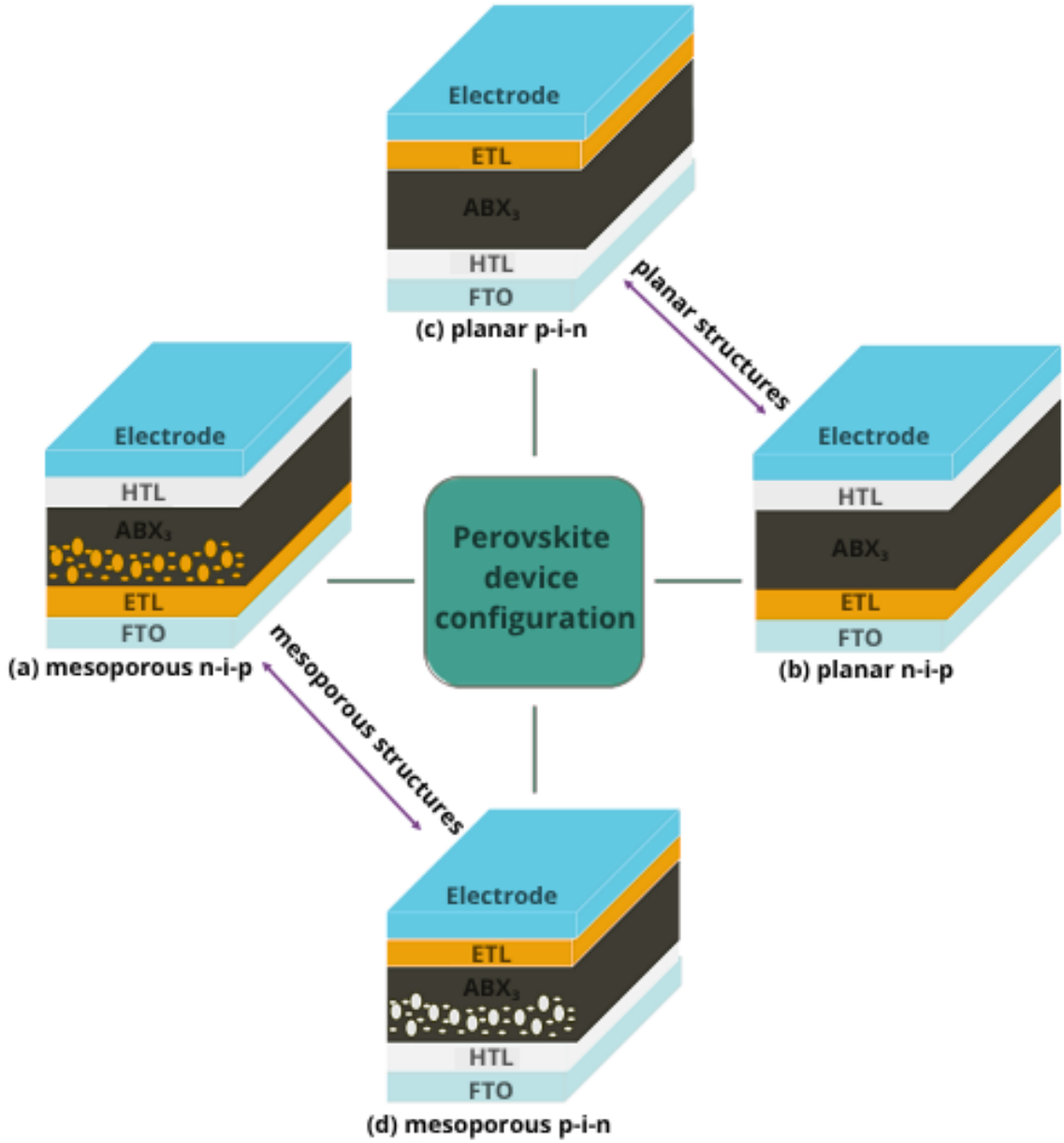



Figure 2.16: Schematic representation of the main structures of PSCs: (a) mesoporous n–i–p, (b) planar n–i–p, (c) planar p–i–n, and (d) mesoporous p–i–n.

However, despite these advantages, mesoporous cells have significant limitations. Firstly, their manufacture requires high-temperature annealing (often $> 450$ °C) to ensure the crystallisation and stability of mesoporous $TiO_2$, which compromises their compatibility with flexible substrates and roll-to-roll industrial processes. Secondly, the presence of multiple interfaces can introduce undesirable recombination sites, reducing the open-circuit voltage ($V_{OC}$). Finally, the porous structure can limit the efficient absorption of light in the near-infrared part of the spectrum ($> 700$ nm), hindering the full exploitation of perovskite's optical potential. In addition, mesoporous cells are often associated with pronounced hysteresis phenomena in I–V curves, linked to charge accumulation and ion migration at interfaces. This affects not only the reproducibility of efficiency measurements but also the long-term stability of the devices [357], [358].

Given these constraints, the scientific community's interest has gradually shifted towards planar architectures, which eliminate the mesoporous scaffolding and allow the use of low-temperature processes that are better suited to large-scale manufacturing and integration on flexible substrates. Nevertheless, mesoporous structures remain of great academic interest because they allow the fundamental mechanisms of transport and recombination in perovskite cells to be explored, and certain hybrid approaches continue to be developed to combine the advantages of both geometries [354].

### *ii.* Planar n–i–p (direct) structures

The planar n–i–p architecture, shown in Figure 2.16(b), is currently one of the most widely studied for PSCs. It consists of a transparent conductive substrate (glass coated with FTO or ITO), followed by an electron transport layer, an active perovskite layer, a hole transport layer, and finally a metal electrode (Ag, Au or sometimes Cu). This configuration is referred to as (direct) because light first passes through the n-layer (ETL). The performance of these devices depends heavily on the materials chosen and the quality of the interfaces. The ETL, usually compact $TiO_2$ or $SnO_2$, plays an essential dual role: it must allow rapid and selective extraction of electrons while effectively blocking holes, and it directly influences the nucleation and crystallisation of the perovskite deposited on its surface. Thus, the composition, morphology and heat treatment conditions of the ETL determine the quality of the active film and, consequently, the overall efficiency [359], [360].

Historically, $TiO_2$ has been widely used as an ETL, particularly in devices such as the FTO/$TiO_2$/$MAPbI_3$/P3HT/Ag structure, which achieved an efficiency of 13.6% with low-temperature processing. However, $TiO_2$ has certain limitations, relatively modest electron mobility, the need for high-temperature annealing for good crystallisation, and instability under UV illumination, which can lead to accelerated device degradation [361]. To overcome these constraints, other materials have been explored: nanoparticulate ZnO, CdSe, $WO_x$, and organic layers such as [6,6]-phenyl-$C_{61}$-butanoate methyl (PCBM). Among these, $SnO_2$ has emerged as the most promising alternative. This material combines several advantages: high optical transparency, superior electron mobility, enhanced chemical stability, and the possibility of low-temperature deposition by various methods such as colloidal spin-coating, thermal decomposition, or atomic layer deposition (ALD). Significant optimisations have been reported, and surface passivation with $PbI_2$ has been shown to achieve a certified efficiency of 20.9% [362], [363].

At the same time, the choice of HTL is also crucial. It must ensure rapid and selective hole extraction, minimise interfacial recombination and maintain chemical compatibility with perovskite. The most commonly used organic materials are Spiro-OMeTAD, PTAA and PEDOT:PSS, while inorganic alternatives such as $NiO_x$ and CuSCN offer better stability properties. The determining factor is the energy alignment between the valence band of the perovskite and the HOMO level of the HTL, in order to avoid any charge transfer barrier. In addition, optical transparency, hole mobility and thermal stability are key parameters in the choice of HTL [364].

#### *iii.* Planar p–i–n (inverted) structures

In the planar p–i–n architecture, illustrated in Figure 2.16c, the order of the layers is reversed compared to the n–i–p configuration. A transparent conductive substrate (ITO or FTO) is first covered with a HTL, followed by the active perovskite layer, then an ETL and finally a metal electrode (often Al, Ag or Cu). This configuration, initially developed based on organic photovoltaic cells, has several major advantages. First, it allows for entirely low-temperature manufacturing, making it perfectly suited to flexible substrates and roll-to-roll industrialisation processes. Secondly, it helps to significantly reduce hysteresis in current-voltage (J–V) curves, a recurring problem in n–i–p architectures. Finally, the p–i–n structure offers better operational stability, thanks to more efficient interface management and improved defect passivation [365], [366].

Early versions of these devices mainly used organic materials, in particular PEDOT:PSS as HTL and PCBM (a fullerene derivative) as ETL. Although these choices quickly achieved attractive efficiencies, they suffered from significant limitations. PEDOT:PSS, for example, is acidic and hygroscopic, promoting perovskite degradation and the diffusion of unwanted ions. PCBM, on the other hand, provides good electron extraction but remains expensive and sensitive to oxidation, which limits the stability of the devices. To overcome these obstacles, research has focused on the use of more robust inorganic materials. Among the promising alternatives, $NiO_x$ has emerged as a stable and transparent HTL, while ZnO and especially $SnO_2$ have proven to be excellent ETLs, combining high electron mobility, compatibility with low-temperature deposition, and improved durability. At the same time, innovative approaches to perovskite deposition, such as the two-step method, solution engineering and thermal evaporation, have improved crystalline quality, reduced interface defects and increased performance reproducibility. Due to these optimisations, planar p–i–n cells have seen their efficiencies grow rapidly, reaching over 23% certified efficiency. Furthermore, their compatibility with low-cost alternative electrodes (e.g., carbon or copper) reinforces their potential for large-scale industrialisation [367]–[370].

Overall, while mesoporous architectures played a fundamental role in the initial demonstration of perovskites' potential, they remain limited by demanding manufacturing processes and less competitive performance. Planar architectures, and in particular the inverted p–i–n configuration, are now the focus of most research efforts. They offer an optimal compromise between high efficiency, low hysteresis, increased stability and compatibility with low-temperature industrial processes, making them the most promising candidates for large-scale commercialisation of perovskite solar cells [240].

### 2.6.2 Operating principle of PSCs

The operation of a PSC is based on the direct conversion of light into electrical current through a series of coordinated steps. When the active perovskite layer is exposed to sunlight, it efficiently absorbs photons and generates electron-hole pairs. These weakly bound carriers quickly separate and diffuse towards the selective transport layers: electrons are directed towards the ETL, while holes migrate towards the HTL. The electrodes then collect these charges and transfer them to the external circuit, producing a usable

electric current. The performance of this mechanism depends mainly on the quality of the interfaces and the energy harmonisation between the perovskite layer and the transport layers. Precise alignment of the conduction and valence levels facilitates charge injection and extraction while reducing recombination losses. This synergy between materials and interfaces determines not only the conversion efficiency but also the long-term stability and reliability of perovskite solar cells [371]–[374].

### 2.6.3 Hysteresis and ion migration in PSCs

A distinctive phenomenon of PSCs is the hysteresis of current–voltage curves, which is highly dependent on the direction and speed of scanning, where the speed of scanning refers to the rate at which the applied voltage is varied during the measurement (typically in V/s or mV/s). This behaviour is mainly attributed to ion migration within the active layer. Under illumination or electrical polarisation, some ions— notably halides ($I^-$, $Br^-$) and organic cations ($MA^+$, $FA^+$)—move through the crystal lattice, particularly through the vacancies and grain boundaries present in polycrystalline films. This ionic mobility causes ions and vacancies to accumulate at the interfaces, locally modifying the electric fields and energy alignment, which disrupts charge extraction and generates the observed hysteresis [375], [376]. This ionic mobility causes ions and vacancies to accumulate at the interfaces, modifying local electric fields and disrupting charge extraction, as illustrated in Figure 2.17.

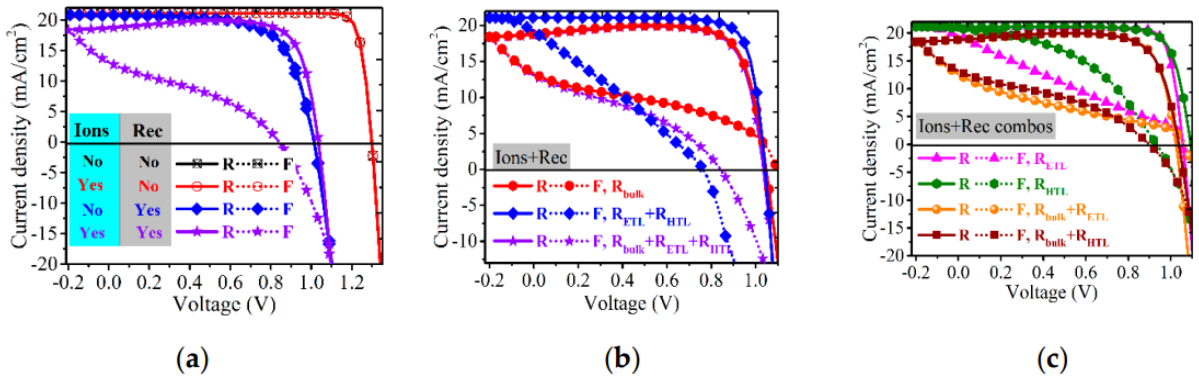



Figure 2.17: Impact of defective ions and recombination on J–V hysteresis. (a) Simulated J–V hysteresis with and without ions and recombination (Rec); (b, c) Hysteresis loops for different combinations of bulk ($R_{bulk}$) and interfacial ($R_{ETL}$, $R_{HTL}$) recombination processes [377].

Theoretical calculations and experimental studies have confirmed that halide vacancies have the lowest activation energies (approximately 0.1–0.8 eV), facilitating their migration at room temperature. For example, the diffusion of iodides, which is much faster than that of organic cations or $Pb^{2+}$ ions, dominates the migration process in $MAPbI_3$ [378]. The accumulation of mobile ions near the electrodes can lead to a phenomenon of temporary interfacial doping, inducing reversible polarisation and, in some cases, a change in the apparent polarity of the device. These transient dynamics explain not only hysteresis but also certain long-term performance instabilities [379].

Beyond the immediate effect on J–V characteristics, ion migration contributes to the gradual degradation of functional layers, undermining the operational stability of devices. To overcome this, various strategies are being explored: reducing defect density through film engineering, passivating interfaces, introducing additives that inhibit ion mobility, or using more stable inorganic and mixed perovskites ($CsPbI_3$, FA/Cs). Understanding and controlling this phenomenon therefore remains essential to improving reliability and considering large-scale commercialisation of perovskite solar cells [380], [381].

## 2.7 Performance and Technological Challenges

Despite spectacular advances, the operational stability of PSCs remains the main obstacle to large-scale industrial adoption. Unlike silicon cells, which can last 20 to 25 years, PSCs degrade rapidly under various environmental and electrical stresses. This instability can be classified into two main categories: extrinsic, related to external factors (humidity, oxygen, heat, UV radiation), and intrinsic, inherent to the material or induced by operating conditions (illumination, electric field, ion migration, interfaces) [248], [382].

### 2.7.1 Efficiency Under Controlled Conditions

Perovskite solar cells currently offer some of the best laboratory yields thanks to their remarkable optoelectronic properties, adjustable bandgap, high absorption coefficient, low defect density and limited non-radiative losses. In strictly controlled environments (inert atmosphere, low humidity, effective encapsulation), they maintain high performance and stability over several hundred hours. However, these record results mainly concern small-area devices ($< 1$ cm$^2$). When scaling up to larger modules exposed to real-world conditions, problems with film uniformity and accelerated degradation arise, leading to a significant decrease in performance. This highlights the importance of developing large-scale reproducible deposition processes, while strengthening the resilience of materials to environmental and operational stresses [383]–[385].

### 2.7.2 Stability and Degradation Mechanisms

#### 2.7.2.1 Extrinsic Degradation

- **Heat and thermal stability**

The operating range of PSCs (–15 to 65 °C) covers several phase transitions (orthorhombic, tetragonal, cubic) that alter optoelectronic properties. While $MAPbI_3$ retains a relatively stable photoactive phase, $FAPbI_3$ and $CsPbI_3$ rapidly switch to inactive phases at room temperature. The addition of bulky cations (PEA, BA) or the mixing of cations ($FA^+/Cs^+$) partially stabilise these active phases. Nevertheless, thermally activated decomposition phenomena appear at temperatures above 85 °C, with the formation of $PbI_2$, a phenomenon aggravated by the diffusion of ions to adjacent layers and their interaction with the electrodes [371]. Carbon-based materials, including graphene, carbon nanotubes (CNTs) and carbon fibers, play a crucial role in enhancing the thermal stability of PSCs by facilitating efficient heat dissipation and suppressing thermally induced degradation pathways [386], [387].

- **Humidity and moisture**

Water is the most feared enemy of perovskite films. Exposure leads to the formation of a monohydrate phase, which is initially reversible but ultimately induces irreversible morphological alterations and a significant loss of efficiency. Partial replacement of iodide with bromide or thiocyanate ($SCN^-$), as well as the introduction of hydrophobic interlayers (thiols, functionalised fullerenes, 2D layers), are effective strategies for limiting moisture infiltration [388]–[390].

- **Oxygen and light (photo-oxidation)**

While oxygen alone has little effect on stability in the dark, the combination of oxygen and light leads to rapid degradation, with a change in color (from black to yellow). This phenomenon is attributed to the formation of superoxide ($O_2^-$) by the capture of photoexcited electrons, which deprotonate organic cations and trigger decomposition [391], [392]. Oxygen diffusion is promoted by grain boundaries and crystal defects, resulting in a strong correlation between photo-oxidation and defect density. Rapid electron extraction by an effective ETL (e.g., $TiO_2$) can compete with the formation of superoxide and limit this mechanism [393]–[395].

- **Interactions with electrodes**

Metal electrodes (Ag, Au, Al, Cu) exhibit marked instability, particularly under illumination and heat. The formation of metal halides (AgI, CuI) or the diffusion of metal ions (Au, Ag, Cu) in perovskite generate non-radiative recombination centers, drastically reducing the PCE. The introduction of diffusion barriers (ITO, ALD-deposited oxides, doped graphene) or the use of alternative electrodes (carbon, hybrid electrodes) are promising avenues for improving stability. However, carbon electrodes still suffer from limited conductivity [396].

#### 2.7.2.2 Intrinsic Degradation

- **Photo instability and segregation**

Under prolonged illumination, perovskite films undergo halide segregation (Hoke effect), cationic segregation and photochemical reactions [397]. These processes induce compositional heterogeneity and a gradual decrease in efficiency [398].

- **Electric field and ion migration**

The application of an external bias promotes the migration of halide ions ($I^-$, $Br^-$) and cations ($MA^+$, $FA^+$) towards the interfaces. This ionic redistribution leads to marked hysteresis in the I–V curves, the formation of voids or $PbI_2$ nanoparticles, and increased recombination at the interfaces [378], [399]. Recent studies have mapped this ionic migration and identified its major role in degradation. Local accumulation of ions alters energy levels, weakens interfaces, and accelerates efficiency loss [400], [401].

### 2.7.3 Challenges for Industrialisation and Upscaling

The transition of perovskite solar cells to large-scale industrial production requires overcoming three major challenges [388]:

- **Uniformity and reproducibility**

Laboratory processes such as spin-coating, which are well suited to fundamental research, must evolve towards scalable deposition techniques (slot-die, spray-coating, co-evaporation) capable of ensuring the formation of homogeneous and reproducible films over large surfaces. Mastering these processes is essential for the industrial viability of the modules [252].

- **Lead toxicity**

Lead, a key element in current performance, raises serious environmental and health concerns. Alternative options based on tin (Sn), germanium (Ge) or bismuth (Bi) are promising, but remain limited in terms of efficiency and stability. At the same time, the development of strategies for the containment, recycling and safe management of lead appears essential in order to reconcile efficiency and sustainability [402], [403].

- **Operational sustainability**

To compete with silicon, PSCs must maintain competitive efficiency (>20%) over several decades. This requires robust encapsulation, effective protection against extrinsic factors (humidity, heat, UV, oxygen), and advanced interface engineering to limit intrinsic phenomena such as ion migration and halide segregation [404].

## 2.8 Tandem Solar Cells (TSCs)

### 2.8.1 Principles and Advantages of Tandem Structures

TSCs are an essential strategy for overcoming the fundamental limitation imposed on single-junction photovoltaic devices. According to the Shockley–Queisser (SQ) limit, the maximum theoretical efficiency of a single-junction cell is restricted by the optical and thermal losses inherent in photon absorption. For crystalline silicon, which currently dominates more than 90% of the global photovoltaic market, this limit is set at around 29.4%, while the best commercial devices already achieve nearly 27–28%, thus approaching the ultimate performance limit [405]–[407]. This approaching saturation calls for a new generation of more efficient photovoltaic architectures. Figure 2.18 shows the record efficiencies of solar cells as a function of their band gap, compared to the Shockley–Queisser theoretical limit for a single junction.

Among the approaches proposed, tandem (or multi-junction) cells appear to be the most promising. The principle is based on the vertical stacking of several sub-cells with different band gaps in order to exploit the spectral complementarity of solar radiation. The top cell, with a wide band gap, absorbs high-energy photons (in the UV and visible ranges), while lower-energy photons are transmitted and then absorbed by the bottom sub-cells with low $E_g$ (often based on silicon). This cascade mechanism significantly reduces losses due to thermalisation and transmission, allowing for near-optimal conversion of the solar spectrum [408], [409]. The integration of perovskites as top cells above silicon or CIGS thus makes it possible to combine the optimal absorption of visible light by perovskite with the excellent infrared absorption of silicon, maximising the use of the solar spectrum [410]. The interconnection between subcells is carried out in 2-terminal (2T, shared current) or 4-terminal (4T, independent voltages) configurations, each presenting compromises in terms

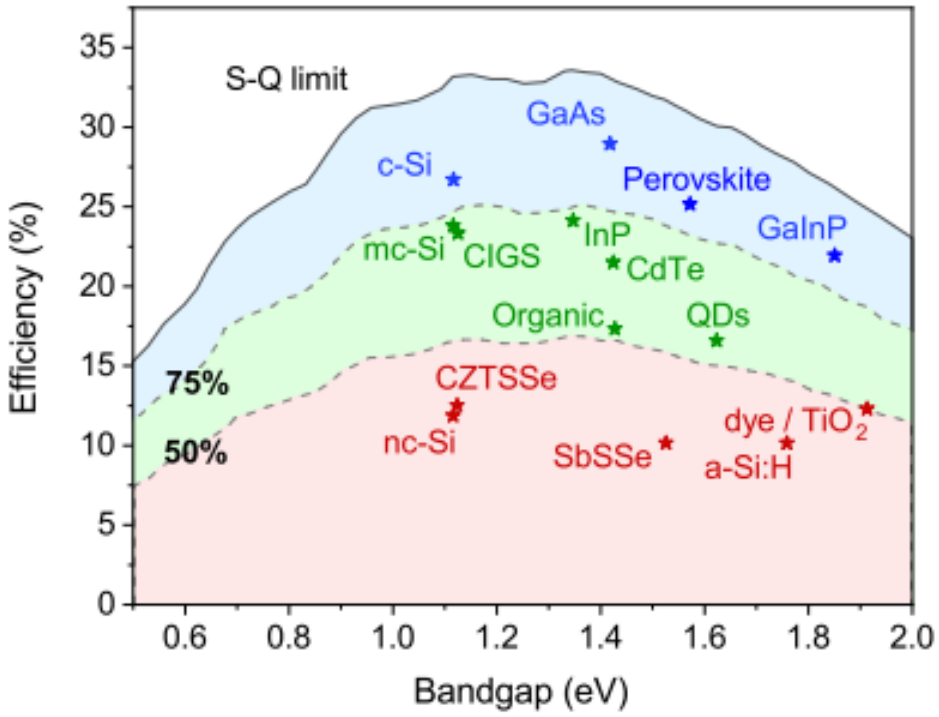



Figure 2.18: Record efficiencies of single-junction solar cells as a function of their bandgap, compared to the Shockley–Queisser theoretical limit [405].

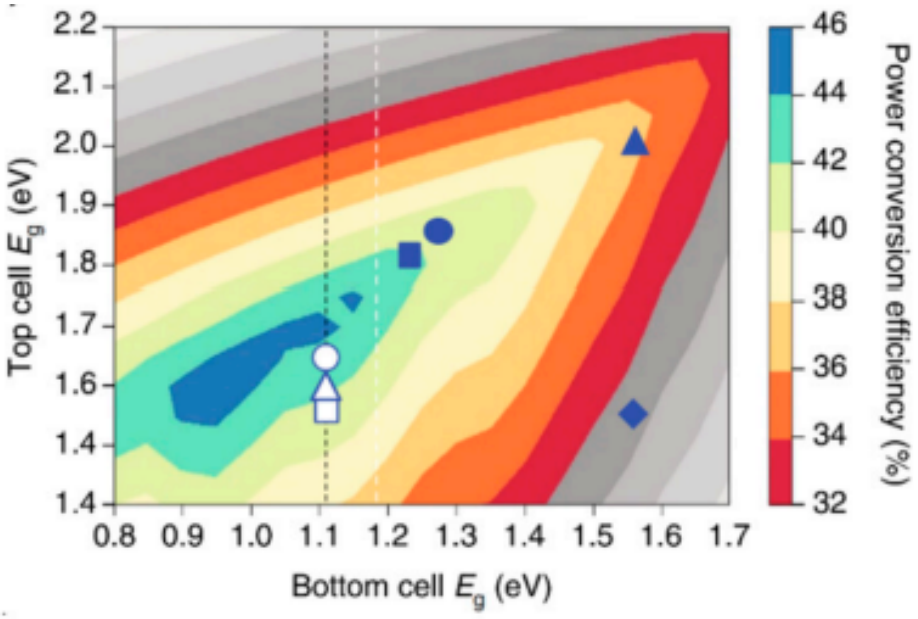



Figure 2.19: Theoretical efficiency limit of two-terminal tandem solar cells as a function of the bandgaps of the top and bottom sub-cells [412].

of complexity and ohmic losses [411]. Figure 2.19 illustrates the theoretical efficiency limit of two-terminal tandem cells as a function of the bandgaps of the upper and lower cells.

In the family of tandem architectures, perovskite/silicon tandem cells (PSTSCs) are emerging as one of the most promising alternatives for the next generation of photo-

voltaics. Their operation is based on the same fundamental steps as for single-junction solar cells: photon absorption, electron-hole pair generation, dissociation and transport of photogenerated carriers to the electrodes [409]. In perovskites, the low binding energy of excitons promotes almost instantaneous dissociation into free carriers, enabling efficient collection even for very thin active layers (<500 nm). In silicon, charge separation relies mainly on the electric field of the p–n junction, reinforced by advanced architectures such as PERC (Passivated Emitter and Rear Contact), TOPCon (Tunnel Oxide Passivated Contact) or high-efficiency heterojunctions (SHJ) [413].

Since the first demonstration in 2014 of a 4T PSTSC with a modest efficiency of 13.4%, progress has been spectacular [414]. By 2015, a monolithic 2T configuration had reached 14.3%, confirming the potential for optimisation through the engineering of interconnection layers and transparent electrodes [415], [416]. Progress was rapid; in 2017, a certified efficiency of 23.5% was achieved, followed by 29.5% in 2020, surpassing the SQ limit of single-junction silicon cells [417]. In 2025, devices exceeding 34% certified efficiency were produced, placing perovskite/silicon tandems at the forefront of advanced photovoltaic technologies [418].

## 2.8.2 Architectures and monolithic integration

Tandem cells can be integrated using two main architectures, monolithic 2T or 4T, to which must be added the crucial importance of transparent intermediate layers (Interconnecting Layers, ICL) in the case of monolithic devices. Each of these approaches has specific advantages and constraints, both in terms of optoelectronics and technology.

### 2.8.2.1 Two-Terminal Architecture (2T)

Series architecture, also known as a two-terminal (2T) configuration, is currently the most studied and promising for perovskite/silicon tandems. In this configuration, the two subcells – perovskite in the top layer and silicon in the bottom layer – are electrically connected in series via an intermediate junction, as illustrated in Figure 2.20(a). This configuration results in a device with only two external contacts, which greatly simplifies the integration and compactness of the module [419]. The operating principle is based on sharing an identical current between the two subcells, while the voltages are added together to provide the final voltage of the tandem. This constraint imposes a limiting current set by the least efficient subcell. Optimising the 2T design therefore requires precise adjustment of the absorption spectra; the perovskite cell must be formulated with a suitable energy gap (often between 1.68 and 1.75 eV) in order to generate a current compatible with that of the silicon cell ($\sim$20 mA/cm$^2$) [420]. Despite this difficulty, the 2T architecture remains the most attractive because it promotes lower manufacturing costs, better industrial integration and record performance already exceeding 32%. However, the success of this configuration depends heavily on the quality of the transparent intermediate layers and the fine control of optical and electrical losses.

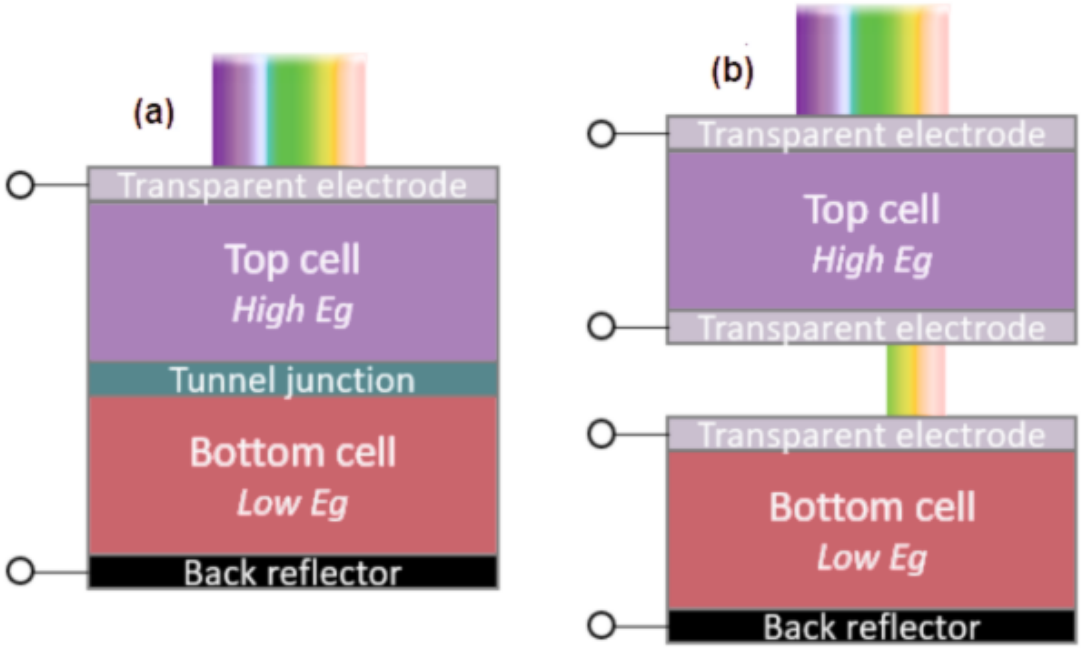



Figure 2.20: Comparative diagrams of tandem solar cell architectures: (a) monolithic 2T architecture with tunnel junction, (b) 4T architecture with electrically independent subcells.

#### 2.8.2.2 Interconnecting Layers (ICL)

Transparent intermediate layers (ICLs) play a central role in monolithic integration, as they simultaneously ensure efficient recombination of carriers between the top cell and the bottom cell, and transmission of incident light to the bottom cell. To fulfil these functions, they must have high optical transparency to minimise losses due to absorption or reflection, sufficient conductivity with precise energy alignment to avoid the creation of transport barriers, and thermal and chemical compatibility with subsequent deposition steps, in particular the crystallisation of perovskite, which remains sensitive to temperatures above 150 °C [421]. The most commonly used materials include ITO, $SnO_2$, ZnO, and ultra-thin $p^+/n^+$ doped tunnel layers that facilitate charge recombination. More recently, hybrid strategies combining metal oxides and ultra-thin organic or metal recombiners have been proposed, limiting non-radiative recombination and improving interface selectivity [409], [422], [423]. Thanks to these advances, interfacial losses have been reduced to less than 5%, and the certified efficiencies of monolithic tandems exceeded 32% in 2025, confirming that optimising ICLs is an essential lever for achieving both maximum efficiency and long-term operational stability [424].

#### 2.8.2.3 Four-Terminal Architecture (4T)

Parallel architecture, or four-terminal (4T) architecture, takes a different approach, in which each subcell operates independently. In this case, the top cell (perovskite) and bottom cell (silicon) each have their own electrical contacts. The two are coupled externally via interconnection electronics [425], rather than through an internal junction as shown in Figure 2.20(b). One of the major advantages of this configuration is its tolerance

to spectroscopic disequilibrium; as each sub-cell operates autonomously, there is no requirement for identical current between them [426]. This allows the full potential of each absorber to be exploited, particularly in non-standard illumination conditions (angular or spectral variations of the sun). In addition, there is greater flexibility in the choice of energy gaps than in the case of 2T [427]. On the other hand, the main disadvantage lies in the technological complexity: high-performance transparent layers must be integrated so that light passes efficiently from the top to the bottom cell, while avoiding losses due to reflection and absorption. External electronic interconnection also requires the addition of specific circuits or modules to combine the voltages and currents of the two sub-cells. Depending on the approach chosen (series connection, parallel connection or power electronics management), this step can lead to additional conversion losses and complicate the module design. This increases the cost and difficulty of integration on an industrial scale, although the flexibility of electrical control remains an advantage for optimisation in real-world conditions [407], [427]–[429].

### 2.8.3 Possible combinations

Research into perovskite-based tandem cells has grown considerably over the last decade, offering unusual flexibility in the choice and combination of materials. The aim is to combine perovskite with other semiconductors in order to take advantage of their complementary optoelectronic properties, improve solar spectrum capture and optimise overall performance. Depending on the strategies adopted, several architectural configurations have emerged, each with its own technological advantages and constraints. Three main families stand out in particular: all-perovskite tandems, perovskite/CIGS tandems, and finally perovskite/silicon tandems, which are currently considered the most promising and advanced route to commercialisation due to the exceptional spectral complementarity and well-established industrial infrastructure of crystalline silicon [236], [419], [430].

#### 2.8.3.1 All-perovskite tandems

Structures based entirely on perovskites (Perovskite/Perovskite Tandem Solar Cells, PPTSC) represent a particularly promising avenue for overcoming the limitations of single-junction cells. They are based on the combination of a top subcell with a wide bandgap (∼1.7–1.8 eV) and a bottom subcell with a reduced bandgap (∼1.1–1.2 eV), often obtained by partially or totally replacing lead with tin (Sn) [431], [432]. This configuration allows for near-ideal spectral optimisation, predicted by detailed equilibrium theory, which indicates a theoretical conversion efficiency that can exceed 45% with optimal gaps (∼1.1 eV and ∼1.73 eV). In practice, progress has been remarkable; in 2025, certified efficiencies of around 28% have already been achieved thanks to low-temperature manufacturing processes that are compatible with solution processing and suitable for flexible substrates [433]–[435]. This approach gives all-perovskite tandems major advantages in terms of lightness, flexibility and low potential cost, paving the way for a variety of applications (building integration, portable electronics, bifacial or semi-transparent devices).

In technological terms, several key advances explain these performances. On the one hand, the flexibility of bandgap adjustment through halogen composition (I/Br) or the incorporation of Pb/Sn alloys facilitates the design of complementary subcells. On the other hand, interface engineering (surface passivation, improved transport layers, thin

tunnel junctions such as NiO/AZO or $SnO_2$ modified by quantum dots) has significantly reduced non-radiative losses and improved charge transport. Strategies such as passivation of surface defects with organic ammoniums (PEAI, BA, CF -PA) or optimisation of selective layers have increased the diffusion length of carriers (>5 µm), favouring thicker absorbing layers and better photon capture [436]. These aspects are illustrated in Figure 2.21, which summarises both the typical 2T architecture, the theoretical efficiency potential and the energy alignment of the functional layers. However, several obstacles remain. The chemical instability of $Sn^{2+}$ (easily oxidised to $Sn^{4+}$), photo-induced halogen degradation, and ion migration remain major obstacles to long-term operational stability. In addition, the limitation of $V_{OC}$ due to the high density of trap states and energy alignment problems at interfaces remains a challenge to be overcome [437]. Finally, new approaches, such as bifacial architectures and semi-transparent tandem cells, are attracting increasing attention because they allow reflected or transmitted light to be exploited, thereby increasing overall energy efficiency [438], [439]. These developments confirm the potential of all-perovskite tandems as one of the most competitive solutions for the next generation of photovoltaics.

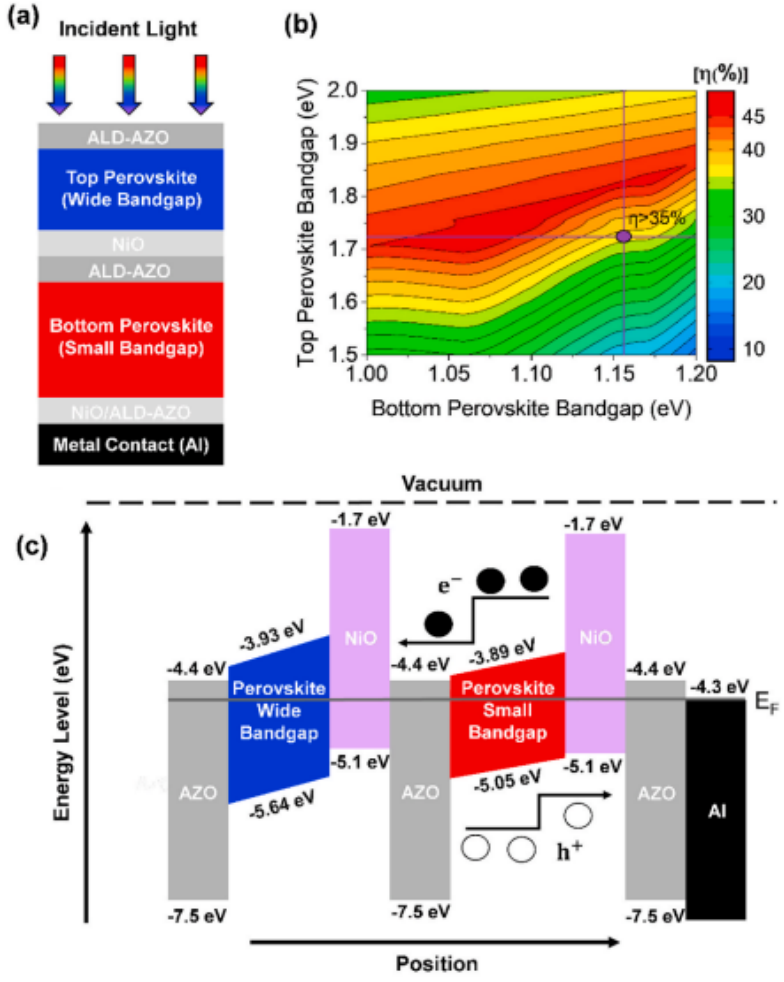



Figure 2.21: (a) Schematic of a 2T all-perovskite tandem solar cell with wide and narrow bandgap sub-cells. (b) Theoretical efficiency map as a function of top and bottom bandgaps. (c) Typical energy-level alignment enabling efficient charge extraction [436].

### 2.8.3.2 Perovskite / CIGS

Perovskite/CIGS tandems represent a promising alternative to perovskite/silicon structures, with specific advantages linked to the properties of thin films. Thanks to its adjustable bandgap (1.0–1.2 eV) and compatibility with flexible substrates, CIGS enables the production of lightweight, durable devices that are suitable for embedded or space applications [440], [441]. These tandems also have a reduced carbon footprint per kWh produced, making them an attractive technology from a sustainable development perspective. Their resistance to radiation opens up particular prospects for photovoltaic energy in extreme environments, such as space.

The characteristics of Perovskite/CIGS cells are illustrated in Figure 2.22, which shows a typical diagram of a perovskite/CIGS tandem and the characteristic energy levels of the subcells, highlighting the band alignment required for efficient carrier extraction. The first monolithic demonstrators date back to 2015, with the integration of a perovskite subcell with an adjusted bandgap (∼1.7 eV) on a CIGS cell [442]. Since then, considerable progress has been made; in 2022, a certified efficiency of 24.2% was achieved for an optimised monolithic structure comprising Cs/FA/MA perovskite combined with LiF, $SnO_2$ and IZO buffer layers [443], while semi-transparent 4T structures demonstrated efficiencies in excess of 26% [444]. Recent approaches combine bandgap engineering, molecular additives (PEAI, RbF), and transport layer optimisation ($SnO_2$, NiO, doped ZnO) to reduce interfacial losses and improve energy alignment [440], [445].

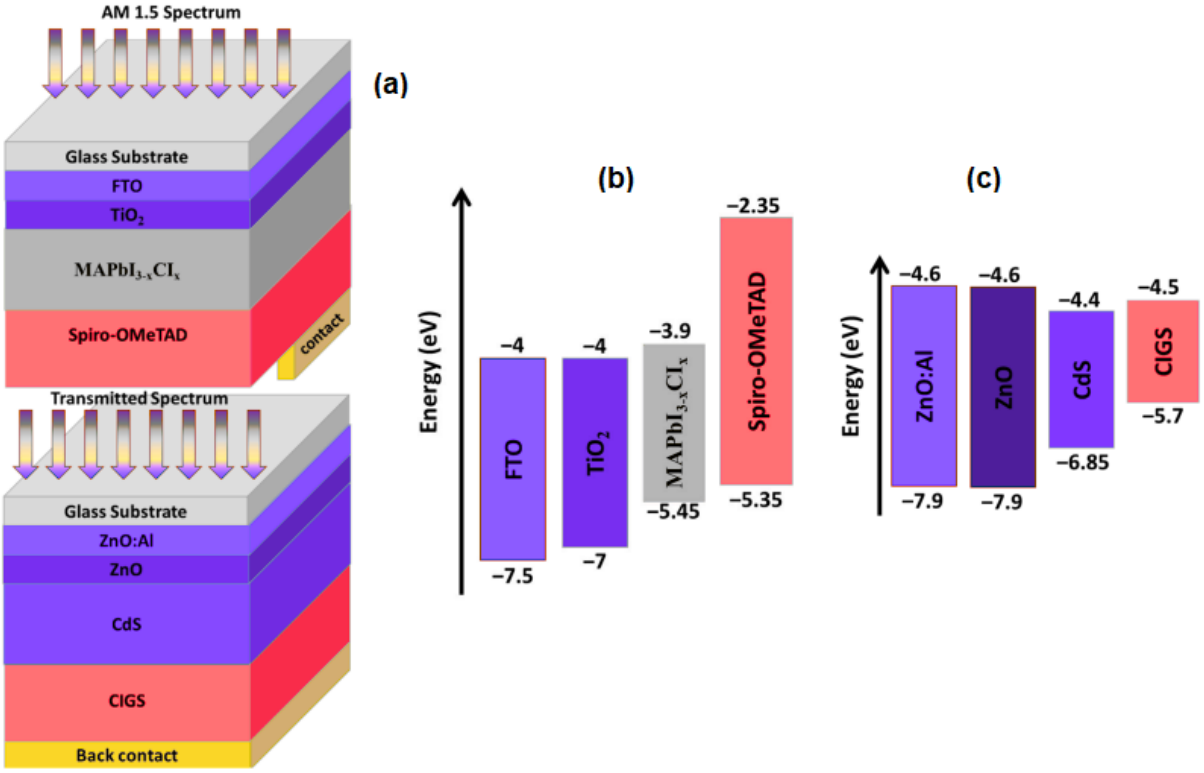



Figure 2.22: (a) Schematic diagram of a perovskite/CIGS tandem, illustrating the device configuration and energy levels of (b) the top subcell and (c) the bottom subcell.

Integration on flexible substrates using low-temperature processes (spin-coating, sputtering, roll-to-roll) is a major advantage for industrial scale-up. Prototype modules measuring a few $cm^2$, achieving efficiencies of 17–19%, have already been produced, although the decrease in efficiency with increasing surface area remains a major challenge [446]–[448]. Furthermore, the management of transparent electrodes (ITO, IZO) and buffer layers ($MoO_x$, CdS) remains crucial in order to limit parasitic absorption and damage related to deposition processes. Moreover, perovskite/CIGS tandems, due to their unique combination of high potential efficiency (∼30% theoretical), flexibility and durability, are positioned as a particularly interesting option for portable terrestrial and space applications. However, their industrialisation will require overcoming issues related to module scalability, long-term stability and interface optimisation [449], [450].

#### 2.8.3.3 Perovskite / Silicon

PSTSCs currently represent the most advanced and credible approach for large-scale industrialisation of photovoltaics. This architecture combines the technological maturity of crystalline silicon, the dominant material on the market for more than three decades, with the remarkable properties of hybrid perovskites, whose adjustable bandgap optimises light absorption [451], [452]. The spectral complementarity is particularly advantageous, the silicon subcell efficiently captures near-infrared light, while the perovskite exploits the visible part of the solar spectrum [409]. Various types of silicon have been explored as the bottom subcell, from conventional crystalline silicon to more advanced architectures such as heterojunction cells (SHJ), passivated TOPCon contacts and interdigitated structures (IBC). Among these, the SHJ configuration is now the most widely used in perovskite/Si tandems, due to its effective passivation and compatibility with low-temperature perovskite deposition processes [453]–[455]. These different architectural approaches are shown in Figure 2.23, which illustrates the general operating principle of PSTSCs and several variants of monolithic tandems incorporating either nanocrystalline Si layer recombination, temperature-limited SHJs, or n-type homojunctions allowing high-temperature processing.

Since the first demonstration by Bailie et al. in 2014 (17.9% in a 4T configuration), spectacular progress has been made [456]. 2T architectures, which are more suited to industrial production, quickly exceeded the thresholds of 25% and then 30% certified efficiency. In 2020, Oxford PV announced commercial modules achieving 29.5%, while records published between 2023 and 2025 are close to 34% [457]. These performances are the result of multiple innovations, including the engineering of perovskite composition (multi-cation and multi-anion alloys to improve stability and finely adjust the bandgap), the optimisation of interconnection layers ($SnO_2$, ITO, doped ZnO, buffer oxides) to reduce resistive and optical losses, and the development of low-temperature deposition processes compatible with silicon substrates [458], [459].

Nevertheless, several challenges remain. Operational stability remains the main obstacle, as cells must maintain more than 80% of their initial performance after 1,000 hours of continuous illumination in order to meet IEC standards [460]. The deposition of perovskite layers on silicon must also be carried out at moderate temperatures to avoid any degradation of the underlying layers, which requires the use of techniques such as spin-coating, slot-die coating or vacuum-assisted evaporation [461], [462]. Furthermore,

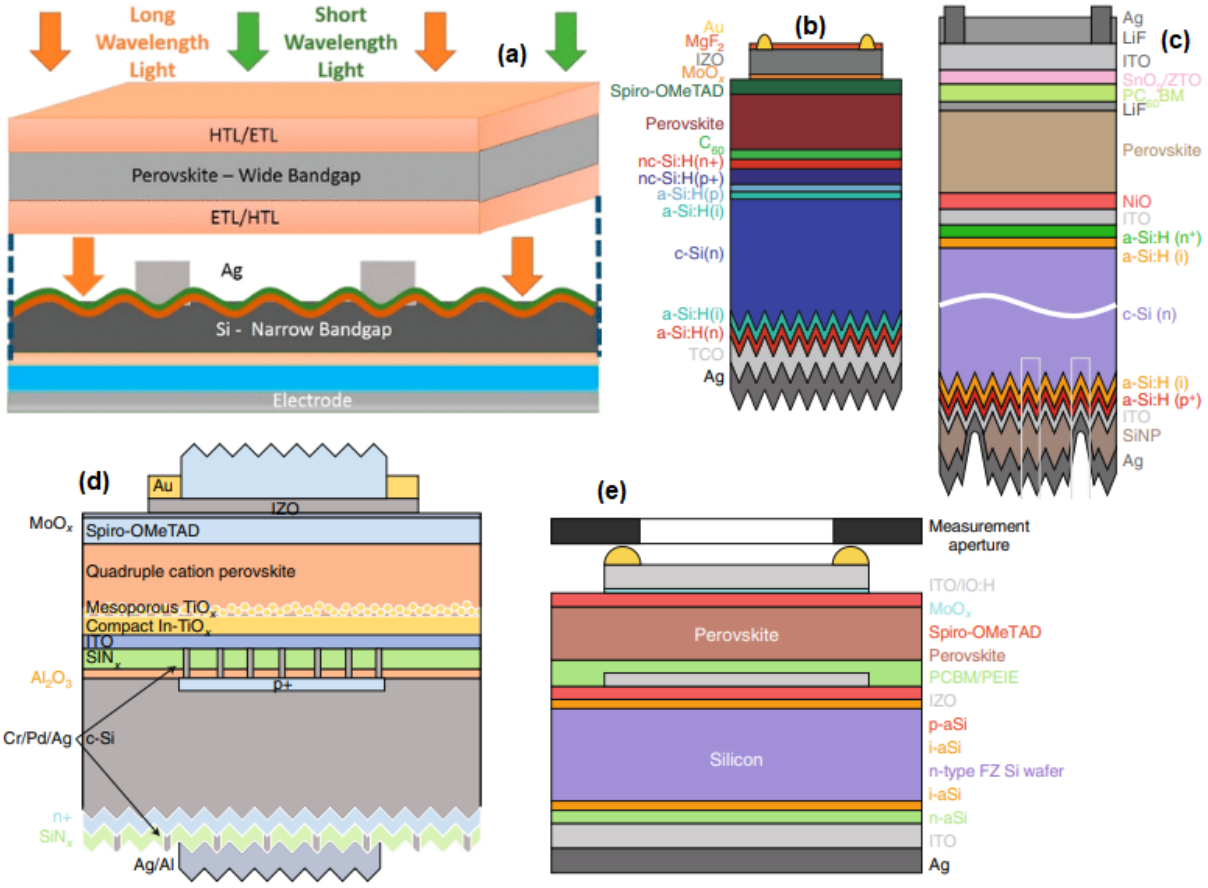



Figure 2.23: Representative schematics of main monolithic perovskite/silicon tandem solar cell architectures [412], [451]: (a) working principle, (b) structure with nc-Si recombination layer, (c) SHJ cell in p–i–n configuration with $SnO_2$ buffer, (d) n-type homo-junction Si cell with metal/ITO recombination, (e) SHJ cell in n–i–p configuration with MoOx buffer.

optimising transparent electrodes (ITO, $In_2O_3$:H, ultra-thin metal films) is crucial to limit parasitic absorption and improve charge carrier extraction [463].

In order to overcome these obstacles, several strategies are being explored: the use of more stable inorganic transport layers (NiO, $SnO_2$, doped PCBM), the introduction of textured surfaces for better light trapping, and the implementation of advanced encapsulation processes providing protection against humidity, UV rays and thermal cycles [464], [465]. At the same time, module-scale demonstrations (>1 m²) are already showing efficiencies of over 25%, paving the way for rapid integration into existing production lines [466].

Compared to other emerging tandems, such as perovskite/CIGS or perovskite/III–V, the PSTSCs have the decisive advantage of exploiting an already massively deployed industrial infrastructure, thus reducing the cost and time of transition to large-scale production [407], [467]. The evolution in the performance of 2T PSTSCs devices is summarised in Table 2.3, which lists the main achievements reported in the literature and highlights the rapid progress in efficiency, now exceeding 30%.

Table 2.3: Summary of reported performance for two-terminal perovskite/silicon tandem cells [409].

| Year | Structure | Absorber | Si type | $E_g$ (eV) | $V_{OC}$ (V) | $J_{SC}$ (mA/cm$^2$) | PCE (%) |
|---|---|---|---|---|---|---|---|
| 2016 | n-i-p | $FA_xMA_{1-x}Pb_yI_{3-y}Br$ | SHJ | - | 1.78 | 14.0 | 18.0 |
| 2016 | n-i-p | $MAPbI_3$ | SHJ | 1.6 | 1.703 | 15.8 | 21.4 |
| 2017 | p-i-n | $Cs_{0.17}FA_{0.83}Pb(Br_{0.17}I_{0.83})_3$ | SHJ | 1.63 | 1.65 | 18.1 | 23.6 |
| 2018 | n-i-p | $MAPbI_3$ | TOPCon | 1.6 | 1.68 | 16.2 | 21.0 |
| 2018 | n-i-p | $Cs_{0.05}Rb_{0.05}FA_{0.765}MA_{0.135}PbI_{2.55}Br_{0.45}$ | SHJ | 1.63 | 1.763 | 17.8 | 24.5 |
| 2018 | p-i-n | $Cs_xFA_{1-x}Pb(Br_{1-y}I_y)_3$ | SHJ | 1.6 | 1.78 | 19.5 | 25.2 |
| 2019 | p-i-n | $(FAPbI_3)_{0.8}(MAPbBr_3)_{0.2}$ | BSF | 1.64 | 1.645 | 16.13 | 21.19 |
| 2020 | p-i-n | $Cs_{0.1}MA_{0.9}Pb(I_{0.9}Br_{0.1})_3$ | SHJ | - | 1.82 | 19.2 | 26.0 |
| 2020 | p-i-n | $Cs_{0.05}(FA_{0.77}MA_{0.23})_{0.95}Pb(I_{0.77}Br_{0.23})_3$ | SHJ | 1.68 | 1.92 | 19.26 | 29.15 |
| 2020 | p-i-n | Perovskite | SHJ | 1.67 | 1.886 | 19.12 | 27.04 |
| 2020 | p-i-n | $Cs_{0.05}MA_{0.15}FA_{0.8}PbBr_{0.75}I_{2.25}$ | SHJ | 1.68 | 1.70 | 19.8 | 25.7 |
| 2021 | p-i-n | $Cs_{0.05}(MA_{0.23}FA_{0.77})_{0.95}Pb(Br_{0.23}I_{0.77})_3$ | SHJ | 1.68 | 1.89 | 19.13 | 28.2 |
| 2021 | p-i-n | $Cs_{0.1}FA_{0.9}PbBr_{0.13}I_{2.8}$ | SHJ | - | 1.808 | 19.79 | 27.48 |
| 2022 | p-i-n | $Cs_{0.22}FA_{0.78}Pb(Br_{0.15}I_{0.85})_3$ | TOPCon | 1.68 | 1.794 | 19.68 | 27.6 |
| 2022 | p-i-n | $Cs_{0.05}(FA_{0.79}MA_{0.21})_{0.95}Pb(I_{0.79}Br_{0.21})_3$ | SHJ | 1.66 | 1.90 | 19.45 | 29.83 |
| 2022 | p-i-n | $Cs_{0.1}FA_{0.1}MA_{0.7}Pb(Br_{0.15}I_{0.85})_3$ | SHJ | 1.65 | 1.92 | 18.95 | 28.6 |
| 2022 | n-i-p | $CsPb(I_xBr_{1-x})_3$ | SHJ | 1.8 | 2.04 | 14.34 | 22.95 |
| 2022 | p-i-n | $Cs_{0.05}FA_{0.8}MA_{0.15}Pb(Br_{0.255}I_{0.755})_3$ | SHJ | 1.69 | 1.92 | 19.8 | 29.3 |
| 2022 | n-i-p | $Cs_{0.05}FA_{0.8}MA_{0.15}PbI_{2.55}Br_{0.45}$ | TOPCon | 1.62 | 1.783 | 14.4 | 17.3 |
| 2022 | p-i-n | $Cs_{0.22}FA_{0.78}Pb(Cl_{0.03}Br_{0.15}I_{0.85})_3$ | TOPCon | 1.68 | 1.79 | 19.68 | 27.63 |
| 2022 | p-i-n | $FA_{0.78}Cs_{0.22}Pb(I_{0.85}Br_{0.15})_3$ | PERC | 1.68 | 1.91 | 19.29 | 28.81 |
| 2022 | p-i-n | $Cs_{0.05}(FA_{0.83}MA_{0.17})_{0.95}Pb(Br_{0.17}I_{0.83})_3$ | TOPCon | 1.63 | 1.80 | 19.2 | 28.2 |
| 2023 | p-i-n | $CsPbBr_{0.15}I_{2.85}$ | SHJ | 1.71 | 1.84 | 17.95 | 25.31 |
| 2023 | p-i-n | $Cs_{0.22}FA_{0.78}Pb(I_{0.85}Br_{0.15})_3$ + 5% $MAPbI_3$ | SHJ | 1.68 | 2.00 | 20.24 | 32.5 |
| 2023 | p-i-n | Perovskite | SHJ | - | 1.82 | 20.4 | 28.4 |
| 2023 | n-i-p | $(FAPbI_3)_{0.83}(MAPbBr_3)_{0.17}$ | SHJ | - | 1.82 | 18.1 | 27.2 |
| 2023 | p-i-n | $Cs_{0.05}(FA_{0.83}MA_{0.17})_{0.95}Pb(I_{0.83}Br_{0.17})_3$ | TOPCon | - | 1.83 | 19.7 | 29.2 |
| 2023 | p-i-n | $Cs_xFA_{1-x}PbI_{3-y}Br_y$ | SHJ | - | 1.68 | 19.47 | 23.22 |
| 2023 | p-i-n | $Cs_{0.05}MA_{0.14}FA_{0.81}Pb(I_{0.8}Br_{0.2})_3$ | SHJ | 1.68 | 1.85 | 19.7 | 28.4 |
| 2024 | p-i-n | $Cs_{0.05}FA_{0.8}MA_{0.15}Pb(I_{0.75}Br_{0.25})_3$ | SHJ | 1.67 | 1.941 | 20.1 | 29.6 |
| 2024 | p-i-n | Perovskite | SHJ | 1.69 | 1.98 | 20.86 | 33.89 |
| 2024 | p-i-n | $Cs_{0.05}FA_{0.95-x}MA_xPb(I_{1-y}Br_y)_3$ | SHJ | 1.67 | 1.869 | 20.32 | 30.52 |
| 2024 | n-i-p | $Cs_{0.05}FA_{0.8}MA_{0.15}Pb(I_{0.75}Br_{0.25})_3$ | TOPCon | - | 1.90 | 18.82 | 28.2 |
| 2024 | p-i-n | $Cs_{0.05}(FA_{0.9}MA_{0.1})_{0.95}Pb(I_{0.8}Br_{0.2})_3$ | SHJ | - | 1.954 | 18.92 | 30.22 |
| 2025 | p-i-n | Perovskite | TOPCon | 1.68 | 1.931 | 19.89 | 31.32 |
| 2025 | p-i-n | $Cs_{0.17}FA_{0.83}Pb(I_{0.83}Br_{0.17})_3$ | TOPCon | 1.68 | 1.977 | 19.41 | 30.36 |
| 2025 | p-i-n | $Cs_{0.05}(FA_{0.77}MA_{0.23})_{0.95}Pb(I_{0.77}Br_{0.23})_3$ | SHJ | 1.68 | 1.92 | 20.3 | 31.5 |
| 2025 | p-i-n | Perovskite | SHJ | 1.68 | 1.912 | 19.92 | 32.19 |

## 2.9 Conclusion

This chapter has provided a detailed overview of PSCs, discussing their constituent materials, manufacturing methods, architectures and operating principles, as well as their current performance and main limitations. We have highlighted the remarkable proper-

ties of these materials, which explain the spectacular progress made in terms of efficiency, but also the technological barriers that still hinder their industrialisation, such as stability, interfacial degradation and control of coupling in tandem structures. These findings highlight that, despite rapid experimental advances, a thorough understanding of the underlying physical mechanisms remains essential to effectively guide the development of new generations of devices. It is with this in mind that the following chapter is devoted to the analytical modelling of a perovskite-based solar cell.

The next chapter aims to develop a rigorous theoretical framework for describing the operation of these cells using fundamental equations (continuity, charge transport, boundary conditions). Through controlled assumptions and analytical resolution of the transport equations, we will seek to extract key parameters such as current density, open-circuit voltage, form factor and conversion efficiency. The results obtained will be compared with experimental data and data from the literature in order to validate the model and discuss its relevance and limitations.

CHAPTER

3

# ANALYTICAL MODELLING OF PEROVSKITE AND TANDEM SOLAR CELLS

## 3.1 Introduction

Analytical modelling and simulation are essential tools for understanding and optimizing the performance of next-generation solar cells. Numerical approaches, such as those implemented with Silvaco TCAD, or with other simulation platforms such as Sentaurus TCAD (Synopsys), COMSOL, or SCAPS-1D, provide an accurate description of device behavior and allow for the integration of a large number of physical and technological parameters. However, their implementation remains computationally expensive and highly dependent on specific experimental data, which can sometimes be difficult to obtain. In addition, analytical modelling offers a simpler and faster approach based on physically relevant assumptions. It provides explicit expressions that directly link physical parameters to performance metrics ($J_{sc}$, $V_{oc}$, FF, PCE), thereby facilitating the analysis of internal mechanisms and parametric studies. These models offer several advantages, speed of execution, ease of implementation, better interpretation of generation, transport, and recombination phenomena, and great utility for sensitivity analyses. They are therefore a suitable tool for the early stages of photovoltaic device design and optimization. Furthermore, this approach does not replace numerical simulations, but complements them by providing a framework for understanding and a tool for guiding device design.

The objective of this chapter is double. First, we develop a rigorous analytical model for a simple n-i-p type perovskite solar cell based on the FTO/$TiO_2$/$MAPbI_3$/Spiro-OMeTAD architecture, based on an experimentally validated design. Secondly, we will extend this approach to perovskite/silicon tandem solar cells, highlighting the particularities associated with multi-junction structures, in particular current limitation and voltage addition. This progression from single cells to tandem cells will demonstrate the potential of analytical models to predict and compare the performance of different architectures, while providing additional insight into numerical simulations.

## 3.2 Analytical modelling of a perovskite solar cell (n-i-p)

Analytical modelling of PSCs is an essential source of information for understanding the internal structure and physical mechanisms that determine their performance [468], [469]. In particular, it allows the evaluation of crucial parameters such as carrier mobility, recombination rate and nature, built-in voltage, and optimization conditions that directly influence device efficiency and stability [470], [471]. One of the major advantages of this approach is its ability to translate complex physical phenomena into analytical equations, providing a faster and more intuitive understanding of PSC behavior [472]. It also allows the effect of various conditions (light intensity, temperature, absorber thickness, etc.) to be explored, paving the way for the design and optimization of new architectures.

The modelling of solar cells is based mainly on two complementary approaches. The first is electrical modelling, which uses equivalent circuits (such as the one- or two-diode model) to describe the current-voltage characteristic quickly and easily. This approach has the advantage of being very easy to use and directly adjustable to experimental data, but it remains limited in terms of the internal physical description of the device. The

second approach, which is more rigorous from a fundamental standpoint, involves using electron and hole continuity equations. This method makes it possible to explicitly link the mechanisms of carrier generation, transport and recombination to the overall performance of the cell. Although it is more complex to implement, it offers better predictive power and a deeper understanding of the physical phenomena involved in the operation of solar cells.

In the literature, several analytical models have been developed using different methodologies. For example, Zahraa S. Ismail *et al.* established an analytical model based on I–V and C–V measurements, describing the dynamic response of PSCs and validated by comparison with experimental data [468]. For his part, M. Zahangir Kabir proposed a model integrating voltage-dependent transport, photonic absorption, and recombination [473]. In another paper, the same author developed a model based on solving the continuity equations for electrons and holes, including drift, diffusion, generation, and recombination (bulk and interfaces) [474]. This model yields analytical expressions for the photocurrent under illumination, to which the contribution of the dark current is added to obtain the total current density.

### 3.2.1 Device modelling

The perovskite solar cell (PSC) studied in this work has the following structure: FTO/$TiO_2$ /Perovskite ($MAPbI_3$)/HTM (Spiro-OMeTAD). This architecture, illustrated in Figure 3.1, was designed to maximize light absorption, promote charge generation, and ensure efficient carrier transport. Each layer plays a specific role: FTO acts as a transparent conductive contact, the $TiO_2$ layer acts as an electron extractor and transporter, $MAPbI_3$ perovskite is the main absorber, while the Spiro-OMeTAD HTM layer ensures the selective transfer of holes to the electrode. As this structure has already been experimentally realised, in this work we assign it a rigorous analytical model that allows us to describe and predict its performance [475].

### 3.2.2 Development of the analytical model

As part of this study, we seek to establish an analytical model describing the operation of the perovskite solar cell studied, whose structure is composed of FTO/$TiO_2$/$MAPbI_3$/HTM. To do this, we have adopted an approach based on solving the steady-state continuity equations for electrons and holes in the absorbing layer ($MAPbI_3$). In a solar cell, photogenerated charge carriers (electrons and holes) move under the combined effect of the internal electric field and diffusion linked to the concentration gradient. Their dynamics are governed by two fundamental equations:

- The continuity equation, which reflects charge conservation and establishes a balance between the phenomena of generation, recombination, and transport.
- The rift-diffusion equation, which describes the current associated with each type of carrier (electron or hole) as a function of mobility, electric field, and concentration gradients.

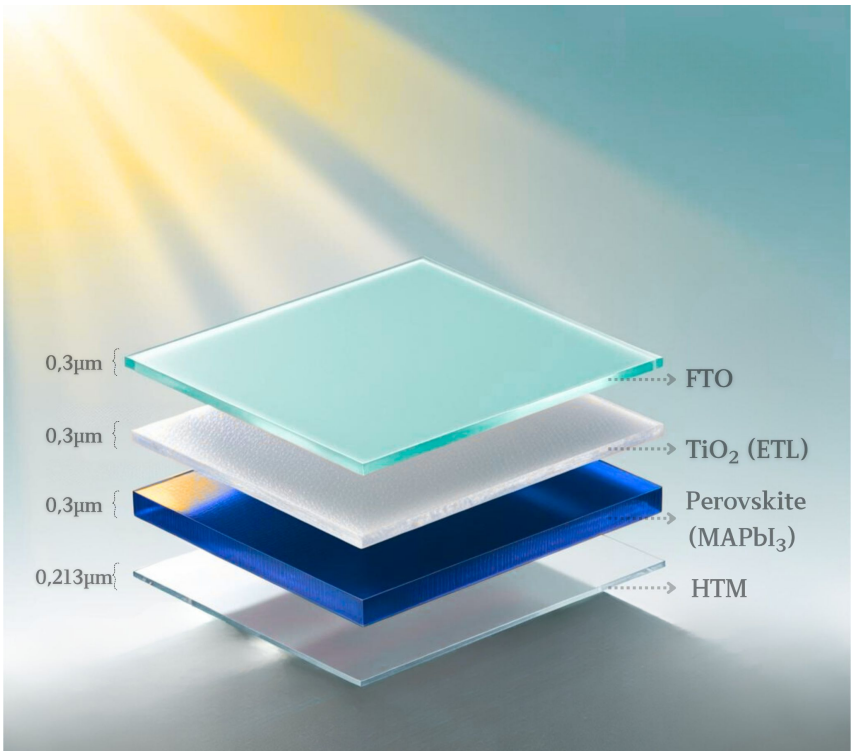



Figure 3.1: Device structure of a $MAPbI_3$-based PSC.

Thus, for electrons with concentration $n$ and holes with concentration $p$, the continuity equations in the steady state are written in the following general form [476], [477]:

$$\frac{\partial n}{\partial t} = \frac{1}{q}\nabla J_n + G - R \tag{3.1}$$

$$\frac{\partial p}{\partial t} = -\frac{1}{q}\nabla J_p + G - R \tag{3.2}$$

Where:

- $n$ and $p$ represent the concentration of electrons and holes, respectively.
- $J_n$ and $J_p$ are the current densities of electron and hole carriers, respectively.
- $G$ refers to the rate of electron-hole pair generation following the absorption of photons in the absorber.
- $R$ translates the recombination rate of carriers in the material

The general form of the drift-diffusion equations for electrons and holes is as follows [476], [477]:

$$J_n = q\mu_n nE + qD_n\frac{\partial n}{\partial x} \tag{3.3}$$

$$J_p = q\mu_p pE - qD_p\frac{\partial p}{\partial x} \tag{3.4}$$

where:

- $\mu_n, \mu_p$ are the electron and hole mobility carriers,
- $D_n, D_p$ are the diffusion coefficients of electrons and holes,
- $q$ is the elementary charge,
- $E$ is the electric field.

In steady state, carrier densities do not vary with time [472], which implies:

$$\frac{\partial n}{\partial t} = \frac{\partial p}{\partial t} = 0 \tag{3.5}$$

Substituting these expressions (3.3) and (3.4) into the continuity equations (3.1) and (3.2) yields a differential system describing the spatial distribution of electrons and holes within the absorbing layer. The equations obtained are of the form:

$$D_n \frac{\partial^2 n(x)}{\partial x^2} + \mu_n E(x) \frac{\partial n(x)}{\partial x} + G(x) - R(x) = 0 \tag{3.6}$$

$$D_p \frac{\partial^2 p(x)}{\partial x^2} - \mu_p E(x) \frac{\partial p(x)}{\partial x} + G(x) - R(x) = 0 \tag{3.7}$$

These two differential equations (3.6) and (3.7) form the basis of the analytical model developed in this work. They enable the physical parameters of the material (mobility, diffusion, electric field, recombination rate) to be linked to the overall performance of the cell (current density, open-circuit voltage, efficiency). In order to find solutions for these differential equations, we have to substitute the expressions for $R(x)$, $E(x)$, and $G(x)$ by their corresponding physical models or approximations.

1. **Recombination R(x)**

We assume that the recombination is negligible, $R(x) = 0$, because the charge carriers are able to migrate over long distances in the perovskite layer without recombining, due to their long diffusion length. In addition, the transport layers quickly collect the carriers before they have time to recombine [478]–[480]. This assumption is based on a solid set of results concerning lead-based halide perovskite materials, in particular $MAPbI_3$ [481]. M. Herz showed that these materials exhibit both high charge carrier mobility (up to 70 $cm^2/V \cdot s$) [482]–[484], and very low recombination rates, particularly in carrier density regimes typical of solar operating conditions [485]. In this regime, recombination is dominated by monomolecular processes via trap states, characterised by very low recombination constants [481].

Several experimental studies have highlighted the long diffusion lengths characteristic of hybrid perovskites, reflecting a low carrier recombination frequency. Thus, in $CH_3NH_3PbI_3$ obtained by solution processing, the diffusion length exceeds 100 nm [478], [484], [486], reaches approximately 1.7 µm for a 390 nm layer [487], and can even exceed 175 µm under sunlight in optimised devices [480]. These distances, which are significantly greater than the usual thickness of the active layer ( 0.3 µm), allow for efficient

collection of carriers before they undergo recombination. In addition, the particularly high absorption coefficient of these materials [488] results in a carrier generation rate that is significantly higher than the recombination rate [489]. This corresponds to negligible recombination in perovskites [490], [491].

Furthermore, defects in $MAPbI_3$ are mainly associated with shallow traps, greatly limiting non-radiative losses (depth $< 50$ meV). Yin et al. [492] and Kim et al. [493] show that the majority of defects in $MAPbI_3$ are associated with shallow traps, which are unlikely to be significant non-radiative recombination. As noted by Wehrenfennig et al. [484], hybrid lead halide perovskites combine two key properties for photovoltaics: excellent mobility and very low recombination. Although interfacial or volume recombination phenomena may occur as reported by Stranks et al. [478] and recently by Kabir [474], this recombination becomes significant mainly in the presence of defects or under suboptimal manufacturing conditions. In well-passivated or well-controlled devices, the trap density remains low enough that recombination remains dynamically slow compared to carrier extraction. Thus, as a first approximation, it is reasonable and common in simplified analytical modelling to neglect recombination in order to evaluate the intrinsic performance of the device. This assumption allows us to focus on the mechanisms of generation and transport.

2. **Electric field E(x)**

The electric field $E(x)$ in a PSC is expressed using the Poisson equation and the specific characteristics of the cell material and structure. In the case of an intrinsic perovskite layer, the electric field can be expressed in a simple way, assuming an undoped material model. The Poisson equation is given by [494]:

$$\frac{\partial^2 \phi}{\partial x^2} = -\frac{\rho}{\varepsilon} \tag{3.8}$$

For an intrinsic perovskite material, we suppose that $\rho = 0$, which simplifies Poisson's equation to:

$$\frac{\partial^2 \phi}{\partial x^2} = 0$$

This assumption reflects an undoped material, which is consistent with the intrinsic nature of $MAPbI_3$. However, it is well established that real devices often exhibit unintentional doping and ion migration, which can induce a non-zero spatial distribution of charges in the perovskite, thereby affecting the electric field profile. The strong ionic character of perovskite crystals makes their controlled doping particularly difficult, but recent studies have shown that unintentional doping, often of the n-type, can reach significant levels, modifying the conductivity and charge distribution [495].

For example, doping with metastable ions has increased the conductivity of $MAPbI_3$ by several orders of magnitude, confirming the presence of residual carriers in the layer. Furthermore, ion migration, particularly of halides and mobile cations, is a well-documented phenomenon in halide perovskites. Under illumination or electrical polarisation, these ions can move and accumulate at interfaces or in the volume, creating space charge regions that locally modify the volume charge density $\rho(x, t)$ and thus the internal electric field [496], [497]. These effects are particularly important under prolonged operating conditions or during thermal stress.

Nevertheless, in high-quality, well-passivated and optimised devices, defect density and ion mobility are minimised, making the approximation $\rho = 0$ reasonable for describing the average behavior of the electric field and the transport mechanisms of photogenerated carriers [496]. This assumption thus allows the intrinsic performance of the cells to be modelled effectively, while recognising that deviations may occur under less ideal experimental conditions. Consequently, the intrinsic layer assumption ($\rho = 0$) is a valid approximation for optimised devices and serves as a basis for understanding the fundamental mechanisms. By integrating Poisson's equation twice, we obtain the expression for the potential:

$$\phi = Ax + B$$

The constants $A$ and $B$ are determined from the boundary conditions, since the voltage falls mainly across the absorbing layer, so:

$$\phi(x = 0) = 0 \quad \text{and} \quad \phi(x = t_p) = V_{bi} - V$$

Where $t_p$ is the thickness of the perovskite layer and $V_{bi}$ is the built-in voltage of the device across the absorber layer as shown in Figure 3.2, and $V$ is the applied voltage. This allows us to determine that:

$$A = \frac{V_{bi} - V}{t_p}$$

The electric field is defined as the derivative of the potential relative to $x$ by this expression:

$$E(x) = -\frac{\partial \phi}{\partial x} = -A$$

Therefore, the electric field $E(x)$ is constant throughout the absorbing layer and is given by [498]:

$$E(x) = \frac{V - V_{bi}}{t_p} \tag{3.9}$$

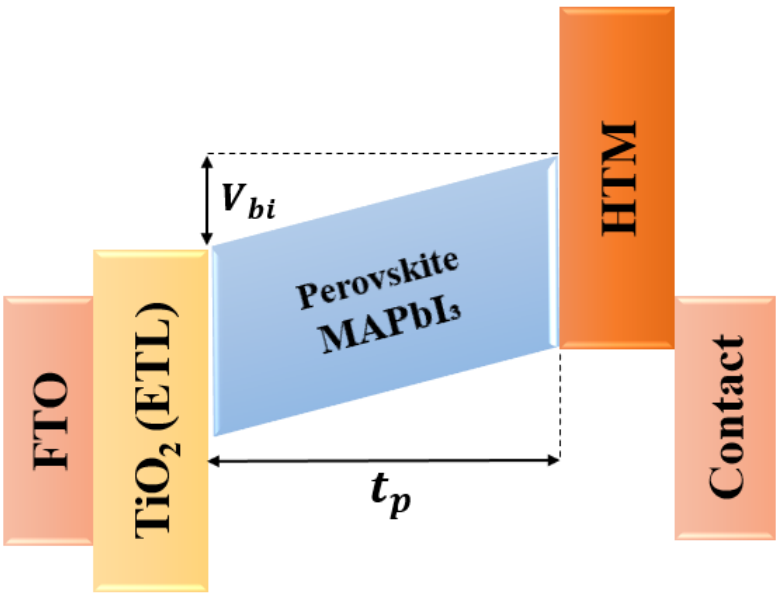



Figure 3.2: Energy diagram displaying perovskite thickness $t_p$ and built-in potential $V_{bi}$.

### 3. Optical generation G(x)

Under illumination, the density of electron-hole pairs generated in the absorbing layer of a solar cell is described by Beer–Lambert's law, which expresses the exponential attenuation of light intensity as a function of penetration depth into the material. The light intensity incident at point $x$ can be written as:

$$I(x) = I_0 e^{-\alpha x}$$

where $I_0$ is the light intensity incident on the surface of the material ($x = 0$) and $\alpha$ is the optical absorption coefficient of perovskite. Since carrier generation is directly proportional to the locally absorbed light intensity, the volume generation density $G(x)$ can be expressed as:

$$G(x) = \alpha I_0 e^{-\alpha x}$$

This equation reflects the fact that most photogenerated carriers occur in regions close to the illuminated surface, with absorption decreasing rapidly with depth. In order to simplify the notation and relate this law to characteristic quantities of the material, two parameters are introduced:

- The average absorption length $\lambda_{\text{ave}} = 1/\alpha$, which corresponds to the average distance travelled by a photon before being absorbed. It is a practical measure of the material absorption capacity. In other words, a lower $\lambda_{\text{ave}}$ means more efficient absorption.
- The effective generation density $G_{\text{eff}} = \alpha I_0$, which combines the effect of the incident photon flux and the absorption coefficient.

The carrier generation density in the perovskite layer can then be rewritten in simplified form [499], [500]:

$$G(x) = G_{\text{eff}} e^{-x/\lambda_{\text{ave}}} \tag{3.10}$$

This relationship is widely used in analytical modelling because it provides a compact way to characterize the spatial distribution of carrier generation as a function of depth in the absorber. To evaluate the total generation in the active layer, the flux of carriers generated is calculated by integrating $G(x)$ over the entire thickness. The maximum generation density $G_{\text{max}}$ is obtained by the following integral:

$$G_{\text{max}} = \int_0^{\infty} G_{\text{eff}} e^{-x/\lambda_{\text{ave}}}\, dx = G_{\text{eff}} \lambda_{\text{ave}} \tag{3.11}$$

This expression highlights the central role of $\lambda_{\text{ave}}$: for a given incident intensity, a longer average absorption length results in increased generation and therefore a higher photocurrent density. In practice, the value of $\lambda_{\text{ave}}$ in hybrid perovskites is in the range of tens to hundreds of nanometers, which explains their remarkable efficiency in absorbing sunlight despite their thin active layer (0.3−0.6 $\mu$m).

After introducing the expressions for the optical generation $G(x)$, the electric field $E(x)$ assumed to be uniform in the perovskite layer, and the recombination $R(x)$, the stationary continuity equations (3.6) and (3.7) transform into two second-order differential equations:

$$\frac{d^2n(x)}{dx^2} + \varepsilon_0 \frac{dn(x)}{dx} + G_n e^{-x/\lambda_{\text{ave}}} = 0 \tag{3.12}$$

$$\frac{d^2p(x)}{dx^2} - \varepsilon_0 \frac{dp(x)}{dx} + G_p e^{-x/\lambda_{\text{ave}}} = 0 \tag{3.13}$$

With:

$$\varepsilon_0 = \frac{qE}{kT}, \quad G_n = \frac{G_{\text{eff}}}{D_n}, \quad \text{and} \quad G_p = \frac{G_{\text{eff}}}{D_p}.$$

These differential equations are solved by finding the general solution, consisting of a homogeneous solution (without optical generation) and a particular solution (which reflects the specific response to the source term $G(x)$). Thus, for electrons, the homogeneous solution is a combination of a decreasing exponential and a constant, while the particular solution is directly related to photo-induced generation. Similarly, holes follow a symmetrical evolution but with an increasing or decreasing exponential dependence depending on the sign of the field. The general solution of equation (3.12) is given by:

$$n_h(x) = A_n e^{-\varepsilon_0 x} + B_n, \qquad n_p(x) = \frac{G_n \lambda_{\text{ave}}^2}{\varepsilon_0 \lambda_{\text{ave}} - 1} e^{-x/\lambda_{\text{ave}}}.$$

We proceed in the same way for equation (3.13), where the general solution is given by the sum of the homogeneous and particular solutions:

$$p_h(x) = A_p e^{\varepsilon_0 x} + B_p, \qquad p_p(x) = -\frac{G_p \lambda_{\text{ave}}^2}{\varepsilon_0 \lambda_{\text{ave}} + 1} e^{-x/\lambda_{\text{ave}}}.$$

The general solutions of the two differential equations (3.12) and (3.13) are thus expressed as follows:

$$n(x) = A_n e^{-\varepsilon_0 x} + B_n + \frac{G_n \lambda_{\text{ave}}^2}{\varepsilon_0 \lambda_{\text{ave}} - 1} e^{-x/\lambda_{\text{ave}}} \tag{3.14}$$

$$p(x) = A_p e^{\varepsilon_0 x} + B_p - \frac{G_p \lambda_{\text{ave}}^2}{1 + \varepsilon_0 \lambda_{\text{ave}}} e^{-x/\lambda_{\text{ave}}} \tag{3.15}$$

These expressions therefore reflect the balance between drift, diffusion and optical generation phenomena in the active layer, and form the basis for the subsequent evaluation of the photogenerated current and dark current. The constants $A_n$, $A_p$, $B_n$, and $B_p$ are to be determined using the boundary conditions for an n–i–p structure (FTO/$TiO_2$/$MAPbI_3$/HTM). They are based on the fundamental principles of charge carrier transport, surface recombination, and continuity at interfaces between different types of materials.

- **First condition** $n(0) = N_{D,\text{eff}}$.

At the $TiO_2$/perovskite interface, it is assumed that the electron concentration in the $TiO_2$ region (n-type) imposes a concentration close to $N_{D,\text{eff}}$ for electrons at this interface. This is based on the fact that $TiO_2$ is a heavily n-type doped material, creating a region where the concentration of majority carriers (electrons) is equivalent to the concentration of donors.

- **Second condition** $J_p(0) = qs_p\left(n_i - \frac{n_i^2}{N_{D,\text{eff}}}\right)$.

It expresses the surface recombination of holes at the interface between perovskite and $TiO_2$. The surface recombination velocity $s_p$ is a parameter that describes the extent to which holes recombine at the $TiO_2$/perovskite interface. $n_i$ is the intrinsic carrier concentration. This condition is used to model charge losses at this interface. This means that holes partially recombine before reaching the $TiO_2$ layer, which is a characteristic of this interface.

- **Third condition** $p(t_p) = N_{A,\text{eff}}$.

It sets the concentration of holes in the HTM layer (p-type) at the perovskite/HTM interface. Since the HTM is doped with an acceptor concentration $N_{A,\text{eff}}$, it is logical that the concentration of majority carriers (holes) should be close to this value at this boundary. This ensures that the majority of holes are effectively injected into the HTM, which is essential for the cell to function properly.

- **Four condition** $J_n(t_p) = qs_n\left(n_i - \frac{n_i^2}{N_{A,\text{eff}}}\right)$.

This condition applies to the perovskite/HTM interface. It corresponds to surface recombination of electrons, governed by the surface recombination velocity $s_n$, which is consistent with the presence of an acceptor layer (HTM) promoting electron capture. In an n–i–p structure, this recombination is useful for preventing electrons from entering the HTM, which would decrease the efficiency of charge separation.

For electrons, at the front interface ($x = 0$), corresponding to contact with the electron-transporting material ($TiO_2$), the electron density must be equal to the effective donor doping density $N_{D,\text{eff}}$. Applying this condition to the general equation (3.14) leads to the following relationship:

$$n(0) = N_{D,\text{eff}} = A_n + B_n + \frac{G_n\lambda_{\text{ave}}^2}{\varepsilon_0\lambda_{\text{ave}} - 1} \tag{3.16}$$

At the other end of the absorber ($x = t_p$), the electric field becomes negligible, so that transport is dominated by diffusion. So equation (3.3) becomes:

$$\begin{aligned} J_n(t_p) &= qD_n\left.\frac{dn}{dx}\right|_{x=t_p} \\ \left.\frac{dn}{dx}\right|_{x=t_p} &= -\varepsilon_0 A_n e^{-\varepsilon_0 t_p} - \frac{G_n\lambda_{\text{ave}}}{\varepsilon_0\lambda_{\text{ave}} - 1}e^{-t_p/\lambda_{\text{ave}}} \end{aligned} \tag{3.17}$$

$$qs_n\left(n_i - \frac{n_i^2}{N_{A,\text{eff}}}\right) = qD_n\left(-\varepsilon_0 A_n e^{-\varepsilon_0 t_p} - \frac{G_n\lambda_{\text{ave}}}{\varepsilon_0\lambda_{\text{ave}} - 1}e^{-t_p/\lambda_{\text{ave}}}\right) \tag{3.18}$$

From this relationship, we can isolate the constant $A_n$:

$$A_n = \frac{-\frac{s_n}{D_n}\left(n_i - \frac{n_i^2}{N_{A,\text{eff}}}\right) - \frac{G_n\lambda_{\text{ave}}}{\varepsilon_0\lambda_{\text{ave}}-1}e^{-t_p/\lambda_{\text{ave}}}}{\varepsilon_0 e^{-\varepsilon_0 t_p}} \tag{3.19}$$

Substituting $A_n$ into equation (3.16) to find $B_n$:

$$B_n = N_{D,\text{eff}} - \left(\frac{-\frac{s_n}{D_n}\left(n_i - \frac{n_i^2}{N_{A,\text{eff}}}\right) - \frac{G_n\lambda_{\text{ave}}}{\varepsilon_0\lambda_{\text{ave}}-1}e^{-t_p/\lambda_{\text{ave}}}}{\varepsilon_0 e^{-\varepsilon_0 t_p}}\right) - \frac{G_n\lambda_{\text{ave}}^2}{\varepsilon_0\lambda_{\text{ave}}-1}$$

$$B_n = N_{D,\text{eff}} + \frac{s_n}{D_n\varepsilon_0 e^{-\varepsilon_0 t_p}}\left(n_i - \frac{n_i^2}{N_{A,\text{eff}}}\right) + \frac{G_n\lambda_{\text{ave}}}{\varepsilon_0\lambda_{\text{ave}}-1}\left(\frac{e^{-t_p/\lambda_{\text{ave}}}}{\varepsilon_0 e^{-\varepsilon_0 t_p}} - \lambda_{\text{ave}}\right) \tag{3.20}$$

Similarly, for holes, boundary conditions are applied to $p(x)$. At the front interface ($x = 0$), the electric field is assumed to be zero or negligible. So, equation (3.4) becomes:

$$\begin{aligned} J_p(0) &= -qD_p\left.\frac{dp}{dx}\right|_{x=0} \\ \left.\frac{dp}{dx}\right|_{x=t_0} &= \varepsilon_0 A_p + \frac{G_p\lambda_{\text{ave}}}{\varepsilon_0\lambda_{\text{ave}}+1} \end{aligned} \tag{3.21}$$

$$qs_p\left(n_i - \frac{n_i^2}{N_{D,\text{eff}}}\right) = -qD_p\left(\varepsilon_0 A_p + \frac{G_p\lambda_{\text{ave}}}{\varepsilon_0\lambda_{\text{ave}}+1}\right) \tag{3.22}$$

This equation allows $A_p$ to be expressed as:

$$A_p = -\frac{s_p}{\varepsilon_0 D_p}\left(n_i - \frac{n_i^2}{N_{D,\text{eff}}}\right) - \frac{G_p\lambda_{\text{ave}}}{\varepsilon_0(\varepsilon_0\lambda_{\text{ave}}+1)} \tag{3.23}$$

Once $A_p$ has been determined, the final boundary condition must be imposed at the other end of the absorber ($x = t_p$), i.e., at the interface with the HTM. At this level, the hole density must be equal to the effective acceptor concentration $N_{A,\text{eff}}$, which ensures continuity of current and correct injection of majority carriers into the HTM. This condition is written as:

$$p(t_p) = N_{A,\text{eff}} = A_p e^{\varepsilon_0 t_p} + B_p - \frac{G_p\lambda_{\text{ave}}^2}{1+\varepsilon_0\lambda_{\text{ave}}}e^{-t_p/\lambda_{\text{ave}}} \tag{3.24}$$

By isolating the constant $B_p$, we obtain:

$$B_p = N_{A,\text{eff}} - \left(-\frac{s_p}{\varepsilon_0 D_p}\left(n_i - \frac{n_i^2}{N_{D,\text{eff}}}\right) - \frac{G_p\lambda_{\text{ave}}}{\varepsilon_0(\varepsilon_0\lambda_{\text{ave}}+1)}\right)e^{\varepsilon_0 t_p} + \frac{G_p\lambda_{\text{ave}}^2}{1+\varepsilon_0\lambda_{\text{ave}}}e^{-t_p/\lambda_{\text{ave}}}$$

$$B_p = N_{A,\text{eff}} + \frac{s_p}{\varepsilon_0 D_p}\left(n_i - \frac{n_i^2}{N_{D,\text{eff}}}\right)e^{\varepsilon_0 t_p} + \frac{G_p\lambda_{\text{ave}}}{\varepsilon_0\lambda_{\text{ave}}+1}\left(\frac{e^{\varepsilon_0 t_p}}{\varepsilon_0} + \lambda_{\text{ave}}e^{-t_p/\lambda_{\text{ave}}}\right) \tag{3.25}$$

The total current density $J$ in the device is obtained as the sum of the electron and hole contributions, $J = J_n + J_p$ [477]. By substituting the expressions of $J_n$ and $J_p$, given by equations (3.3) and (3.4), into this relation, the current density can be expressed as:

$$J = q\mu_n nE + qD_n\frac{\partial n}{\partial x} + q\mu_p pE - qD_p\frac{\partial p}{\partial x} \tag{3.26}$$

This equation highlights the two fundamental transport mechanisms inside the perovskite layer. The first is the drift current, which arises from the motion of charge carriers (electrons and holes) under the influence of the internal electric field. The second is the diffusion current, which results from spatial variations of carrier concentrations, described by the gradients $\frac{\partial n}{\partial x}$ and $\frac{\partial p}{\partial x}$. At the interface $x = 0$, the spatial gradients of the carrier concentrations are assumed to be negligible. Physically, this assumption means that the distribution of carriers is nearly uniform at this boundary, so diffusion plays an insignificant role. Under this condition, the diffusion terms vanish from the expression, and the current density simplifies to:

$$J = q\mu_n nE + q\mu_p pE \tag{3.27}$$

This simplified form shows that, at $x = 0$, the current is governed exclusively by drift, and therefore directly depends on the carrier densities, their mobilities, and the electric field present in the active region. We replace the carrier concentrations $n$ and $p$ by their constant values $B_n$ and $B_p$, respectively, at $x = 0$, because they represent the majority of charge carriers contributing to the current at this point. Substituting them into the current density relation gives:

$$J = qE(\mu_n B_n + \mu_p B_p) \tag{3.28}$$

By expanding the expressions of $B_n$ and $B_p$, the current density can be written as:

$$\begin{aligned} J = qE\Bigg[&\mu_n\left(N_{D,\text{eff}} + \frac{s_n}{D_n\varepsilon_0 e^{-\varepsilon_0 t_p}}\left(n_i - \frac{n_i^2}{N_{A,\text{eff}}}\right) + \frac{G_n\lambda_{\text{ave}}}{\varepsilon_0\lambda_{\text{ave}} - 1}\left(\frac{e^{-t_p/\lambda_{\text{ave}}}}{\varepsilon_0 e^{-\varepsilon_0 t_p}} - \lambda_{\text{ave}}\right)\right) \\ &+ \mu_p\left(N_{A,\text{eff}} + \frac{s_p}{\varepsilon_0 D_p}\left(n_i - \frac{n_i^2}{N_{D,\text{eff}}}\right)e^{\varepsilon_0 t_p} + \frac{G_p\lambda_{\text{ave}}}{\varepsilon_0\lambda_{\text{ave}} + 1}\left(\frac{e^{\varepsilon_0 t_p}}{\varepsilon_0} + \lambda_{\text{ave}}e^{-t_p/\lambda_{\text{ave}}}\right)\right)\Bigg] \end{aligned} \tag{3.29}$$

At this stage, the current density expression contains both drift contributions, linked to the effective doping concentrations and surface recombination terms, and photogeneration contributions, which depend on the absorption length $\lambda_{\text{ave}}$ and the generation rates $G_n$ and $G_p$. Next, we substitute the relations $\varepsilon_0 = \frac{q(V-V_{bi})}{kTt_p}$, $E = \frac{V-V_{bi}}{t_p}$, and the expressions of $G_p$ and $G_n$ in terms of the maximum generation rate $G_{\max}$. This yields the compact form of the total current density:

$$
\begin{aligned}
J = q\frac{(V-V_{bi})}{t_p}\Bigg(\Bigg[\mu_n\left(N_{D,\text{eff}} + \frac{s_n kTt_p(n_i - \frac{n_i^2}{N_{A,\text{eff}}})}{D_n q(V-V_{bi})e^{-\frac{q(V-V_{bi})}{kT}}}\right) \\
+ \mu_p\left(N_{A,\text{eff}} + \frac{s_p kTt_p(n_i - \frac{n_i^2}{N_{D,\text{eff}}})e^{\frac{q(V-V_{bi})}{kT}}}{q(V-V_{bi})D_p}\right)\Bigg] \\
+ G_{\max}\Bigg[\frac{\mu_n}{D_n\left(\frac{q(V-V_{bi})}{kTt_p}\lambda_{\text{ave}} - 1\right)}\left(\frac{e^{-t_p/\lambda_{\text{ave}}}}{\frac{q(V-V_{bi})}{kTt_p}e^{-\frac{q(V-V_{bi})}{kT}}} - \lambda_{\text{ave}}\right) \\
+ \frac{\mu_p}{D_p\left(\frac{q(V-V_{bi})}{kTt_p}\lambda_{\text{ave}} + 1\right)}\left(\frac{e^{\frac{q(V-V_{bi})}{kT}}}{\frac{q(V-V_{bi})}{kTt_p}} + \lambda_{\text{ave}}e^{-t_p/\lambda_{\text{ave}}}\right)\Bigg]\Bigg)
\end{aligned}
\tag{3.30}
$$

From the general expression for current density (Equation 3.30), it is possible to clearly distinguish two fundamental contributions to charge transport in the perovskite cell. In fact, current density can be broken down into two parts [501]:

- A dark current ($J_{\text{dark}}$), which is independent of the optical generation phenomenon and reflects the behaviour of the cell in the absence of light.
- A photogenerated current ($J_{\text{phot}}$), which is directly related to the absorption of photons and the generation of electron–hole pairs.

This separation allows for a more detailed analysis of the origin of each contribution to the total current and facilitates the study of the physical mechanisms limiting the device performance. The dark current is expressed by:

$$
\begin{aligned}
J_{\text{dark}} = q\frac{(V-V_{bi})}{t_0}\Bigg[\mu_n\left(N_{D,\text{eff}} + \frac{s_n kTt_p\left(n_i - \frac{n_i^2}{N_{A,\text{eff}}}\right)}{D_n q(V-V_{bi})e^{-\frac{q(V-V_{bi})}{kT}}}\right) \\
+ \mu_p\left(N_{A,\text{eff}} + \frac{s_p kTt_p\left(n_i - \frac{n_i^2}{N_{D,\text{eff}}}\right)e^{\frac{q(V-V_{bi})}{kT}}}{q(V-V_{bi})D_p}\right)\Bigg]
\end{aligned}
\tag{3.31}
$$

This component reflects contributions due mainly to charge transport under the action of the internal electric field and to recombination phenomena at the interfaces. It determines the behaviour of the cell in darkness and allows the identification of losses associated with leakage currents and recombination. Consequently, the photogenerated current is given by:

$$
\begin{aligned}
J_{\text{phot}} = \frac{q(V-V_{bi})G_{\max}}{t_p}\Bigg[\frac{\mu_n}{D_n\left(\frac{q(V-V_{bi})}{kTt_p}\lambda_{\text{ave}} - 1\right)}\left(\frac{e^{-t_p/\lambda_{\text{ave}}}}{\frac{q(V-V_{bi})}{kTt_p}e^{-\frac{q(V-V_{bi})}{kT}}} - \lambda_{\text{ave}}\right) \\
+ \frac{\mu_p}{D_p\left(\frac{q(V-V_{bi})}{kTt_p}\lambda_{\text{ave}} + 1\right)}\left(\frac{e^{\frac{q(V-V_{bi})}{kT}}}{\frac{q(V-V_{bi})}{kTt_p}} + \lambda_{\text{ave}}e^{-t_p/\lambda_{\text{ave}}}\right)\Bigg]
\end{aligned}
\tag{3.32}
$$

This component is proportional to $G_{\max}$, the maximum carrier generation in the perovskite layer, and depends on the average absorption length $\lambda_{\text{ave}}$. It reflects the optoelectronic contribution of the device: a more efficient absorbing layer in converting photons into charge carriers results in a higher $J_{\text{phot}}$.

As a result, Equation (3.31) describes the intrinsic electrical behaviour of the cell (dark part), while Equation (3.32) highlights the photo-induced response under illumination. The combination of these two expressions makes it possible to accurately model the current–voltage ($J$–$V$) curve of the perovskite solar cell, distinguishing between the influence of purely electrical parameters (mobilities, recombination rates, doping) and optical parameters (generation rate, absorption).

To model the spectral performance of the cell, it is necessary to obtain the EQE (external quantum efficiency) and IQE (internal quantum efficiency) as a function of the wavelength $\lambda_{ave}$. These two quantities are commonly used to evaluate the optoelectronic efficiency of photovoltaic devices. The external quantum efficiency, which measures the quantity of incident photons converted into charge carriers, can be expressed by this formula [502]:

$$\text{EQE}(\lambda) = \frac{J_{\text{phot}}\, h\, c}{q\, P_{\text{inc}}\, \lambda_{ave}} \tag{3.33}$$

In this expression, the EQE depends directly on:

- $J_{\text{phot}}$ is the photo-generated current, i.e., the contribution to the total current resulting solely from optical generation.
- $P_{\text{inc}}$ is the light power incident on the cell.
- $h$ is Planck's constant and $c$ is the speed of light.
- $\lambda_{ave}$ is the average wavelength of absorption.

This expression reflects the ratio between the number of carriers collected and the number of incident photons. By substituting $J_{\text{phot}}$ in the expression of EQE:

$$\text{EQE}(\lambda_{ave}) = \frac{(V - V_{bi})\, h\, c\, G_{\text{eff}}}{\lambda_{ave}\, P_{\text{inc}}\, t_p} \left[ \frac{\mu_n}{D_n \left( \frac{q(V-V_{bi})}{kTt_p} \lambda_{ave} - 1 \right)} \left( \frac{e^{-t_p/\lambda_{ave}}}{\frac{q(V-V_{bi})}{kTt_p} e^{-\frac{q(V-V_{bi})}{kT}}} - \lambda_{ave} \right) + \right.$$
$$\left. \frac{\mu_p}{D_p \left( \frac{q(V-V_{bi})}{kTt_p} \lambda_{ave} + 1 \right)} \left( \frac{e^{\frac{q(V-V_{bi})}{kT}}}{\frac{q(V-V_{bi})}{kTt_p}} + \lambda_{ave} e^{-t_p/\lambda_{ave}} \right) \right] \tag{22}$$

We can note that the EQE depends on both optical parameters ($\lambda_{ave}$, $P_{\text{inc}}$, $G_{\text{eff}}$) and electrical transport parameters ($\mu_n$, $\mu_p$, $D_n$, $D_p$, $V - V_{bi}$), highlighting the close interaction between photon generation and charge collection.

In contrast to the EQE, which takes into account the total incident light flux (including losses due to reflection and transmission), the IQE measures only the conversion efficiency of the photons that actually arrive in the cell, after the light crosses the reflection and transmission barriers. Therefore, IQE can be expressed as follows [502]:

$$\mathrm{IQE}(\lambda) = \frac{\mathrm{EQE}(\lambda)}{1 - R_\lambda - T_\lambda} \tag{23}$$

Where:

- $R_\lambda$ is the reflection coefficient, representing the fraction of light reflected at the surface of the cell.
- $T_\lambda$ is the transmission coefficient, corresponding to the fraction of light passing through the device without being absorbed.

Consequently, the IQE allows the intrinsic performance of the absorbing layer to be isolated, independently of external optical losses (reflection, transmission). The comparison between EQE and IQE therefore provides an essential diagnostic tool; a significant difference between the two indicates the existence of significant optical losses, while a close match indicates that the limitations are mainly due to internal recombination and charge transport.

After developing a mathematical model describing the current density $J$, composed of two main contributions: the dark current $J_{\mathrm{dark}}$ (independent of generation) and the photocurrent $J_{\mathrm{phot}}$ (dependent on generation), and defined the expressions for external quantum efficiency (EQE) and internal quantum efficiency (IQE), we undertook the development of a program in MATLAB. The purpose of this software is to plot the characteristic curves $J$–$V$, EQE and IQE. These analytical tools are an essential step towards:

- Increasing understanding of the physical mechanisms governing solar cell operation,
- Evaluating its overall performance,
- Identifying possible improvements in structure and materials.

The methodology adopted for programming is represented in the form of a flowchart, as shown in Figure 3.3, which illustrates the different steps followed, from the definition of input parameters to the generation of curves and final results. In addition to this flowchart, A detailed pseudocode is presented in Appendix .1. This summarises the numerical procedure for implementing the main equations and provides a clear basis for understanding and reproducing the calculation.

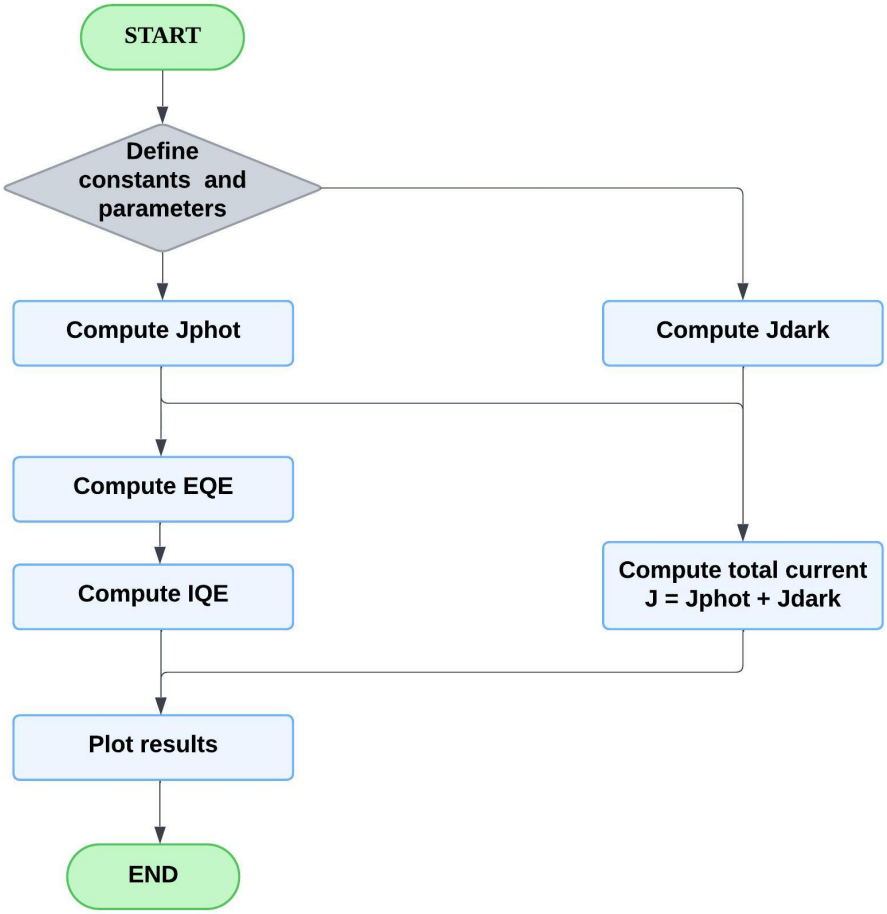



Figure 3.3: Flow chart of MATLAB code used.

### 3.2.3 Analytical results and validation

#### 3.2.3.1 Comparison and validation with experimental results

Running the program developed in MATLAB produced the current–voltage ($J$–$V$) characteristic curves from the analytical model. These results were then compared with the experimental data reported in the literature [475] in order to assess the validity and reliability of the proposed model. Figure 4.9 illustrates this comparison.

Analysis of the curves shows that the analytically predicted short-circuit current density ($J_{sc}$) is approximately 2 mA/cm$^2$ higher than that observed experimentally. This discrepancy can be explained by the fact that, in real devices, several loss mechanisms come into play, such as recombination, parasitic resistances and certain defects at the interfaces. These mechanisms tend to reduce the actual current collected, whereas the analytical model is based on simplifying assumptions in which the interfaces are assumed to be perfect and recombination phenomena are greatly minimised, which naturally leads to an overestimation of ideal performance.

A similar trend is observed for the open-circuit voltage ($V_{oc}$), whose value from the model exceeds the experimentally obtained value by 0.15 V. Again, this discrepancy is

attributable to the model's failure to take into account certain physical losses, particularly those related to series and shunt resistances. Series resistance, generally associated with contacts, transport layers or defects in the base materials, causes an internal voltage drop that limits both $J_{sc}$ and $V_{oc}$. Shunt resistance, linked to leakage paths or the presence of mixed domains, contributes to additional losses by reducing the fill factor and open-circuit voltage.

In addition to these mechanisms, there are other phenomena such as non-radiative recombination at interfaces, volume recombination due to deep traps, and effects specific to perovskites such as ion migration or hysteresis, which locally modify the shape of the experimental curves [503]–[507]. However, these discrepancies do not invalidate the analytical model. On the contrary, they confirm that it accurately reflects general trends and provides a consistent representation of how the cell works, while highlighting its limitations in the face of the complexity of real-world devices. To support this analysis, Table 3.1 summarises the main photovoltaic parameters derived from the model and from experience.

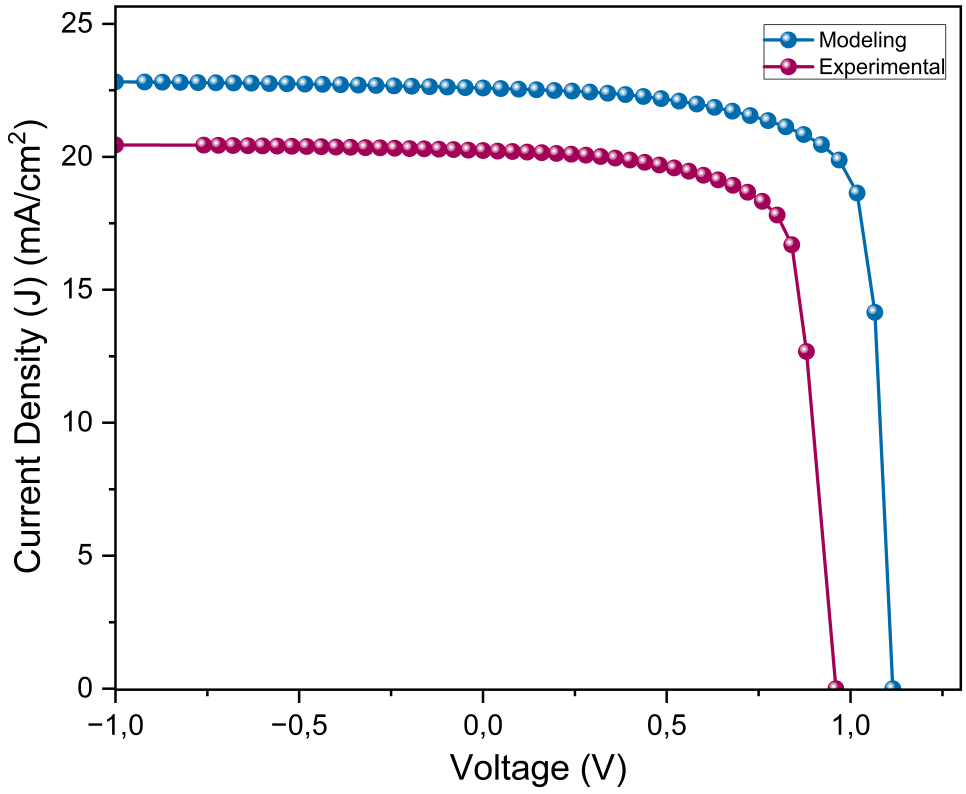



Figure 3.4: $J$–$V$ curves comparison showing the experimental data [475] validating the analytical model of the PSC.

The comparison clearly highlights the model's tendency to overestimate $J_{sc}$ and $V_{oc}$ while underestimating the fill factor (FF). This limitation results in an overall efficiency value (PCE) that is slightly lower than that of the experiment (12.8% versus 13.15%). This discrepancy clearly illustrates the impact of parasitic resistances and recombination mechanisms not considered in the modelling.

Ultimately, analysis of the results shows that the analytical model is an effective tool for describing the idealised characteristics of the cell and predicting its overall behaviour.

Table 3.1: Main photovoltaic parameters extracted from the analytical model and experimental measurements.

| **Parameter** | $J_{sc}$ **(mA/cm$^2$)** | $V_{oc}$ **(V)** | $P_{max}$ **(mW/cm$^2$)** | **FF (%)** | **PCE (%)** |
|---|---|---|---|---|---|
| Experimental [475] | 20.62 | 0.96 | 13.15 | 66.41 | 13.15 |
| Analytical model | 22.82 | 1.114 | 12.748 | 50.11 | 12.8 |

However, comparison with experimental data highlights the importance of real loss phenomena, which will need to be incorporated into future improvements to the model in order to obtain an even more accurate quantitative prediction.

#### 3.2.3.2 Analysis of external and internal quantum efficiencies (EQE and IQE)

After validating the current–voltage ($J$–$V$) characteristics of the analytical model by comparing it with experimental data, it is appropriate to further evaluate the performance of the solar cell by examining its spectral response. In this context, the study of external quantum efficiency and internal quantum efficiency is a complementary and essential tool. These two quantities not only make it possible to assess the ability of the n-i-p perovskite cell (FTO/$TiO_2$/$MAPbI_3$/Spiro-OMeTAD) to convert incident photons into collected charges, but also to highlight the optical losses and recombination mechanisms predicted by the model. The spectral performance of the PSC is analysed using the EQE and IQE curves, calculated using the analytical model developed in the previous sections. Figure 3.5 shows these two curves as a function of wavelength, illustrating the spectral response of the cell in the range from 0.3 to 1.0 µm.

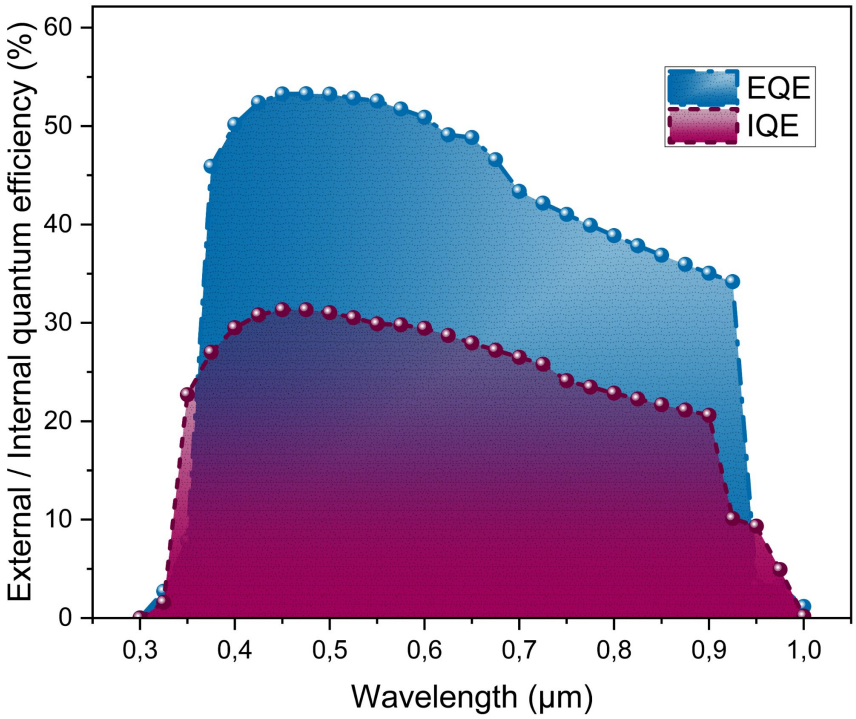



Figure 3.5: External quantum efficiency (EQE) and internal quantum efficiency (IQE) curves derived from the analytical model for the n-i-p perovskite cell.

The EQE, shown in blue, expresses the fraction of incident photons effectively converted into collected charges, taking into account optical losses due to reflection and transmission. It reaches a maximum of approximately 55% between 0.45 and 0.55 µm, reflecting optimal absorption of the active layer in the visible range. From 0.6 µm onwards, a gradual decrease in EQE is observed, as a result of the reduction in the absorption coefficient of perovskite as it approaches its optical gap (∼1.55 eV, or ∼0.8 µm). Beyond 0.9 µm, the EQE drops rapidly towards zero, confirming the absence of significant absorption in the near-infrared.

The IQE, shown in purple, reflects the fraction of generated carriers that are actually collected, regardless of initial optical losses. It broadly follows the same spectral trend as the EQE, with a maximum of around 30% at 0.45–0.55 µm. The difference between the two curves is particularly marked in the ultraviolet (0.3–0.4 µm), where it can reach nearly 20%, highlighting significant optical losses related to surface reflection and parasitic absorption in the transport layers. This difference then gradually decreases towards 0.7–0.8 µm, reflecting a better match between carrier generation and collection in the region where perovskite absorbs most efficiently.

Finally, the simultaneous decrease in both curves beyond 0.9 µm reflects the intrinsic limitation of the material imposed by its energy gap. The absence of marked fluctuations or fine oscillations suggests that the analytical model simplifies certain optical phenomena (such as interference or scattering), which would be more visible in a real cell. Overall, these results confirm the consistency of the analytical model in describing the spectral response of the cell, while highlighting its limitations related to the approximations adopted. They provide a solid basis for evaluating optical performance and pave the way for future optimisations incorporating a more detailed description of optical losses and transport phenomena.

#### 3.2.3.3 Influence of the thickness of the absorbing layer on performance

Figure 3.6 illustrates the $J$–$V$ curves obtained by analytical modelling for different thicknesses of the $MAPbI_3$ perovskite layer, while Table 3.2 summarises the corresponding main photovoltaic parameters. The results highlight a gradual improvement in the overall performance of the cell as the thickness of the absorbing layer increases from 0.26 µm to 0.35 µm.

Table 3.2: Photovoltaic parameters derived from the analytical model as a function of the thickness of the $MAPbI_3$ layer.

| $t_p$ **(µm)** | $J_{sc}$ **(mA/cm$^2$)** | $V_{oc}$ **(V)** | $P_{max}$ **(mWh/cm$^2$)** | **FF (%)** | **PCE (%)** |
|---|---|---|---|---|---|
| 0.26 | 20.94 | 0.9984 | 11.952 | 57.164 | 11.9 |
| 0.28 | 21.89 | 1.057 | 12.366 | 53.426 | 12.3 |
| 0.30 | 22.82 | 1.114 | 12.748 | 50.116 | 12.7 |
| 0.325 | 23.96 | 1.185 | 14.03 | 49.393 | 14.03 |
| 0.35 | 25.049 | 1.254 | 15.678 | 49.875 | 15.6 |

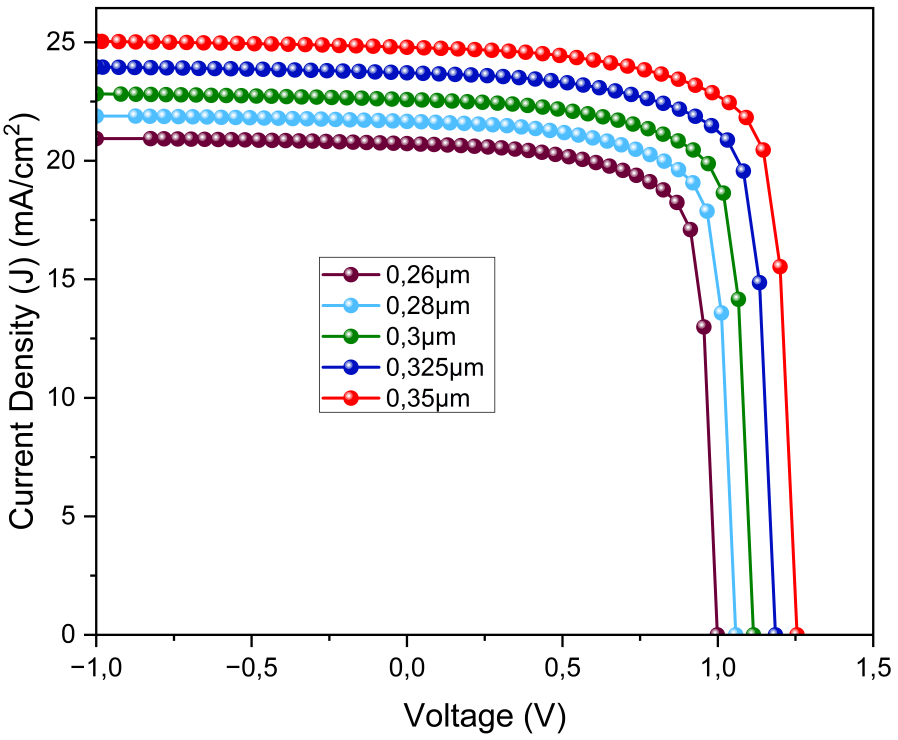



Figure 3.6: $J$–$V$ curves from the analytical model for different thicknesses of the $MAPbI_3$ perovskite layer (0.26 µm to 0.35 µm).

Firstly, the $J_{sc}$ increases significantly, from 20.94 mA/cm$^2$ to 25.05 mA/cm$^2$, reflecting greater photon absorption in the absorber. This trend is also accompanied by an increase in $V_{oc}$ from 0.998 V to 1.254 V, contributing to the increase in maximum power output. As a result, the efficiency improves from 11.9% to 15.6%, confirming the central role of perovskite thickness in the trade-off between optical absorption and electrical collection.

However, this improvement is accompanied by a decrease in the fill factor, which drops from 57.2% to 49.9% as thickness increases. This deterioration can be attributed to several physical mechanisms. On the one hand, the increase in thickness lengthens the distance travelled by charge carriers, thereby increasing the probability of recombination, particularly near interfaces. This recombination reduces the current at the maximum power point, negatively impacting the FF. On the other hand, a thicker layer induces greater volume resistance, linked to limitations in carrier mobility and the potential presence of intrinsic defects. This additional resistance results in ohmic losses, particularly noticeable at high current densities, which alters the curvature of the $J$–$V$ characteristic. Finally, the absorption-transport trade-off becomes more pronounced, while a thick layer promotes increased carrier generation, their collection remains hampered by limited diffusion processes and increased recombination.

These results confirm that optimising the thickness of the perovskite layer is a key parameter in the design of high-efficiency solar cells. Too little thickness limits absorption and reduces photocurrent, while too much thickness degrades charge transport and penalises FF. The optimal thickness is therefore around 0.35 µm, where the compromise between optical generation and electrical collection allows an efficiency of close to 15.6% to be achieved within the analytical model developed.

#### 3.2.3.4 Influence of ETL ($TiO_2$) doping on photovoltaic performance

Figure 3.7 shows the effect of $TiO_2$-based electron transport layer (ETL) doping on the characteristic parameters of the perovskite solar cell, namely the short-circuit current ($J_{sc}$), open-circuit voltage ($V_{oc}$), fill factor (FF) and power conversion efficiency (PCE). In order to identify the optimal doping level, a representative range of donor concentrations was considered: $10^{14}$ cm$^{-3}$, $5 \times 10^{14}$ cm$^{-3}$, $10^{15}$ cm$^{-3}$ (reference value), $10^{16}$ cm$^{-3}$, $5 \times 10^{16}$ cm$^{-3}$ and $10^{17}$ cm$^{-3}$.

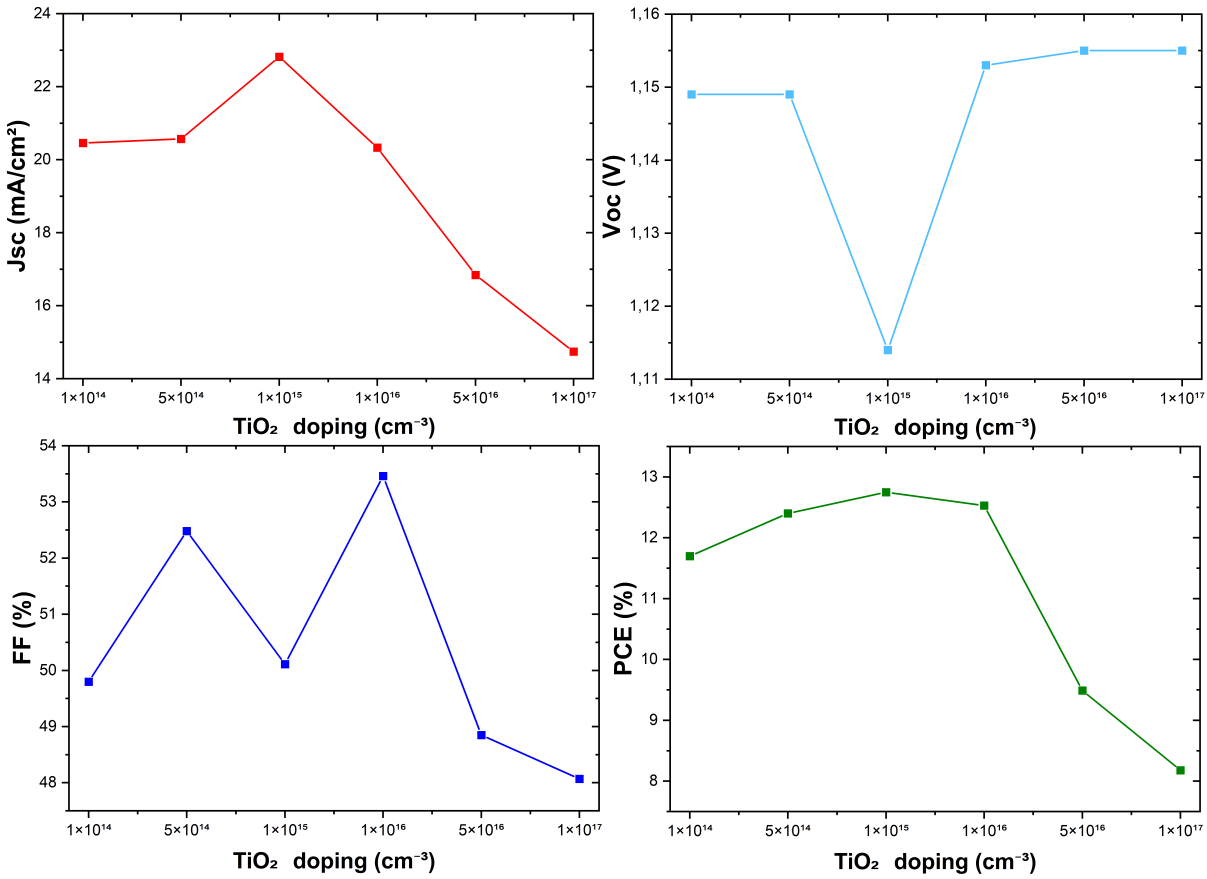



Figure 3.7: Influence of ETL ($TiO_2$) doping on device parameters.

The evolution of the $J_{sc}$ shows a significant improvement when the donor concentration increases from $10^{14}$ cm$^{-3}$ to $10^{15}$ cm$^{-3}$, reaching a maximum value of approximately 23 mA/cm$^2$. This effect is attributed to improved conductivity of $TiO_2$, which facilitates the transport and collection of photogenerated electrons while maintaining a relatively low level of recombination. In contrast, for higher doping levels ($\geq 10^{16}$ cm$^{-3}$), $J_{sc}$ decreases significantly. This decrease is due to an increase in surface defects and non-radiative recombination at the $TiO_2$/perovskite interface, which are direct consequences of excessive electron density in the ETL, modifying the internal electric field and reducing the selectivity of charge extraction. The $V_{oc}$ remains broadly stable ($\sim$1.15 V), confirming that $TiO_2$ doping has a moderate influence on the Fermi level shift and band alignment. However, a slight drop in $V_{oc}$ is observed at $10^{15}$ cm$^{-3}$, reflecting a trade-off between improved transport and a temporary increase in recombination losses. At higher doping levels, the $V_{oc}$ returns to a stable value, suggesting that the limiting mechanism remains

primarily related to recombination rather than a major change in energy alignment.

The FF evolves in a non-monotonic manner with doping. A relatively high value is obtained at $10^{16}$ cm$^{-3}$, indicating a reduction in series resistance and an improvement in ETL selectivity. However, for very low ($10^{14}$ cm$^{-3}$) or very high ($\geq 5 \times 10^{16}$ cm$^{-3}$) doping levels, the FF decreases due to low conductivity or excessive losses through interfacial recombination, respectively. This confirms that the FF is particularly sensitive to the balance between electron conduction and recombination. The PCE trend directly follows that of the $J_{sc}$, with a maximum reached for a doping of $10^{15}$ cm$^{-3}$, a value that offers the best compromise between efficient charge transport and limited recombination losses. Above $10^{16}$ cm$^{-3}$, the increase in recombination and parasitic resistance leads to a gradual deterioration in efficiency, which drops to around 8% for $10^{17}$ cm$^{-3}$.

The choice of doping levels studied is based on a systematic approach aimed at covering a representative spectrum of experimental and theoretical conditions for $TiO_2$-based ETL. The lightly doped range ($\sim 10^{14}$ cm$^{-3}$) allows the reproduction of classic experimental conditions for $TiO_2$-based ETL, where conductivity is limited but recombination is minimised. The moderately doped range ($10^{15}$ cm$^{-3}$) is considered optimal, as it ensures efficient electron transport while maintaining a favourable balance between conductivity and selectivity. The highly doped range ($\geq 10^{16}$ cm$^{-3}$) allows analysis of the deleterious effects of excess free carriers, such as increased non-radiative recombination, destabilisation of band alignment and reduction of the internal field, which result in a drop in overall performance. As a result, it appears that a doping level of $10^{15}$ cm$^{-3}$ is an optimal reference value, confirming the trends reported in the literature and validating its use in $TiO_2$-based perovskite structures as ETL.

## 3.3 Extension to analytical modelling of tandem cells

After developing and validating an analytical model for single-junction PSCs (FTO/ $TiO_2$/$MAPbI_3$/Spiro-OMeTAD) in the previous sections, this study extends to the modelling of tandem solar cells, in particular those combining a perovskite top and a silicon bottom cell. The transition from a single-junction architecture to a tandem structure aims to overcome the limitations inherent in single-layer cells, in particular the limited efficiency imposed by the use of a single band gap. As noted in Chapter 2, the major advantage of tandem cells lies in their ability to exploit a wider portion of the solar spectrum by stacking two subcells with complementary bandgaps ( 1.55 eV for perovskite and 1.12 eV for silicon). This spectral complementarity paves the way for theoretical efficiencies exceeding 30%, well beyond the limit imposed on single-junction cells. A monolithic 2T Perovskite/Silicon tandem solar cell (TSC) is designed with a top perovskite solar cell (PSC) and a bottom silicon-based sub-cell, where both cells are connected in series. The structure of the TSC is shown in Figure 3.8.

### 3.3.1 Analytical model of perovskite/silicon tandem cells

In order to develop a rigorous analytical description of the perovskite/silicon tandem cell, it is necessary to consider separately the electrical behaviour of each of the subcells that

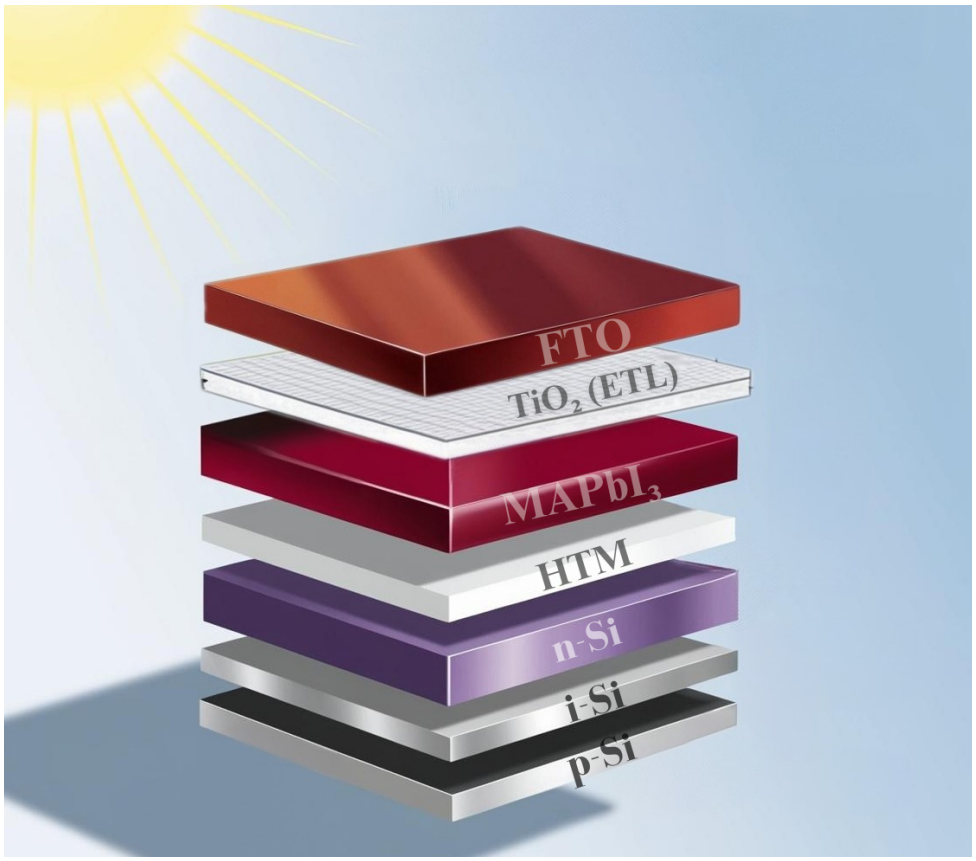



Figure 3.8: Perovskite/Silicon tandem solar cell device schematic.

make up the device. The tandem cell is composed of a top perovskite-based cell and a bottom silicon cell. In the previous sections, we have already established and validated the analytical model of the top cell, whose current-voltage (J–V) characteristics were determined from continuity equations and the model derived from carrier drift-diffusion transport. We now turn our attention to modelling the bottom cell, taking into account its intrinsic properties and the dominant physical mechanisms.

The analytical modelling of the bottom subcell (silicon) follows a similar approach to that applied to the top subcell (perovskite), using the same continuity equations but unlike perovskite cells, silicon cells have specific characteristics related to the nature of the material, including a longer minority carrier lifetime and increased sensitivity to recombination phenomena. Two main recombination mechanisms must be taken into account, radiative recombination and non-radiative Shockley–Read–Hall (SRH) recombination [508]. Radiative recombination, described by the following equation, depends on the concentration of electrons and holes:

$$R_{\text{direct}} = C(np - n_i^2) \tag{3.34}$$

Where $C$ is the bimolecular recombination coefficient, and $n_i$ represents the intrinsic carrier concentration in silicon. As for SRH recombination, it reflects the influence of trap states in the silicon band gap. Its general expression is written as:

$$R_{\text{SRH}} = \frac{(np - n_i^2)}{(n + n_i e^{E_t/(k_B T)})\tau_p + (p + p_i e^{-E_t/(k_B T)})\tau_n} \tag{3.35}$$

Where $E_t$ represents the energy level of the trap, while $\tau_n$ and $\tau_p$ denote the trapping lifetimes of electrons and holes, respectively [509]. These two mechanisms constitute the main recombination pathways that determine the current collection efficiency in the silicon subcell.

Another fundamental aspect to consider is the carrier generation profile in the bottom subcell. Incident light passing through the perovskite layer is partially absorbed in the top cell, so that only a fraction of the initial intensity reaches the silicon layer. The transmitted light intensity, which is the source of generation in the silicon, can be described by an exponential decay as a function of the perovskite thickness and its absorption coefficient. Thus, the generation intensity at the silicon interface is given by:

$$G_0 = G_{\text{eff}} e^{-t_p/\lambda_{\text{ave}}} \tag{3.36}$$

Inside silicon, this light intensity also propagates exponentially according to the expression:

$$G_{\text{si}}(x) = G_0 e^{-\alpha x} \tag{3.37}$$

To accurately model the dynamics of charge carriers in the silicon subcell, recombination mechanisms and generation profiles are incorporated into the previously derived continuity differential equations (3.6) and (3.7). These equations, based on the principles of drift–diffusion, describe the evolution of electron and hole concentrations in the silicon layer. From the initial continuity equations adapted to the lower subcell, the following expressions are obtained:

$$D_{n,\text{bot}} \frac{\partial^2 n_b(x)}{\partial x^2} + \mu_{n,\text{bot}} E(x) \frac{\partial n_b(x)}{\partial x} + G_{\text{si}}(x) - C n_b(x) = 0 \tag{3.38}$$

$$D_{p,\text{bot}} \frac{\partial^2 p_b(x)}{\partial x^2} - \mu_{p,\text{bot}} E(x) \frac{\partial p_b(x)}{\partial x} + G_{\text{si}}(x) - C p_b(x) = 0 \tag{3.39}$$

Where $D_{n,\text{bot}}$ and $D_{p,\text{bot}}$ are the diffusion coefficients of electrons and holes, $\mu_{n,\text{bot}}$ and $\mu_{p,\text{bot}}$ are their respective mobilities, and $E(x)$ is the electric field. This approach assumes that recombination is proportional to the product of carrier concentrations, reflecting a bimolecular process that dominates in silicon under illumination. To simplify the analysis and obtain analytical solutions, the equations are reformulated by introducing normalised terms and considering an electric field dependent on the applied voltage. By defining $\varepsilon_0$ as the normalised drift term and $\gamma$ as the effective recombination rate, the differential equations become:

$$\frac{\partial^2 n_b(x)}{\partial x^2} + \varepsilon_0 \frac{\partial n_b(x)}{\partial x} + \frac{G_0}{D_{n,\text{bot}}} e^{-\alpha x} - \gamma n_b(x) = 0 \tag{3.40}$$

$$\frac{\partial^2 p_b(x)}{\partial x^2} - \varepsilon_0 \frac{\partial p_b(x)}{\partial x} + \frac{G_0}{D_{p,\text{bot}}} e^{-\alpha x} - \gamma p_b(x) = 0 \tag{3.41}$$

Where $\varepsilon_{0,\text{bottom}} = \frac{q(V_{\text{bottom}} - V_{\text{bi,bottom}})}{k_B T t_b}$ translates the influence of the internal electric field, with $q$ the elementary charge, $V_{\text{bottom}}$ the voltage applied to the silicon subcell, $V_{\text{bi,bottom}}$ the internal barrier voltage, $k_B$ the Boltzmann constant, $T$ the temperature, and $t_b$ the thickness of the silicon layer. $\gamma = C/D$ represents a normalised recombination term, approximating the effective recombination rate and simplifying the non-linear interaction.

These equations are solved using the classic method of superimposing a homogeneous solution and a particular solution. The homogeneous part is associated with contributions due solely to transport and recombination, while the particular solution directly accounts for optical generation. After calculation, the general solutions are written as:

$$n_b(x) = A'_n e^{\beta_1 x} + B'_n e^{\beta_2 x} + \frac{(G_0/D_{n,\text{bot}})}{(\alpha^2 - \varepsilon_0 \alpha - \gamma)} e^{-\alpha x} \tag{3.42}$$

$$p_b(x) = A'_p e^{\beta_1 x} + B'_p e^{\beta_2 x} - \frac{(G_0/D_{p,\text{bot}})}{(\alpha^2 - \varepsilon_0 \alpha - \gamma)} e^{-\alpha x} \tag{3.43}$$

With:

$$\beta_1 = \frac{-\varepsilon_0 + \sqrt{\varepsilon_0^2 + 4\gamma}}{2}, \quad \beta_2 = \frac{-\varepsilon_0 - \sqrt{\varepsilon_0^2 + 4\gamma}}{2}$$

$A'_n$, $B'_n$, $A'_p$, and $B'_p$ are constants determined by the boundary conditions at the interfaces of the silicon subcell.

These solutions highlight the dependence of carrier profiles on depth $x$, with exponential decay linked to light absorption and modulation by the exponential terms $\beta_1 x$ and $\beta_2 x$, which reflect transport and recombination dynamics. The difference in sign in the particular term between $n_b(x)$ and $p_b(x)$ stems from the opposite polarity of electron and hole currents, consistent with the drift-diffusion equations.

To determine the constants of the analytical solutions for electron $n_b(x)$ and hole $p_b(x)$ concentrations in the silicon subcell, four boundary conditions reflecting the physical properties at the layer interfaces must be applied. These conditions are formulated in terms of carrier densities and currents at the boundaries of the $t_b$ thickness of the silicon subcell, and they take into account the interaction with the top perovskite subcell in the tandem configuration. The boundary conditions are defined as follows:

- **First condition** $n_b(0) = N_{\text{Deff,bot}}$

Where $N_{\text{Deff,bot}}$ represents the effective density of donor dopants at the interface with the intermediate recombination layer, imposing an equilibrium electron concentration.

- **Second condition** $J_{nb}(t_b) = q s_{\text{n,bot}} \left( n_{\text{i,bot}} - \frac{n_{\text{i,bot}}^2}{N_{\text{Aeff,bot}}} \right)$

Where $J_{n,b}$ is the electron current density, $q$ is the elementary charge, $s_{\text{n,bot}}$ is the surface recombination velocity for electrons, $n_{\text{i,bot}}$ is the intrinsic concentration, and $N_{\text{Aeff,bot}}$ is the effective acceptor density at the rear. This condition models surface recombination at the rear electrode, adjusted by the difference between the intrinsic concentration and the doping-dependent recombination term.

- **Third condition** $J_{pb}(0) = qs_{\mathrm{p,bot}}\left(n_{\mathrm{i,bot}} - \frac{n_{\mathrm{i,bot}}^2}{N_{\mathrm{Deff,bot}}}\right) + J_{\mathrm{p,top}}$

Where $J_{p,b}$ is the hole current density, $s_{\mathrm{p,bot}}$ is the surface recombination velocity for holes, and $J_{\mathrm{p,top}}$ is the hole current from the perovskite subcell. The term $J_{\mathrm{p,top}}$ reflects the contribution of holes generated in the perovskite that cross the recombination interface to the silicon subcell. The appearance of $J_{\mathrm{p,top}}$ in the third condition is not arbitrary; it is directly linked to the fundamental role of holes in the top layer of the device (typically the hole transport or collection layer). When a photon is absorbed in the active layer, an electron-hole pair is generated. The electron is conducted to the electron transport layer, while the hole must be extracted to the hole transport layer, located on the upper side. However, in order for the total current to remain continuous throughout the thickness of the device, a boundary condition must be imposed that expresses the passage of collected holes at the upper interface. This is precisely what the term $J_{\mathrm{p,top}}$ represents.

- **Four condition** $p_b(t_b) = N_{\mathrm{Aeff,bot}}$

Where $N_{\mathrm{Aeff,bot}}$ is the effective acceptor density at the rear, imposing an equilibrium concentration of holes at the interface with the rear electrode.

These boundary conditions are consistent with the physics of semiconductors in a tandem structure. The contribution of the perovskite subcell is limited to the hole current $J_{\mathrm{p,top}}$, because the electrons generated in the perovskite are collected by the front transparent electrode (FTO), while the holes pass through the intermediate recombination interface to be collected by the silicon subcell. This asymmetry reflects the selectivity of the contacts and the separation of currents in a series configuration. By applying these four conditions to the expressions of solutions (3.42) and (3.43), a system of linear equations is solved to determine the constants. This process requires substitution of the exponential terms and the particular term in the conditions, followed by numerical or analytical solution depending on the specific material parameters.

Once the constants have been determined, the electron and hole current densities are calculated using the drift-diffusion equations. The total current density of the silicon subcell ($J_{\mathrm{bottom}}$) is expressed as the sum of the contributions from electrons and holes, adjusted by the applied voltage. The analytical expression for $J_{\mathrm{bottom}}$ is given by:

$$
\begin{aligned}
J_{\mathrm{bottom}} = \frac{q(V_{\mathrm{bottom}} - V_{\mathrm{bi,bottom}})}{t_b}\Bigg[\mu_{\mathrm{n,bot}}\Bigg(N_{\mathrm{Deff,bot}} - \frac{G_0/D_{\mathrm{n,bot}}}{\alpha^2 - \varepsilon_0\alpha - \gamma} - \frac{s_{\mathrm{n,bot}}\left(n_{\mathrm{i,bot}} - \frac{n_{\mathrm{i,bot}}^2}{N_{\mathrm{Aeff,bot}}}\right)}{D_{\mathrm{n,bot}}(\beta_1 e^{\beta_1 t_b} - \beta_2 e^{\beta_2 t_b})} \\
+ \frac{\beta_2 e^{\beta_2 t_b}\left(N_{\mathrm{Deff,bot}} - \frac{G_0/D_{\mathrm{n,bot}}}{\alpha^2-\varepsilon_0\alpha-\gamma}\right)}{\beta_1 e^{\beta_1 t_b} - \beta_2 e^{\beta_2 t_b}} - \frac{\frac{G_0}{D_{\mathrm{n,bot}}}\frac{\alpha}{\alpha^2-\varepsilon_0\alpha-\gamma}e^{-\alpha t_b}}{\beta_1 e^{\beta_1 t_b} - \beta_2 e^{\beta_2 t_b}}\Bigg) \\
+ \mu_{\mathrm{p,bot}}\Bigg(\frac{N_{\mathrm{Aeff,bot}}}{e^{\beta_2 t_b}} + \frac{\frac{G_0}{D_{\mathrm{p,bot}}}e^{-\alpha t_b}}{(\alpha^2 - \varepsilon_0\alpha - \gamma)e^{\beta_2 t_b}} \\
- \frac{e^{\beta_1 t_b}\left(s_{\mathrm{p,bot}}\left(n_{\mathrm{i,bot}} - \frac{n_{\mathrm{i,bot}}^2}{N_{\mathrm{Deff,bot}}}\right) + J_{\mathrm{p,top}} - \frac{D_{\mathrm{p,bot}}\beta_2}{e^{\beta_2 t_b}}\left(N_{\mathrm{Aeff,bot}} + \frac{G_0/D_{\mathrm{p,bot}}}{\alpha^2-\varepsilon_0\alpha-\gamma}e^{-\alpha t_b}\right) - \frac{G_0\alpha}{\alpha^2-\varepsilon_0\alpha-\gamma}\right)}{e^{\beta_2 t_b} D_{\mathrm{p,bot}}\left(\beta_1 - \frac{\beta_2 e^{\beta_1 t_b}}{e^{\beta_2 t_b}}\right)}\Bigg)\Bigg]
\end{aligned}
\tag{3.44}
$$

Based on the individual $J$–$V$ characteristics of the top and bottom subcells, derived from analytical modelling, it becomes possible to comprehensively evaluate the performance of the monolithic tandem cell. In a series-connected tandem architecture, current continuity requires that both subcells operate at the same current density at all times. This fundamental constraint stems from the series electrical configuration, where the total current flowing through the device is limited by the subcell generating the lowest photocurrent at a given voltage. On the other hand, the total voltage developed by the tandem corresponds to the sum of the individual voltages of the subcells at this common current, reflecting the addition of the contributions of each complementary band gap [510]. In order to predict the efficiency of the tandem cell, we calculate the $J_{\mathrm{SC}}$, $V_{\mathrm{OC}}$ and $FF$ based on the following equations:

$$J_{\mathrm{Tandem}} = \min(J_{\mathrm{top}}, J_{\mathrm{bottom}}) \tag{3.45}$$

$$V_{\mathrm{Tandem}} = V_{\mathrm{top}} + V_{\mathrm{bottom}} \tag{3.46}$$

## 3.3.2 Analytical results for the tandem cell

### 3.3.2.1 Comparison of J–V characteristics and photovoltaic parameters

In order to evaluate the electrical performance of the proposed tandem cell, a MATLAB script was developed based on the analytical expressions established for the subcells. This program allows the individual current–voltage characteristics of the two subcells to be plotted and the electrical response of the tandem device in series configuration to be simulated. Figure 4.21 shows the J–V curves obtained analytically for the upper perovskite subcell, the lower silicon subcell, and the resulting tandem cell. The corresponding photovoltaic performance is summarised in Table 3.3.

Table 3.3: Performance parameters for sub-cells and tandem cells.

| **Performance parameters** | $J_{\mathrm{sc}}$ **(mA/cm$^2$)** | $V_{\mathrm{oc}}$ **(V)** | **FF (%)** | **PCE (%)** |
|---|---|---|---|---|
| Perovskite Top Cell | 22.82 | 1.11 | 50.3 | 12.75 |
| Silicon Bottom Cell | 21.51 | 0.60 | 67.99 | 8.77 |
| Perovskite/Silicon Tandem Cell | 21.51 | 1.71 | 71.63 | 26.35 |

The analysis shows that the short-circuit current of the tandem cell is limited by the silicon sub-cell, whose $J_{\mathrm{sc}}$ reaches 21.51 mA/cm$^2$, which is lower than that of the perovskite sub-cell (22.82 mA/cm$^2$). This limitation confirms that, in a series tandem configuration, the overall device is constrained by the cell generating the lowest current. On the other hand, the open-circuit voltage of the tandem cell, equal to 1.71 V, corresponds exactly to the sum of the open-circuit voltages of the two sub-cells (1.11 V for perovskite and 0.60 V for silicon), which demonstrates the accuracy of the modelling and the consistency of the series coupling. Furthermore, the fill factor of the tandem cell reaches 71.63%, which is higher than that of each of the sub-cells (50.3% for perovskite and 67.99% for silicon).

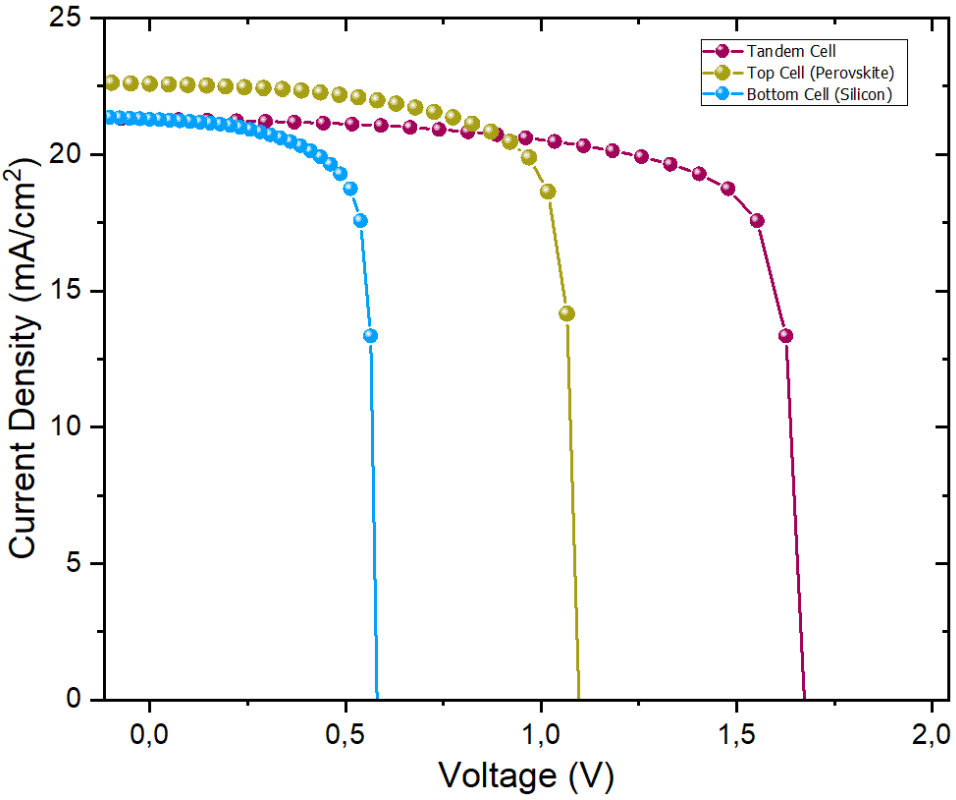



Figure 3.9: J–V characteristics for the perovskite top-cell, silicon bottom-cell, and perovskite/silicon tandem cell.

This improvement reflects more efficient charge collection and reduced resistive losses, made possible by the complementary nature of the two materials. Finally, the efficiency of the tandem cell reaches 26.35%, significantly higher than that of the individual sub-cells (12.75% for perovskite and 8.77% for silicon).

These findings confirm the value of tandem architecture, where the judicious combination of the two materials makes it possible to overcome the intrinsic limitations of single-junction cells by simultaneously exploiting the advantages of perovskite wide bandgap and silicon narrow bandgap. The combined increase in open-circuit voltage and fill factor translates directly into a substantial gain in efficiency, highlighting the relevance of the tandem concept for the next generation of high-efficiency photovoltaic cells.

#### 3.3.2.2 Influence of the thickness of the intrinsic silicon layer

The performance of a tandem cell depends heavily on the geometric and optoelectronic optimisation of each of its subcells. In particular, the thickness of the intrinsic silicon (i-Si) layer in the lower subcell plays a decisive role in the balance between photon absorption and recombination losses. Figure 3.10 illustrates the evolution of the tandem cell efficiency as a function of the thickness of this layer. It shows that efficiency reaches a maximum value of 26.35% for an optimal thickness of 1.70 $\mu$m. At this dimension, the silicon layer ensures sufficient light absorption while maintaining efficient collection of photogenerated carriers.

When the thickness is less than 1.70 $\mu$m, the cell suffers from absorption losses, thus

limiting the number of carriers generated and therefore the available photocurrent. On the other hand, for thicknesses greater than 1.70 $\mu$m, the photogenerated carriers are more susceptible to volume recombination, which results in a gradual decrease in overall efficiency. These results highlight the existence of an optimal compromise between optical absorption and electron transport in the silicon subcell. Optimising this geometric parameter is therefore essential for maximising the efficiency of perovskite/silicon tandem architectures.

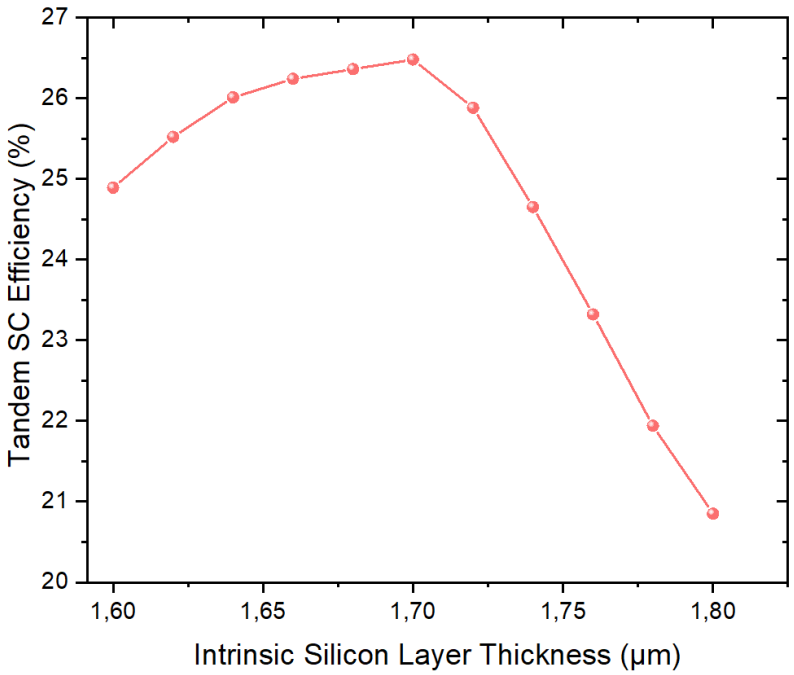



Figure 3.10: Efficiency of the tandem cell as a function of the thickness of the intrinsic silicon layer.

#### 3.3.2.3 Optimisation of the perovskite layer thickness

The thickness of the perovskite absorber in the top subcell directly influences the spectral distribution of light between the top and bottom subcells. Figure 3.11 illustrates the variation in short-circuit current of the two subcells as a function of perovskite layer thickness. It can be seen that by increasing the thickness of the perovskite from 0.2 $\mu$m to 0.4 $\mu$m, the $J_{sc}$ of the top cell increases from 21 to 24 mA/cm$^2$, reflecting better photon absorption in this layer. Conversely, the $J_{sc}$ of the silicon subcell gradually decreases from 23.5 to 20.5 mA/cm$^2$, a direct consequence of the reduction in the light flux transmitted to the bottom cell. This evolution illustrates the competition between the two subcells in the distribution of the incident solar spectrum. The equilibrium point between the two behaviours is reached at a thickness of 0.27 $\mu$m, where the two curves intersect ($J_{sc,top} = J_{sc,bottom} = 22.1$ mA/cm$^2$). This point corresponds to the matched current condition, which is essential for the optimal functioning of a monolithic tandem architecture. Indeed, current continuity requires that the tandem cell operate at the current limited by the weaker subcell, which justifies the critical importance of this thickness adjustment. Figure 3.12 confirms this result by showing the overall efficiency of the tandem cell as a function of perovskite layer thickness. The efficiency reaches its maximum

precisely at a thickness close to 0.27 $\mu$m, a value that balances effective absorption in the top subcell and sufficient photon transmission to the bottom subcell. This optimisation demonstrates that controlling the thickness of the perovskite layer is a key parameter for achieving spectral balance between the two subcells and for maximising the efficiency of the perovskite/silicon tandem architecture.

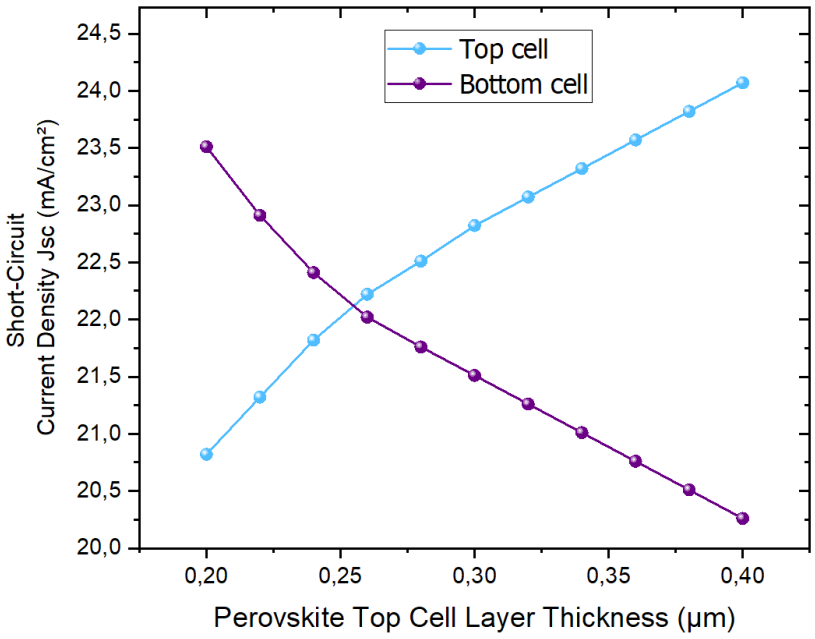



Figure 3.11: Short-circuit current of the top and bottom subcells as a function of perovskite layer thickness.

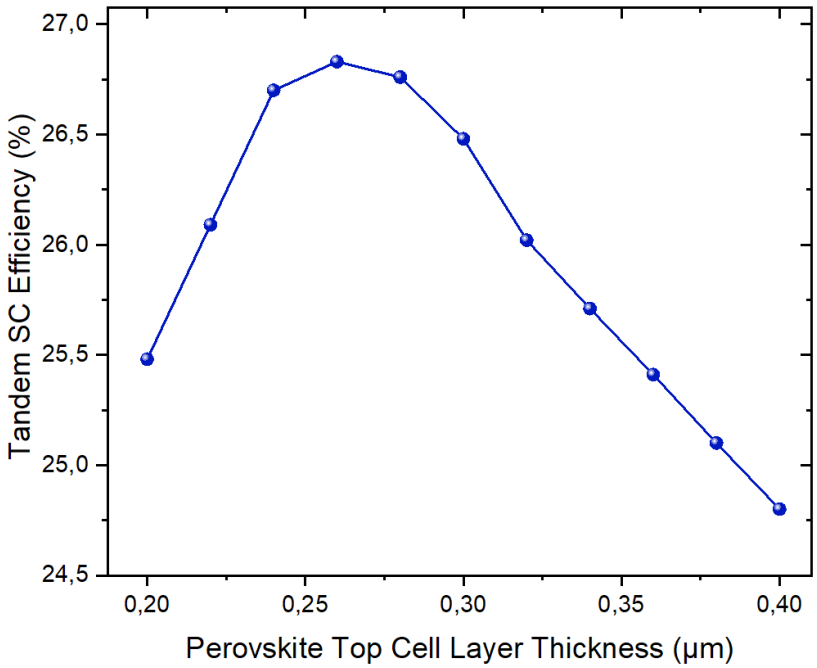



Figure 3.12: Overall efficiency of the tandem cell as a function of perovskite layer thickness.

#### 3.3.2.4 Current Matching and Performance Analysis of the Tandem Cell

Figure 3.13 shows the J–V characteristics of the perovskite and silicon subcells, as well as of the tandem cell, obtained after optimising the perovskite absorber thickness. The two subcells operate in a current-matched regime, with a common short-circuit current density of 22.1 mA/cm$^2$. This confirms that a perovskite layer thickness of 0.27 $\mu$m ensures optimal spectral sharing, which is essential for maximising the performance of a series-connected tandem architecture. The tandem cell exhibits an open-circuit voltage of 1.72 V, corresponding to the sum of the $V_{oc}$ values of the individual subcells. Furthermore, the fill factor (FF = 70.76%) highlights excellent charge extraction and an effective reduction in resistive losses.

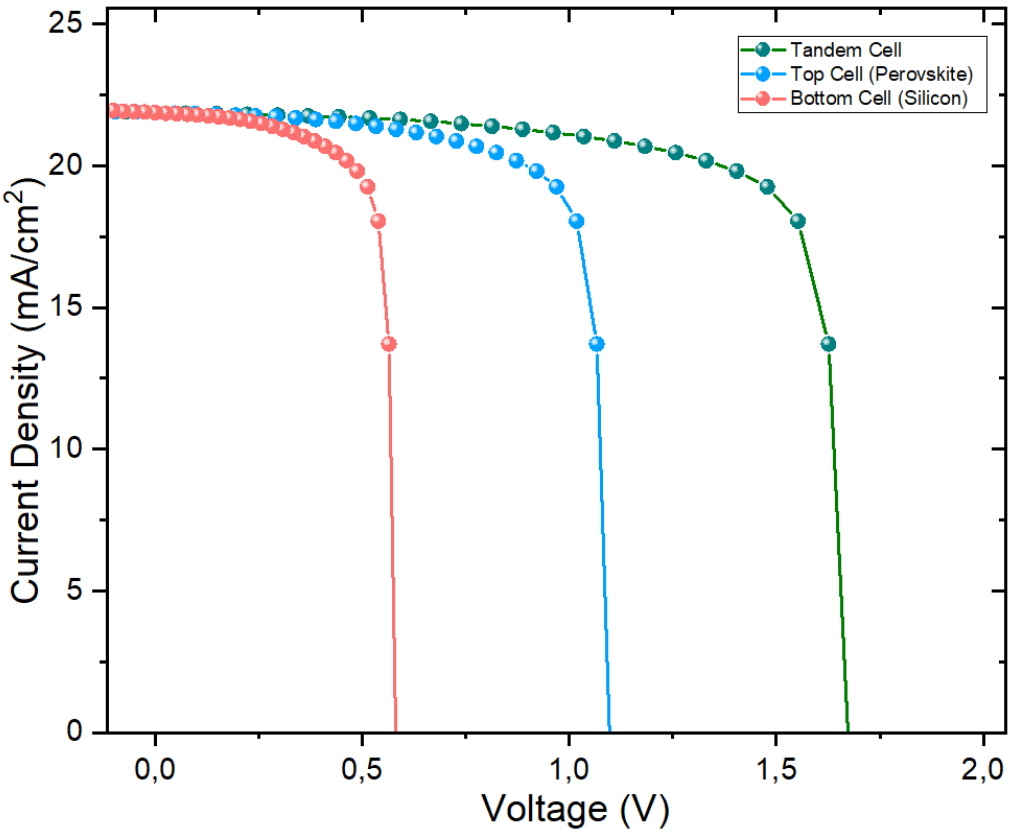



Figure 3.13: J–V curves in current-matched mode for the perovskite subcell, silicon subcell, and the optimised tandem cell.

As reported in Table 3.4, the tandem cell achieves a remarkable power conversion efficiency (PCE) of 26.83%, significantly higher than that of the individual subcells (12.35% for the perovskite top cell and 9.31% for the silicon bottom cell). This substantial improvement demonstrates that current matching, achieved through precise optimisation of the top absorber thickness, is a key factor in reaching record efficiencies in perovskite/silicon tandem solar cells.

Table 3.4: Performance parameters of the perovskite and silicon subcells and the perovskite/silicon tandem cell under current-matched conditions.

| **Performance parameters** | $J_{sc}$ **(mA/cm$^2$)** | $V_{oc}$ **(V)** | **FF (%)** | **PCE (%)** |
|---|---|---|---|---|
| Perovskite Top Cell | 22.1 | 1.10 | 50.8 | 12.35 |
| Silicon Bottom Cell | 22.1 | 0.62 | 67.94 | 9.31 |
| Perovskite/Silicon Tandem Cell | 22.1 | 1.72 | 70.76 | 26.83 |

## 3.4 Conclusion

In this chapter, a comprehensive analytical model of single-junction perovskite solar cells was developed, validated and extended to perovskite/silicon tandem cells. The approach based on continuity equations made it possible to accurately describe the mechanisms of carrier generation, transport and recombination, and to derive analytical expressions for current and voltage. The use of these models has led to the accurate reproduction of J–V curves and the determination of characteristic photovoltaic parameters. The study of the tandem device highlighted the critical role of current matching between subcells and the decisive influence of the thickness of the absorbing layers on overall performance. The results obtained show a clear gain in conversion efficiency compared to single-junction cells, thus underlining the advantage of tandem architecture in overcoming the limitations imposed by a single bandgap. These analytical developments provide a solid basis for interpreting and predicting the performance of real devices. However, in order to confirm these theoretical results and assess the impact of more complex technological parameters, a numerical simulation study is essential.

The following chapter will focus on numerical simulation using Silvaco TCAD. We will first present the modelling of a single-junction perovskite solar cell, the results of which will be validated by comparison with analytical and experimental approaches. Next, a parametric study will be conducted to analyse the impact of certain material and structural parameters on performance. Finally, the analysis will be extended to the perovskite/silicon tandem heterojunction architecture, allowing us to evaluate the potential of this advanced configuration for achieving high efficiencies.

CHAPTER

# 4

# NUMERICAL SIMULATION USING SILVACO SOFTWARE AND ANALYSIS OF RESULTS

# 4.1 Introduction

Understanding and optimising the performance of next-generation solar cells relies on a complementary combination of analytical models and numerical simulations. In the previous chapter, an analytical model was developed to accurately describe the fundamental mechanisms of carrier generation, transport and recombination in perovskite solar cells, and then extended to perovskite/silicon tandem architectures. This model made it possible to obtain analytical expressions for current-voltage (J-V) curves and to estimate characteristic photovoltaic parameters, while highlighting the importance of factors such as the thickness of the absorbing layers and the nature of the constituent materials. However, despite its relevance, such an approach necessarily relies on a number of simplifying assumptions (homogeneity of materials, ideal interfaces, limited recombination) that reduce its ability to accurately represent actual experimental and technological conditions.

In order to overcome these limitations, it is essential to use numerical simulation, which is a powerful tool for analysing and predicting the behaviour of photovoltaic devices. Unlike analytical modelling, numerical approaches allow for the integration of a large number of physical and technological parameters, doping profiles, interface defects, complex recombination phenomena, spectral dependence of absorption, and effects related to the nature of the transport layers. Silvaco TCAD software is the platform of choice in this field. With its advanced simulation modules, it offers the ability to realistically model multilayer devices such as perovskite solar cells and quantitatively evaluate the impact of design choices on overall performance.

In this chapter, we use Silvaco TCAD to supplement and validate the analytical results obtained previously. First, we present the design and simulation of a single-junction perovskite solar cell, detailing the choices of materials, parameters and simulation conditions. The results will be compared to the analytical model developed in Chapter 3 as well as to experimental data, thus allowing for cross-validation. Subsequently, a parametric study will be conducted to explore the influence of the nature of the perovskite material in particular, the comparison between a reference perovskite ($MAPbI_3$) and a Ruddlesden–Popper-type perovskite as well as the effect of the hole transport layer, notably with the replacement of Spiro-OMeTAD by other organic and inorganic materials. Finally, the most efficient configuration resulting from this optimisation will serve as the starting point for the design of a perovskite/silicon heterojunction tandem cell. We will analyse the performance of this advanced architecture in comparison with that of the single-junction cell, and we will identify the main levers for improvement to achieve high efficiencies.

# 4.2 Overview of Silvaco Software

## 4.2.1 Introduction and operating principle of the software

The development and optimisation of modern semiconductor devices now relies on the use of advanced simulation tools capable of accurately reproducing technological processes and the electrical and optoelectronic behaviour of the structures under study. Among

these tools, Technology Computer-Aided Design (TCAD) environments play a central role. They make it possible to predict the evolution of the structure resulting from the manufacturing stages (process simulation) and to evaluate the electrical and optical characteristics of the devices under different polarisation conditions (device simulation)[511]–[513].

Silvaco TCAD software (Silicon Valley Corporation) is one of the most comprehensive and widely used suites for the design, analysis and optimisation of semiconductor devices. Its integrated environment brings together several specialised modules (such as ATHENA, ATLAS, DeckBuild, DevEdit, and TonyPlot), each dedicated to a specific stage of the simulation flow, defining the geometry of the structure, mesh generation, implantation of doping profiles, resolution of physical equations, and visualisation of results[514]. This software is based on numerical resolution of the fundamental physical equations describing charge carrier transport and generation-recombination phenomena in materials. These equations mainly include:

- The Poisson equation, linking the electrostatic potential to the local charge density.
- The continuity equations for electrons and holes describe the temporal evolution of carrier densities as a function of currents, generation rates and recombination rates.
- The carrier transport equations, obtained from approximations of the Boltzmann equation, are available in different forms (drift-diffusion model, energy-balance model, hydrodynamic model) depending on the level of accuracy required.

The approach adopted consists of defining the geometry of the device, its constituent materials, its doping profiles and its boundary conditions. The simulation domain is discretised in the form of a mesh, then solved using robust numerical methods (Newton, Gummel, or hybrid iterations). At the end of this process, the simulator predicts measurable experimental quantities such as current-voltage characteristics (I–V), carrier density, internal electric field, and external and internal quantum efficiency.

### 4.2.2 Modules and tools in Silvaco TCAD

Silvaco TCAD software is an integrated platform comprising several specialised modules, each dedicated to a specific stage of semiconductor device modelling and simulation. The common environment, called **DeckBuild**, manages and coordinates the different tools and provides the interface between them. Together, they cover the entire design cycle, from virtual device fabrication to electrical and optical characterisation[515]. Figure 4.1 illustrates the simulation flow in Silvaco, showing the main input and output steps in the ATLAS module. The main modules of Silvaco TCAD are[515], [516]:

- **ATLAS**

Two- and three-dimensional device simulator based on advanced physical models. ATLAS is at the heart of the simulation process, solving fundamental Poisson, continuity and transport equations to predict the electrical, optical and electro-optical performance of solar cells. The structure of the device is described by a 2D/3D grid (mesh), defined using ASCII instructions. This discretisation is based on calculation nodes, the number of which is limited to 20,000 for each simulation, a constraint imposed by ATLAS.

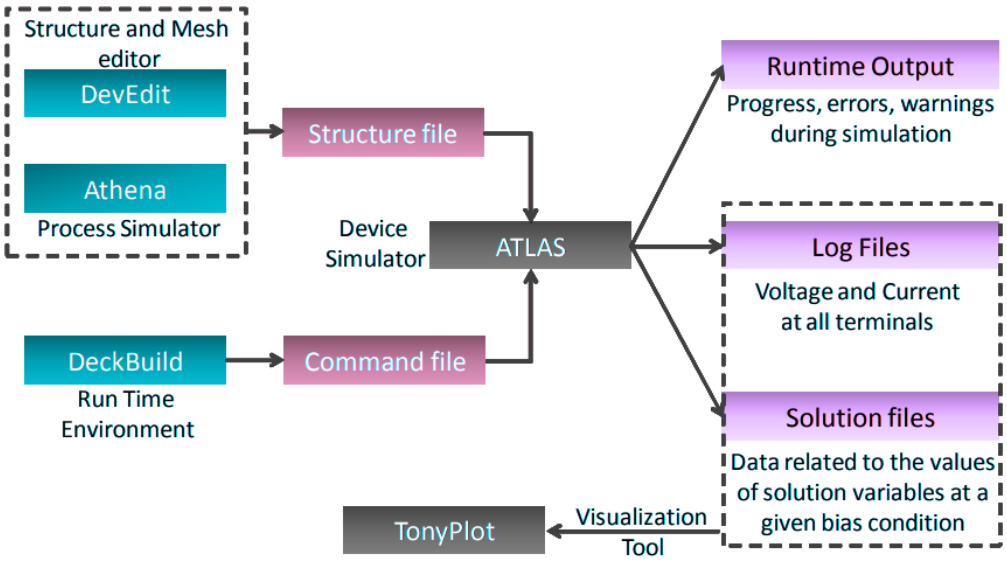



Figure 4.1: Silvaco simulation workflow displaying ATLAS inputs and outputs[516].

- **ATHENA**

Environment designed for simulating technological manufacturing processes. It virtually reproduces the key stages in device production (ion implantation, diffusion, oxidation, layer deposition, lithography, etc.). ATHENA incorporates several specialised sub-modules, such as SSuprem4 (implantation and diffusion), Elite (topographical simulation), Optolith (lithography) and Flash (advanced implantation). Although this module was not directly used in this work, it is an essential complement for linking process simulation to device simulation.

- **DeckBuild**

Interactive interface that serves as a simulation management platform. It allows editing input files, launching calculations and monitoring their progress. The interface consists of two main areas, the top part for editing commands and the bottom part for displaying intermediate results. DeckBuild also offers advanced features such as automatic DOE (Design of Experiments) generation, parameter extraction, and a rich library of examples covering various fields (electronics, optics, magnetics).

- **DevEdit**

Graphical tool for creating, editing and meshing structures. It enables the definition of a suitable grid (2D or 3D) and control of the simulation level of detail by concentrating refinement in critical areas (junctions, interfaces, thin layers). This mesh optimisation strikes a balance between accuracy and computation time, making it an indispensable tool for complex structures.

- **TonyPlot**

Programs for visualising and graphically analysing results. These programs can be used to plot simulated electrical characteristics (I–V, C–V, EQE), examine 1D profiles (carrier density, electric field) or 2D/3D maps (potential distribution, optical absorption). TonyPlot also offers advanced overlay, annotation and export features, facilitating comparison between multiple simulations and the preparation of figures for scientific reports or publications.

### 4.2.3 Cell construction using Silvaco

As part of this study, the PSC under consideration was constructed and simulated using Silvaco ATLAS software, based on an architecture that had already been experimentally validated. The device studied is based on an (FTO/$TiO_2$/$MAPbI_3$/HTL) structure, which was chosen for its proven performance and widespread adoption in the scientific community. The simulation is based on a precise definition of each layer of the device, in order to reproduce its physical, electrical and optical properties as accurately as possible.

The technological and physical parameters selected to accurately represent the cell, such as layer thicknesses, doping concentrations, dielectric constants, band gaps, electronic affinities and carrier mobilities, were carefully chosen based on previous experimental and theoretical work. More specifically, the parametric database is based on the reference experimental study conducted by I. Montoya *et al.* [475], supplemented by other contributions from the literature, in order to ensure the consistency and reliability of the simulation [517]–[525]. All of these values are summarised in Table 4.1, which is the main reference for the subsequent validation and optimisation steps.

Table 4.1: Physical and technological parameters of the PSC simulated in Silvaco ATLAS [475].

| **Parameter** | **FTO** | **$TiO_2$** | **$MAPbI_3$** | **HTM** |
|---|---|---|---|---|
| Thickness (µm) | 0.3 | 0.3 | 0.3 | 0.213 |
| Bandgap (eV) | 3.5 | 3.2 | 1.55 | 3.0 |
| Electron Affinity (eV) | 4.0 | 4.1 | 3.9 | 2.2 |
| Dielectric Permittivity ($\varepsilon_0$) | 9 | 10 | 6.5 | 3 |
| Electron Mobility ($cm^2/V \cdot s$) | 20 | 20 | 2 | $10^{-4}$ |
| Hole Mobility ($cm^2/V \cdot s$) | 10 | 10 | 2 | $10^{-4}$ |
| Donor Density $N_D$ ($cm^{-3}$) | $2 \times 10^{19}$ | $1 \times 10^{15}$ | $1 \times 10^{9}$ | – |
| Acceptor Density $N_A$ ($cm^{-3}$) | – | – | $1 \times 10^{9}$ | $2 \times 10^{19}$ |

With this approach, the PSC modelled in Silvaco ATLAS closely corresponds to a real device that has already been experimentally produced, which not only validates the relevance of the digital model adopted, but also provides a solid basis for the parametric study and performance optimization of the single-junction cell.

### 4.2.4 General simulation methodology and configuration steps

The implementation of a simulation in Silvaco ATLAS is based on a rigorous workflow, defined in an input file executed via the DeckBuild environment. This file contains a sequence of successive commands describing the device geometry, material properties, experimental conditions, and numerical methods used to solve the transport equations. Each step corresponds to a specific phase of numerical modelling and must be carefully configured to ensure the reliability of the results and their consistency with experimental data. The general structure of the simulation process is shown schematically in Figure 4.2, which illustrates the modular organization of command groups in the ATLAS software, from the definition of the initial structure to the final analysis of the device's performance.

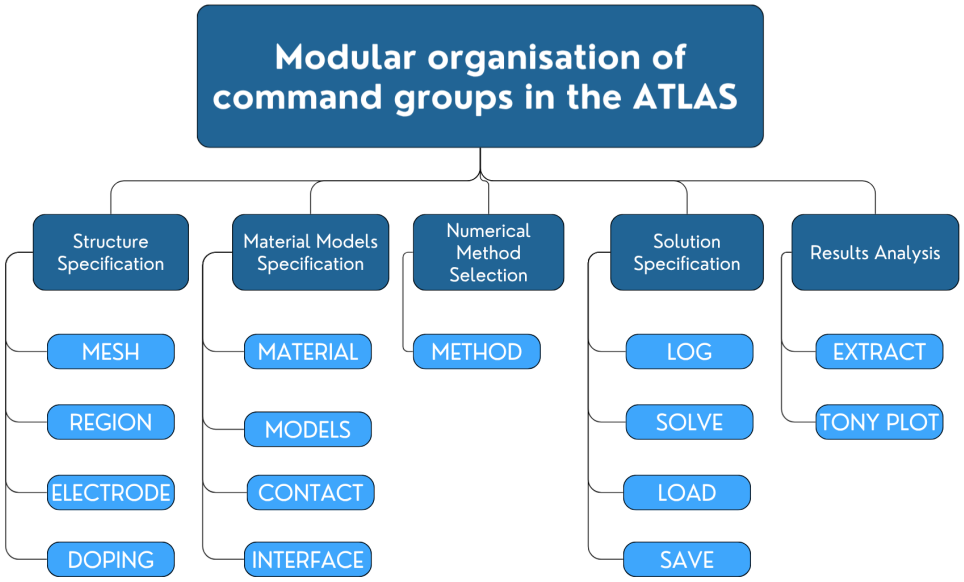



Figure 4.2: Modular organization of command groups in the ATLAS software.

1. **Mesh Definition**

The first step in numerical simulation in Silvaco ATLAS is to define the device mesh, i.e., the spatial discretizations of the structure into a set of calculation points. The quality of the mesh directly affects the accuracy of the results as well as the calculation time. A mesh that is too large may smooth out or neglect certain local physical phenomena, while a mesh that is too fine results in a considerably longer simulation time. In order to optimize this trade-off, it is common practice to apply local refinement in critical areas such as heterogeneous interfaces, junctions or thin layers, which allows for better capture of steep gradients in electrical potential or carrier density.

In Silvaco ATLAS, the mesh can be defined in two ways: the automatic method (`MESHAUTO`), which generates a mesh adapted to the geometry of the device with minimal user intervention, and the manual method (`MESH`, `X.MESH`, `Y.MESH`), which offers more precise control over the distribution of nodes, particularly at critical interfaces or thin layers. In the specific case of photovoltaic devices, characterised by a planar structure that is layered and uniform in the X direction, automatic meshing is commonly preferred because it allows the thickness of the active layers to be effectively discretised while reducing the complexity of the simulation. This is the approach that was adopted in our study. Figure 4.3 shows the automatic mesh obtained for the solar cell under study. It illustrates the spatial discretisation of the structure and highlights the distribution of nodes across the different layers, reflecting the resolution used in the numerical simulation.

2. **Region and Doping Definition**

After defining the mesh, the second step is to specify the different regions that make up the solar cell. Each region corresponds to an essential functional layer in the architecture under study. In Silvaco ATLAS, these regions are defined using the `REGION` command, which associates a material with a geometric portion of the device. At this

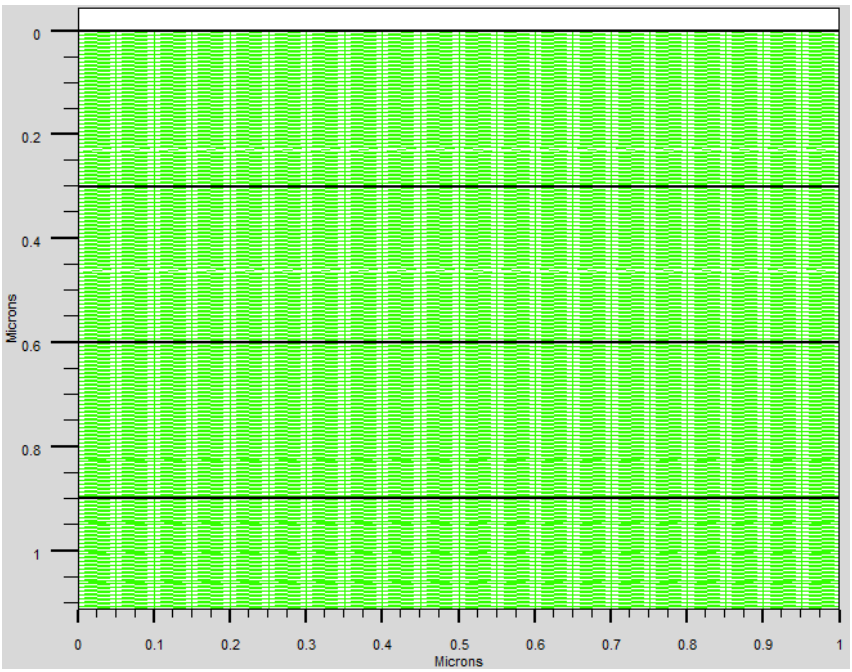



Figure 4.3: Visualisation of the automatic meshing of the simulated structure.

stage, the main parameters entered are the geometric parameters (thicknesses) and basic electrical characteristics (doping type and concentration), which are decisive factors in the distribution of carriers and the profile of electric fields in the structure. The more detailed physical properties of the materials (band gap, electron affinity, mobilities, etc.) will be defined later using the `MATERIAL` command.

In our simulation, the chosen architecture is an n-i-p type PSC composed of four main layers: a transparent conductive layer (FTO), an electron transport layer ($TiO_2$), an active absorbing layer ($MAPbI_3$), and finally a hole transport material (Spiro-OMeTAD). The device regions are defined, as shown in Listing 4.1.

Listing 4.1: Definition of regions and doping in ATLAS.

```
set FT1_thk=0.3       # thickness of FTO
set TI_thk=0.3        # thickness of ETL (TiO2)
set PVR_thk=0.3       # thickness of perovskite MAPbI3
set htm_thk=0.213     # thickness of HTM (Spiro-OMeTAD)

region num=1 user.material=FTO          bottom thick=$FT1_thk ny=40
   conductor
region num=2 user.material=TiO2         bottom thick=$TI_thk  ny=40
   donor=1e15
region num=3 user.material=Perovskite   bottom thick=$PVR_thk ny=40
   donor=1e9
region num=4 user.material=HTM          bottom thick=$htm_thk ny=30
   acceptor=1e19
```

In this configuration, the FTO is treated as a degenerate conductor, the $TiO_2$ is n-doped at a concentration of $10^{15}$ $cm^{-3}$ to ensure electronic selectivity, the perovskite is lightly n-doped ($10^9$ $cm^{-3}$) to maintain a quasi-intrinsic region favorable to photogener-

ation, and the Spiro-OMeTAD is p-doped ($10^{19}$ $cm^{-3}$) to facilitate hole extraction. In this configuration, the FTO is treated as a degenerate conductor, the $TiO_2$ is n-doped at a concentration of $10^{15}$ $cm^{-3}$ to ensure electronic selectivity, the perovskite is lightly n-doped ($10^{9}$ $cm^{-3}$) to maintain a quasi-intrinsic region favorable to photogeneration, and the Spiro-OMeTAD is p-doped ($2\times10^{9}$ $cm^{-3}$) to facilitate hole extraction. Figure 4.4 illustrates the configuration of the simulated device. Subfigure 4.4(a) shows the structure in different regions corresponding to the functional layers of the solar cell, while Subfigure 4.4(b) highlights the doping profile assigned to each of these regions.

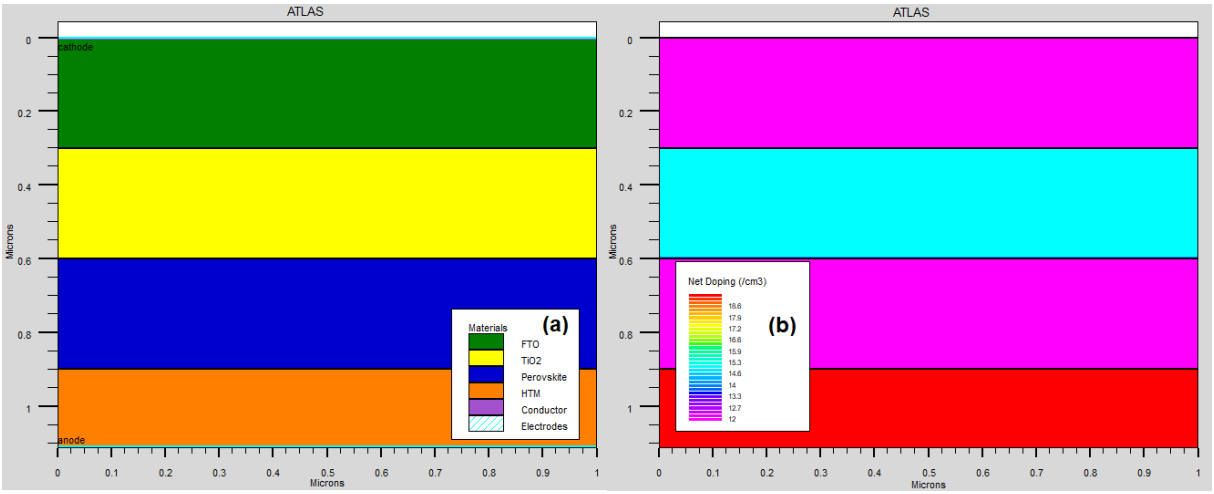



Figure 4.4: (a) Schematic representation of the regions of the perovskite solar cell defined in ATLAS; (b) Doping profile associated with the different regions.

### 3. Electrode Definition

After specifying the regions, it is necessary to define the electrodes that provide electrical contact between the device and the external circuit. This step is crucial because it determines the injection and collection of charge carriers, and therefore the overall electrical performance of the cell. In SILVACO ATLAS, electrodes are defined by the `ELECTRODE` command (abbreviated to `elec` in the script), which allows you to specify their position (at the top or bottom of the device), their type (ohmic or Schottky contact), and specific properties such as the work function or optical transparency.

In the architecture studied, the cathode is placed on the FTO layer, serving both as an electronic contact and an optical window for light entry. The anode, on the other hand, is positioned at the bottom of the device, constituting the back contact for hole collection. The practical implementation in our simulation is illustrated in Listing 4.2. This configuration reflects the typical *n-i-p* structure of perovskite cells, in which the transparent cathode (FTO) allows selective extraction of electrons, while the rear anode collects holes. Figure 4.5 below illustrates the position of the electrodes in the device stack.

Listing 4.2: Definition of electrodes in ATLAS.

```
elec num=1 name=cathode top    material=FTO y.min=0 y.max=$FT1_thk
elec num=2 name=anode   bottom
```

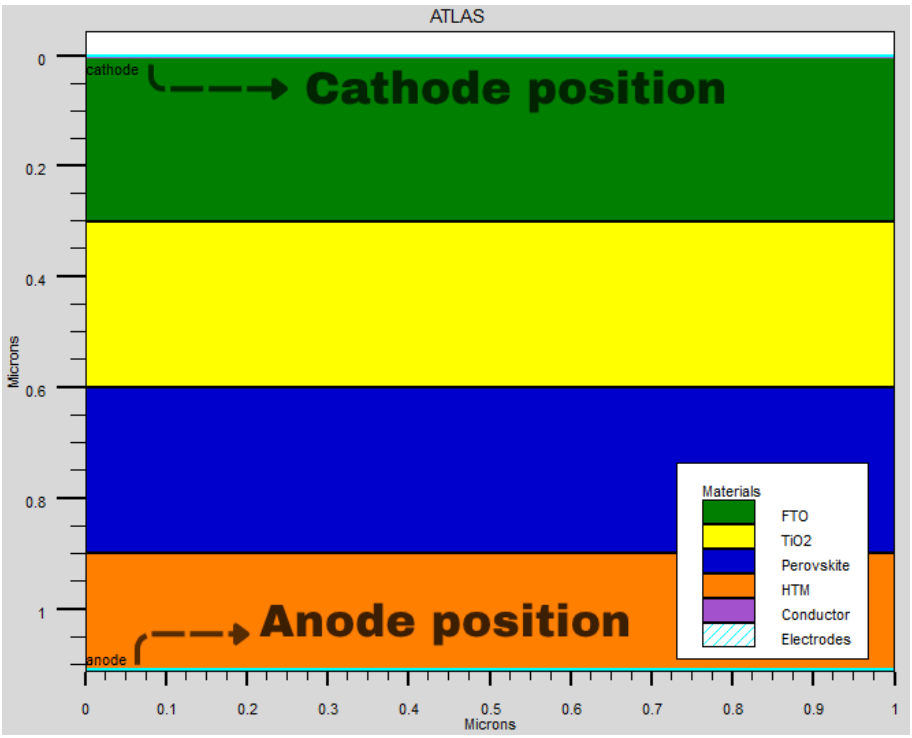



Figure 4.5: Diagram of the simulated perovskite cell structure, showing the position of the electrodes (cathode at the top on the FTO layer, anode at the bottom in rear contact).

### 4. Materials Specification

Once the geometric structure has been established (mesh, regions and electrodes), the next step is to specify the physical properties of the materials used. In Silvaco ATLAS, this is mainly done using the `MATERIAL` command, which allows the fundamental electronic parameters (band gap, electron affinity, effective state densities, dielectric permittivity, carrier lifetimes, etc.) to be introduced, as well as the optical characteristics ($n$, $k$). In order to ensure consistent and accurate modelling of optical phenomena, the spectral properties of materials are integrated using $n$–$k$ files. Their availability depends on the internal Silvaco library: when the material is already referenced in the database, it can be defined directly using the command `sopra=MAPbI3.nk`. However, if this data is not included, an external file containing the experimental optical indices must be provided manually using the command `index.file=MAPbI3.nk`.

This approach ensures that absorption and dispersion are accurately taken into account, which is essential for the reliability and robustness of the simulation results. In our simulation, $MAPbI_3$ perovskite, which acts as the active absorbing layer, was defined based on parameters from a solar cell structure that has already been experimentally produced. The aim is to accurately reproduce the observed performance using values consistent with the experimental results. The implementation adopted is illustrated in Listing 4.3.

Listing 4.3: Definition of material parameters in ATLAS.

```
material material=Perovskite user.default=organic EG300=1.55 affinity
   =3.83 NC300=1e19 NV300=1e17 permittivity=150 taup=1.e-6 taun=1.e-6
    qe.exc=0 rst.exc=0.25 lds.exc=0.01 \
taus.exc=1e-9 s.binding=2 pheff.exc=1
mobility material=Perovskite mun0=0.1 mup0=0.1 e0n.pfmob=1e4 e0p.
   pfmob=1e4
material material=Perovskite index.file=MAPbI3.nk
```

5. **Choice of Physical Models**

A key step in the simulation involves activating physical models, which describe the fundamental mechanisms of transport and recombination in devices. In ATLAS, these models are called up using the `MODELS` command and allow phenomena such as Shockley–Read–Hall (SRH) recombination, Langevin-type bimolecular recombination, exciton effects, and electric field-dependent mobility (Poole–Frenkel) to be taken into account as needed. In the specific case of perovskite-based solar cells, we have activated a set of adapted models in order to accurately reproduce the dominant mechanisms of the material. The implementation adopted for the active perovskite layer ($MAPbI_3$), which constitutes the core of the device, is illustrated in Listing 4.4.

Listing 4.4: Activation of physical models in ATLAS.

```
models material=Perovskite pfmob langevin singlet s.dissoc srh
```

This choice makes it possible to combine the consideration of Shockley–Read–Hall (SRH) recombination linked to defects, bimolecular recombination described by the Langevin model, the excitonic contribution with the formation and dissociation of singlet excitons, and the dependence of mobility on the electric field (Poole–Frenkel mobility).

6. **Numerical Methods**

The resolution of coupled equations (Poisson, continuity and carrier transport) relies on the use of robust numerical solvers. In this work, the Newton–Raphson method was preferred due to its accuracy and efficiency in handling highly non-linear systems, which are characteristic of perovskite-based solar cells. To ensure stable convergence, the `autonr` option was activated, allowing automatic adaptation of the Newton step when convergence becomes difficult. In addition, the convergence control parameters were configured as follows: `maxtrap=10` (maximum number of damping correction attempts) and `itlimit=50` (maximum number of iterations per step). This configuration ensures a compromise between stability, speed and accuracy of calculations. As an example, the implementation in the simulation script is shown in Listing 4.5.

Listing 4.5: Definition of numerical methods in ATLAS.

```
method newton autonr maxtrap=10 itlimit=50
```

7. **Simulation Conditions**

In this step, the simulation conditions were defined in order to faithfully reproduce the experimental environment. The incident illumination is modelled by a beam normal to the plane of the device, normalised to the AM1.5G solar spectrum. A spectral scan is then performed in the 0.3–1.5 µm range, discretised into 60 points, in order to describe the optical absorption and carrier generation in the active layer. The numerical solver is first initialised in dark mode, then illumination is activated to simulate operation under illumination. A wavelength scan is performed in the range 0.3–1.0 µm, with a step of 0.025 µm, thus allowing the spectral response of the device to be analysed. Finally, a voltage scan is applied in the range 0–1.5 V, in both forward and reverse modes, in order to obtain the J–V characteristics under standardised illumination and to evaluate the possible hysteresis effect.

8. **Extraction and Analysis of Results**

At the end of the simulations, the results are saved as output files, including both log files (`.log`) containing the overall curves (electrical and optical characteristics) and solution files (`.str`) describing the internal profiles of the device. The main parameters extracted are current density as a function of voltage (J–V), $V_{oc}$, $J_{sc}$, fill factor, and PCE. In addition, internal profiles such as carrier density, electric field, electrostatic potential, and optical distribution of the light field can be analysed to better understand the physical mechanisms at work. These results are visualised directly in TonyPlot/TonyPlot3D for rapid qualitative analysis, then exported to external environments (e.g., OriginLab) for advanced post-processing, including analytical adjustments, comparisons with experimental data, or optimised graphical representations.

## 4.3 Simulation and optimisation of single-junction PSC

### 4.3.1 Verification of cell operation

In order to validate the proper functioning of the cell, simulations were performed using Silvaco Atlas to analyse the energy profile of the FTO/$TiO_2$/$MAPbI_3$/HTM (Spiro-OMeTAD) structure under different experimental conditions. These simulations make it possible to track changes in conduction and valence levels in three distinct regimes: thermodynamic equilibrium, forward bias under illumination, and reverse bias under illumination. The study of these three regimes highlights the dynamics of charge carriers, energy alignment at interfaces, and the junction's ability to efficiently generate and extract photocurrent.

#### 4.3.1.1 Thermodynamic equilibrium (0 V, darkness)

Figure 4.6 shows the band diagram of the cell at thermodynamic equilibrium, i.e., in the absence of illumination and external polarisation. In this state, the energy levels of the conduction and valence bands adjust to form a profile characteristic of heterojunctions. The Fermi level appears to be almost aligned throughout the structure, reflecting overall thermal equilibrium. Marked band discontinuities are observed at the $TiO_2$/$MAPbI_3$ and

$MAPbI_3$/HTM interfaces, reflecting the potential barriers opposing holes and electrons, respectively. Although no current is generated in this state, this configuration provides the energy reference necessary to understand the cell's actual operating regimes.

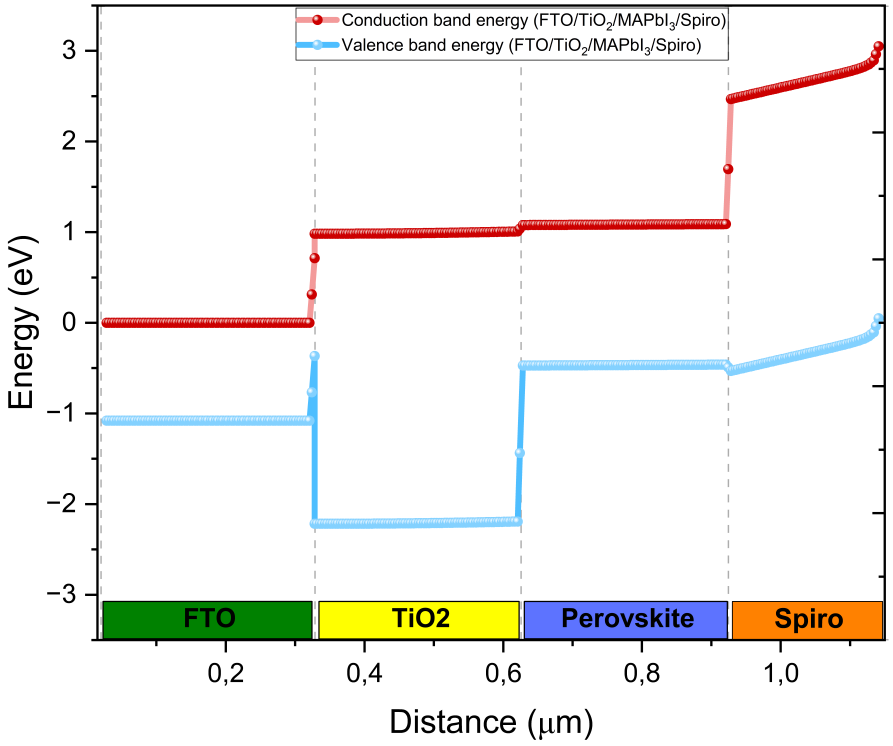



Figure 4.6: Band diagram of the cell at thermodynamic equilibrium (0 V, darkness).

#### 4.3.1.2 Forward bias under illumination

Figure 4.7 illustrates the configuration of the cell under forward bias and illumination. The absorption of photons in the $MAPbI_3$ generates electron–hole pairs. The applied voltage partially reduces the internal electric field, resulting in a flattening of the conduction and valence bands. This reduction in the potential barrier facilitates the transfer of electrons from $TiO_2$ to perovskite and holes from perovskite to HTM. The quasi-Fermi levels of electrons (in $TiO_2$) and holes (in HTM) diverge under the effect of illumination, and their difference corresponds directly to the open-circuit voltage. This regime highlights the crucial role of interfaces in charge selectivity. However, too high a voltage promotes recombination, thus limiting efficiency.

#### 4.3.1.3 Reverse bias under illumination

Figure 4.8 shows the band diagram when the cell is subjected to reverse bias under illumination. In this case, the internal electric field is strengthened, which amplifies the separation of photogenerated charges and facilitates their extraction to the selective contacts. Electrons are accelerated towards the top electrode, while holes are rapidly directed towards the bottom electrode. This configuration maximizes the short-circuit current by severely limiting recombination. Carrier transport is then dominated by the action of the electric field, ensuring efficient and near-perfect extraction of photogenerated charges.

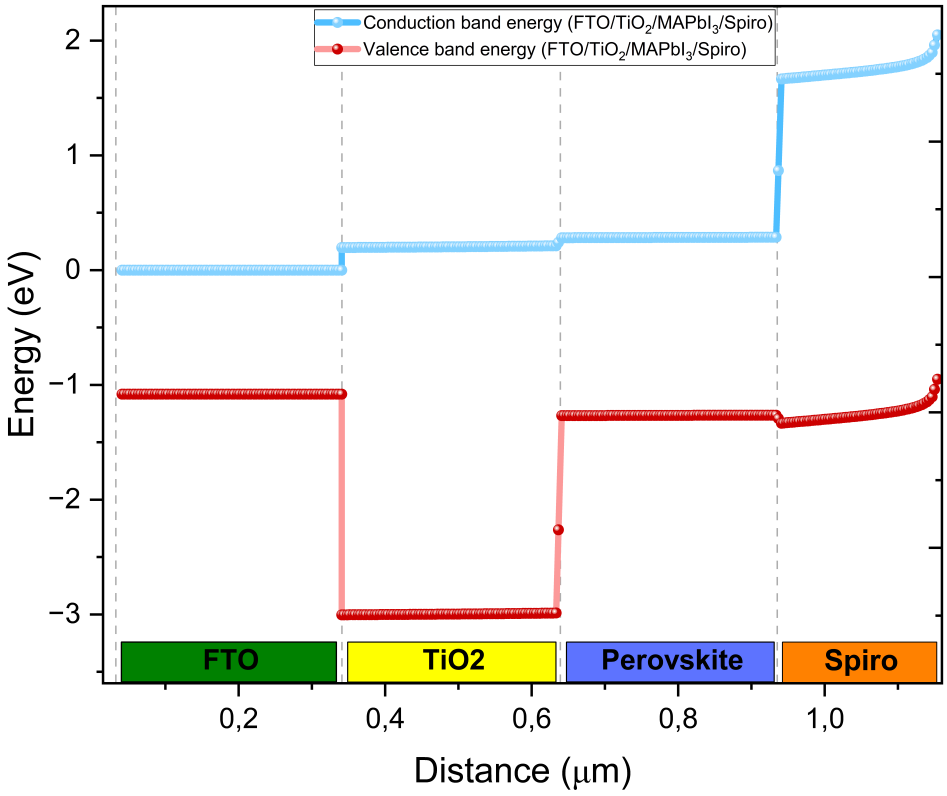



Figure 4.7: Band diagram under forward bias and illumination.

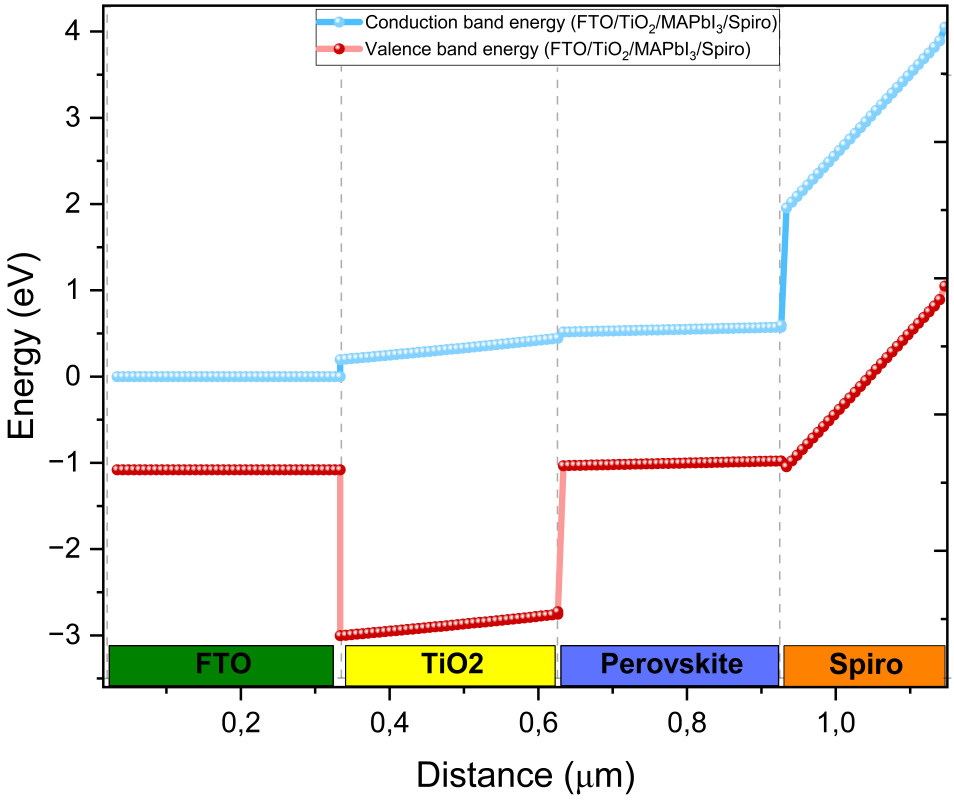



Figure 4.8: Band diagram under reverse bias and illumination.

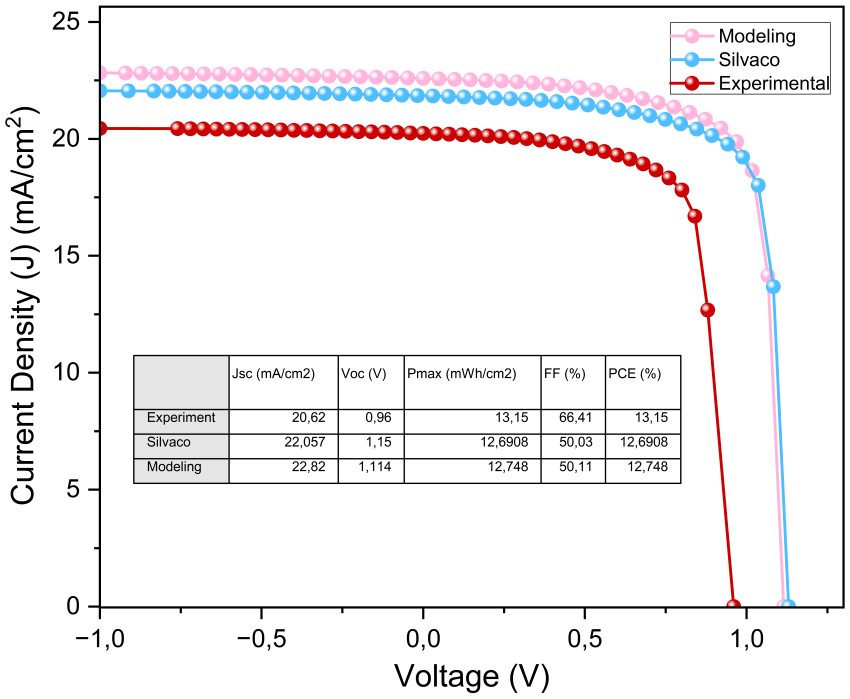
#### 4.3.1.4 General interpretation

Cross-analysis of these three regimes confirms the proper functioning of the FTO/$TiO_2$/$MAPbI_3$/HTM perovskite solar cell. At equilibrium, the interfacial barriers ensure contact selectivity. In forward bias, charge generation and extraction become possible, with a limitation imposed by recombination phenomena. Finally, reverse polarisation promotes optimal charge separation and extraction, maximising the photocurrent. These results show that Silvaco simulation accurately reproduces the expected behaviour of a perovskite photovoltaic cell.

### 4.3.2 Cross-validation of results

#### 4.3.2.1 Analysis of current–voltage characteristics (J–V)

Figure 4.9 illustrates the comparison of current–voltage (J–V) characteristic curves obtained for the PSC with an FTO/$TiO_2$/$MAPbI_3$/Spiro-OMeTAD structure, comparing three distinct approaches: numerical simulation using Silvaco Atlas, analytical modelling developed in the previous chapter, and experimental data [526], [527]. The aim of this comparison is to verify the ability of numerical models to reproduce the actual behavior of the device and to identify discrepancies related to the approximations inherent in each method. In general, the three curves show the expected profile for a photovoltaic cell: a high short-circuit current density, a quasi-flat regime where the collection of photogenerated charges remains efficient, followed by a sharp drop in current when the voltage reaches the open-circuit value. This qualitative superposition confirms that the fundamental phenomena of carrier generation, separation, and extraction are well described by the two numerical approaches, which succeed in reproducing the trends observed experimentally.




| | Jsc (mA/cm2) | Voc (V) | Pmax (mWh/cm2) | FF (%) | PCE (%) |
|---|---|---|---|---|---|
| Experiment | 20,62 | 0,96 | 13,15 | 66,41 | 13,15 |
| Silvaco | 22,057 | 1,15 | 12,6908 | 50,03 | 12,6908 |
| Modeling | 22,82 | 1,114 | 12,748 | 50,11 | 12,748 |

Figure 4.9: Comparative J–V curves between simulation, modelling, and experiments for the FTO/$TiO_2$/$MAPbI_3$/HTM PSC.

However, quantitative analysis reveals certain discrepancies. The experimental $J_{sc}$ (20.62 mA/cm$^2$) is lower than the values obtained by simulation (22.06 mA/cm$^2$ with Silvaco, 22.82 mA/cm$^2$ for the analytical model). This overestimation can be explained by the fact that models often idealise operating conditions by minimising or neglecting certain real losses, in particular non-radiative recombination, optical losses, and limitations due to internal resistances. Regarding $V_{oc}$, the experimental measurement gives 0.96 V, while simulations predict higher values (1.15 V with Silvaco, 1.114 V for analytical modelling). This discrepancy reflects an overestimation of the electronic properties of perovskite and an underestimation of recombination phenomena and interface defects in the models. The fill factor is the most contrasting parameter; measurements indicate a value of 66.41%, reflecting good charge collection quality, while simulations give values around 50%. This divergence highlights the difficulty models have in correctly integrating resistive losses (series and parallel resistance) and interfacial disorders, which strongly influence the shape of the J–V curve and therefore the final performance. As a result, the experimental efficiency reaches 13.15%, while simulations predict slightly lower values (12.69% for Silvaco, 12.74% for the analytical model). This relatively modest difference confirms that the models accurately reproduce the general trend of the device, but fail to realistically capture all the dissipative phenomena that limit actual performance.

In order to understand the origin of these discrepancies, it is necessary to examine the assumptions and limitations specific to each approach. Analytical modelling, by its very nature, relies on physical simplifications: homogeneous distributions, reduced or neglected recombination, perfect contacts, which tend to overestimate the ideal performance of the device. Numerical simulation using Silvaco, on the other hand, incorporates more comprehensive recombination models (SRH, radiative, Auger) and a detailed spatial description, but it is often based on 'optimistic' material parameters (mobilities, lifetimes, trap densities) and the assumption of ideal interfaces and ohmic contacts. The experiment, on the other hand, reflects all the real imperfections: non-radiative recombination accentuated by surface defects or grain boundaries, optical losses (reflection, parasitic absorption), as well as dynamic phenomena specific to perovskite (ion migration, hysteresis). Each of these mechanisms affects the performance parameters differently. Overall, the cross-comparison highlights satisfactory consistency between the three approaches. Simulations and analytical modelling make it possible to correctly predict the order of magnitude of photovoltaic parameters and reproduce the essential mechanisms of cell operation. However, the observed discrepancies, particularly in $V_{oc}$, $J_{sc}$, and, even more so, fill factor, serve as a reminder that numerical models are based on idealised assumptions and do not fully take into account the complexity of experimental losses. This validation thus confirms the relevance of the simulation tools used, while highlighting the need for cautious interpretation when comparing theoretical results with actual devices.

#### 4.3.2.2 Optical study: absorption and transmission spectra

Figure 4.10 shows the spectral absorption and transmission curves of a PSC with an FTO/$TiO_2$/$MAPbI_3$/Spiro-OMeTAD structure, obtained in the wavelength range between 0.2 and 1 µm. Analysis of these curves together allows the optical properties of the device to be characterised and provides a better understanding of its interaction with incident radiation, a fundamental parameter for optimising photovoltaic efficiency. Ab-

sorption, represented by the blue curve, shows high efficiency in the visible spectrum region, particularly between 0.4 and 0.8 µm, where the active material has a high absorption coefficient. This behavior is typical of halogenated perovskites, whose band gap (approximately 1.55 eV) is perfectly suited to capturing visible photons. In this range, the cell efficiently converts light into electron–hole pairs, which is the main driver of current generation. The gradual increase in absorption from $\sim$ 0.3 µm corresponds to the absorption threshold of $MAPbI_3$ and confirms the suitability of the material for exploiting the energy-rich region of the solar spectrum.

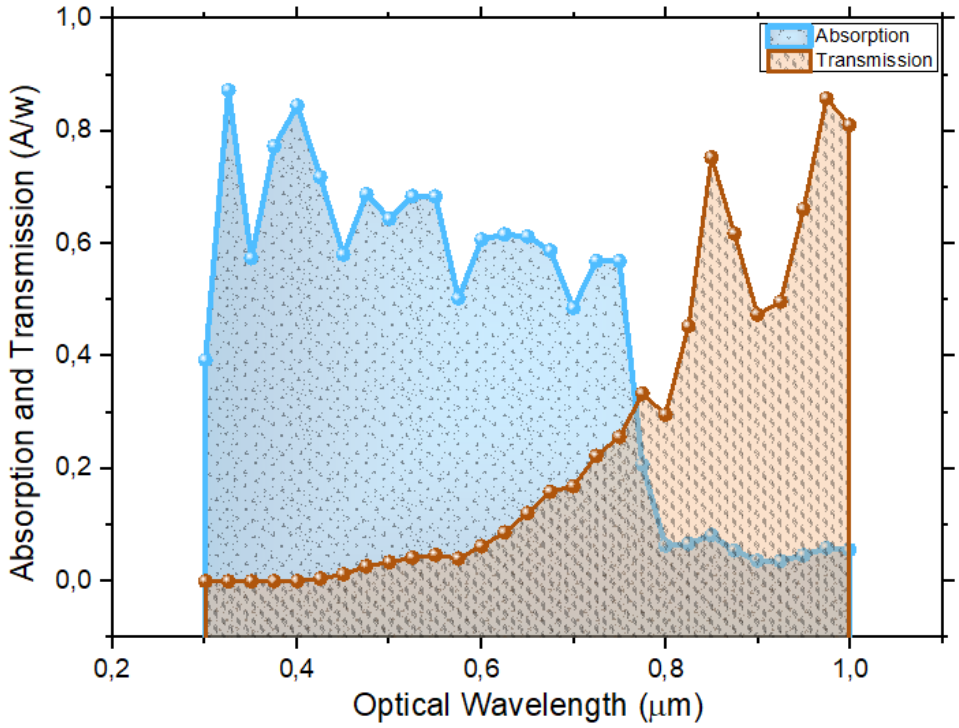



Figure 4.10: Spectral absorption and transmission curves as a function of optical wavelength for a PSC.

Conversely, transmission (brown curve) remains relatively low in the ultraviolet and visible ranges, but increases significantly for wavelengths above 0.8 µm. This change reflects the decrease in perovskite absorption efficiency in the near infrared, where incident photons do not have sufficient energy to cross the band gap. As a result, a significant portion of the light flux is transmitted through the cell without being converted into electrical energy. This phenomenon is an intrinsic limitation of single-junction cells based on $MAPbI_3$, since a significant fraction of solar radiation, particularly in the infrared, is not exploited. These results highlight the remarkable efficiency of the cell in the visible region, which represents the most energy-dense portion of the solar spectrum, but also reveal its limitations with regard to infrared. To compensate for these optical losses, several avenues for optimisation can be considered. The introduction of optical management layers (e.g., nanophotonic structures or anti-reflective layers) would increase light trapping and reduce residual transmission. In addition, the integration of infrared-absorbing materials or coupling with a complementary cell in a tandem configuration could extend the spectral response and improve overall efficiency.

#### 4.3.2.3 Comparative analysis of EQE and IQE between numerical simulation (Silvaco) and analytical model

The spectral performance of perovskite solar cells is analysed by studying both the external quantum efficiency (EQE) and the internal quantum efficiency (IQE). These two complementary indicators make it possible to distinguish, on the one hand, the cell overall capacity to convert incident photons into collected electrons (EQE) and, on the other hand, the intrinsic efficiency of the internal processes of converting absorbed photons (IQE). Figure 4.11 shows that both approaches (Silvaco simulation and analytical model) exhibit a similar overall trend, with an optimal response in the visible region (0.4–0.7 µm), where the EQE reaches approximately 50–55%. This behavior reflects the remarkable efficiency of the perovskite material $MAPbI_3$ in absorbing visible light and generating charge carriers. However, some differences appear at the extremes of the spectrum. In the ultraviolet ($\lambda < 0.3$ µm), the EQE remains low, mainly due to reflection and parasitic absorption phenomena in the transport layers (ETL/HTL). Nevertheless, the Silvaco curve rises more rapidly than that of the analytical model, which can be explained by the inclusion of complex optical losses (multiple reflections, interference, residual absorption) in the numerical simulation. In the infrared ($\lambda > 0.8$ µm), both curves show a marked decrease in EQE, due to the inability of low-energy photons to cross the perovskite band gap. Nevertheless, the Silvaco simulation shows a more gradual decline, punctuated by oscillations, while the analytical model predicts a sharper drop. These oscillations are attributed to the effects of optical interference and internal reflections incorporated into the numerical model but neglected in the simplified analytical approach.

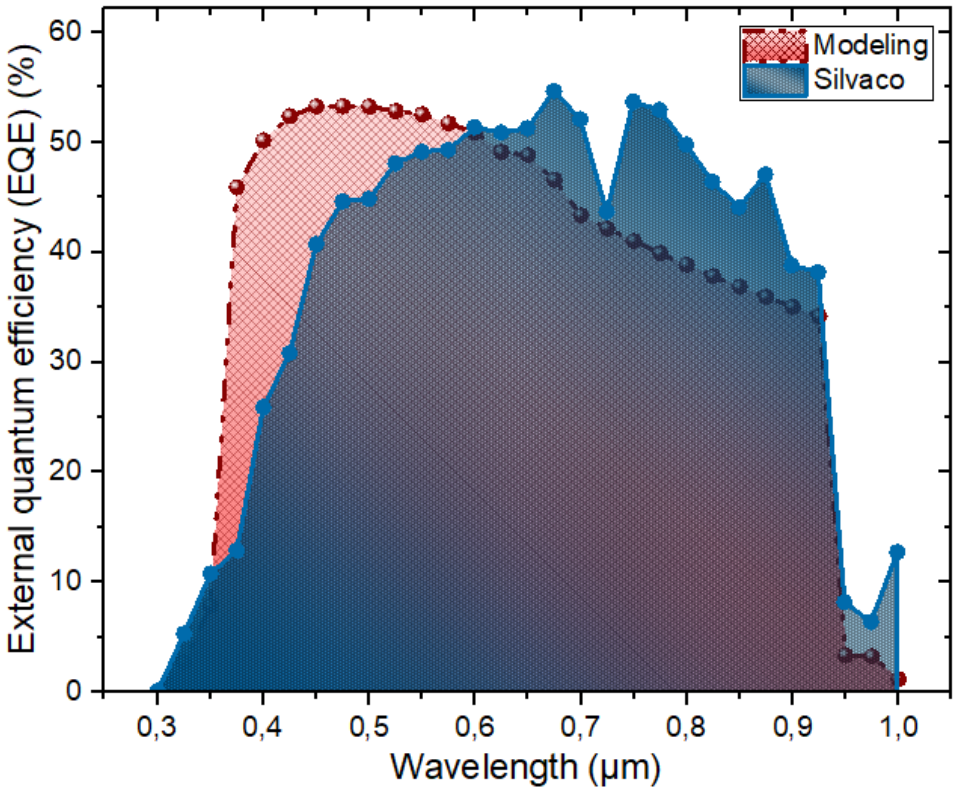



Figure 4.11: EQE of Silvaco simulation and analytical modelling for PSC.

Figure 4.12 illustrates the internal quantum efficiency (IQE), which provides information on the conversion efficiency of photons actually absorbed, regardless of initial optical losses. The two curves show a trend comparable to that of the EQE, with maximum values reaching approximately 30–35% in the visible region. This reflects the good collection of carriers generated in this spectral range, confirming the central role of $MAPbI_3$. In the ultraviolet, the Silvaco simulation shows a higher IQE value than the analytical model. This result can be explained by the consideration of interface-specific recombination and parasitic absorption in the transport layers, which are difficult to model in a simplified analytical framework. In the visible region (0.5–0.8 µm), the IQE remains high for both approaches, but the simulation retains an advantage, reflecting better consideration of carrier transport and non-radiative recombination. Finally, in the infrared ($\lambda > 0.8$ µm), the IQE drops in both cases due to the limitation imposed by the $MAPbI_3$ band gap. However, the Silvaco simulation predicts a smoother decay and oscillations due to optical interference, while the analytical model shows a more abrupt drop due to its simplification of physical phenomena.

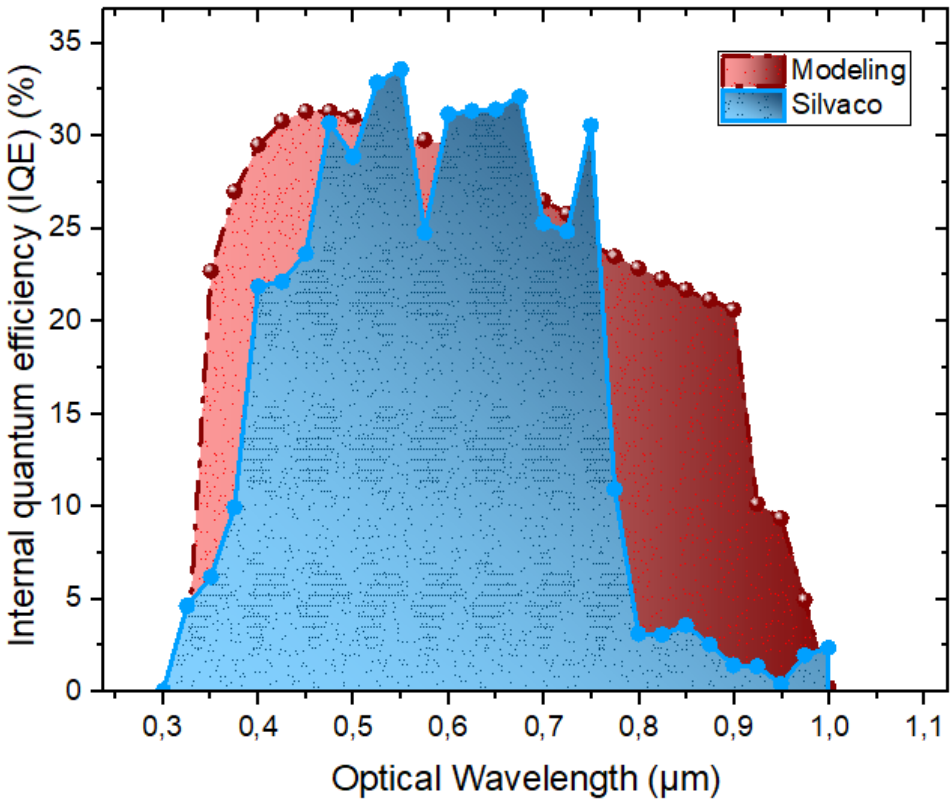



Figure 4.12: IQE of Silvaco simulation and analytical modelling for PSC.

A comparison of external and internal quantum yields shows that the two approaches agree on the overall trend, confirming the strong performance of the $FTO/TiO_2/MAPbI_3$/Spiro-OMeTAD cell in the visible range, but also its limitations in the UV and IR ranges. The differences observed are mainly due to Silvaco's more detailed consideration of complex phenomena such as parasitic optical losses in transport layers, multiple reflections at interfaces, and localised recombination. The analytical model, although simpler, captures the essence of the spectral behaviour but tends to overestimate efficiency at the extremes of the spectrum.

## 4.3.3 Parametric analysis of the impact of materials on the performance of PSC

### 4.3.3.1 Impact of Absorbing Material on the Performance of PSC

After validating the FTO/$TiO_2$/$MAPbI_3$/Spiro-OMeTAD reference cell, which was experimentally produced and reproduced by simulation in Silvaco, this section investigates the influence of replacing the absorbing material on cell performance. Although $MAPbI_3$ has achieved remarkable efficiencies over the past decade, it still has major limitations, particularly in terms of chemical and operational stability. In particular, this material is sensitive to moisture, oxygen, heat and light, leading to rapid degradation of its optoelectronic properties. These weaknesses are a major obstacle to its large-scale commercialisation.

To overcome these limitations, the integration of Ruddlesden–Popper (RP) 2D/3D hybrid structures has been proposed. The full structure is $(BA)_2(MA)_{n-1}Pb_nI_{3n-1}$, where BA = $CH_3(CH_2)_3NH_3$, MA = $CH_3NH_3$, and $n$ determines the thickness of the lead iodide perovskite layer. These structures combine the attributes of three-dimensional perovskites (greater efficiencies) and two-dimensional perovskites (greater environmental stability) by incorporating bulky organic cations (e.g., butylammonium, $BA^+$), to provide spacing between the perovskite layers while maintaining good optoelectronic performance [528]–[532]. In this study, two RP hybrids were considered as alternatives to $MAPbI_3$: $(BA)_2(MA)_2Pb_3I_8$ and $(BA)_2(MA)_3Pb_4I_{11}$. The simulation parameters used for these perovskite materials studied are summarized in Table 4.2.

Table 4.2: Physical and electrical parameters of simulated hybrid perovskite layers.

| **Parameter** | **$(BA)_2(MA)_2Pb_3I_8$ (n=3) [533], [534]** | **$(BA)_2(MA)_3Pb_4I_{11}$ (n=4) [533], [534]** |
|---|---|---|
| Bandgap (eV) | 1.75 | 1.70 |
| Electron Mobility ($cm^2/V \cdot s$) | 0.1 | 0.1 |
| Hole Mobility ($cm^2/V \cdot s$) | 0.1 | 0.1 |
| Dielectric Permittivity ($\varepsilon_0$) | 50 | 45 |

These architectures exploit bulky organic cations (e.g., butylammonium, BA) that intercalate between inorganic octahedra, providing better stability against humidity and increased passivation of surface defects. However, this structural modification can affect charge carrier transport and spectral absorption, implying a trade-off between stability and optoelectronic performance. Figure 4.13 shows the simulated J–V characteristic curves for the solar cell as a function of the absorbing material, while Table 4.3 lists the extracted electrical parameters.

The $MAPbI_3$-based reference cell has a $J_{sc}$ of 22.06 mA/$cm^2$ and a $V_{oc}$ of 1.15 V. The relatively low fill factor (50.03%) results in an efficiency of 12.69%. These results confirm the advantages of this material in terms of broadband absorption and high photogenerated carrier generation. Nevertheless, losses due to non-radiative recombination and limitations in electron transport explain the reduced FF and moderate $V_{oc}$. These limitations justify the search for more stable and efficient alternatives.

Table 4.3: Electrical parameters extracted from simulated J–V curves for different perovskite materials in the FTO/$TiO_2$/Perovskite/Spiro-OMeTAD cell.

| **Perovskite** | $J_{sc}$ **(mA/cm$^2$)** | $V_{oc}$ **(V)** | **Fill Factor (%)** | **PCE (%)** |
|---|---|---|---|---|
| $MAPbI_3$ (3D) | 22.06 | 1.15 | 50.03 | 12.69 |
| $(BA)_2(MA)_2Pb_3I_8$ | 22.65 | 1.32 | 61.08 | 18.32 |
| $(BA)_2(MA)_3Pb_4I_{11}$ | 15.54 | 1.20 | 63.14 | 11.79 |

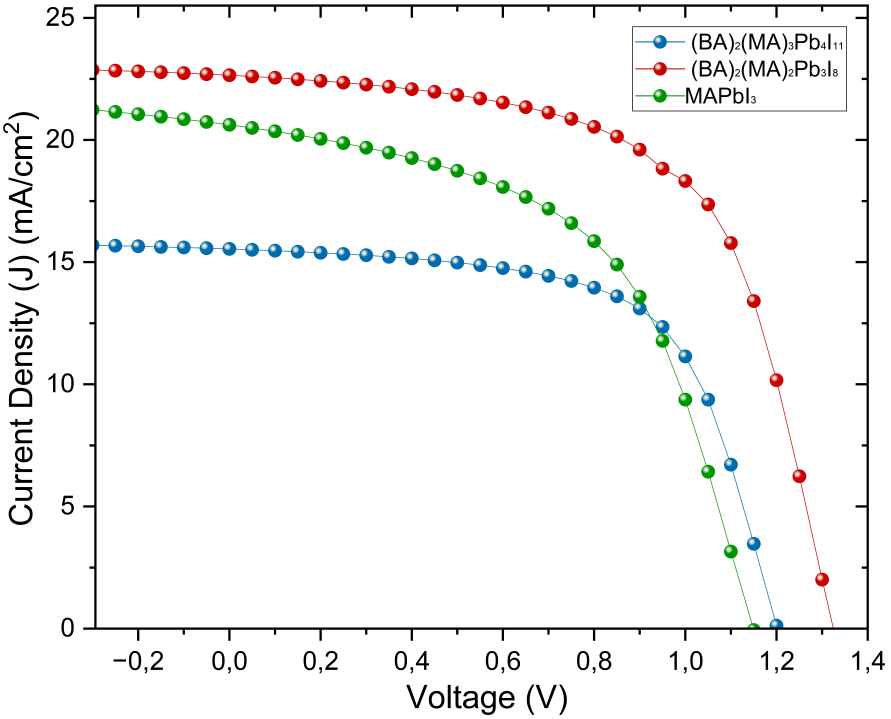



Figure 4.13: Simulated J–V curves obtained by varying the perovskite material in the reference cell FTO/$TiO_2$/Perovskite/Spiro-OMeTAD.

The introduction of the $(BA)_2(MA)_2Pb_3I_8$ structure leads to a significant improvement in cell performance. The $J_{sc}$ reaches 22.65 mA/cm$^2$, while the $V_{oc}$ increases significantly to 1.32 V. The FF also increases to 61.08%, leading to a high PCE of 18.32%. These results reflect a reduction in non-radiative recombination due to improved defect passivation and partial suppression of trap states. The presence of organic 2D layers provides protection against moisture and improves chemical stability, while preserving the continuity of the inorganic 3D structure that ensures efficient vertical charge transport. This compromise makes $(BA)_2(MA)_2Pb_3I_8$ particularly attractive for the development of stable and high-performance solar cells.

The second hybrid structure, $(BA)_2(MA)_3Pb_4I_{11}$, exhibits more mixed performance. Although the $V_{oc}$ (1.20 V) and FF (63.14%) are high, the $J_{sc}$ drops significantly to 15.54 mA/cm$^2$, limiting the overall efficiency to 11.79%. This decrease in $J_{sc}$ suggests less efficient spectral absorption and lower mobility of photogenerated carriers, leading to incomplete charge collection. The microstructure of the film, which is possibly less homogeneous and subject to increased trap density, further accentuates parasitic recom-

bination. Thus, despite increased chemical stability and good FF, this configuration suffers from optoelectronic limitations that restrict its overall efficiency.

The comparison between $MAPbI_3$ and the two 2D/3D hybrids highlights the advantages of using Ruddlesden–Popper structures. The improvement in $V_{oc}$ and FF in the case of $(BA)_2(MA)_2Pb_3I_8$ reflects a better balance between stability, defect passivation and charge transport, leading to significantly higher conversion efficiency (18.32% compared to 12.69% for $MAPbI_3$). On the other hand, the example of $(BA)_2(MA)_3Pb_4I_{11}$ highlights that optimising the crystal structure and spectral absorption remains crucial—a more stable material is not necessarily more efficient. These results illustrate the need to find an optimal compromise between environmental stability (provided by 2D layers) and electronic and optical performance (ensured by 3D continuity). With this in mind, $(BA)_2(MA)_2Pb_3I_8$ appears to be a promising candidate for next-generation perovskite solar cells, combining high efficiency and robustness against degradation.

#### 4.3.3.2 Influence of Hole Transport Layer (HTL) Doping

The HTL plays a decisive role in the overall efficiency of PSCs, as it determines both the extraction of positive carriers and the selectivity of the interfaces. The introduction of controlled doping into these layers is a commonly used strategy to modulate their conductivity, reduce ohmic losses and improve the overall efficiency of the cell. However, this doping must remain optimal, as too low a doping level results in poor conduction and limits hole transport, while excessive doping promotes trap formation and non-radiative recombination.

The comparative analysis conducted in this work focuses on several HTL materials, including reference organic compounds (Spiro-OMeTAD, PTAA, P3HT, PolyTPD, PEDOT:PSS) and promising inorganic alternatives (CuSCN, $NiO_x$). Each material was studied at different doping concentrations in order to highlight its specific behavior and identify the optimal conditions for maximising photovoltaic performance. The simulation parameters used for these various HTL materials studied are summarized in Table 4.4.

Table 4.4: Physical and electrical parameters of alternative HTLs.

| **Parameter** | **PTAA [535]** | **P3HT [535]** | **PolyTPD [536]** | **PEDOT:PSS [537]** | **CuSCN [538]** | **$NiO_x$ [539]** |
|---|---|---|---|---|---|---|
| Bandgap (eV) | 3.1 | 2.0 | 3.1 | 3.0 | 3.6 | 3.6 |
| Electron Mobility ($cm^2/V \cdot s$) | $10^{-6}$ | $10^{-4}$ | $10^{-6}$ | $10^{-6}$ | $10^{-5}$ | $10^{-5}$ |
| Hole Mobility ($cm^2/V \cdot s$) | 1.4 | 0.01 | 0.05 | 0.5 | 0.05 | 0.1 |
| Dielectric Permittivity ($\varepsilon_0$) | 3.2 | 3.5 | 3.2 | 3.8 | 8.0 | 11.0 |

- **Spiro-OMeTAD**

Spiro-OMeTAD remains the most widely used hole transport layer in perovskite solar cells, particularly in FTO/$TiO_2$/$MAPbI_3$/HTL reference architectures. Its high hole selectivity and compatibility with deposition processes make it a high-performance material. However, its relatively low intrinsic conductivity limits its effectiveness as an HTL. To compensate for this shortcoming, doping is a commonly used strategy to improve charge transport and reduce resistive losses. In this case, the impact of Spiro-OMeTAD doping was studied through simulations performed in Silvaco on an FTO/$TiO_2$/$(BA)_2(MA)_2Pb_3I_8$ /HTM cell structure. The progression of the J–V curves of the perovskite cell with Spiro-OMeTAD as the HTL material is shown in Figure 4.14, with different concentrations of doping, while Table 4.5 presents the photovoltaic parameters. The dopant concentration was gradually increased in a range from $2 \times 10^9$ to $5 \times 10^{19}$ $cm^{-3}$.

Table 4.5: Photovoltaic parameters extracted from the simulated J–V curves for each Spiro-OMeTAD doping concentration.

| **Material** | **Doping ($cm^{-3}$)** | **$J_{sc}$ ($mA/cm^2$)** | **$V_{oc}$ (V)** | **FF (%)** | **PCE (%)** |
|---|---|---|---|---|---|
| Spiro-OMeTAD | $1 \times 10^{18}$ | 23.50 | 1.33 | 71.11 | 22.15 |
| | $1 \times 10^{19}$ | 23.30 | 1.33 | 66.15 | 20.47 |
| | $5 \times 10^{19}$ | 23.23 | 1.33 | 60.31 | 18.60 |

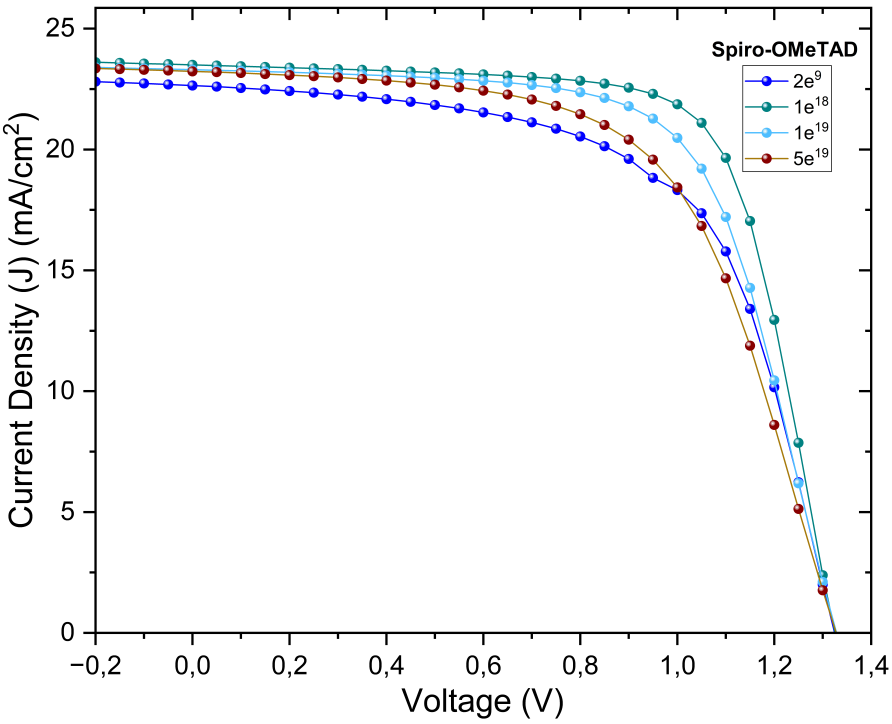



Figure 4.14: Simulated J–V curves of the PSC with Spiro-OMeTAD as the HTL at different doping concentrations.

The results obtained highlight a significant change in the photovoltaic performance of the cell as a function of the doping concentration. At low doping levels, the cell performs correctly but is limited by the low conductivity of Spiro-OMeTAD, which causes ohmic losses and restricts the fill factor. When moderate doping is introduced, particularly around $1 \times 10^{18}$ cm$^{-3}$, a notable improvement in performance is observed: the short-circuit current reaches 23.50 mA/cm$^2$, the open-circuit voltage remains at 1.33 V, the fill factor rises to 71.11%, and the conversion efficiency reaches a maximum of 22.15%. This improvement is attributed to the increased conductivity of Spiro-OMeTAD, which facilitates hole extraction and transport, reduces Joule losses, and promotes interface selectivity with perovskite.

However, when the doping concentration is increased beyond this optimal value, particularly for $1\times10^{19}$ and $5\times10^{19}$ cm$^{-3}$, a gradual deterioration in performance is observed. The fill factor decreases to 66.15% and then 60.31%, and efficiency drops to 20.47% and 18.60%, respectively. This deterioration is linked to the appearance of structural defects and additional recombination centres induced by excess dopants. In this case, the balance between improved conductivity and increased recombination is disrupted, compromising the overall efficiency of the device. Thus, the study clearly shows that doping Spiro-OMeTAD has a non-linear influence on cell performance. A moderate concentration optimises hole transport while limiting recombination, whereas excessive doping leads to a degradation of the material optoelectronic properties. These results confirm that precise control of the doping level is a key parameter for optimising both the efficiency and stability of perovskite solar cells using Spiro-OMeTAD as HTL.

- **PTAA**

Figure 4.15 and Table 4.6 illustrate the effect of doping the PTAA (Poly[bis(4-phenyl)(2,4,6-trimethylphenyl)amine]) hole transport layer on the photovoltaic performance of the FTO/$TiO_2$/$(BA)_2(MA)_2Pb_3I_8$/HTM solar cell. PTAA was chosen for its thermal and chemical stability and favorable electronic properties, making it an attractive alternative to Spiro-OMeTAD. However, its effectiveness depends heavily on the level of doping introduced, which directly influences conductivity, carrier transport, and recombination processes. The evolution of the simulated J–V curves shows that increasing the concentration of dopants in the PTAA layer leads to a gradual improvement in performance up to an optimal value. For an initial low concentration of $1\times10^{9}$ cm$^{-3}$, the fill factor reaches 65.33% and efficiency remains limited to 22.05%, mainly due to the reduced conductivity of the layer and the associated ohmic losses. When the concentration is increased to $1 \times 10^{17}$ cm$^{-3}$, a clear improvement is observed with an increase in the fill factor to 69.47% and a maximum efficiency of 23.92%. This optimisation is attributed to improved hole mobility and reduced resistive losses, thus promoting more efficient carrier transport without altering charge separation.

It is important to note that the $J_{sc}$ remains virtually constant at around 26 mA/cm$^2$ and that the $V_{oc}$ remains stable at 1.33 V for all concentrations studied. These results indicate that PTAA doping does not significantly affect photo-induced charge generation or the potential barrier at the interfaces. Performance variations are therefore mainly related to transport dynamics and hole extraction quality. However, beyond the optimum level, a deterioration in performance is observed. For higher doping levels, in the

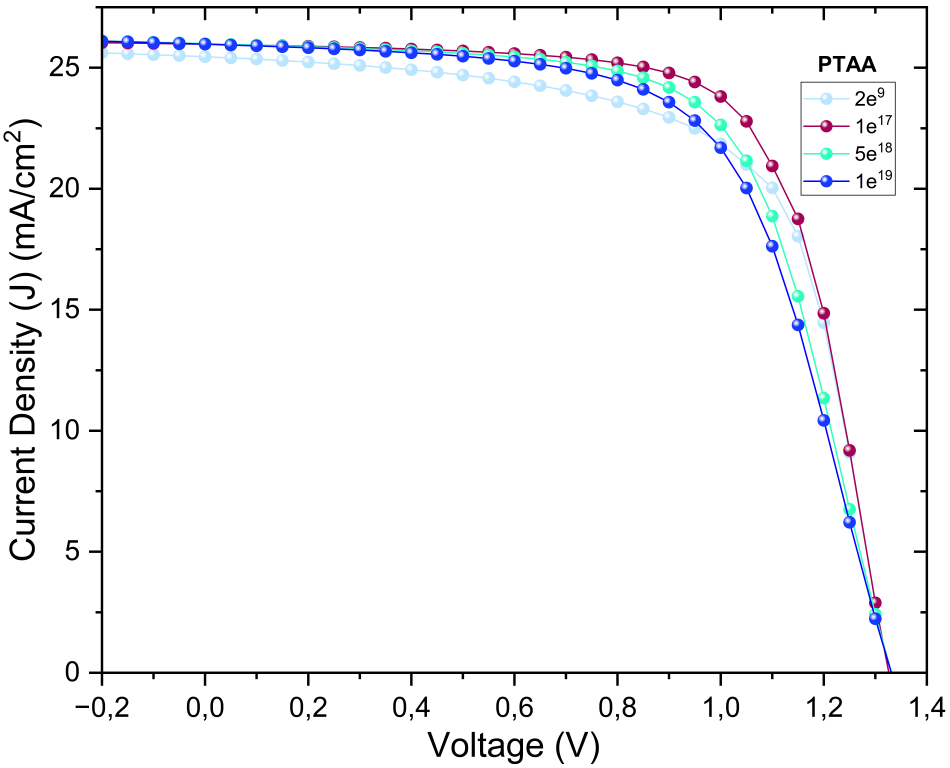



Figure 4.15: Simulated J–V curves of the PSC with PTAA as the HTL at different doping concentrations.

Table 4.6: Photovoltaic parameters extracted from the simulated J–V curves for each PTAA doping concentration.

| **Material** | **Doping** ($\mathbf{cm^{-3}}$) | $J_{sc}$ ($\mathbf{mA/cm^2}$) | $V_{oc}$ **(V)** | **FF (%)** | **PCE (%)** |
|---|---|---|---|---|---|
| PTAA | $1 \times 10^{9}$ | 25.46 | 1.33 | 65.33 | 22.05 |
| | $1 \times 10^{17}$ | 25.97 | 1.33 | 69.47 | 23.92 |
| | $5 \times 10^{18}$ | 26.00 | 1.33 | 65.42 | 22.63 |
| | $1 \times 10^{19}$ | 25.97 | 1.33 | 62.75 | 21.69 |

order of $5 \times 10^{18}$ $cm^{-3}$ and $1 \times 10^{19}$ $cm^{-3}$, the fill factor drops to 65.42% and 62.75% respectively, while efficiency decreases to 22.63% and then 21.69%. This trend can be explained by the appearance of unfavorable mechanisms such as an increase in non-radiative recombination and the formation of charge traps, linked to an excess of dopants in the polymer matrix. In conclusion, the study demonstrates that PTAA exhibits behaviour that is highly dependent on its doping level, with the existence of an optimal window that effectively balances the conductivity and selectivity of the layer. Moderate doping in the order of $1 \times 10^{17}$ $cm^{-3}$ proves to be the ideal compromise, maximising PCE without inducing additional losses. These results thus confirm the potential of PTAA as a robust alternative material to Spiro-OMeTAD, provided that its doping is carefully adjusted to ensure stable and high performance.

- **PolyTPD**

Figure 4.16 and Table 4.7 highlight the effect of doping the PolyTPD material used as a hole transport layer in the FTO/$TiO_2$/$(BA)_2(MA)_2Pb_3I_8$/HTM cell. This polymer is known for its good stability and its ability to ensure efficient extraction of positive carriers. However, as with other HTL materials, its performance depends heavily on the level of doping applied, which determines its electrical conductivity, hole mobility, and the balance of recombination processes.

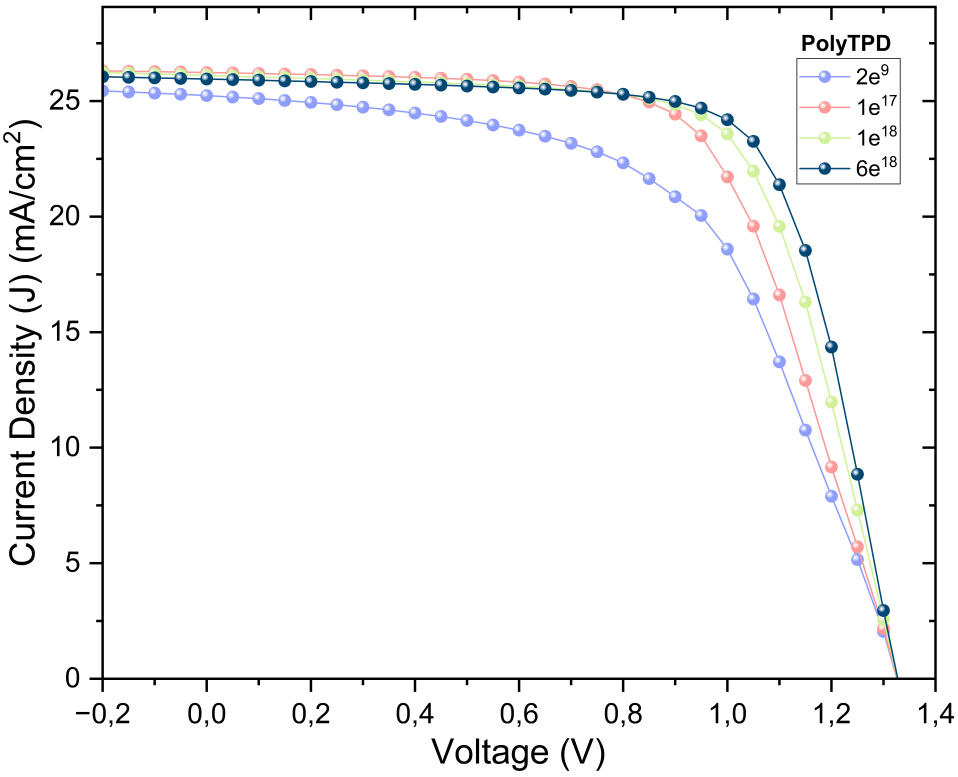



Figure 4.16: Simulated J–V curves of the PSC with PolyTPD as the HTL at different doping concentrations.

Table 4.7: Photovoltaic parameters extracted from the simulated J–V curves for each PolyTPD doping concentration.

| **Material** | **Doping** ($cm^{-3}$) | $J_{sc}$ ($mA/cm^2$) | $V_{oc}$ (V) | **FF (%)** | **PCE (%)** |
|---|---|---|---|---|---|
| PolyTPD | $1 \times 10^9$ | 25.24 | 1.33 | 56.91 | 19.04 |
| | $1 \times 10^{17}$ | 26.23 | 1.33 | 64.15 | 22.31 |
| | $1 \times 10^{18}$ | 26.11 | 1.33 | 68.06 | 23.58 |
| | $6 \times 10^{18}$ | 25.95 | 1.33 | 70.87 | 24.41 |

The evolution of the simulated J–V curves shows a clear improvement in performance as the dopant concentration increases from low values to an optimal range. For an initial concentration of $1 \times 10^9$ $cm^{-3}$, the fill factor is limited to 56.91% and the efficiency does not exceed 19.04%, reflecting insufficient charge transport and significant ohmic losses.

When the concentration reaches $1 \times 10^{17}$ cm$^{-3}$, the fill factor increases to 64.15% and the efficiency reaches 22.31%, reflecting a notable improvement in hole transport and a reduction in parasitic resistances. Optimal behavior is observed for concentrations in the range of $1 \times 10^{18}$ to $6 \times 10^{18}$ cm$^{-3}$. In this case, the fill factor rises to 70.87% and the PCE reaches 24.41%, which is higher than that obtained with PTAA. This improvement can be attributed to the increased conductivity of the doped PolyTPD layer, allowing for more efficient hole extraction and a significant reduction in resistive losses. It is important to note that the $J_{sc}$ remains stable at around 26 mA/cm$^2$ and that the $V_{oc}$ remains constant at 1.33 V, regardless of the doping level. This invariance confirms that doping does not affect the generation of photo-induced carriers or the potential barrier at the interfaces. The variations observed in overall efficiency are therefore mainly related to the transport and extraction of holes within the HTL layer. However, beyond this optimal range, performance saturation occurs, suggesting that even higher concentrations would not bring about significant improvements and could even induce counterproductive effects such as an increase in defects or non-radiative recombination. Therefore, controlled doping of PolyTPD proves to be an effective strategy for improving the performance of perovskite solar cells, with an optimal compromise around $1 \times 10^{18}$ to $6 \times 10^{18}$ cm$^{-3}$. At this level, the material combines good conductivity with preserved charge selectivity, achieving a conversion efficiency of over 24%. These results confirm the potential of PolyTPD as a promising alternative to replace or complement other HTL materials such as Spiro-OMeTAD and PTAA, while offering better operational stability.

- **P3HT**

Figure 4.17 and Table 4.8 illustrate the effect of doping the P3HT (Poly(3-hexylthiophene)) polymer, used as a hole transport layer (HTL), on the performance of the FTO/$TiO_2$/$(BA)_2(MA)_2Pb_3I_8$/HTM cell. P3HT is an organic material that has been extensively studied in photovoltaics due to its good energy affinity with perovskite and its ease of implementation. However, its intrinsic properties, in particular hole mobility, remain highly dependent on the level of doping applied. Thus, the controlled introduction of dopants improves its electrical conductivity and reduces ohmic losses, but must be carefully optimised to avoid the occurrence of non-radiative recombination.

Table 4.8: Photovoltaic parameters extracted from the simulated J–V curves for each P3HT doping concentration.

| **Material** | **Doping (cm$^{-3}$)** | $J_{sc}$ **(mA/cm$^2$)** | $V_{oc}$ **(V)** | **FF (%)** | **PCE (%)** |
|---|---|---|---|---|---|
| P3HT | $1 \times 10^9$ | 24.34 | 1.33 | 56.14 | 18.10 |
| | $5 \times 10^{16}$ | 25.16 | 1.33 | 63.09 | 21.03 |
| | $1 \times 10^{17}$ | 25.24 | 1.33 | 64.40 | 21.53 |
| | $3 \times 10^{18}$ | 25.03 | 1.33 | 69.90 | 23.10 |

Simulated J–V curves show that, for a low doping concentration ($1\times10^9$ cm$^{-3}$), the cell performance is limited, the fill factor (FF) only reaches 56.14% and the PCE remains modest at 18.10%, reflecting insufficient charge transport and high series resistance. When the concentration is increased to $5\times10^{16}$ cm$^{-3}$, the FF rises to 63.09% and the PCE

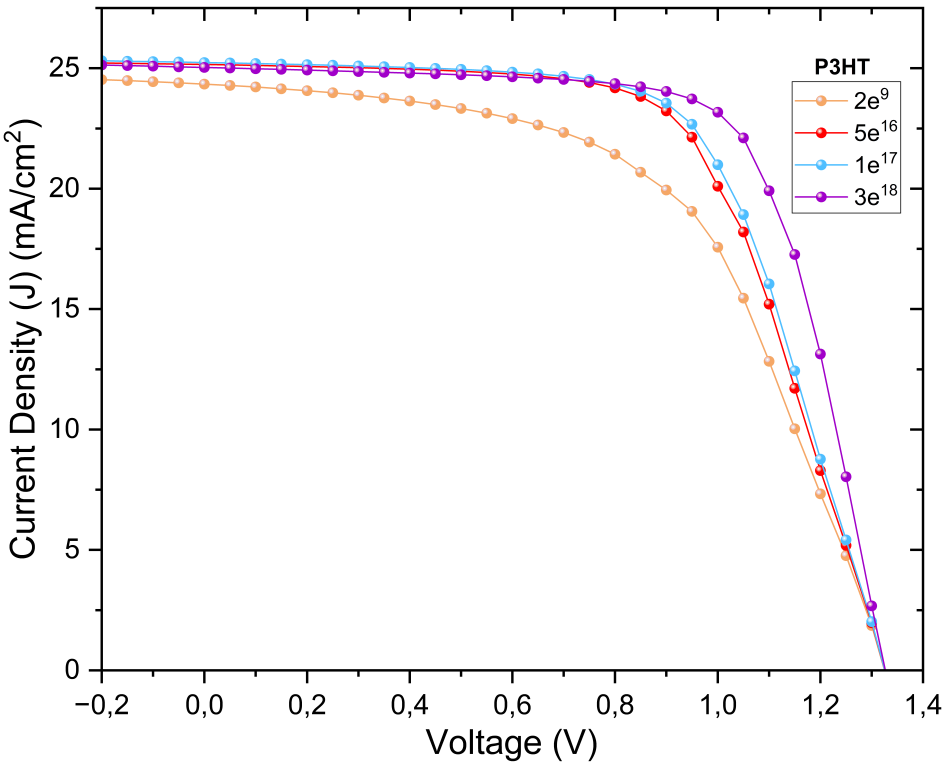



Figure 4.17: Simulated J–V curves of the PSC with P3HT as the HTL at different doping concentrations.

increases to 21.03%, reflecting a clear improvement in hole extraction and a reduction in ohmic losses. Optimal behavior is observed at an intermediate concentration of $1\times10^{17}$ $cm^{-3}$, the PCE reaches 21.53%, with an FF of 64.40%. Finally, at the highest simulated doping level ($3\times10^{18}$ $cm^{-3}$), the cell displays a record fill factor of 69.90% and a maximum efficiency of 23.10%, while maintaining a stable Jsc of around 25 $mA/cm^2$ and a constant Voc of 1.33 V. This improvement reflects the optimisation of hole transport in the doped layer, significantly reducing internal losses and stabilising photovoltaic parameters.

It should be noted that, unlike other HTLs such as PTAA or PolyTPD, the effect of doping on P3HT remains more moderate. The overall efficiency does not exceed 23%, which is still lower than the maximum values obtained with PTAA (∼23.92%) or PolyTPD (∼24.4%). Nevertheless, the stability of the Voc and the consistency of the Jsc demonstrate that doping mainly affects conduction and hole extraction, without disrupting photo-induced generation or the potential barrier at the interfaces. Overall, optimising P3HT doping allows for a gradual and measured improvement in performance, with an optimal range of around $10^{17}$ to $10^{18}$ $cm^{-3}$. These results confirm that, although P3HT offers slightly lower performance than PTAA or PolyTPD, it remains an attractive alternative for HTL layers due to its ease of deposition, low cost and compatibility with large-scale manufacturing processes.

- **PEDOT:PSS**

Figure 4.18 and Table 4.9 illustrate the effect of doping PEDOT:PSS (Poly( 3,4-ethylenedioxythiophene):Poly(styrene sulfonate)), used as a hole transport layer (HTL),

on the performance of the FTO/$TiO_2$/$(BA)_2(MA)_2Pb_3I_8$/HTM cell. Although PEDOT:PSS is widely used in organic and hybrid solar cells due to its easily handled aqueous solution and compatibility with low-cost deposition processes, it generally suffers from limited intrinsic conductivity and reduced stability with respect to moisture and oxygen. The introduction of controlled doping therefore appears to be an effective strategy for increasing the conductivity of this layer, reducing ohmic losses and improving hole extraction, while modulating interfacial interactions with perovskite.

Table 4.9: Photovoltaic parameters extracted from the simulated J–V curves for each PEDOT:PSS doping concentration.

| **Material** | **Doping** ($cm^{-3}$) | $J_{sc}$ ($mA/cm^2$) | $V_{oc}$ (V) | **FF** (%) | **PCE** (%) |
|---|---|---|---|---|---|
| PEDOT:PSS | $1 \times 10^9$ | 20.15 | 0.98 | 44.01 | 8.65 |
| | $1 \times 10^{17}$ | 21.65 | 1.07 | 53.51 | 12.35 |
| | $1 \times 10^{19}$ | 22.11 | 1.18 | 56.12 | 14.68 |
| | $1 \times 10^{21}$ | 22.32 | 1.29 | 57.73 | 16.66 |

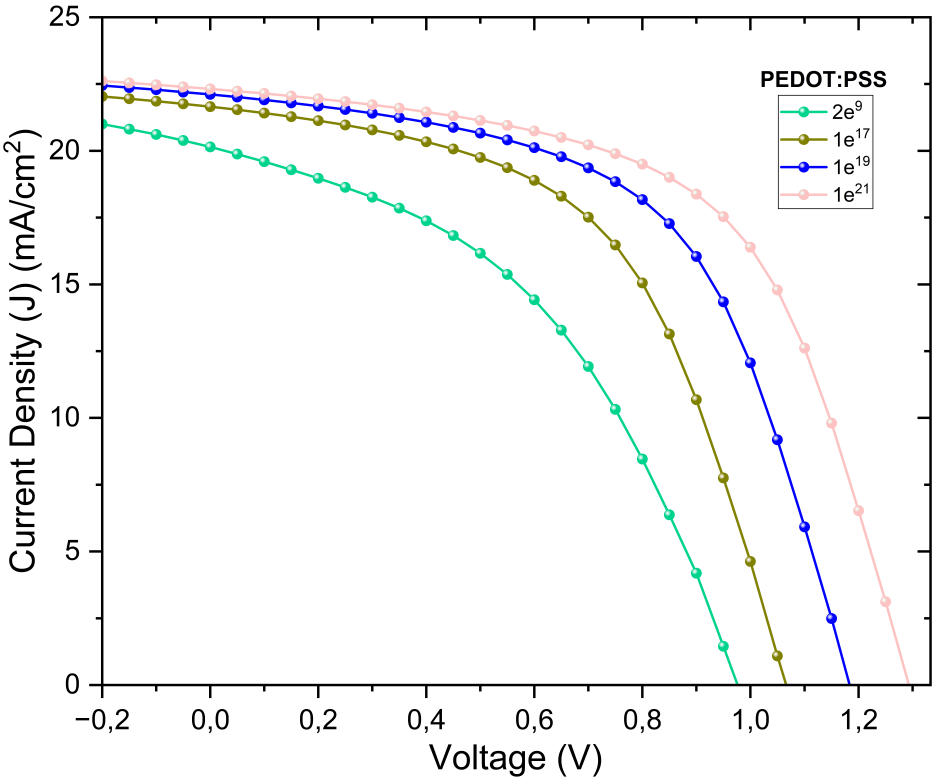



Figure 4.18: Simulated J–V curves of the PSC with PEDOT:PSS as the HTL at different doping concentrations.

Simulation results show that at low doping concentrations ($1\times10^9$ $cm^{-3}$), cell performance is modest, with an EPC of only 8.65%, a fill factor limited to 44.01% and a Voc of 0.98 V. These values reflect inefficient hole extraction and strong recombination at the interfaces. However, as the dopant concentration increases, a clear improvement in performance is observed. For an intermediate concentration of $1\times10^{17}$ $cm^{-3}$, the Jsc

reaches 21.65 mA/cm$^2$, the Voc rises to 1.07 V, and the PCE climbs to 12.35%. This trend becomes more pronounced at higher doping levels, at $1\times10^{19}$ cm$^{-3}$, the cell has a PCE of 14.68%, with an FF of 56.12% and a Voc of 1.18 V, confirming that doping promotes the reduction of ohmic losses and improves the selectivity of the HTL/perovskite interface. The best performance is obtained for the highest concentration tested, $1\times10^{21}$ cm$^{-3}$, where the PCE reaches 16.66%. This improvement results from a combination of factors, a gradual increase in Voc (up to 1.29 V), a moderate improvement in Jsc (22.32 mA/cm$^2$) and an increase in FF (57.73%). These results demonstrate that doping PEDOT:PSS mainly contributes to optimising conduction and charge separation, limiting recombination losses and enhancing carrier extraction efficiency.

However, it should be noted that, even at its optimal level, PEDOT:PSS remains less efficient than other HTLs such as Spiro-OMeTAD or PolyTPD, due to its inherently lower Voc potential and limited stability. Thus, while doping significantly improves performance, the gap with high-performance transport layers remains significant. The investigation of PEDOT:PSS highlights the essential role of doping in improving the performance of perovskite cells, but also reveals the intrinsic limitations of this material. Its moderate efficiency, combined with often lower stability, suggests that it remains better suited to low-cost devices and large-area processes than as a reference solution for high-performance perovskite cells.

- **CuSCN and $NiO_x$**

Inorganic materials such as CuSCN (cuprous thiocyanate) and $NiO_x$ (nickel oxide) are attracting growing interest as hole transport layers (HTL) for perovskite solar cells, mainly due to their chemical stability, high optical transparency and compatibility with low-temperature deposition processes. Unlike organic HTLs, these materials have more limited hole mobilities and less ideal interfaces with perovskite, which can limit their performance. Nevertheless, controlled doping is a promising strategy for improving their electrical conductivity, optimising carrier extraction and limiting ohmic losses. Figure 4.19 shows the simulated J–V curves for the FTO/$TiO_2$/$(BA)_2(MA)_2Pb_3I_8$/HTM solar cell using CuSCN (Fig. 4.19a) and $NiO_x$ (Fig. 4.19b) as HTL, under different doping concentrations. The corresponding photovoltaic performance is summarised in Table 4.10. In both cases, a gradual improvement in $J_{sc}$, $V_{oc}$ and fill factor is observed as the doping concentration increases, reflecting improved charge extraction and reduced interfacial recombination.

For CuSCN, a clear improvement in performance is observed with increased doping. The Jsc increases from 24.39 mA/cm$^2$ at low doping ($1\times10^9$ cm$^{-3}$) to 26.84 mA/cm$^2$ at a doping of $5\times10^{19}$ cm$^{-3}$. At the same time, the Voc increases from 0.99 V to 1.23 V, indicating a reduction in recombination losses and more efficient separation of photogenerated charges. The fill factor increases from 44.13% to 56.80%, reflecting a decrease in internal resistive losses and better conduction in the layer. As a result, the PCE increases from 10.60% to 18.75%. However, beyond this doping level, the improvement tends to stabilise, suggesting that excessive concentrations of dopants can induce undesirable phenomena such as charge trap formation or additional non-radiative recombination.

$NiO_x$ follows a similar trend, although its overall performance remains slightly lower than that of CuSCN. The current density Jsc increases from 21.73 mA/cm$^2$ at low doping

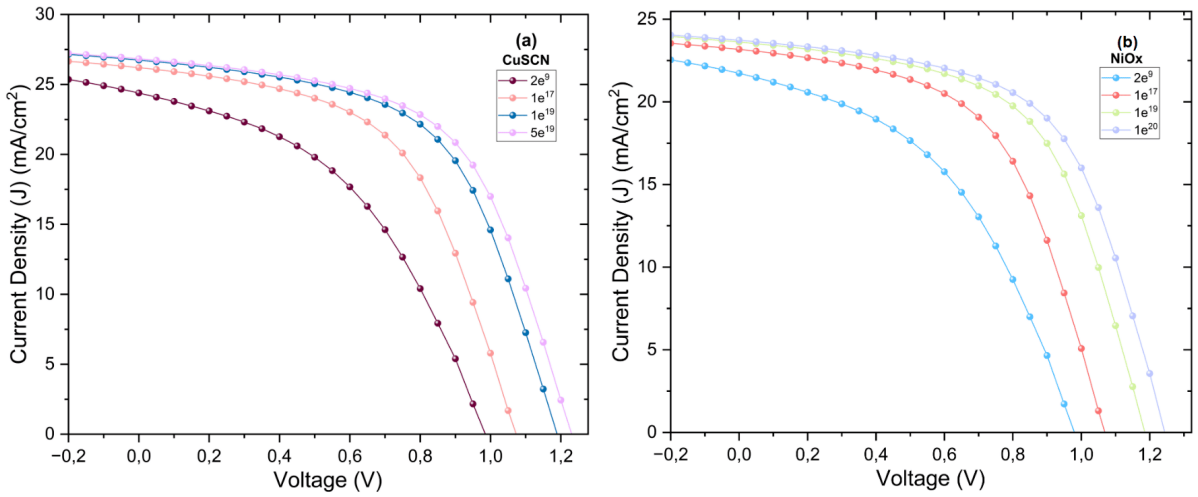



Figure 4.19: Simulated J–V curves of the PSC with CuSCN (a) and $NiO_x$ (b) as the HTL at different doping concentrations.

Table 4.10: Photovoltaic parameters extracted from the simulated J–V curves for each CuSCN and $NiO_x$ doping concentration.

| **Material** | **Doping ($cm^{-3}$)** | $J_{sc}$ **($mA/cm^2$)** | $V_{oc}$ **(V)** | **FF (%)** | **PCE (%)** |
|---|---|---|---|---|---|
| CuSCN | $1 \times 10^9$ | 24.39 | 0.99 | 44.13 | 10.60 |
| | $1 \times 10^{17}$ | 26.20 | 1.07 | 53.59 | 15.06 |
| | $1 \times 10^{19}$ | 26.74 | 1.19 | 56.30 | 17.90 |
| | $5 \times 10^{19}$ | 26.84 | 1.23 | 56.80 | 18.75 |
| $NiO_x$ | $1 \times 10^9$ | 21.73 | 0.98 | 44.45 | 9.46 |
| | $1 \times 10^{17}$ | 23.17 | 1.07 | 54.36 | 13.46 |
| | $1 \times 10^{19}$ | 23.62 | 1.19 | 57.10 | 15.99 |
| | $1 \times 10^{20}$ | 23.73 | 1.24 | 57.97 | 17.10 |

($1\times10^9$ $cm^{-3}$) to 23.73 $mA/cm^2$ at a concentration of $1\times10^{20}$ $cm^{-3}$. The Voc also increases from 0.98 V to 1.24 V, confirming a gradual reduction in recombination at the interfaces. The fill factor improves significantly, from 44.45% to 57.97%, leading to a marked increase in PCE, which reaches a maximum of 17.10%. As in the case of CuSCN, a saturation effect is observed at the highest concentrations, suggesting an intrinsic limit to the benefit provided by doping.

The comparative analysis between CuSCN and $NiO_x$ highlights several key points. Both materials benefit significantly from doping, but their maximum performance remains lower than that obtained with doped organic HTLs such as Spiro-OMeTAD or PTAA. CuSCN achieves a slightly higher PCE than $NiO_x$, which can be attributed to slightly higher hole mobility and better interfacial compatibility with the perovskite layer. However, $NiO_x$ has the advantage of remarkable mechanical and chemical robustness, making it a promising candidate for stable and durable devices. In both cases, moderate doping appears to be the most effective strategy for optimising performance, while an excess of dopants leads to increased recombination and limits efficiency gains.

## 4.4 Simulation of the Perovskite/Silicon Heterojunction (HJT) Tandem Cell

### 4.4.1 Selection of the Highest Performing Perovskite Subcell

In light of the results obtained in the previous section, the optimised perovskite sub-cell, configured according to the (FTO/$TiO_2$/$(BA)_2(MA)_2Pb_3I_8$/PolyTPD) architecture, was selected to form the top cell of the tandem architecture studied. This structure was chosen because of its harmonious combination of electrical performances, which make it a particularly promising candidate for integration into a multi-junction device.Indeed, this cell has a high short-circuit current density, reflecting efficient absorption of the solar spectrum in the visible region and abundant generation of photogenerated carriers. It is also distinguished by a stable open-circuit voltage, reflecting the good crystalline quality of the perovskite and the control of recombination phenomena at the interfaces, ensuring efficient charge separation. Added to this is a competitive fill factor, which indicates reduced resistive losses and optimised charge extraction.

All of these parameters result in remarkable power conversion efficiency in a simple junction configuration, confirming the relevance of this architecture as a solid basis for advanced design. Furthermore, the perovskite used in this structure has a wide bandgap, which is a major advantage for tandem integration. This characteristic not only allows high-energy photons (in the ultraviolet and visible ranges) to be exploited efficiently, but also enables a significant portion of the light flux to be transmitted to the lower subcell. This spectral complementarity paves the way for better use of the entire solar spectrum and helps to overcome the efficiency limit imposed on single-junction cells by the Shockley–Queisser model.Thus, the (FTO/$TiO_2$/$(BA)_2(MA)_2Pb_3I_8$/PolyTPD) cell, due to its intrinsic photovoltaic performance and optical compatibility with a silicon sub-cell, is a rational and strategic choice for the development of a high-performance perovskite/silicon tandem device.

### 4.4.2 Tandem Architecture Design

The tandem architecture studied is based on the combination of an upper perovskite subcell and a lower heterojunction silicon (HJT) subcell, forming a multi-junction device capable of synergistically exploiting the entire solar spectrum. The complete structure is shown in Figure 4.20, highlighting the stacking of the different layers and the intermediate ZnO layer that provides the interface between the two sub-cells. The presence of this ZnO layer is a key element of the design, due to its electronic, optical and technological properties, which are particularly well suited to a tandem configuration. Electronically, ZnO acts as a selective electron transporter, promoting their efficient extraction from the perovskite subcell, while simultaneously blocking holes. This selective role reduces interfacial recombination, ensuring optimal separation of photogenerated carriers. Optically, ZnO is distinguished by its wide energy gap (3.3 eV) and high transparency in the visible and ultraviolet ranges, which limits losses due to parasitic absorption and ensures efficient transmission of incident light to the silicon subcell. Finally, from a technological standpoint, ZnO is remarkably compatible with low-temperature deposition processes,

thus preserving the structural and electronic integrity of perovskite layers, which are particularly sensitive to heat.

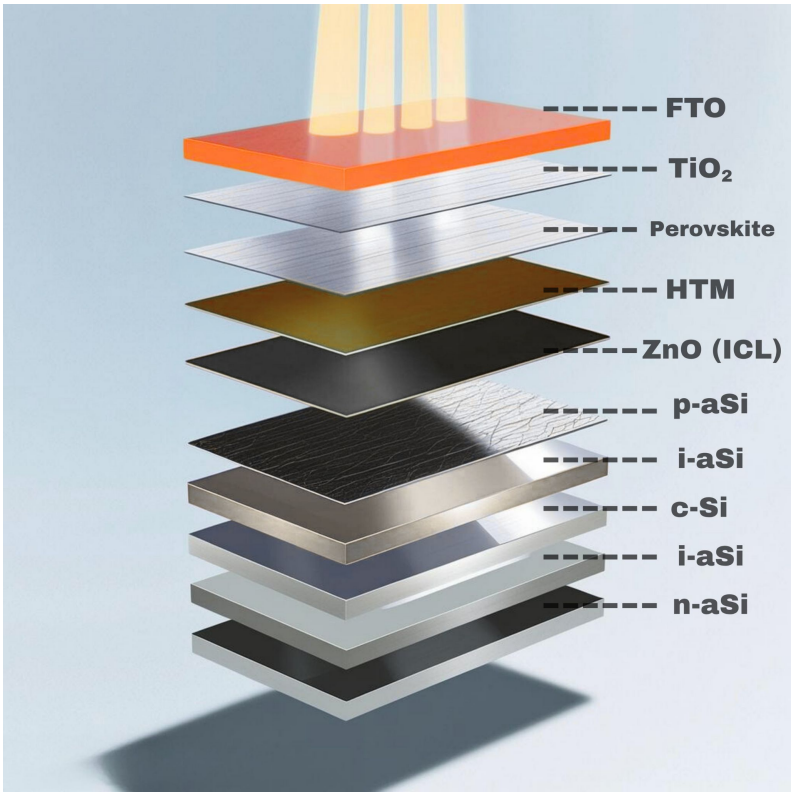



Figure 4.20: Device structure of the tandem Perovskite/Si HJT solar cell.

The lower subcell consists of a heterojunction silicon (HJT) device, whose architecture combines the advantages of crystalline silicon (c-Si) and amorphous thin films. It comprises a high-quality crystalline silicon substrate covered with a thin intrinsic layer of hydrogenated amorphous silicon (a-Si:H-i), which is itself framed by two p- and n-doped layers (a-Si:H-p and a-Si:H-n). This design ensures effective passivation of surface defects, significantly reducing recombination at the interfaces, while ensuring fast and selective charge transfer. This configuration is also distinguished by its high efficiency potential and operational stability, making it the technology of choice for the lower part of the tandem.

The physical and electrical parameters used to simulate this architecture are summarised in Table 4.11. They include band gap values, electron and hole mobilities, and the dielectric constants of the different layers (*ZnO*, *a-Si:H*, *c-Si*). The choice of these materials is not arbitrary but is based on their spectral complementarity: the perovskite subcell, with its wide bandgap, efficiently absorbs the visible and ultraviolet range, while the silicon HJT subcell exploits the near-infrared range. The combination of these two absorbers provides almost complete coverage of the solar spectrum, maximising carrier generation and paving the way for higher efficiencies than those achieved with single cells.

Table 4.11: Physical and electrical parameters for ZnO and Si HJT cell layers.

| Parameter | ZnO | a-Si:H-p | a-Si:H-i | a-Si:H-n | c-Si |
|---|---|---|---|---|---|
| Bandgap (eV) | 3.3 | 1.72 | 1.72 | 1.72 | 1.12 |
| Electron mobility ($cm^2/V \cdot s$) | 100 | 0.01 | 0.1 | 1 | 1350 |
| Hole mobility ($cm^2/V \cdot s$) | 25 | 1 | 0.1 | 0.01 | 480 |
| Dielectric constant | 9 | 11.9 | 11.9 | 11.9 | 11.9 |

### 4.4.3 Comparative Analysis of Photovoltaic Performance: Optimised Perovskite Cell and Perovskite/Silicon HJT Tandem Cell

#### 4.4.3.1 Analysis of J–V Curves

Figure 4.21 and Table 4.12 present the results of the current–voltage (J–V) characteristic simulation for the optimised PSC and for the tandem architecture incorporating a top perovskite subcell and a bottom heterojunction silicon (HJT) subcell. This comparison highlights the significant differences in performance between the two devices and allows the actual contribution of the tandem configuration to be evaluated.The results show that the optimised perovskite cell (FTO/$TiO_2$/$(BA)_2(MA)_2Pb_3I_8$/PolyTPD) achieves a $J_{sc}$ of 25.95 mA/$cm^2$, a $V_{oc}$ of 1.33 V, a fill factor (FF) of 70.87%, and an efficiency (PCE) of 24.41%. In comparison, the tandem architecture shows significantly higher performance, with $J_{sc}$ increased to 32.23 mA/$cm^2$, $V_{oc}$ of 1.32 V, FF of 70.59%, and PCE reaching 30.07%. These results demonstrate the major advantage of perovskite/silicon coupling, which makes it possible to exceed the efficiency threshold typically limited by the Shockley–Queisser law in single-junction cells.

Table 4.12: Electrical parameters extracted from the J–V characteristics of the optimized perovskite cell and perovskite/silicon HJT tandem cell.

| Cell Type | $J_{sc}$ (mA/$cm^2$) | $V_{oc}$ (V) | FF (%) | PCE (%) |
|---|---|---|---|---|
| Perovskite/Silicon HJT Tandem | 32.23 | 1.32 | 70.59 | 30.07 |
| Optimized Perovskite Cell | 25.95 | 1.33 | 70.87 | 24.41 |

The most significant improvement concerns current density. This increase stems directly from the spectral complementarity between the two sub-cells: perovskite efficiently captures photons in the visible range, while HJT silicon exploits the near-infrared range. The tandem thus benefits from a broader use of the solar spectrum, which translates into increased charge carrier generation and an increase in overall current. The open-circuit voltage, on the other hand, remains similar in both configurations (1.33 V for the perovskite cell and 1.32 V for the tandem). This behaviour can be explained by the $V_{oc}$

limitation rule in tandem architectures, which depends on the subcell with the lowest intrinsic voltage — in this case, perovskite. The fill factor has comparable values in both devices, 70.87% and 70.59% respectively. This similarity confirms the control of series and shunt resistances, as well as the satisfactory management of recombination phenomena in both architectures.

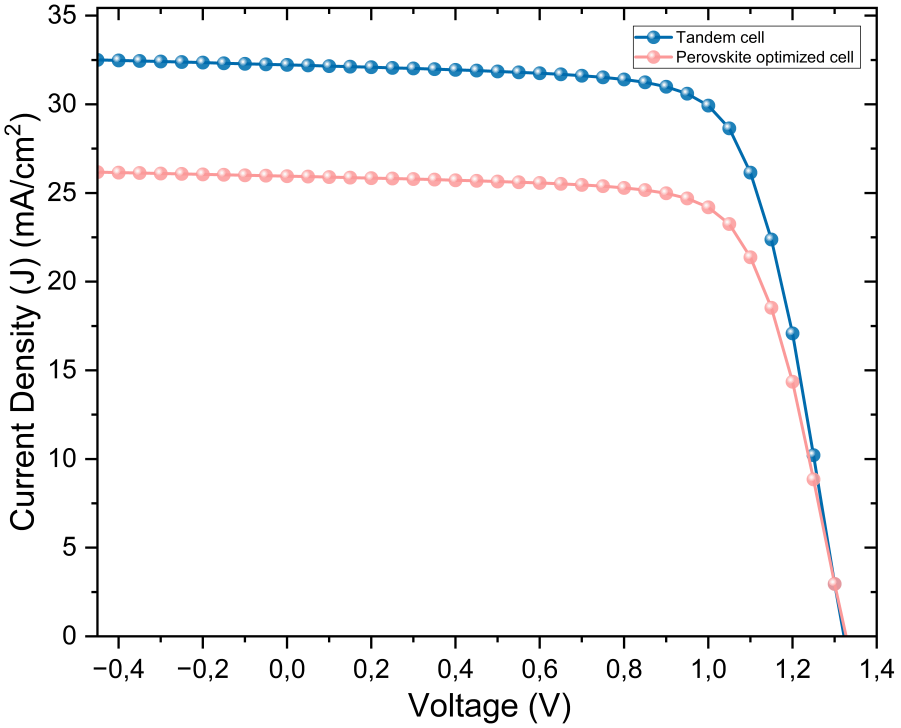



Figure 4.21: Simulated J–V curves of the optimised PSC and the perovskite/silicon heterojunction (HJT) tandem cell.

As a result, the tandem PCE reaches 30.07%, a substantial gain of approximately 5.7 percentage points compared to the single cell, illustrating the full potential of tandem structures to overcome the limitations of conventional photovoltaic cells. However, these results must be analysed in light of the residual losses inherent in the tandem architecture. Interfacial recombination at the ZnO and amorphous silicon layers may slightly affect the fill factor. Furthermore, although ZnO is highly transparent due to its wide bandgap (3.3 eV), residual absorption remains, marginally limiting the amount of light transmitted to the silicon. The comparison between the single cell and the tandem configuration clearly highlights the benefits of the perovskite/silicon approach. The tandem architecture synergistically exploits the spectral complementarity and electronic properties of wide- and narrow-bandgap materials, thereby exceeding the efficiency of single-junction cells. These results confirm that integrating an HJT silicon subcell beneath an optimised perovskite cell is a highly promising avenue for the development of new-generation, high-efficiency photovoltaic devices.

#### 4.4.3.2 Spectral Analysis: Absorption, Transmission and Optical Losses

Spectral analysis is an essential step in understanding the origin of the photovoltaic performance of the devices studied. Figure 4.22 illustrates the absorption and transmission pro-

files obtained for the optimised perovskite cell and for the perovskite/silicon HJT tandem architecture. These curves highlight the spectral distribution of absorbed or transmitted light energy and allow comparison of each configuration's ability to exploit different portions of the solar spectrum (0.3–1.0 µm). The (FTO/$TiO_2$/$(BA)_2(MA)_2Pb_3I_8$/PolyTPD) single perovskite cell has particularly high absorption in the visible region, typically between 0.35 and 0.60 µm, in line with the material's high absorption coefficient in this range. In this same region, transmission is almost zero, reflecting the ability of the active layer to intercept almost all incident photons. Beyond 0.6 µm, absorption decreases rapidly, while transmission increases sharply. This reflects the inability of perovskite to efficiently capture lower-energy photons (near infrared), which limits current generation in this area of the spectrum. As a result, the optimised perovskite cell performs well in the visible range but remains deficient in the infrared, where a significant fraction of solar radiation is lost through transmission.

The integration of the silicon HJT subcell profoundly alters these profiles. In the visible region (0.3–0.6 µm), absorption remains comparable to that of perovskite alone, since the top cell already efficiently captures this part of the spectrum. However, in the near infrared (0.7–1.0 µm), residual transmission is greatly reduced, as light not absorbed by the perovskite is intercepted by the silicon subcell. This spectral overlap gives the tandem cell extended absorption across the entire relevant solar spectrum, exploiting both visible photons (via perovskite) and near-infrared photons (via silicon).

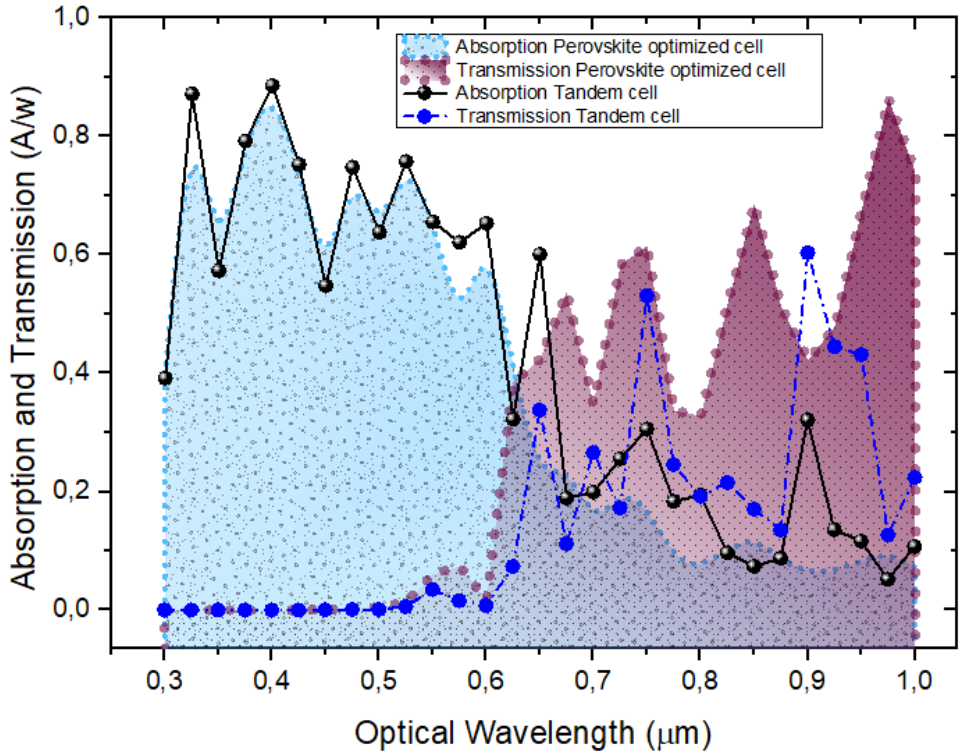



Figure 4.22: Absorption and transmission profiles of the optimised perovskite device and the perovskite/silicon tandem device.

The spectral complementarity effect is thus clearly demonstrated: while the single cell allowed a significant proportion of photons with wavelengths greater than 0.7 µm to pass through, the tandem cell manages to capture a significant fraction of them, thereby re-

ducing optical losses. These results highlight the importance of choosing materials based on their band gap. Perovskite, with an optimal band gap for visible light, acts as an effective absorber of high-energy photons. Silicon, meanwhile, complements this absorption by intercepting low-energy photons in the infrared range, which escape perovskite alone.

This synergy makes it possible to exploit a broader spectrum and significantly increase the generated current density, which explains the superiority of the tandem configuration observed in the J–V curves. The marked decrease in infrared transmission for the tandem cell confirms better photon–electron conversion in this spectral range. Nevertheless, there are still some optical losses related to reflection at the interfaces and residual absorption of the intermediate layer (ZnO), which could be minimised by advanced optical engineering strategies (anti-reflective layers, surface texturing).

#### 4.4.3.3 Study of external quantum efficiency and internal quantum efficiency

Figure 4.23 illustrates the external quantum efficiency (EQE) spectra for the optimised perovskite cell and for the perovskite/silicon tandem cell. The optimised perovskite cell ($FTO/TiO_2/(BA)_2(MA)_2Pb_3I_8$/PolyTPD) has an EQE peak of around 55% in the visible region, mainly between 0.4 and 0.7 µm, corresponding to the perovskite strong absorption zone. However, beyond 0.8 µm, a rapid drop in EQE is observed, reflecting the inability of perovskite to efficiently exploit near-infrared photons. This spectral limitation restricts the ability of the single cell to convert a significant portion of solar radiation.

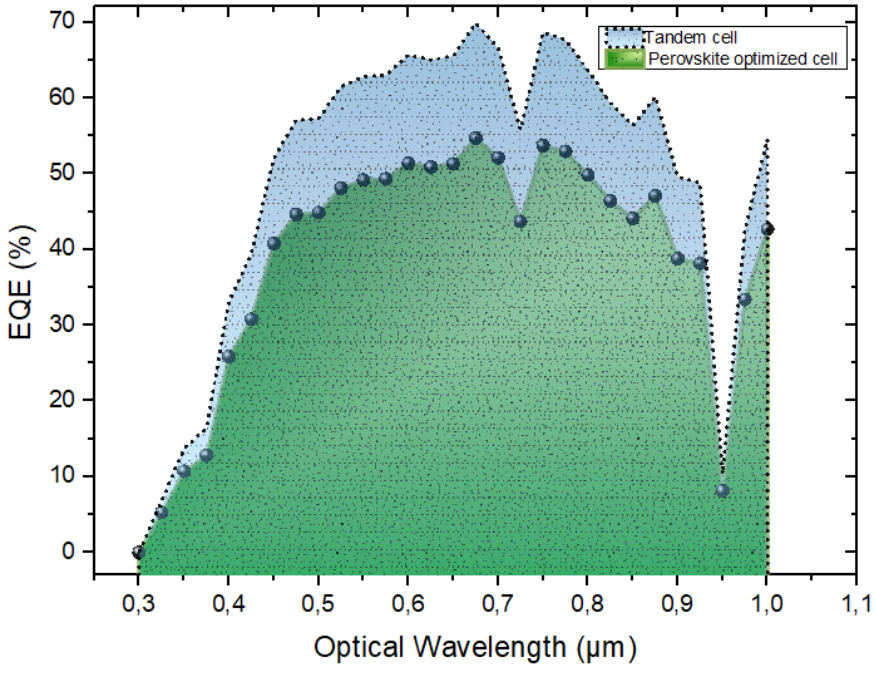



Figure 4.23: EQE spectra of the optimized perovskite device and the perovskite/silicon tandem device.

Conversely, the perovskite/silicon tandem cell has a higher overall EQE, with a peak of 68%, representing a net gain over the single cell. The improvement is particularly marked in the 0.4–0.8 µm range, where the complementarity between the two sub-cells allows for better utilisation of the solar spectrum. In addition, the tandem cell retains significant

EQE up to 1.0 µm, thanks to the absorption of silicon in the near infrared, which is not the case for the perovskite cell alone. These results demonstrate the relevance of the tandem architecture, which reduces transmission losses in the IR and increases the density of the current generated by efficiently exploiting a wider portion of the solar spectrum.

Figure 4.24 shows the internal quantum efficiency (IQE) spectra for the two configurations studied. Since IQE is independent of optical losses, it is a more direct indicator of the quality of carrier collection and recombination phenomena in the active layers and at the interfaces. The optimised perovskite cell shows an IQE peak of around 35% in the visible region (0.4–0.7 µm). This value, which is lower than the EQE, suggests that although light is efficiently absorbed, some of the photogenerated charges are lost through recombination before they can be collected. The gradual decrease in IQE beyond 0.8 µm reflects both the low absorption of perovskite and the increase in non-radiative recombination at these wavelengths.

The perovskite/silicon tandem cell, on the other hand, achieves a maximum IQE of around 45%, which is a significant improvement over the single cell. This result reflects a significant improvement in charge collection quality, in particular thanks to the reduction in recombination at the interfaces and the complementary use of the two active materials. The contribution of silicon is particularly visible in the 0.7–1.0 µm region, where the IQE remains high while that of perovskite alone collapses. Thus, the increase in IQE in the tandem cell demonstrates not only better spectral absorption, but also better management of internal electronic processes, leading to increased overall efficiency.

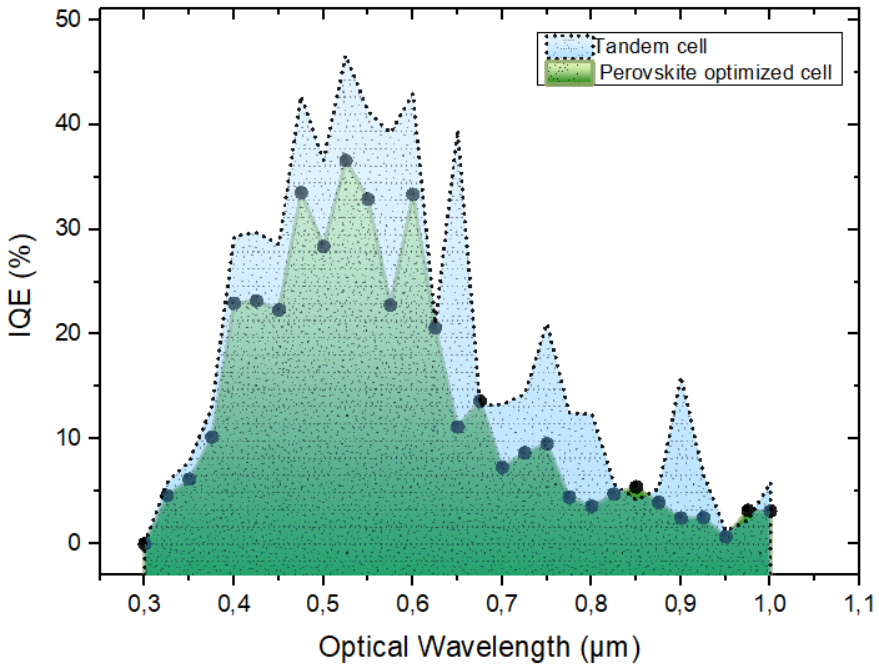



Figure 4.24: IQE spectra of the optimized perovskite device and the perovskite/silicon tandem device.

A comparison of the EQE and IQE spectra highlights the decisive contribution of the tandem architecture compared to the optimised perovskite cell. In the single-junction cell, although absorption is efficient in the visible range, photon–electron conversion remains limited to short-wavelength photons, while losses become significant in the near-infrared

due to the perovskite low ability to exploit this part of the spectrum. The integration of a silicon sub-cell profoundly changes this situation, the complementary nature of the band gaps extends the absorption range, ensuring more complete utilisation of the solar spectrum. This spectral extension results not only in an improvement in EQE, but also in a significant increase in IQE. Indeed, the tandem cell not only collects more photons, it also optimises the probability of collecting photogenerated carriers by reducing recombination losses and improving interface management. This dual improvement, both optical and electronic, explains the observed increase in short-circuit current density and, consequently, in PCE. The results obtained confirm that combining a perovskite layer with a wide bandgap with a silicon absorber with a narrower bandgap is a particularly effective approach for overcoming the intrinsic limitations of single cells. This spectral and electronic synergy justifies the growing interest in tandem architectures as a promising solution for the development of high-efficiency photovoltaic devices.

#### 4.4.3.4 Influence of temperature on the performance of tandem photovoltaic cells

The influence of temperature on the photovoltaic performance of the perovskite/silicon HJT tandem cell was studied in depth over a range between 265 K and 360 K. The results presented in Figure 4.25 highlight the evolution of the J–V curves as a function of temperature, while Figure 4.26 and Table 4.13 provide a precise quantification of the evolution of characteristic parameters such as short-circuit current density, open-circuit voltage, fill factor and power conversion efficiency. Analysis of these results reveals contrasting trends that reflect the complex interaction between the mechanisms of generation, recombination and transport of charge carriers under thermal stress.

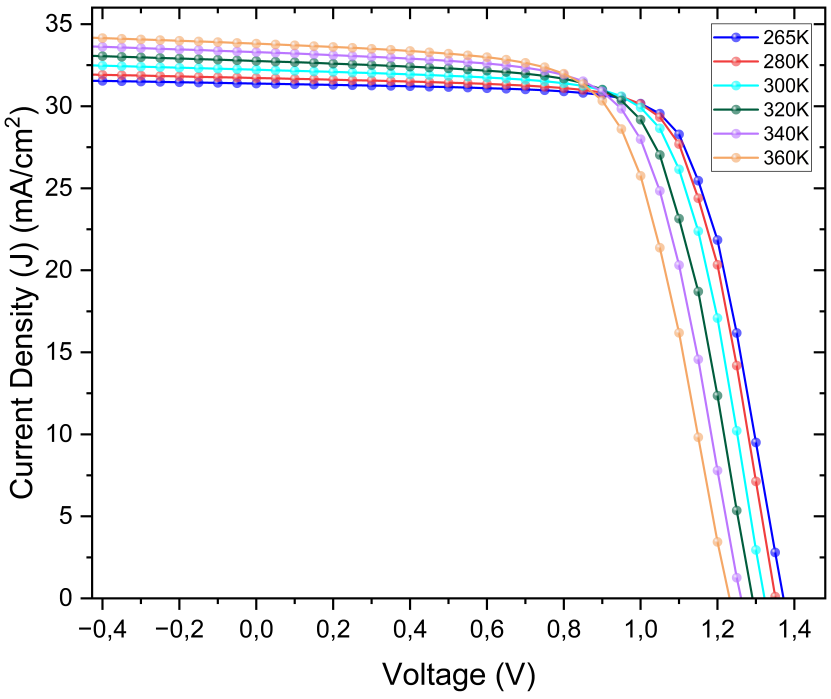



Figure 4.25: Simulated J–V curves of the perovskite/silicon HJT tandem cell across the temperature range from 265 K to 360 K.

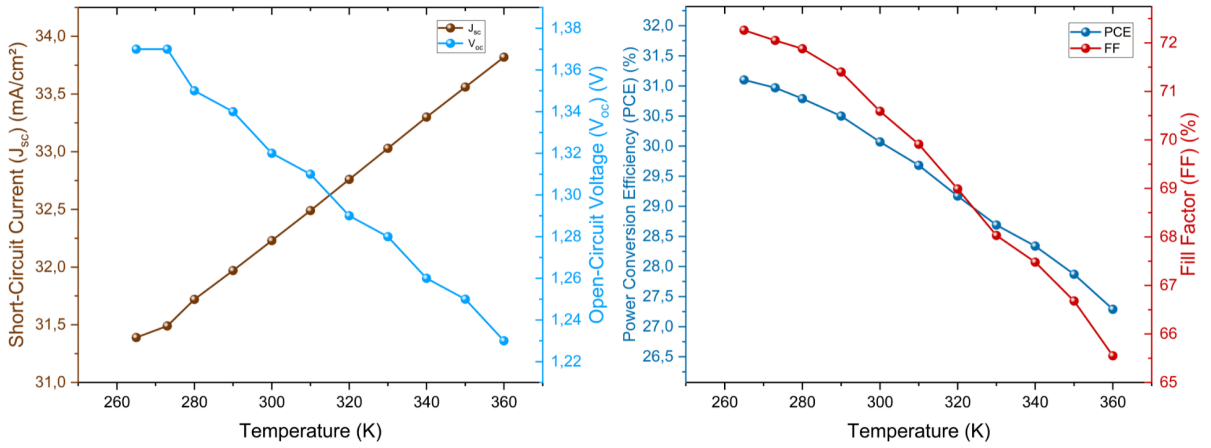



Figure 4.26: Temperature dependence of the $J_{sc}$, $V_{oc}$, FF, and PCE of the perovskite/silicon HJT tandem cell.

Table 4.13: Photovoltaic performance metrics of the perovskite/silicon HJT tandem cell at different operating temperatures.

| **Temperature (K)** | $J_{sc}$ **(mA/cm²)** | $V_{oc}$ **(V)** | **FF (%)** | **PCE (%)** |
|---|---|---|---|---|
| 265 | 31.39 | 1.37 | 72.26 | 31.10 |
| 273 | 31.49 | 1.37 | 72.05 | 30.97 |
| 280 | 31.72 | 1.35 | 71.88 | 30.79 |
| 290 | 31.97 | 1.34 | 71.40 | 30.50 |
| 300 | 32.23 | 1.32 | 70.59 | 30.07 |
| 310 | 32.49 | 1.31 | 69.91 | 29.68 |
| 320 | 32.76 | 1.29 | 68.99 | 29.17 |
| 330 | 33.03 | 1.28 | 68.03 | 28.69 |
| 340 | 33.30 | 1.26 | 67.48 | 28.34 |
| 350 | 33.56 | 1.25 | 66.68 | 27.87 |
| 360 | 33.82 | 1.23 | 65.55 | 27.29 |

The rise in temperature is accompanied by a slight increase in short-circuit current density, which rises from 31.39 mA/cm$^2$ at 265 K to 33.82 mA/cm$^2$ at 360 K. This slight gain can be explained mainly by two physically based mechanisms: a shift in the absorption limit (reduction in effective bandwidth with temperature), which allows marginally more photons to be absorbed at longer wavelengths, and carrier transport mobility, which is sometimes improved at higher temperatures, locally reducing ohmic losses and promoting extraction. However, these effects remain limited; the increase in $J_{sc}$ does not compensate for the losses induced by other parameters.

The $V_{oc}$ decreases markedly, from 1.37 V at 265 K to 1.23 V at 360 K. This decrease can be explained by the increase in reverse saturation current due to the thermal activation of recombination mechanisms (radiative and non-radiative), the increase in intrinsic carrier concentration and the increase in recombination rates at defects and interfaces. In thermodynamic terms, the reduction in $V_{oc}$ is a direct consequence of the exponential increase in reversible processes limiting the available voltage. In the case of perovskites, additional phenomena such as ion migration and the dynamic evolution of trap states

with temperature can also contribute to this degradation of $V_{oc}$ by locally modifying the internal fields and the quality of the interfaces. The fill factor follows a similar trend, decreasing from 72.26% at 265 K to 65.55% at 360 K. This decrease reflects the increase in effective resistive losses (increasing series resistance due to the performance of contacts and conductive layers at high temperatures, or variations in conductivity) and the increase in recombination, which degrades the slope of the J–V curve near the maximum power point. The cumulative effect on $V_{oc}$ and FF leads to a continuous decrease in PCE, which falls from 31.10% at 265 K to 27.29% at 360 K. In other words, the marginal improvement in $J_{sc}$ is largely offset by the significant loss in voltage and effective power extraction.

Beyond the quantitative description, physical interpretation highlights several factors responsible for thermal sensitivity. First, an increase in non-radiative recombination, amplified by the thermal activation of recombination centers and by the thermal diffusion of carriers. Second, possible ion migration in perovskite, which locally modifies band alignment and causes hysteresis and instability phenomena under heating. Third, degradation of interfaces (ZnO/perovskite, perovskite/HTL, and a-Si/c-Si) and contacts, which increase series resistances and promote leakage paths. Finally, minimal optical changes (variation in refractive index), which, although secondary, can slightly affect the optical coupling between sub-cells. These mechanisms, combined, explain why the cell remains efficient but gradually loses efficiency as the temperature rises.

On a practical level, these results highlight the need for a thermal management strategy for high-efficiency tandem devices. Possible solutions include optimising and passivating interfaces to reduce recombination at high temperatures, using HTL/ETL materials and contacts that are less sensitive to heat, improving encapsulation and thermal dissipation (heat sinks, substrates with high thermal conductivity), and controlling trap densities through deposition processes and post-deposition treatments. Furthermore, quantifying the temperature coefficient of $V_{oc}$ and PCE and extracting activation energies for recombination mechanisms would be useful in guiding materials engineering and predicting behavior under real-world conditions. In sum, the thermal study shows that a perovskite/silicon HJT tandem cell maintains high performance over the range studied but remains sensitive to temperature. The increase in $J_{sc}$ is insufficient to compensate for the decrease in $V_{oc}$ and FF, resulting in a net reduction in PCE. These observations justify the systematic integration of thermal optimisation and interface engineering approaches in the design of perovskite–silicon tandems for real-world applications where temperature fluctuations are inevitable.

### 4.4.4 Prospects for optimisation

Although the perovskite/silicon HJT tandem architecture has demonstrated remarkable performance in our simulations, it can still be improved and offers considerable room for progress. One initial avenue for optimisation concerns the precise control of the thickness of the perovskite layer. If the layer is too thin, absorption in the visible range is limited, while if it is too thick, photon transmission to the silicon subcell is reduced. Fine-tuning this parameter is therefore crucial in order to maximise optical coupling between the two subcells. A second avenue for improvement lies in the development of highly transparent intermediate layers with optimised transport selectivity. These layers must both ensure

efficient carrier extraction and minimise optical losses, which requires the engineering of new materials with low parasitic absorption and increased mobility.

Furthermore, reducing non-radiative recombination remains a major challenge. Interface engineering and advanced defect passivation, both in perovskite and silicon, are promising strategies for increasing carrier lifetime and improving open-circuit voltage. Finally, exploring perovskites with tunable bandgaps represents a strategic opportunity. Precise adjustment of the band width would make it possible to adapt the spectral response of the top subcell for optimal matching with silicon, which is essential for achieving theoretical efficiencies close to the Shockley–Queisser limit for tandem cells. These avenues for optimisation, combined with appropriate thermal management and more stable manufacturing processes, pave the way for a new generation of high-efficiency, sustainable perovskite/silicon tandem cells that could significantly exceed current performance levels.

## 4.5 Conclusion

This chapter was a key step in the cross-validation of the work, combining analytical modelling, numerical simulation and available experimental data. The use of Silvaco TCAD made it possible to refine the study by incorporating more realistic physical phenomena, such as recombination at interfaces, layer inhomogeneity and spectral dependence of absorption. The results obtained for the single-junction perovskite cell showed good agreement between the different approaches, thus reinforcing the reliability of the model. In addition, the parametric study highlighted the decisive impact of the properties of the hole transport layer (HTL), in particular the role of doping and material choice on overall efficiency. The comparison between several HTLs (organic and inorganic) identified alternatives that are more stable and efficient than Spiro-OMeTAD, confirming the importance of fine interface engineering to improve carrier extraction and reduce losses.

In a second step, the most promising configuration was selected to design a perovskite/silicon HJT tandem cell. Simulation results highlighted the spectral complementarity of the two sub-cells, enabling almost complete coverage of the solar spectrum and a substantial improvement in current density and conversion efficiency compared to single-junction cells. Analysis of the EQE and IQE spectra, as well as the study of the J-V curves, confirmed that the tandem architecture is a preferred route for exceeding the efficiency limit of conventional photovoltaic cells. Finally, the effect of temperature on performance was studied, showing a moderate increase in short-circuit current but a significant decrease in open-circuit voltage, fill factor and overall efficiency. These results remind us that thermal management remains a crucial challenge in ensuring the operational stability and durability of devices.

# GENERAL CONCLUSION

This thesis is part of ongoing efforts to develop next-generation photovoltaic technologies capable of meeting global energy and environmental challenges. Given the structural and technological limitations of conventional silicon-based solar cells, perovskite materials have emerged as a promising alternative, offering a unique compromise between performance, ease of manufacture, and flexibility of integration. The main objective of this work was to deepen our understanding of the physical mechanisms governing the operation of perovskite-based solar cells and their tandem derivatives, using an integrated approach combining analytical modelling, numerical simulation, and experimental validation. This hierarchical methodology has made it possible to establish a clear correlation between the fundamental phenomena of carrier generation, transport, and recombination and the overall performance observed in the devices. It has also led to the proposal of targeted optimization strategies aimed at improving the efficiency, stability, and reproducibility of next-generation perovskite solar cells.

Analytically, a comprehensive and rigorous model was established to describe the electrical behavior of a single-junction perovskite solar cell. This model is based on the joint solution of the carrier continuity equations and Poisson's equation, explicitly integrating optical generation and the internal electric field within the absorbing layer. Within the framework of the assumptions adopted, recombination in perovskite was neglected, which simplified the analysis and allowed closed analytical expressions to be obtained that directly link carrier profiles to the photogenerated current density. Precise treatment of the boundary conditions at the interfaces between the different functional layers (ETL/perovskite and perovskite/HTL) was carried out, allowing charge exchanges and extraction phenomena at the contacts to be taken into account. This analytical model led to the derivation of an explicit expression for the current-voltage characteristic $J(V)$, capable of reproducing the electrical behavior of the n–i–p structure studied with high fidelity. The entire theoretical development was implemented numerically using a MATLAB program specifically designed for this work. This code not only solves the established analytical equations, but also plots the $J$–$V$ curves, automatically extracts the characteristic photovoltaic parameters ($J_{sc}$, $V_{oc}$, $FF$, and $PCE$), and compares the theoretical results with the available experimental data. This comparison showed remarkable consistency between the model and experimental observations, confirming the validity of the approximations used and the model's ability to describe the dominant physical mechanisms of

carrier transport and generation.

In addition, an in-depth parametric study was conducted to assess the impact of key design parameters on cell performance. The parametric analysis showed that the thickness of the perovskite layer has a decisive influence on overall efficiency, directly modulating optical generation and carrier collection, while doping of the $TiO_2$ layer (ETL) significantly affects cell performance by influencing charge extraction efficiency. Finally, the model was extended to a perovskite/silicon tandem configuration, allowing the exploration of optical and electrical coupling effects between subcells. The joint optimization of the absorbing thicknesses ensured current matching between the two subcells and achieved an overall efficiency of 26.83%, illustrating the relevance of the proposed analytical model for the rational design of tandem architectures. This model is therefore a robust and computationally inexpensive predictive tool, providing a solid basis for the analysis, design, and optimization of new generations of high-efficiency perovskite and hybrid solar cells.

The simulation stage, carried out using Silvaco TCAD software, enabled accurate simulation of the perovskite cell with an FTO/$TiO_2$/$MAPbI_3$/Spiro-OMeTAD structure. The results obtained were validated by cross-checking with the analytical model developed in Chapter 3 and experimental data from the literature for the same configuration, confirming the reliability and consistency of the proposed model. In a second step, a material optimization study was conducted to improve the stability and performance of the cell. Replacing the 3D $MAPbI_3$ perovskite with a Ruddlesden–Popper-type 2D/3D hybrid perovskite resulted in improved stability while maintaining high efficiency. At the same time, a comparative analysis of HTLs, evaluating several organic and inorganic materials, showed that the PolyTPD compound offers the most effective combination in terms of efficiency and durability. Based on this optimized configuration, the cell was integrated into a perovskite/silicon HJT tandem architecture, demonstrating excellent spectral complementarity between the two subcells and achieving efficiencies greater than 30%, exceeding the limit of single-junction cells. Finally, an in-depth thermal study was conducted over a wide temperature range to assess operational stability. The results showed that an increase in temperature leads to an increase in $J_{sc}$ but is accompanied by a decrease in $V_{oc}$, fill factor (FF), and PCE, highlighting the need for optimized thermal management to ensure the long-term reliability of the devices.

The work presented in this thesis has enabled an in-depth exploration of the behavior of perovskite-based solar cells, combining analytical modelling, numerical simulation, and experimental validation. After establishing and comparing the developed model with simulation results and experimental data, the analysis revealed consistent trends and identified the key parameters influencing the overall performance of the devices. This integrated approach has thus made it possible to link the fundamental physics of transport and recombination processes to the observed performance, providing a solid basis for structural optimization and the design of new, more efficient architectures. Several prospects emerge from this work. On a theoretical level, enriching the analytical model by integrating complex recombination mechanisms, a non-uniform electric field, and more realistic internal optical modelling would increase its accuracy and scope. On a numerical level, exploring three- or four-terminal (3T and 4T) tandem architectures would offer greater flexibility in current matching and energy loss management. Finally, the inte-

gration of coupled thermo-optical simulations and accelerated aging studies would be an essential step in evaluating the stability and durability of the devices, with a view to transferring them to reliable industrial production. Overall, this thesis has laid the foundations for a comprehensive, coherent, and integrated understanding of how perovskite solar cells and their tandem derivatives work, linking fundamental physics with analytical modelling and advanced numerical simulation. The results obtained demonstrate the considerable potential of these technologies to reach a new threshold of efficiency, stability, and durability, and actively contribute to the rise of new-generation photovoltaic solutions capable of providing a sustainable response to global energy challenges.

# BIBLIOGRAPHY


[1] H. Gagarin, S. Sridhar, I. Lange, and M. D. Bazilian, "Considering non-power generation uses of coal in the United States," *Renewable and Sustainable Energy Reviews*, vol. 124, p. 109 790, May 2020, ISSN: 1364-0321. DOI: 10.1016/j.rser.2020.109790.

[2] S. Rajput and R. K. Pathak, "Charting the Course for Energy Transformation," en, in *Seismic Exploration to Reservoir Excellence*, S. Rajput and R. K. Pathak, Eds., Singapore: Springer Nature, 2025, pp. 3–72, ISBN: 978-981-96-1293-2. DOI: 10.1007/978-981-96-1293-2_1.

[3] X. Yang, J. Pang, F. Teng, R. Gong, and C. Springer, "The environmental co-benefit and economic impact of China's low-carbon pathways: Evidence from linking bottom-up and top-down models," *Renewable and Sustainable Energy Reviews*, vol. 136, p. 110 438, Feb. 2021, ISSN: 1364-0321. DOI: 10.1016/j.rser.2020.110438.

[4] A. G. Olabi, K. Obaideen, K. Elsaid, *et al.*, "Assessment of the pre-combustion carbon capture contribution into sustainable development goals SDGs using novel indicators," *Renewable and Sustainable Energy Reviews*, vol. 153, p. 111 710, Jan. 2022, ISSN: 1364-0321. DOI: 10.1016/j.rser.2021.111710.

[5] J. Curtin, C. McInerney, B. Ó Gallachóir, C. Hickey, P. Deane, and P. Deeney, "Quantifying stranding risk for fossil fuel assets and implications for renewable energy investment: A review of the literature," *Renewable and Sustainable Energy Reviews*, vol. 116, p. 109 402, Dec. 2019, ISSN: 1364-0321. DOI: 10.1016/j.rser.2019.109402.

[6] A. Bouich, I. G. Pradas, M. A. Khan, and Y. H. Khattak, "Opportunities, Challenges, and Future Prospects of the Solar Cell Market," en, *Sustainability*, vol. 15, no. 21, p. 15 445, Jan. 2023, ISSN: 2071-1050. DOI: 10.3390/su152115445.

[7] A. G. Olabi, K. Elsaid, K. Obaideen, *et al.*, "Renewable energy systems: Comparisons, challenges and barriers, sustainability indicators, and the contribution to UN sustainable development goals," *International Journal of Thermofluids*, vol. 20, p. 100 498, Nov. 2023, ISSN: 2666-2027. DOI: 10.1016/j.ijft.2023.100498.

[8] F. J. M. M. Nijsse, J.-F. Mercure, N. Ameli, *et al.*, "The momentum of the solar energy transition," en, *Nat Commun*, vol. 14, no. 1, p. 6542, Oct. 2023, ISSN: 2041-1723. DOI: 10.1038/s41467-023-41971-7.

[9] Q. Hassan, P. Viktor, T. J. Al-Musawi, *et al.*, "The renewable energy role in the global energy Transformations," *Renewable Energy Focus*, vol. 48, p. 100 545, Mar. 2024, ISSN: 1755-0084. DOI: 10.1016/j.ref.2024.100545.

[10] D. Lincot, "The new paradigm of photovoltaics: From powering satellites to powering humanity," *Comptes Rendus Physique*, Demain l'énergie, vol. 18, no. 7, pp. 381–390, Sep. 2017, ISSN: 1631-0705. DOI: 10.1016/j.crhy.2017.09.003.

[11] L. Fraas, "Chapter 1: History of Solar Cell Development," in Jun. 2014, ISBN: 978-3-319-07529-7. DOI: 10.1007/978-3-319-07530-3_1.

[12] S. Tonzani, "Sun power," en, *Nature Mater*, vol. 9, no. 1, S10–S11, May 2010, ISSN: 1476-4660. DOI: 10.1038/nmat2645.

[13] A. Goetzberger, J. Luther, and G. Willeke, "Solar cells: Past, present, future," *Solar Energy Materials and Solar Cells*, PVSEC 12 Part I, vol. 74, no. 1, pp. 1–11, Oct. 2002, ISSN: 0927-0248. DOI: 10.1016/S0927-0248(02)00042-9.

[14] J. Perlin, "Silicon Solar Cell Turns 50," Aug. 2004.

[15] C. Yang, W. Hu, J. Liu, *et al.*, "Achievements, challenges, and future prospects for industrialization of perovskite solar cells," en, *Light Sci Appl*, vol. 13, no. 1, p. 227, Sep. 2024, ISSN: 2047-7538. DOI: 10.1038/s41377-024-01461-x.

[16] A. O. Ali, A. T. Elgohr, M. H. El-Mahdy, *et al.*, "Advancements in photovoltaic technology: A comprehensive review of recent advances and future prospects," *Energy Conversion and Management: X*, vol. 26, p. 100 952, Apr. 2025, ISSN: 2590-1745. DOI: 10.1016/j.ecmx.2025.100952.

[17] C. E. Fritts, "On a new form of selenium cell, and some electrical discoveries made by its use," en, *American Journal of Science*, vol. s3-26, no. 156, pp. 465–472, Dec. 1883. DOI: 10.2475/ajs.s3-26.156.465.

[18] 2. P. Jowett, *Global solar capacity to surpass 7.5 TW in 2035, says GlobalData*, en-US, Publication Title: pv magazine International, Jun. 2025. [Online]. Available: https://www.pv-magazine.com/2025/06/03/global-solar-capacity-to-surpass-7-5-tw-in-2035-says-globaldata/ (visited on 07/29/2025).

[19] T. I.-P. 2. S. o. G. P. M. r. a. p. m. f. s. p. g. P. c. s. 2. 2. TW, w. m. t. 6. G. i. i. 2. a. A. m. p. f. d. t. oversupply with more than, I. V. C. t. Grow, H. B. t. Strength, and v. o. t. g. P. i. IEA-PVPS, *2025: A landmark year for solar energy*, en-US, Publication Title: pv magazine International, Jun. 2025. [Online]. Available: https://www.pv-magazine.com/2025/06/09/2025-a-landmark-year-for-solar-energy/ (visited on 07/29/2025).

[20] A. Jäger-Waldau, "Snapshot of photovoltaics - March 2025," en, *EPJ Photovolt.*, vol. 16, p. 22, 2025, ISSN: 2105-0716. DOI: 10.1051/epjpv/2025012.

[21] M. Peters, T. Schmidt, D. Wiederkehr, and M. Schneider, "Shedding light on solar technologies'A techno-economic assessment and its policy implications," *Energy Policy*, vol. 39, pp. 6422–6439, Oct. 2011. DOI: 10.1016/j.enpol.2011.07.045.

[22] A. A. Firoozi, A. A. Firoozi, and M. R. Maghami, "Harnessing photovoltaic innovation: Advancements, challenges, and strategic pathways for sustainable global development," *Energy Conversion and Management: X*, vol. 27, p. 101 058, Jul. 2025, ISSN: 2590-1745. DOI: 10.1016/j.ecmx.2025.101058.

[23] R. C.j., K. H. Lim, J. C. Kurnia, S. Roy, B. J. Bora, and B. J. Medhi, "Towards sustainable power generation: Recent advancements in floating photovoltaic technologies," *Renewable and Sustainable Energy Reviews*, vol. 194, p. 114 322, Apr. 2024, ISSN: 1364-0321. DOI: 10.1016/j.rser.2024.114322.

[24] A. Chandrakar and A. Khare, "A comprehensive review of flexible perovskite solar cells: Materials, mechanisms, properties, applications, and commercialization status," *Solar Energy*, vol. 298, p. 113 649, Sep. 2025, ISSN: 0038-092X. DOI: 10.1016/j.solener.2025.113649.

[25] S. Aftab, M. Mukhtar, B. S. Goud, F. Kabir, H. H. Hegazy, and J. H. Kim, "Cutting-edge developments in perovskite solar cells: The role of dimensional and mixed-dimensional engineering," *Journal of Alloys and Compounds*, vol. 1006, p. 176 341, Nov. 2024, ISSN: 0925-8388. DOI: 10.1016/j.jallcom.2024.176341.

[26] S. Khatoon, S. Kumar Yadav, V. Chakravorty, *et al.*, "Perovskite solar cell's efficiency, stability and scalability: A review," *Materials Science for Energy Technologies*, vol. 6, pp. 437–459, Jan. 2023, ISSN: 2589-2991. DOI: 10.1016/j.mset.2023.04.007.

[27] Y. Liu, Z. Zhang, T. Wu, *et al.*, "Cost Effectivities Analysis of Perovskite Solar Cells: Will it Outperform Crystalline Silicon Ones?" en, *Nano-Micro Lett.*, vol. 17, no. 1, p. 219, Apr. 2025, ISSN: 2150-5551. DOI: 10.1007/s40820-025-01744-x.

[28] D. Bogdanov, A. Gulagi, A. Aghahosseini, *et al.*, "On the role of solar photovoltaics in global energy transition scenarios," *Progress in Photovoltaics Research and Applications*, vol. 25, pp. 727–745, Aug. 2017. DOI: 10.1002/pip.2885.

[29] M. Victoria, N. Haegel, I. M. Peters, *et al.*, "Solar photovoltaics is ready to power a sustainable future," *Joule*, vol. 5, no. 5, pp. 1041–1056, May 2021, ISSN: 2542-4351. DOI: 10.1016/j.joule.2021.03.005.

[30] H. H. Pourasl, R. V. Barenji, and V. M. Khojastehnezhad, "Solar energy status in the world: A comprehensive review," *Energy Reports*, vol. 10, pp. 3474–3493, Nov. 2023, ISSN: 2352-4847. DOI: 10.1016/j.egyr.2023.10.022.

[31] H. Lee, "Analysis of Current-Voltage Hysteresis and Ageing Characteristics for CH3NH3PbI3-xClxBased Perovskite Thin Film Solar Cells," These de doctorat, Université Paris-Saclay (ComUE), Jan. 2018.

[32] D. V. Sylvain, "Developpement de cellules photovoltaïques à hétérojonction de silicium et contacts interdigités en face arrière," fr,

[33] *Solar Constant - an overview \textbar ScienceDirect Topics*. [Online]. Available: https://www.sciencedirect.com/topics/engineering/solar-constant (visited on 07/30/2025).

[34] O. Ibrahim Elmi, "Nouvelles structures de cellules solaires à base de silicium : Texturation, passivation et association de réseaux de nanostructures métalliques avec une couche Down-Conversion," These de doctorat, Lille 1, Mar. 2017.

[35] M. Kim, "Analysis of Ion Migration and Ageing Characteristics for Triple-cation and CH3NH3PbI3-xClx Perovskite Based Thin-Film Solar Cells," en,

[36] *Standard Spectra and Test Conditions*. [Online]. Available: https://www.greenrhinoenergy.com/solar/radiation/spectra.php (visited on 07/30/2025).

[37] D. Barolet, F. Christiaens, and M. Hamblin, "Infrared and Skin: Friend or Foe," *Journal of Photochemistry and Photobiology B: Biology*, vol. 155, Dec. 2015. DOI: 10.1016/j.jphotobiol.2015.12.014.

[38] A. A. Ali, E. El Fadaly, and I. S. Ahmed, "Near-infrared reflecting blue inorganic nano-pigment based on cobalt aluminate spinel via combustion synthesis method," *Dyes and Pigments*, vol. 158, pp. 451–462, Nov. 2018, ISSN: 0143-7208. DOI: 10.1016/j.dyepig.2018.05.058.

[39] Y. Li, "Cellules solaires p-i-n à base de pérovskites halogénées," These de doctorat, Université Grenoble Alpes, Feb. 2022.

[40] T. Ishii, K. Otani, T. Takashima, and Y. Xue, "Solar spectral influence on the performance of photovoltaic (PV) modules under fine weather and cloudy weather conditions," *Progress in Photovoltaics: Research and Applications*, vol. 21, Nov. 2011. DOI: 10.1002/pip.1210.

[41] R. Daxini and Y. Wu, "Review of methods to account for the solar spectral influence on photovoltaic device performance," *Energy*, vol. 286, p. 129 461, Jan. 2024, ISSN: 0360-5442. DOI: 10.1016/j.energy.2023.129461.

[42] Ø. G. Martinsen and A. Heiskanen, "Chapter 2 - Electrolytics," in *Bioimpedance and Bioelectricity Basics (Fourth Edition)*, Ø. G. Martinsen and A. Heiskanen, Eds., Oxford: Academic Press, Jan. 2023, pp. 7–36, ISBN: 978-0-12-819107-1. DOI: 10.1016/B978-0-12-819107-1.00014-5.

[43] P. Paranthaman, W. Wong-Ng, and R. Bhattacharya, *Semiconductor Materials for Solar Photovoltaic Cells*. Sep. 2015, ISBN: 978-3-319-20330-0. DOI: 10.1007/978-3-319-20331-7.

[44] F. Baig, "Numerical analysis for efficiency enhancement of thin film solar cells.," en, PhD Thesis, Universitat Politècnica de València, Valencia (Spain), Feb. 2019. DOI: 10.4995/Thesis/10251/118801.

[45] O. Guesmi, M. Ben Arbia, F. Saidi, M. Ben Rabeh, and H. Maaref, "Experimental and computational studies of CCTS material: Novel design of solar cell for high efficiency," *Solar Energy*, vol. 262, p. 111 806, Sep. 2023, ISSN: 0038-092X. DOI: 10.1016/j.solener.2023.111806.

[46] S. Akhil, S. Akash, A. Pasha, *et al.*, "Review on perovskite silicon tandem solar cells: Status and prospects 2T, 3T and 4T for real world conditions," *Materials & Design*, vol. 211, p. 110 138, Dec. 2021, ISSN: 0264-1275. DOI: 10.1016/j.matdes.2021.110138.

[47] W. Tress, "Maximum Efficiency and Open-Circuit Voltage of Perovskite Solar Cells," in Jul. 2016, pp. 53–77, ISBN: 978-3-319-35112-4. DOI: 10.1007/978-3-319-35114-8_3.

[48] P. Kumar, "Development of Thin Film Semitransparent Sb2S3 Solar Cells," eng, 2025.

[49] Y. H. Khattak, "Modeling of High Power Conversion Efficiency Thin Film Solar Cells," en, PhD Thesis, Universitat Politècnica de València, Valencia (Spain), Feb. 2019. DOI: 10.4995/Thesis/10251/118802.

[50] M. I. Alkhatab, "Material studies for flexible 3rd generation solar cells," en,

[51] M. A. Green, E. D. Dunlop, M. Yoshita, *et al.*, "Solar cell efficiency tables (Version 63)," en, *Progress in Photovoltaics: Research and Applications*, vol. 32, no. 1, pp. 3–13, 2024, ISSN: 1099-159X. DOI: 10.1002/pip.3750.

[52] A. Machín and F. Márquez, "Advancements in Photovoltaic Cell Materials: Silicon, Organic, and Perovskite Solar Cells," en, *Materials*, vol. 17, no. 5, p. 1165, Jan. 2024, ISSN: 1996-1944. DOI: 10.3390/ma17051165.

[53] P. Priya and A. A. Stonier, "Emerging innovations in solar photovoltaic (PV) technologies: The perovskite solar cells and more," *Energy Reports*, vol. 14, pp. 216–242, Dec. 2025, ISSN: 2352-4847. DOI: 10.1016/j.egyr.2025.06.003.

[54] B. P. Singh, S. K. Goyal, and P. Kumar, "Solar PV cell materials and technologies: Analyzing the recent developments," *Materials Today: Proceedings*, CRMSC-2021, vol. 43, pp. 2843–2849, Jan. 2021, ISSN: 2214-7853. DOI: 10.1016/j.matpr.2021.01.003.

[55] N. Erhard and A. Holleitner, "13 - Semiconductor nanowires studied by photocurrent spectroscopy," in *Semiconductor Nanowires*, ser. Woodhead Publishing Series in Electronic and Optical Materials, J. Arbiol and Q. Xiong, Eds., Woodhead Publishing, Jan. 2015, pp. 365–391, ISBN: 978-1-78242-253-2. DOI: 10.1016/B978-1-78242-253-2.00013-X.

[56] P. Augustine, "Chapter 13 - Two-dimensional layered materials for efficient photodetection," in *Applications of Multifunctional Nanomaterials*, ser. Micro and Nano Technologies, S. Thomas, N. Kalarikkal, and A. R. Abraham, Eds., Elsevier, Jan. 2023, pp. 265–280, ISBN: 978-0-12-820557-0. DOI: 10.1016/B978-0-12-820557-0.00015-1.

[57] K. C. Kao, "3 - Optical and Electro-Optic Processes," in *Dielectric Phenomena in Solids*, K. C. Kao, Ed., San Diego: Academic Press, Jan. 2004, pp. 115–212, ISBN: 978-0-12-396561-5. DOI: 10.1016/B978-012396561-5/50013-X.

[58] D. L. Andrews, "Electromagnetic Radiation," in *Encyclopedia of Spectroscopy and Spectrometry*, J. C. Lindon, Ed., Oxford: Elsevier, Jan. 1999, pp. 397–401, ISBN: 978-0-12-226680-5. DOI: 10.1006/rwsp.2000.0055.

[59] S. N. Ahmed, "2 - Interaction of radiation with matter," in *Physics and Engineering of Radiation Detection (Second Edition)*, S. N. Ahmed, Ed., Elsevier, Jan. 2015, pp. 65–155, ISBN: 978-0-12-801363-2. DOI: 10.1016/B978-0-12-801363-2.00002-4.

[60] K. P. Schäfers, K. Bolwin, F. Büther, *et al.*, "1.10 - High-Resolution Small Animal Imaging," in *Comprehensive Biomedical Physics*, A. Brahme, Ed., Oxford: Elsevier, Jan. 2014, pp. 181–211, ISBN: 978-0-444-53633-4. DOI: 10.1016/B978-0-444-53632-7.00110-6.

[61] A. M. Oni, A. S. M. Mohsin, M. M. Rahman, and M. B. Hossain Bhuian, "A comprehensive evaluation of solar cell technologies, associated loss mechanisms, and efficiency enhancement strategies for photovoltaic cells," *Energy Reports*, vol. 11, pp. 3345–3366, Jun. 2024, ISSN: 2352-4847. DOI: 10.1016/j.egyr.2024.03.007.

[62] B. G. Streetman, "18 - Semiconductors and Transistors," in *Reference Data for Engineers (Ninth Edition)*, W. M. Middleton and M. E. Van Valkenburg, Eds., Woburn: Newnes, Jan. 2002, pp. 18–1, ISBN: 978-0-7506-7291-7. DOI: 10.1016/B978-075067291-7/50020-0.

[63] L. C. Hirst, "Principles of Solar Energy Conversion*," in *Comprehensive Renewable Energy (Second Edition)*, T. M. Letcher, Ed., Oxford: Elsevier, Jan. 2022, pp. 234–255, ISBN: 978-0-12-819734-9. DOI: 10.1016/B978-0-12-819727-1.00112-6.

[64] M. A. M. Al-Alwani, A. B. Mohamad, N. A. Ludin, A. A. H. Kadhum, and K. Sopian, "Dye-sensitised solar cells: Development, structure, operation principles, electron kinetics, characterisation, synthesis materials and natural photosensitisers," *Renewable and Sustainable Energy Reviews*, vol. 65, pp. 183–213, Nov. 2016, ISSN: 1364-0321. DOI: 10.1016/j.rser.2016.06.045.

[65] M. Schleuning, I. Y. Ahmet, R. v. d. Krol, and M. M. May, "The role of selective contacts and built-in field for charge separation and transport in photoelectrochemical devices," en, *Sustainable Energy & Fuels*, vol. 6, no. 16, pp. 3701–3716, 2022. DOI: 10.1039/D2SE00562J.

[66] T. Lv, J. Li, N. Arif, *et al.*, "Polarization and external-field enhanced photocatalysis," *Matter*, vol. 5, no. 9, pp. 2685–2721, Sep. 2022, ISSN: 2590-2385. DOI: 10.1016/j.matt.2022.06.004.

[67] S. Sengottain, K. A. Hammoodi, E. Tamma, *et al.*, "A technical appraisal of solar photovoltaic-integrated single slope single basin solar still for simultaneous energy and water generation," *Case Studies in Thermal Engineering*, vol. 54, p. 104 032, Feb. 2024. DOI: 10.1016/j.csite.2024.104032.

[68] M. J. Hossain, M. Sun, and K. O. Davis, "Photon management in silicon photovoltaic cells: A critical review," *Solar Energy Materials and Solar Cells*, vol. 267, p. 112 715, Apr. 2024, ISSN: 0927-0248. DOI: 10.1016/j.solmat.2024.112715.

[69] L. Derbali, A. Zarroug, and H. Ezzaouia, "Minority carrier lifetime and efficiency improvement of multicrystalline silicon solar cells by two-step process," *Renewable Energy*, vol. 77, pp. 331–337, May 2015, ISSN: 0960-1481. DOI: 10.1016/j.renene.2014.12.014.

[70] G. Sharma Gaudel, S.-J. Yu, D. Parajuli, *et al.*, "Reflectance Minimization of GaAs Solar Cell with Single- and Double-Layer Anti-Reflection Coatings: A Simulation Study," en, *Coatings*, vol. 15, no. 2, p. 204, Feb. 2025, ISSN: 2079-6412. DOI: 10.3390/coatings15020204.

[71] G. G. Njema, J. K. Kibet, and S. M. Ngari, "Performance optimization of a novel perovskite solar cell with power conversion efficiency exceeding 37% based on methylammonium tin iodide," *Next Energy*, vol. 6, p. 100 182, Jan. 2025, ISSN: 2949-821X. DOI: 10.1016/j.nxener.2024.100182.

[72] M. Bošnjaković, R. Santa, Z. Crnac, and T. Bošnjaković, "Environmental Impact of PV Power Systems," en, *Sustainability*, vol. 15, no. 15, p. 11 888, Jan. 2023, ISSN: 2071-1050. DOI: 10.3390/su151511888.

[73] S. Panagoda, G. Tilanka, I. Sandunika, *et al.*, "Advancements In Photovoltaic (Pv) Technology for Solar Energy Generation," vol. 43, pp. 30–72, Jul. 2023.

[74] A. M. Humada, M. Hojabri, S. Mekhilef, and H. M. Hamada, "Solar cell parameters extraction based on single and double-diode models: A review," en, *Renewable and Sustainable Energy Reviews*, vol. 56, pp. 494–509, Apr. 2016, ISSN: 13640321. DOI: 10.1016/j.rser.2015.11.051.

[75] T. Campos, "Thèse soutenue à Paris-Saclay, le 16 mai 2023, par," fr,

[76] G. Uddin, "Development of Simplified In Situ Processing Routes for Rear-Side Patterning of Silicon Heterojunction Interdigitated Back Contact (SHJ-IBC) Solar Cells," en,

[77] *External quantum efficiency measurement of solar cell*. Jul. 2017. DOI: 10.1109/QIR.2017.8168528.

[78] *Quantum Efficiency \textbar PVEducation*. [Online]. Available: https://www.pveducation.org/pvcdrom/solar-cell-operation/quantum-efficiency (visited on 08/01/2025).

[79] O. Almora, C. I. Cabrera, J. Garcia-Cerrillo, T. Kirchartz, U. Rau, and C. J. Brabec, "Quantifying the Absorption Onset in the Quantum Efficiency of Emerging Photovoltaic Devices," en, *Advanced Energy Materials*, vol. 11, no. 16, p. 2 100 022, 2021, ISSN: 1614-6840. DOI: 10.1002/aenm.202100022.

[80] F. Khaleda, V. Balakrishnan, and N. Abd Rahim, "Spectral response and quantum efficiency evaluation of solar cells: A review," in Jan. 2021, pp. 525–566, ISBN: 978-0-12-823710-6. DOI: 10.1016/B978-0-12-823710-6.00014-5.

[81] N. Ali, S. Attique, A. Rahimi-Iman, *et al.*, "Beyond lead: Progress in stable and non-toxic lower-dimensional perovskites for high-performance photodetection," *Sustainable Materials and Technologies*, vol. 38, e00759, Dec. 2023, ISSN: 2214-9937. DOI: 10.1016/j.susmat.2023.e00759.

[82] *Principles of Photovoltaics, Photovoltaic Materials \textbar Solar Energy*. [Online]. Available: https://www.greenrhinoenergy.com/solar/technologies/pv_cells.php (visited on 08/02/2025).

[83] P. Ghosh, S. Senthilarasu, T. Nixon, and S. Krishnamurthy, "Influence of Nanostructures in Perovskite Solar Cells," en, in *Reference Module in Materials Science and Materials Engineering*, Elsevier, 2016, B9780128035818040625, ISBN: 978-0-12-803581-8. DOI: 10.1016/B978-0-12-803581-8.04062-5.

[84] Congxinhe, *PV Cell Construction and Working*, en-US, Publication Title: Solar N Plus, Jun. 2024. [Online]. Available: https://www.solarnplus.com/pv-cell-construction-and-working/ (visited on 08/02/2025).

[85] N. Mariotti, M. Bonomo, and C. Barolo, "Emerging Photovoltaic Technologies and Eco-Design—Criticisms and Potential Improvements," in Jan. 2020, ISBN: 978-1-78984-822-9. DOI: 10.5772/intechopen.88327.

[86] G. Nazir, A. Rehman, J. Gautam, *et al.*, "Advancements in flexible Perovskite solar cells and their integration into self-powered wearable optoelectronic systems," *Advanced Powder Materials*, vol. 4, no. 4, p. 100 304, Aug. 2025, ISSN: 2772-834X. DOI: 10.1016/j.apmate.2025.100304.

[87] L. Shen, Z. Li, and T. Ma, "Analysis of the power loss and quantification of the energy distribution in PV module," en, *Applied Energy*, vol. 260, p. 114 333, Feb. 2020, ISSN: 03062619. DOI: 10.1016/j.apenergy.2019.114333.

[88] M. Dhankhar, O. Pal Singh, and V. Singh, "Physical principles of losses in thin film solar cells and efficiency enhancement methods," en, *Renewable and Sustainable Energy Reviews*, vol. 40, pp. 214–223, Dec. 2014, ISSN: 13640321. DOI: 10.1016/j.rser.2014.07.163.

[89] R. Vaillon, O. Dupré, R. B. Cal, and M. Calaf, "Pathways for mitigating thermal losses in solar photovoltaics," en, *Sci Rep*, vol. 8, no. 1, p. 13 163, Sep. 2018, ISSN: 2045-2322. DOI: 10.1038/s41598-018-31257-0.

[90] J.-F. Lelièvre, "Elaboration de SiNx:H par PECVD: Optimisation des Proprieties Optiques, Passivantes et Structurales pour Applications Photovoltaïques," PhD Thesis, Apr. 2007.

[91] V. Eze, K. Richard, U. K.J, and W. Okafor, "Factors Influencing the Efficiency of Solar Energy Systems," vol. 6, pp. 119–131, Dec. 2024. DOI: 10.36079/lamintang.jetas-0603.748.

[92] S. Sadhukhan, S. Acharya, T. Panda, *et al.*, "Chapter 4 - Evolution of high efficiency passivated emitter and rear contact (PERC) solar cells," in *Sustainable Developments by Artificial Intelligence and Machine Learning for Renewable Energies*, K. Kumar, R. S. Rao, O. Kaiwartya, M. S. Kaiser, and S. Padmanaban, Eds., Elsevier, Jan. 2022, pp. 63–129, ISBN: 978-0-323-91228-0. DOI: 10.1016/B978-0-323-91228-0.00007-0.

[93] A. S. Garcia, "Theoretical Studies in Solar Cell Physics," eng, Doctoral thesis, University of Agder, 2022.

[94] I. Ramiro, "Chapter 3 - Working Principles of a Solar Cell," in *Fundamentals of Solar Cells and Photovoltaic Systems Engineering*, M. Victoria, Ed., Academic Press, Jan. 2025, pp. 59–97, ISBN: 978-0-323-96105-9. DOI: 10.1016/B978-0-323-96105-9.00003-3.

[95] *Solar Electricity, 2nd Edition \textbar Wiley*, en, Publication Title: Wiley.com. [Online]. Available: https://www.wiley.com/en-us/Solar+Electricity%2C+2nd+Edition-p-9780471988526 (visited on 08/03/2025).

[96] W. Shockley and W. T. Read, "Statistics of the Recombinations of Holes and Electrons," *Phys. Rev.*, vol. 87, no. 5, pp. 835–842, Sep. 1952. DOI: 10.1103/PhysRev.87.835.

[97] R. N. Hall, "Electron-Hole Recombination in Germanium," *Phys. Rev.*, vol. 87, no. 2, pp. 387–387, Jul. 1952. DOI: 10.1103/PhysRev.87.387.

[98] J. Nelson, "The Physics of Solar Cells," *The physics of solar cells, by Jenny Nelson. London: Imperial College Press, 2003*, vol. 57, May 2003, ISSN: 978-1-86094-340-9. DOI: 10.1142/p276.

[99] M. B. Askari, V. Mirzaei Mahmoud Abadi, and M. Mirhabibi, "Types of Solar Cells and Application," *American Journal of Optics and Photonics*, vol. 3, p. 2015, Aug. 2015. DOI: 10.11648/j.ajop.20150305.17.

[100] S. Sharma, K. K. Jain, and A. Sharma, "Solar Cells: In Research and Applications—A Review," en, *Materials Sciences and Applications*, vol. 6, no. 12, pp. 1145–1155, Dec. 2015. DOI: 10.4236/msa.2015.612113.

[101] A. M. Bagher, M. M. A. Vahid, and M. Mohsen, "Types of Solar Cells and Application," En, *Am. J. Opt. Photonics*, vol. 3, no. 5, pp. 94–113, Aug. 2015, ISSN: 2330-8494. DOI: 10.11648/j.ajop.20150305.17.

[102] C. Ballif, F.-J. Haug, M. Boccard, P. Verlinden, and G. Hahn, "Status and perspectives of crystalline silicon photovoltaics in research and industry," *Nature Reviews Materials*, vol. 7, Mar. 2022. DOI: 10.1038/s41578-022-00423-2.

[103] V. Sharma and S. Chandel, "Performance and degradation analysis for long term reliability of solar photovoltaic systems: A review," en, *Renewable and Sustainable Energy Reviews*, vol. 27, pp. 753–767, Nov. 2013, ISSN: 13640321. DOI: 10.1016/j.rser.2013.07.046.

[104] E. Kondolot Solak and E. Irmak, "Advances in organic photovoltaic cells: A comprehensive review of materials, technologies, and performance," en, *RSC Advances*, vol. 13, no. 18, pp. 12 244–12 269, 2023. DOI: 10.1039/D3RA01454A.

[105] N. Shah, A. A. Shah, P. K. Leung, *et al.*, "A Review of Third Generation Solar Cells," en, *Processes*, vol. 11, no. 6, p. 1852, Jun. 2023, ISSN: 2227-9717. DOI: 10.3390/pr11061852.

[106] *Best Research-Cell Efficiency Chart \textbar Photovoltaic Research \textbar NREL*. [Online]. Available: https://www.nrel.gov/pv/cell-efficiency (visited on 08/10/2025).

[107] V. V. Tyagi, N. A. A. Rahim, N. A. Rahim, and J. A. /. Selvaraj, "Progress in solar PV technology: Research and achievement," *Renewable and Sustainable Energy Reviews*, vol. 20, pp. 443–461, Apr. 2013, ISSN: 1364-0321. DOI: 10.1016/j.rser.2012.09.028.

[108] J. Pastuszak and P. Węgierek, "Photovoltaic Cell Generations and Current Research Directions for Their Development," en, *Materials*, vol. 15, no. 16, p. 5542, Jan. 2022, ISSN: 1996-1944. DOI: 10.3390/ma15165542.

[109] F. Ferrazza, "Chapter IB-1 - Crystalline Silicon: Manufacture and Properties," in *Practical Handbook of Photovoltaics (Second Edition)*, A. McEvoy, T. Markvart, and L. Castañer, Eds., Boston: Academic Press, Jan. 2012, pp. 79–97, ISBN: 978-0-12-385934-1. DOI: 10.1016/B978-0-12-385934-1.00004-0.

[110] T. Aziz, H. Fan, F. Khan, M. Haroon, and L. Cheng, "Modified silicone oil types, mechanical properties and applications," *Polymer Bulletin*, vol. 76, Apr. 2019. DOI: 10.1007/s00289-018-2471-2.

[111] M. A. Green, "Solar cells: Operating principles, technology, and system applications," 1982.

[112] T. Saga, "Advances in crystalline silicon solar cell technology for industrial mass production," en, *NPG Asia Mater*, vol. 2, no. 3, pp. 96–102, Jul. 2010, ISSN: 1884-4057. DOI: 10.1038/asiamat.2010.82.

[113] S. A. U. Hasan, M. A. Zahid, S. Park, and J. Yi, "Stability Challenges for a Highly Efficient Perovskite/Silicon Tandem Solar Cell: A Review," en, *Solar RRL*, vol. 8, no. 6, p. 2 300 967, 2024, ISSN: 2367-198X. DOI: 10.1002/solr.202300967.

[114] Solaron, *Manufacturing Polycrystalline Silicon \textbar Solaron*, en-US, May 2019. [Online]. Available: https://solaron.net/solar/manufacturing-polycrystalline-silicon/ (visited on 08/09/2025).

[115] J. Kim, M. Rabelo, S. P. Padi, H. Yousuf, E.-C. Cho, and J. Yi, "A Review of the Degradation of Photovoltaic Modules for Life Expectancy," en, *Energies*, vol. 14, no. 14, p. 4278, Jan. 2021, ISSN: 1996-1073. DOI: 10.3390/en14144278.

[116] R. Basnet, L. Jones, M. A. Azmie, M. Jones, M. McCann, and M. Ernst, "Advancing circular economy of silicon Photovoltaics: Current status and challenges of PV module reuse," *Solar Energy Materials and Solar Cells*, vol. 292, p. 113 816, Oct. 2025, ISSN: 0927-0248. DOI: 10.1016/j.solmat.2025.113816.

[117] H. J. Jeon, H. Park, G. Koyyada, S. Alhammadi, and J. H. Jung, "Optimal Cooling System Design for Increasing the Crystal Growth Rate of Single-Crystal Silicon Ingots in the Czochralski Process Using the Crystal Growth Simulation," en, *Processes*, vol. 8, no. 9, p. 1077, Sep. 2020, ISSN: 2227-9717. DOI: 10.3390/pr8091077.

[118] S. Kar and S. Dey, "Alternate Photovoltaic Material: Its Environmental Consequences," en, in *Encyclopedia of Renewable and Sustainable Materials*, Elsevier, 2020, pp. 250–264, ISBN: 978-0-12-813196-1. DOI: 10.1016/B978-0-12-803581-8.11052-5.

[119] C.-w. Lan, C.-K. Hsieh, and W.-C. Hsu, "Czochralski Silicon Crystal Growth for Photovoltaic Applications," in Mar. 2010, pp. 25–39, ISBN: 978-3-642-02043-8. DOI: 10.1007/978-3-642-02044-5_2.

[120] M. Di Sabatino, R. Hendawi, and A. Sanchez Garcia, "Silicon Solar Cells: Trends, Manufacturing Challenges, and AI Perspectives," *Crystals*, vol. 14, p. 167, Feb. 2024. DOI: 10.3390/cryst14020167.

[121] admin-lk, *Les fours de cristallisation du silicium photovoltaïque*, fr-FR, Publication Title: Encyclopédie de l'énergie, May 2017. [Online]. Available: https://www.encyclopedie-energie.org/les-fours-de-cristallisation-du-silicium-photovoltaique/ (visited on 08/03/2025).

[122] A. Razzaq, T. G. Allen, W. Liu, Z. Liu, and S. De Wolf, "Silicon heterojunction solar cells: Techno-economic assessment and opportunities," *Joule*, vol. 6, no. 3, pp. 514–542, Mar. 2022, ISSN: 2542-4351. DOI: 10.1016/j.joule.2022.02.009.

[123] A. Richter, M. Hermle, and S. Glunz, "Reassessment of the Limiting Efficiency for Crystalline Silicon Solar Cells," *IEEE Journal of Photovoltaics*, vol. 3, pp. 1184–1191, Jul. 2013. DOI: 10.1109/JPHOTOV.2013.2270351.

[124] A. Le Donne, V. Trifiletti, and S. Binetti, "New Earth-Abundant Thin Film Solar Cells Based on Chalcogenides," English, *Front. Chem.*, vol. 7, Apr. 2019, ISSN: 2296-2646. DOI: 10.3389/fchem.2019.00297.

[125] K. L. Chopra, P. D. Paulson, and V. Dutta, "Thin-film solar cells: An overview," en, *Progress in Photovoltaics: Research and Applications*, vol. 12, no. 2-3, pp. 69–92, 2004, ISSN: 1099-159X. DOI: 10.1002/pip.541.

[126] J. Ramanujam, D. Bishop, T. Todorov, *et al.*, "Flexible CIGS, CdTe and a-Si:H based thin film solar cells: A review," *Progress in Materials Science*, vol. 110, p. 100 619, Nov. 2019. DOI: 10.1016/j.pmatsci.2019.100619.

[127] K. D. G. I. Jayawardena, L. J. Rozanski, C. A. Mills, M. J. Beliatis, N. A. Nismy, and S. R. P. Silva, "'Inorganics-in-Organics': Recent developments and outlook for 4G polymer solar cells," en, *Nanoscale*, vol. 5, no. 18, pp. 8411–8427, Aug. 2013, ISSN: 2040-3372. DOI: 10.1039/C3NR02733C.

[128] F. Meillaud, M. Boccard, G. Bugnon, *et al.*, "Recent advances and remaining challenges in thin-film silicon photovoltaic technology," *Materials Today*, vol. 18, no. 7, pp. 378–384, Sep. 2015, ISSN: 1369-7021. DOI: 10.1016/j.mattod.2015.03.002.

[129] A. Maalouf, T. Okoroafor, Z. Jehl, V. Babu, and S. Resalati, "A comprehensive review on life cycle assessment of commercial and emerging thin-film solar cell systems," *Renewable and Sustainable Energy Reviews*, vol. 186, p. 113 652, Oct. 2023, ISSN: 1364-0321. DOI: 10.1016/j.rser.2023.113652.

[130] A. Marshall, *Solaire photovoltaïque : Les technologies et leurs trajectoires*, fr-FR, Publication Title: Encyclopédie de l'énergie, Mar. 2019. [Online]. Available: https://www.encyclopedie-energie.org/solaire-photovoltaique-les-technologies-et-leurs-trajectoires/ (visited on 08/08/2025).

[131] L. Hughes, N. Bristow, T. Korochkina, *et al.*, "Assessing the potential of steel as a substrate for building integrated photovoltaic applications," *Applied Energy*, vol. 229, pp. 209–223, Nov. 2018, ISSN: 0306-2619. DOI: 10.1016/j.apenergy.2018.07.119.

[132] F. Batista, A. S. Guimarães, and A. I. Palmero-Marrero, "Building Integrated Photovoltaics: A multi-level design review for optimized implementation," *Renewable and Sustainable Energy Reviews*, vol. 220, p. 115 837, Sep. 2025, ISSN: 1364-0321. DOI: 10.1016/j.rser.2025.115837.

[133] A. Mdallal, A. Yasin, M. Mahmoud, M. A. Abdelkareem, A. H. Alami, and A. G. Olabi, "A comprehensive review on solar photovoltaics: Navigating generational shifts, innovations, and sustainability," *Sustainable Horizons*, vol. 13, p. 100 137, Mar. 2025, ISSN: 2772-7378. DOI: 10.1016/j.horiz.2025.100137.

[134] H. J. T. Nkuissi, F. K. Konan, B. Hartiti, *et al.*, "Toxic Materials Used in Thin Film Photovoltaics and Their Impacts on Environment," en, in *Reliability and Ecological Aspects of Photovoltaic Modules*, IntechOpen, Jan. 2020, ISBN: 978-1-78984-823-6. DOI: 10.5772/intechopen.88326.

[135] M. G. Buonomenna, "Inorganic Thin-Film Solar Cells: Challenges at the Terawatt-Scale," *Symmetry*, vol. 15, p. 1718, Sep. 2023. DOI: 10.3390/sym15091718.

[136] S. Al-Ali, A. G. Olabi, and M. Mahmoud, "A review of solar photovoltaic technologies: Developments, challenges, and future perspectives," *Energy Conversion and Management: X*, vol. 27, p. 101 057, Jul. 2025, ISSN: 2590-1745. DOI: 10.1016/j.ecmx.2025.101057.

[137] M. Moreno, R. Ambrosio, A. Torres, *et al.*, "Amorphous, Polymorphous, and Microcrystalline Silicon Thin Films Deposited by Plasma at Low Temperatures," en, in *Crystalline and Non-crystalline Solids*, IntechOpen, Jun. 2016, ISBN: 978-953-51-2446-7. DOI: 10.5772/63522.

[138] R. Jaiswal, A. Kumar, and A. Yadav, "Chapter 23 - Nanomaterials based solar cells," in *Nanotechnology in the Automotive Industry*, ser. Micro and Nano Technologies, H. Song, T. A. Nguyen, G. Yasin, N. B. Singh, and R. K. Gupta, Eds., Elsevier, Jan. 2022, pp. 467–484, ISBN: 978-0-323-90524-4. DOI: 10.1016/B978-0-323-90524-4.00025-6.

[139] Y. Zhao, X. Zhang, and B. Yan, "Hydrogenated Amorphous Silicon Thin Film," en, in *Handbook of Photovoltaic Silicon*, Springer, Berlin, Heidelberg, 2019, pp. 639–692, ISBN: 978-3-662-56472-1. DOI: 10.1007/978-3-662-56472-1_27.

[140] R. W. Miles, K. M. Hynes, and I. Forbes, "Photovoltaic solar cells: An overview of state-of-the-art cell development and environmental issues," *Progress in Crystal Growth and Characterization of Materials*, vol. 51, no. 1, pp. 1–42, Jan. 2005, ISSN: 0960-8974. DOI: 10.1016/j.pcrysgrow.2005.10.002.

[141] V. Avrutin, N. Izyumskaya, and H. Morkoç, "Semiconductor solar cells: Recent progress in terrestrial applications," *Superlattices and Microstructures*, vol. 49, no. 4, pp. 337–364, Apr. 2011, ISSN: 0749-6036. DOI: 10.1016/j.spmi.2010.12.011.

[142] P. Sharma and R. K. Mishra, "Comprehensive study on photovoltaic cell's generation and factors affecting its performance: A Review," en, *Mater Renew Sustain Energy*, vol. 14, no. 1, p. 21, Feb. 2025, ISSN: 2194-1467. DOI: 10.1007/s40243-024-00292-5.

[143] W. Cao, J. Li, H. Chen, and J. Xue, "Transparent electrodes for organic optoelectronic devices: A review," *Journal of Photonics for Energy*, vol. 4, Oct. 2014. DOI: 10.1117/1.JPE.4.040990.

[144] M. Girtan and B. Negulescu, "A review on oxide/metal/oxide thin films on flexible substrates as electrodes for organic and perovskite solar cells," *Optical Materials: X*, vol. 13, p. 100 122, Jan. 2022, ISSN: 2590-1478. DOI: 10.1016/j.omx.2021.100122.

[145] A. Shah, "Thin-Film Silicon Solar Cells Thin-Film Silicon Solar Cells," *Practical Handbook of Photovoltaics*, pp. 209–281, Dec. 2012, ISSN: 9780123859341. DOI: 10.1016/B978-0-12-385934-1.00008-8.

[146] M. Tsuji, T. Aramoto, H. Ohyama, T. Hibino, and K. Omura, "Characterization of CdS Thin-Film in High Efficient CdS/CdTe Solar Cells," *Journal of Crystal Growth*, vol. 214-215, pp. 1142–1147, Jul. 2000. DOI: 10.1016/S0022-0248(00)00291-8.

[147] A. Morales-Acevedo, "Thin film CdS/CdTe solar cells: Research perspectives," *Solar Energy*, vol. 80, pp. 675–681, Jun. 2006. DOI: 10.1016/j.solener.2005.10.008.

[148] S. Surabhi, KumarAnurag, S. Rajpal, and S. R. Kumar, "A new route for preparing CdTe thin films by chemical bath deposition," *Materials Today: Proceedings*, International Conference on Materials, Processing & Characterization, vol. 44, pp. 1463–1467, Jan. 2021, ISSN: 2214-7853. DOI: 10.1016/j.matpr.2020.11.635.

[149] M. O. Mavukkandy, S. A. McBride, D. M. Warsinger, N. Dizge, S. W. Hasan, and H. A. Arafat, "Thin film deposition techniques for polymeric membranes–A review," *Journal of Membrane Science*, vol. 610, p. 118 258, Sep. 2020, ISSN: 0376-7388. DOI: 10.1016/j.memsci.2020.118258.

[150] A. Cao, T. Tan, H. Zhang, Y. Du, Y. Sun, and G. Zha, "Electronic structures and optical properties of the CdTe/CdS heterojunction interface from the first-principles calculations," *Physica B: Condensed Matter*, vol. 545, pp. 323–329, Sep. 2018, ISSN: 0921-4526. DOI: 10.1016/j.physb.2018.06.035.

[151] M. A. Scarpulla, B. McCandless, A. B. Phillips, *et al.*, "CdTe-based thin film photovoltaics: Recent advances, current challenges and future prospects," *Solar Energy Materials and Solar Cells*, vol. 255, p. 112 289, Jun. 2023, ISSN: 0927-0248. DOI: 10.1016/j.solmat.2023.112289.

[152] W. A. Badawy, "A review on solar cells from Si-single crystals to porous materials and quantum dots," *Journal of Advanced Research*, vol. 6, no. 2, pp. 123–132, Mar. 2015, ISSN: 2090-1232. DOI: 10.1016/j.jare.2013.10.001.

[153] C. Zhang, T. Qi, W. Wang, *et al.*, "High efficiency CIGS solar cells on flexible stainless steel substrate with SiO2 diffusion barrier layer," *Solar Energy*, vol. 230, pp. 1033–1039, Dec. 2021. DOI: 10.1016/j.solener.2021.11.006.

[154] M. Nakamura, K. Yamaguchi, Y. Kimoto, Y. Yasaki, T. Kato, and H. Sugimoto, "Cd-Free Cu(In,Ga)(Se,S)2 thin-film solar cell with record efficiency of 23.35%," *IEEE Journal of Photovoltaics*, vol. 9, pp. 1863–1867, Sep. 2019. DOI: 10.1109/JPHOTOV.2019.2937218.

[155] P. Reinhard, Chiril, Bl, *et al.*, "Review of Progress Toward 20% Efficiency Flexible CIGS Solar Cells and Manufacturing Issues of Solar Modules," *Photovoltaics, IEEE Journal of*, vol. 3, pp. 572–580, Jun. 2013. DOI: 10.1109/jphotov.2012.2226869.

[156] K. Machkih, R. Oubaki, and M. Makha, "A Review of CIGS Thin Film Semiconductor Deposition via Sputtering and Thermal Evaporation for Solar Cell Applications," en, *Coatings*, vol. 14, no. 9, p. 1088, Sep. 2024, ISSN: 2079-6412. DOI: 10.3390/coatings14091088.

[157] V. Kumar, R. Prasad, N. B. Chaure, and U. P. Singh, "Advancement in Copper Indium Gallium Diselenide (CIGS)-Based Thin-Film Solar Cells," en, in *Recent Advances in Thin Film Photovoltaics*, U. P. Singh and N. B. Chaure, Eds., Singapore: Springer Nature, 2022, pp. 5–39, ISBN: 978-981-19-3724-8. DOI: 10.1007/978-981-19-3724-8_2.

[158] B. M. Kayes, H. Nie, R. Twist, *et al.*, "27.6% Conversion efficiency, a new record for single-junction solar cells under 1 sun illumination," in *2011 37th IEEE Photovoltaic Specialists Conference*, Jun. 2011, pp. 000 004–000 008. DOI: 10.1109/PVSC.2011.6185831.

[159] T. Kenning, *Alta Devices sets GaAs solar cell efficiency record at 29.1%, joins NASA space station testing*, en-US, Publication Title: PV Tech, Dec. 2018. [Online]. Available: https://www.pv-tech.org/alta-devices-sets-gaas-solar-cell-efficiency-record-at-29-1-joins-nasa-spac/ (visited on 08/10/2025).

[160] P. Dai, Z. Xu, Y. Lu, *et al.*, *GaN Film Grown by Molecular Beam Epitaxy*. Oct. 2022. DOI: 10.1109/ICICM56102.2022.10011369.

[161] M. Yamaguchi, F. Dimroth, N. J. Ekins-Daukes, N. Kojima, and Y. Ohshita, "Overview and loss analysis of III–V single-junction and multi-junction solar cells," en, *EPJ Photovolt.*, vol. 13, p. 22, 2022, ISSN: 2105-0716. DOI: 10.1051/epjpv/2022020.

[162] *Silicon-based Multijunction Solar Cell Reaches Record Efficiency of 36.1 Percent - Fraunhofer ISE*, en, Publication Title: Fraunhofer Institute for Solar Energy Systems ISE, Sep. 2023. [Online]. Available: https://www.ise.fraunhofer.de/en/press-media/news/2023/silicon-based-multijunction-solar-cell-reaches-record-efficiency-of361-percent.html (visited on 08/10/2025).

[163] A. T. Raisa, S. N. Sakib, M. J. Hossain, K. A. Rocky, and A. Kowsar, "Advances in multijunction solar cells: An overview," *Solar Energy Advances*, vol. 5, p. 100 105, Jan. 2025, ISSN: 2667-1131. DOI: 10.1016/j.seja.2025.100105.

[164] N. Mukwevho, A. Mkhohlakali, N. Ntsasa, *et al.*, "Methodological approaches for resource recovery from end-of-life panels of different generations of photovoltaic technologies – A review," *Renewable and Sustainable Energy Reviews*, vol. 207, p. 114 980, Jan. 2025, ISSN: 1364-0321. DOI: 10.1016/j.rser.2024.114980.

[165] S. Ananthakumar, J. R. Kumar, and S. M. Babu, "Third-Generation Solar Cells: Concept, Materials and Performance - An Overview," en, in *Emerging Nanostructured Materials for Energy and Environmental Science*, S. Rajendran, M. Naushad, K. Raju, and R. Boukherroub, Eds., Cham: Springer International Publishing, 2019, pp. 305–339, ISBN: 978-3-030-04474-9. DOI: 10.1007/978-3-030-04474-9_7.

[166] K. Lu, "Comparison and Evaluation of Different Types of Solar Cells," *Applied and Computational Engineering*, vol. 23, pp. 263–270, Nov. 2023. DOI: 10.54254/2755-2721/23/20230664.

[167] X. Zhao, Y. Du, W. Li, Z. Zhao, and M. Lei, "Organic/inorganic hybrids for intelligent sensing and wearable clean energy applications," en, *Adv Compos Hybrid Mater*, vol. 6, no. 5, p. 176, Sep. 2023, ISSN: 2522-0136. DOI: 10.1007/s42114-023-00751-z.

[168] M. S. A. Kamel, A. Al-jumaili, M. Oelgemöller, and M. V. Jacob, "Inorganic nanoparticles to overcome efficiency inhibitors of organic photovoltaics: An in-depth review," en, *Renewable and Sustainable Energy Reviews*, vol. 166, no. C, 2022.

[169] L. Lu, T. Zheng, Q. Wu, A. M. Schneider, D. Zhao, and L. Yu, "Recent Advances in Bulk Heterojunction Polymer Solar Cells," *Chem. Rev.*, vol. 115, no. 23, pp. 12 666–12 731, Dec. 2015, ISSN: 0009-2665. DOI: 10.1021/acs.chemrev.5b00098.

[170] H. Fu, L. Yuxiang, J. Yu, *et al.*, "High Efficiency (15.8%) All-Polymer Solar Cells Enabled by a Regioregular Narrow Bandgap Polymer Acceptor," *Journal of the American Chemical Society*, vol. 143, Feb. 2021. DOI: 10.1021/jacs.0c12527.

[171] S. Dowland, T. Lutz, A. Ward, *et al.*, "Direct Growth of Metal Sulfide Nanoparticle Networks in Solid-State Polymer Films for Hybrid Inorganic–Organic Solar Cells," *Advanced Materials*, vol. 23, no. 24, pp. 2739–2744, 2011, ISSN: 1521-4095. DOI: 10.1002/adma.201100625.

[172] Y. Guo, Y. Li, O. Awartani, *et al.*, "A Vinylene-Bridged Perylenediimide-Based Polymeric Acceptor Enabling Efficient All-Polymer Solar Cells Processed under Ambient Conditions," *Advanced Materials*, vol. 28, no. 38, pp. 8483–8489, 2016, ISSN: 1521-4095. DOI: 10.1002/adma.201602387.

[173] G. Zhang, X. Xu, Y. W. Lee, H. Y. Woo, Y. Li, and Q. Peng, "Achieving a High Fill Factor and Stability in Perylene Diimide–Based Polymer Solar Cells Using the Molecular Lock Effect between 4,4'-Bipyridine and a Tri(8-hydroxyquinoline)aluminum(III) Core," en, *Advanced Functional Materials*, vol. 29, no. 29, p. 1 902 079, 2019, ISSN: 1616-3028. DOI: 10.1002/adfm.201902079.

[174] H. Haloui, K. Touafek, and A. Khelifa, "Modeling of a hybrid thermal photovoltaic (PVT) collector based on thin film organic solar cells," *Electric Power Systems Research*, vol. 210, p. 108 131, Sep. 2022, ISSN: 0378-7796. DOI: 10.1016/j.epsr.2022.108131.

[175] V. M. Moorthy and V. M. Srivastava, "Device Modeling of Organic Photovoltaic Cells with Traditional and Inverted Cells Using s-SWCNT:C60 as Active Layer," en, *Nanomaterials*, vol. 12, no. 16, p. 2844, Jan. 2022, ISSN: 2079-4991. DOI: 10.3390/nano12162844.

[176] Y. K. Kim, T. H. Lee, J. Yeop, *et al.*, "Hetero-tandem organic solar cells drive water electrolysis with a solar-to-hydrogen conversion efficiency up to 10%," *Applied Catalysis B: Environmental*, vol. 309, p. 121 237, Jul. 2022, ISSN: 0926-3373. DOI: 10.1016/j.apcatb.2022.121237.

[177] A. Gambhir, P. Sandwell, and J. Nelson, "The future costs of OPV – A bottom-up model of material and manufacturing costs with uncertainty analysis," *Solar Energy Materials and Solar Cells*, vol. 156, Jun. 2016. DOI: 10.1016/j.solmat.2016.05.056.

[178] C. M. Nkinyam, C. O. Ujah, K. C. Nnakwo, and D. V. V. Kallon, "Insight into organic photovoltaic cell: Prospect and challenges," *Unconventional Resources*, vol. 5, p. 100 121, Jan. 2025, ISSN: 2666-5190. DOI: 10.1016/j.uncres.2024.100121.

[179] B. H. S. Miranda, L. d. Q. Corrêa, G. A. Soares, *et al.*, "Efficient fully roll-to-roll coated encapsulated organic solar module for indoor applications," *Solar Energy*, vol. 220, pp. 343–353, May 2021, ISSN: 0038-092X. DOI: 10.1016/j.solener.2021.03.025.

[180] X. Meng, Z. Xing, X. Hu, and Y. Chen, "Large-area Flexible Organic Solar Cells: Printing Technologies and Modular Design," zh, *zggx*, vol. 40, no. 12, pp. 1522–1566, Nov. 2022, ISSN: 0256-7679. DOI: 10.1007/s10118-022-2803-4.

[181] R. Ilmi, A. Haque, and M. Khan, "High efficiency small molecule-based donor materials for organic solar cells," *Organic Electronics*, vol. 58, pp. 53–62, Mar. 2018. DOI: 10.1016/j.orgel.2018.03.048.

[182] J. Wang, Y. Cui, Y. Xu, *et al.*, "A New Polymer Donor Enables Binary All-Polymer Organic Photovoltaic Cells with 18% Efficiency and Excellent Mechanical Robustness," en, *Advanced Materials*, vol. 34, no. 35, p. 2 205 009, 2022, ISSN: 1521-4095. DOI: 10.1002/adma.202205009.

[183] T. Zhang, C. An, Y. Cui, *et al.*, "A Universal Nonhalogenated Polymer Donor for High-Performance Organic Photovoltaic Cells," en, *Advanced Materials*, vol. 34, no. 2, p. 2 105 803, 2022, ISSN: 1521-4095. DOI: 10.1002/adma.202105803.

[184] Z. Wang, A. Tang, H. Wang, *et al.*, "Organic photovoltaic cells offer ultrahigh $V_{OC}$ of ˜ 1.2 V under AM 1.5G light and a high efficiency of 21.2 % under indoor light," *Chemical Engineering Journal*, vol. 451, p. 139 080, Jan. 2023, ISSN: 1385-8947. DOI: 10.1016/j.cej.2022.139080.

[185] A. Rafique, I. Ferreira, G. Abbas, and A. C. Baptista, "Recent Advances and Challenges Toward Application of Fibers and Textiles in Integrated Photovoltaic Energy Storage Devices," en, *Nano-Micro Lett.*, vol. 15, no. 1, p. 40, Jan. 2023, ISSN: 2150-5551. DOI: 10.1007/s40820-022-01008-y.

[186] H. Spanggaard and F. C. Krebs, "A brief history of the development of organic and polymeric photovoltaics," *Solar Energy Materials and Solar Cells*, The development of organic and polymer photovoltaics, vol. 83, no. 2, pp. 125–146, Jun. 2004, ISSN: 0927-0248. DOI: 10.1016/j.solmat.2004.02.021.

[187] N. Hossain, M. H. Mobarak, M. A. Mimona, *et al.*, "Advances and significances of nanoparticles in semiconductor applications – A review," *Results in Engineering*, vol. 19, p. 101 347, Sep. 2023, ISSN: 2590-1230. DOI: 10.1016/j.rineng.2023.101347.

[188] P. V. Kamat, "Boosting the Efficiency of Quantum Dot Sensitized Solar Cells through Modulation of Interfacial Charge Transfer," *Acc. Chem. Res.*, vol. 45, no. 11, pp. 1906–1915, Nov. 2012, ISSN: 0001-4842. DOI: 10.1021/ar200315d.

[189] S. Samukawa, "Quantum dot superlattice structure for high efficiency solar cells utilizing a bio-template and damage-free neutral beam etching," in *2012 IEEE 11th International Conference on Solid-State and Integrated Circuit Technology*, Oct. 2012, pp. 1–4. DOI: 10.1109/ICSICT.2012.6467698.

[190] O. E. Semonin, J. M. Luther, and M. C. Beard, "Quantum dots for next-generation photovoltaics," *Materials Today*, vol. 15, no. 11, pp. 508–515, Nov. 2012, ISSN: 1369-7021. DOI: 10.1016/S1369-7021(12)70220-1.

[191] L. Li, T. J. Daou, I. Texier, T. T. Kim Chi, N. Q. Liem, and P. Reiss, "Highly Luminescent CuInS2/ZnS Core/Shell Nanocrystals: Cadmium-Free Quantum Dots for In Vivo Imaging," *Chem. Mater.*, vol. 21, no. 12, pp. 2422–2429, Jun. 2009, ISSN: 0897-4756. DOI: 10.1021/cm900103b.

[192] M. Xing, Y. Zhang, Q. Shen, and R. Wang, "Temperature dependent photovoltaic performance of TiO2/PbS heterojunction quantum dot solar cells," *Solar Energy*, vol. 195, pp. 1–5, Jan. 2020, ISSN: 0038-092X. DOI: 10.1016/j.solener.2019.11.010.

[193] S. Kumar, M. Nehra, A. Deep, D. Kedia, N. Dilbaghi, and K.-H. Kim, "Quantum-sized nanomaterials for solar cell applications," *Renewable and Sustainable Energy Reviews*, vol. 73, pp. 821–839, Jun. 2017, ISSN: 1364-0321. DOI: 10.1016/j.rser.2017.01.172.

[194] B. D. Chernomordik, A. R. Marshall, G. F. Pach, J. M. Luther, and M. C. Beard, "Quantum Dot Solar Cell Fabrication Protocols," *Chem. Mater.*, vol. 29, no. 1, pp. 189–198, Jan. 2017, ISSN: 0897-4756. DOI: 10.1021/acs.chemmater.6b02939.

[195] G. Shilpa, P. M. Kumar, D. K. Kumar, *et al.*, "Recent advances in the development of high efficiency quantum dot sensitized solar cells (QDSSCs): A review," *Materials Science for Energy Technologies*, vol. 6, pp. 533–546, Jan. 2023, ISSN: 2589-2991. DOI: 10.1016/j.mset.2023.05.001.

[196] P. Kumar, R. Kumar, I. Iliev, *et al.*, "Engineered Quantum Dot Solar Cells: From Fundamentals to Applications," *Plasmonics*, pp. 1–21, Mar. 2025. DOI: 10.1007/s11468-025-02915-7.

[197] A. Azam, M. P. Suryawanshi, Y. Liu, *et al.*, "Quantum Dots-Enabled Downshifting and Downconversion Strategies for Enhanced Photovoltaics," *ACS Nano*, Aug. 2025, ISSN: 1936-0851. DOI: 10.1021/acsnano.5c04988.

[198] A. A. Ganesan, A. J. Houtepen, and R. W. Crisp, "Quantum Dot Solar Cells: Small Beginnings Have Large Impacts," en, *Applied Sciences*, vol. 8, no. 10, p. 1867, Oct. 2018, ISSN: 2076-3417. DOI: 10.3390/app8101867.

[199] J. H. Markna and P. K. Rathod, "Review on the efficiency of quantum dot sensitized solar cell: Insights into photoanodes and QD sensitizers," *Dyes and Pigments*, vol. 199, p. 110 094, Mar. 2022, ISSN: 0143-7208. DOI: 10.1016/j.dyepig.2022.110094.

[200] P. Surarapu, J. Rama, P. Ande, *et al.*, "Quantum Dot Sensitized Solar Cells: A Promising Avenue for Next-Generation Energy Conversion," *Asia Pacific Journal of Energy and Environment*, vol. 7, pp. 111–120, Dec. 2020. DOI: 10.18034/apjee.v7i2.728.

[201] Z. Li, L. Zhu, R. Wang, Y. Dong, and J. Hou, "Feasibility and challenges of quantum dot solar cells in urban renewal photovoltaic buildings," *Solar Energy*, Jun. 2025. DOI: 10.1016/j.solener.2025.113647.

[202] M. Noman, M. S. Ahmad, and S. Bai, "Chapter 2 - Dye-sensitized solar cells: A comprehensive introduction," in *Dye-Sensitized Solar Cells*, A. K. Pandey, S. Shahabuddin, and M. S. Ahmad, Eds., Academic Press, Jan. 2022, pp. 25–43, ISBN: 978-0-12-818206-2. DOI: 10.1016/B978-0-12-818206-2.00001-3.

[203] K. Prajapat, U. Mahajan, K. Sahu, M. Dhonde, and P. M. Shirage, "The Evolution of natural Dye-Sensitized solar Cells: Current Advances and future outlook," *Solar Energy*, vol. 284, p. 113 081, Dec. 2024, ISSN: 0038-092X. DOI: 10.1016/j.solener.2024.113081.

[204] S. Colodrero, M. Calvo, and H. M?guez, "Photon Management in Dye Sensitized Solar Cells," in Feb. 2010, ISBN: 978-953-307-052-0. DOI: 10.5772/8077.

[205] J. Gong, K. Sumathy, Q. Qiao, and Z. Zhou, "Review on dye-sensitized solar cells (DSSCs): Advanced techniques and research trends," *Renewable and Sustainable Energy Reviews*, vol. 68, pp. 234–246, Feb. 2017, ISSN: 1364-0321. DOI: 10.1016/j.rser.2016.09.097.

[206] L. Y. Lin and K. C. Ho, "Dye-sensitized solar cells," in *Encyclopedia of Modern Optics*, vol. 1-5, Elsevier, Jan. 2018, pp. 270–281, ISBN: 978-0-12-809283-5. DOI: 10.1016/B978-0-12-803581-8.09545-X.

[207] M. A. Saeed, K. Yoo, H. C. Kang, J. W. Shim, and J.-J. Lee, "Recent developments in dye-sensitized photovoltaic cells under ambient illumination," *Dyes and Pigments*, vol. 194, p. 109 626, Oct. 2021, ISSN: 0143-7208. DOI: 10.1016/j.dyepig.2021.109626.

[208] R. Jiang, H. Michaels, N. Vlachopoulos, and M. Freitag, "Chapter 8 - Beyond the Limitations of Dye-Sensitized Solar Cells," in *Dye-Sensitized Solar Cells*, M. Soroush and K. K. S. Lau, Eds., Academic Press, Jan. 2019, pp. 285–323, ISBN: 978-0-12-814541-8. DOI: 10.1016/B978-0-12-814541-8.00008-2.

[209] K. Sharma, V. Sharma, and S. S. Sharma, "Dye-Sensitized Solar Cells: Fundamentals and Current Status," en, *Nanoscale Res Lett*, vol. 13, no. 1, p. 381, Nov. 2018, ISSN: 1556-276X. DOI: 10.1186/s11671-018-2760-6.

[210] S. Iswarya, A. Dharshini, B. Scholastica Mary Vithiya, and T. Augustine Arul Prasad, "Evolving smart homes to exploring space, dye-sensitized solar cells (DSSC) as a sustainable energy model for the future world—A review," *Next Energy*, vol. 8, p. 100 328, Jul. 2025, ISSN: 2949-821X. DOI: 10.1016/j.nxener.2025.100328.

[211] "Advancements in the Development of Various Types of Dye-Sensitized Solar Cells: A Comparative Review," en-US, *Energy Engineering*, vol. 118, no. 4, pp. 737–759, May 2021, ISSN: 0199-8595. DOI: 10.32604/EE.2021.016157.

[212] D. Gernaat, H. S. De Boer, L. Dammeier, and D. Vuuren, "The role of residential rooftop photovoltaic in long-term energy and climate scenarios," *Applied Energy*, vol. 279, p. 115 705, Dec. 2020. DOI: 10.1016/j.apenergy.2020.115705.

[213] M. Asif, R. Sharieff, M. Olawale, and M. I. Khan, "Unlocking the potential of unregulated rooftops for solar PV on residential buildings: Identifying and addressing key challenges," *Energy Nexus*, vol. 18, p. 100 447, Jun. 2025, ISSN: 2772-4271. DOI: 10.1016/j.nexus.2025.100447.

[214] A. Tripathi, S. L. Gundebommu, H. Mishra, *et al.*, "Integration of Solar PV Panels in Electric Vehicle Charging Infrastructure: Benefits, Challenges, and Environmental Implications," *Energy Science & Engineering*, vol. 13, pp. 2135–2152, Feb. 2025. DOI: 10.1002/ese3.70014.

[215] M. Yamaguchi, D. Frank, J. Geisz, and N. Ekins-Daukes, "Multi-junction solar cells paving the way for super high-efficiency," *Journal of Applied Physics*, vol. 129, p. 240 901, Jun. 2021. DOI: 10.1063/5.0048653.

[216] L. A. Iturralde Carrera, M. G. Garcia-Barajas, C. D. Constantino-Robles, J. M. Álvarez-Alvarado, Y. Castillo-Alvarez, and J. Rodríguez-Reséndiz, "Efficiency and Sustainability in Solar Photovoltaic Systems: A Review of Key Factors and Innovative Technologies," en, *Eng*, vol. 6, no. 3, p. 50, Mar. 2025, ISSN: 2673-4117. DOI: 10.3390/eng6030050.

[217] K. S. Srivishnu, M. N. Rajesh, S. Prasanthkumar, and L. Giribabu, "Photovoltaics for indoor applications: Progress, challenges and perspectives," *Solar Energy*, vol. 264, p. 112 057, Nov. 2023, ISSN: 0038-092X. DOI: 10.1016/j.solener.2023.112057.

[218] C. N. Nwagu, C. O. Ujah, D. V. V. Kallon, and V. S. Aigbodion, "Integrating solar and wind energy into the electricity grid for improved power accessibility," *Unconventional Resources*, vol. 5, p. 100 129, Jan. 2025, ISSN: 2666-5190. DOI: 10.1016/j.uncres.2024.100129.

[219] Q. Chen, N. De Marco, Y. ( Yang, *et al.*, "Under the spotlight: The organic–inorganic hybrid halide perovskite for optoelectronic applications," *Nano Today*, vol. 10, no. 3, pp. 355–396, Jun. 2015, ISSN: 1748-0132. DOI: 10.1016/j.nantod.2015.04.009.

[220] T. D. Raju, V. Murugadoss, K. A. Nirmal, T. D. Dongale, A. V. Kesavan, and T. G. Kim, "Advancements in perovskites for solar cell commercialization: A review," *Advanced Powder Materials*, vol. 4, no. 2, p. 100 275, Apr. 2025, ISSN: 2772-834X. DOI: 10.1016/j.apmate.2025.100275.

[221] R. A. Afre and D. Pugliese, "Perovskite Solar Cells: A Review of the Latest Advances in Materials, Fabrication Techniques, and Stability Enhancement Strategies," en, *Micromachines*, vol. 15, no. 2, p. 192, Feb. 2024, Publisher: Multidisciplinary Digital Publishing Institute, ISSN: 2072-666X. DOI: 10.3390/mi15020192.

[222] L. Zhang, L. Mei, K. Wang, *et al.*, "Advances in the Application of Perovskite Materials," en, *Nano-Micro Lett.*, vol. 15, no. 1, p. 177, Jul. 2023, ISSN: 2150-5551. DOI: 10.1007/s40820-023-01140-3.

[223] H. L. Wells, "Über die Cäsium- und Kalium-Bleihalogenide," en, *Zeitschrift für anorganische Chemie*, vol. 3, no. 1, pp. 195–210, 1893, _eprint: https://onlinelibrary.wiley.com/do ISSN: 1521-3749. DOI: 10.1002/zaac.18930030124.

[224] B. R. Editorial, *A History of Perovskite Solar Cells*, en-us. [Online]. Available: https://blog.bccresearch.com/a-history-of-perovskite-solar-cells (visited on 09/15/2025).

[225] *History of Perovskites and Perovskite Solar Cells*, en. [Online]. Available: https://www.ossila.com/pages/history-and-evolution-of-perovskites (visited on 09/15/2025).

[226] D. Weber, "CH3NH3SnBrxI3-x (x = 0-3), ein Sn(II)-System mit kubischer Perowskitstruktur / CH3NH3SnBrxI3-x(x = 0-3), a Sn(II)-System with Cubic Perovskite Structure," en, *Zeitschrift für Naturforschung B*, vol. 33, no. 8, pp. 862–865, Aug. 1978, Publisher: De Gruyter, ISSN: 1865-7117. DOI: 10.1515/znb-1978-0809.

[227] D. B. Mitzi, "Introduction: Perovskites," *Chem. Rev.*, vol. 119, no. 5, pp. 3033–3035, Mar. 2019, Publisher: American Chemical Society, ISSN: 0009-2665. DOI: 10.1021/acs.chemrev.8b00800.

[228] *Scholars@Duke publication: Transport, optical, and magnetic properties of the conducting halide perovskite ch3nh3sni3*, en. [Online]. Available: https://scholars.duke.edu/publication/1044878 (visited on 09/15/2025).

[229] D. B. Mitzi, S. Wang, C. A. Feild, C. A. Chess, and A. M. Guloy, "Conducting Layered Organic-inorganic Halides Containing <110>-Oriented Perovskite Sheets," eng, *Science*, vol. 267, no. 5203, pp. 1473–1476, Mar. 1995, ISSN: 0036-8075. DOI: 10.1126/science.267.5203.1473.

[230] A. Kojima, K. Teshima, Y. Shirai, and T. Miyasaka, "Organometal Halide Perovskites as Visible-Light Sensitizers for Photovoltaic Cells," *J. Am. Chem. Soc.*, vol. 131, no. 17, pp. 6050–6051, May 2009, Publisher: American Chemical Society, ISSN: 0002-7863. DOI: 10.1021/ja809598r.

[231] J.-H. Im, C.-R. Lee, J.-W. Lee, S.-W. Park, and N.-G. Park, "6.5% efficient perovskite quantum-dot-sensitized solar cell," en, *Nanoscale*, vol. 3, no. 10, pp. 4088–4093, Oct. 2011, Publisher: The Royal Society of Chemistry, ISSN: 2040-3372. DOI: 10.1039/C1NR10867K.

[232] M. M. Lee, J. Teuscher, T. Miyasaka, T. N. Murakami, and H. J. Snaith, "Efficient Hybrid Solar Cells Based on Meso-Superstructured Organometal Halide Perovskites," *Science*, vol. 338, no. 6107, pp. 643–647, Nov. 2012, Publisher: American Association for the Advancement of Science. DOI: 10.1126/science.1228604.

[233] Z. Wang and Y. Jiang, "Advances in perovskite solar cells: Film morphology control and interface engineering," *Journal of Cleaner Production*, vol. 317, p. 128 368, Oct. 2021, ISSN: 0959-6526. DOI: 10.1016/j.jclepro.2021.128368.

[234] M. Saliba, T. Matsui, J.-Y. Seo, *et al.*, "Cesium-containing triple cation perovskite solar cells: Improved stability, reproducibility and high efficiency," en, *Energy & Environmental Science*, vol. 9, no. 6, pp. 1989–1997, 2016, Publisher: Royal Society of Chemistry. DOI: 10.1039/C5EE03874J.

[235] M. Rani, M. M. Khan, A. Numan, *et al.*, "Breaking barriers: Addressing challenges in perovskite solar cell development," *Journal of Alloys and Compounds*, vol. 1010, p. 177 648, Jan. 2025, ISSN: 0925-8388. DOI: 10.1016/j.jallcom.2024.177648.

[236] C. Luo, H. Gu, B. Zhang, S. M. Park, M. Wei, and Y. Hou, "Perovskite Tandems: The Next Big Leap in Photovoltaic Technology," en, *Advanced Materials*, vol. n/a, no. n/a, e08331, _eprint: https://advanced.onlinelibrary.wiley.com/doi/pdf/10.1002/adma.20250 ISSN: 1521-4095. DOI: 10.1002/adma.202508331.

[237] L. K. Ono, E. J. Juarez-Perez, and Y. Qi, "Progress on Perovskite Materials and Solar Cells with Mixed Cations and Halide Anions," en, *ACS Appl. Mater. Interfaces*, vol. 9, no. 36, pp. 30 197–30 246, Sep. 2017, ISSN: 1944-8244, 1944-8252. DOI: 10.1021/acsami.7b06001.

[238] J. W. Turnley, S. Agarwal, and R. Agrawal, "Rethinking tolerance factor analysis for chalcogenide perovskites," en, *Materials Horizons*, vol. 11, no. 19, pp. 4802–4808, 2024, Publisher: Royal Society of Chemistry. DOI: 10.1039/D4MH00689E.

[239] Z. Li, M. Yang, J.-S. Park, S.-H. Wei, J. Berry, and K. Zhu, "Stabilizing Perovskite Structures by Tuning Tolerance Factor: Formation of Formamidinium and Cesium Lead Iodide Solid-State Alloys," *Chemistry of Materials*, vol. 28, Dec. 2015. DOI: 10.1021/acs.chemmater.5b04107.

[240] A. J. Olasoji, J. K. Park, H. J. Lee, Y. Song, D. S. Lee, and S. H. Im, "Metal halide perovskites: A platform for next-generation multifunctional devices," en, *Adv. Ind. Eng. Chem.*, vol. 1, no. 1, p. 12, Jul. 2025, ISSN: 3059-3867. DOI: 10.1007/s44405-025-00011-2.

[241] M. I. Pintor Monroy, I. Goldberg, K. Elkhouly, *et al.*, "All-Evaporated, All-Inorganic $CsPbI_3$ Perovskite-Based Devices for Broad-Band Photodetector and Solar Cell Applications," en, *ACS Appl. Electron. Mater.*, vol. 3, no. 7, pp. 3023–3033, Jul. 2021, ISSN: 2637-6113, 2637-6113. DOI: 10.1021/acsaelm.1c00252.

[242] R. Singh, S. Sandhu, H. Yadav, and J.-J. Lee, "A stable triple-cation (Cs+-MA+-FA+) perovskite powder formation under ambient conditions for a hysteresis-free high efficiency solar cells," *ACS Applied Materials & Interfaces*, vol. 11, Jul. 2019. DOI: 10.1021/acsami.9b09121.

[243] H. Xiang, P. Liu, R. Ran, W. Wang, W. Zhou, and Z. Shao, "Two-dimensional Dion-Jacobson halide perovskites as new-generation light absorbers for perovskite solar cells," *Renewable and Sustainable Energy Reviews*, vol. 166, p. 112 614, Sep. 2022, ISSN: 1364-0321. DOI: 10.1016/j.rser.2022.112614.

[244] L. Zhang, M. Zhang, H. Wang, *et al.*, "Diverse Perovskite Solar Cells: Progress, Challenges, and Perspectives," en, *Advanced Materials*, vol. n/a, no. n/a, e12221, _eprint: https://advanced.onlinelibrary.wiley.com/doi/pdf/10.1002/adma.202512221, ISSN: 1521-4095. DOI: 10.1002/adma.202512221.

[245] L. Fan, M. Yu, W. Hu, *et al.*, "Reducing charge-recombination losses in photovoltaic cells by spontaneous reconstruction of n/p homojunction in a monolithic perovskite film using black phosphorus nanosheets," *Chemical Engineering Journal*, vol. 479, p. 147 861, Jan. 2024, ISSN: 1385-8947. DOI: 10.1016/j.cej.2023.147861.

[246] R. Jindal, A. Tripathi, C. Mohan, A. Garg, and R. S. Varma, "Lead-free halide double perovskites for sustainable environmental applications," *Chemical Physics Impact*, vol. 9, p. 100 770, Dec. 2024, ISSN: 2667-0224. DOI: 10.1016/j.chphi.2024.100770.

[247] Y. Wang, Z. Cheng, J. Li, K. Lv, Z. Li, and H. Zhao, "Innovative Approaches to Large-Area Perovskite Solar Cell Fabrication Using Slit Coating," en, *Molecules*, vol. 29, no. 20, p. 4976, Jan. 2024, Publisher: Multidisciplinary Digital Publishing Institute, ISSN: 1420-3049. DOI: 10.3390/molecules29204976.

[248] A. U. I. Shah and E. L. Meyer, "Perovskite-based solar cells in photovoltaics for commercial scalability: Current progress, challenges, mitigations and future prospectus," *Solar Energy*, vol. 286, p. 113 172, Jan. 2025, ISSN: 0038-092X. DOI: 10.1016/j.solener.2024.113172.

[249] H. J. Kim, G. S. Han, and H. S. Jung, "Managing the lifecycle of perovskite solar cells: Addressing stability and environmental concerns from utilization to end-of-life," *eScience*, vol. 4, no. 2, p. 100 243, Apr. 2024, ISSN: 2667-1417. DOI: 10.1016/j.esci.2024.100243.

[250] M. K Rao, S. D N, S. Kumar, S. Y N, and M. M G, "Review on persistent challenges of perovskite solar cells' stability," *Solar Energy*, vol. 218, pp. 469–491, Apr. 2021. DOI: 10.1016/j.solener.2021.03.005.

[251] P. Wu, S. Wang, X. Li, and F. Zhang, "Beyond efficiency fever: Preventing lead leakage for perovskite solar cells," *Matter*, vol. 5, no. 4, pp. 1137–1161, Apr. 2022, ISSN: 2590-2385. DOI: 10.1016/j.matt.2022.02.012.

[252] M. B. Faheem, B. Khan, J. Z. Hashmi, *et al.*, "Insights from scalable fabrication to operational stability and industrial opportunities for perovskite solar cells and modules," *Cell Reports Physical Science*, vol. 3, no. 4, p. 100 827, Apr. 2022, ISSN: 2666-3864. DOI: 10.1016/j.xcrp.2022.100827.

[253] B. Chen, S. Wang, Y. Song, C. Li, and F. Hao, "A critical review on the moisture stability of halide perovskite films and solar cells," *Chemical Engineering Journal*, vol. 430, p. 132 701, Feb. 2022, ISSN: 1385-8947. DOI: 10.1016/j.cej.2021.132701.

[254] J. Euvrard, "Section: Halide Perovskites," en,

[255] S. Thomson, "Observing Phase Transitions in a Halide Perovskite Using Temperature Dependent Photoluminescence Spectroscopy," en, 2018.

[256] L.-Q. Xie, L. Chen, Z.-A. Nan, *et al.*, "Understanding the Cubic Phase Stabilization and Crystallization Kinetics in Mixed Cations and Halides Perovskite Single Crystals," en, *J. Am. Chem. Soc.*, vol. 139, no. 9, pp. 3320–3323, Mar. 2017, ISSN: 0002-7863, 1520-5126. DOI: 10.1021/jacs.6b12432.

[257] *Br-Induced Suppression of Low-Temperature Phase Transitions in Mixed-Cation Mixed-Halide Perovskites | Chemistry of Materials*. [Online]. Available: https://pubs.acs.org/doi/10.1021/acs.chemmater.4c01670 (visited on 09/15/2025).

[258] H. Li, F. Li, Z. Shen, *et al.*, "Photoferroelectric perovskite solar cells: Principles, advances and insights," *Nano Today*, vol. 37, p. 101 062, Apr. 2021, ISSN: 1748-0132. DOI: 10.1016/j.nantod.2020.101062.

[259] B. Kim, J. Kim, and N. Park, "First-principles identification of the charge-shifting mechanism and ferroelectricity in hybrid halide perovskites," *Scientific Reports*, vol. 10, Nov. 2020. DOI: 10.1038/s41598-020-76742-7.

[260] L. Zhang, S. Cui, Q. Guo, *et al.*, "Anisotropic Performance of High-Quality MAPbBr 3 Single-Crystal Wafers," *ACS Applied Materials & Interfaces*, vol. 12, pp. 51 616–51 627, Nov. 2020. DOI: 10.1021/acsami.0c14582.

[261] A. Bonadio, F. P. Sabino, A. L. M. Freitas, M. R. Felez, G. M. Dalpian, and J. A. Souza, "Comparing the Cubic and Tetragonal Phases of MAPbI3 at Room Temperature," *Inorg. Chem.*, vol. 62, no. 19, pp. 7533–7544, May 2023, Publisher: American Chemical Society, ISSN: 0020-1669. DOI: 10.1021/acs.inorgchem.3c00874.

[262] T. Ye, K. Wang, S. Ma, *et al.*, "Strain-relaxed tetragonal MAPbI3 results in efficient mesoporous solar cells," en, *Nano Energy*, vol. 83, p. 105 788, May 2021, ISSN: 22112855. DOI: 10.1016/j.nanoen.2021.105788.

[263] Z. Chen, L. Dong, H. Tang, Y. Yu, L. Ye, and J. Zang, "Direct synthesis of cubic phase CsPbI3 nanowires," en, *CrystEngComm*, vol. 21, no. 9, pp. 1389–1396, Feb. 2019, Publisher: The Royal Society of Chemistry, ISSN: 1466-8033. DOI: 10.1039/C8CE02111B.

[264] I. N. Flerov, M. V. Gorev, K. S. Aleksandrov, A. Tressaud, J. Grannec, and M. Couzi, "Phase transitions in elpasolites (ordered perovskites)," *Materials Science and Engineering: R: Reports*, vol. 24, no. 3, pp. 81–151, Nov. 1998, ISSN: 0927-796X. DOI: 10.1016/S0927-796X(98)00015-1.

[265] S. Zhang, Y. Zhou, Z. Shen, *et al.*, "High-efficiency and stable perovskite solar cells via bidentate chelation for facet-engineered growth of FAPbI3 (111) crystals," *Chemical Engineering Journal*, vol. 516, p. 164 079, Jul. 2025, ISSN: 1385-8947. DOI: 10.1016/j.cej.2025.164079.

[266] D. Kumar, J. Kaur, P. P. Mohanty, R. Ahuja, and S. Chakraborty, "Recent Advancements in Nontoxic Halide Perovskites: Beyond Divalent Composition Space," *ACS Omega*, vol. 6, no. 49, pp. 33 240–33 252, Dec. 2021, Publisher: American Chemical Society. DOI: 10.1021/acsomega.1c05333.

[267] X. Jiang, Z. Zang, Y. Zhou, H. Li, Q. Wei, and Z. Ning, "Tin Halide Perovskite Solar Cells: An Emerging Thin-Film Photovoltaic Technology," *Acc. Mater. Res.*, vol. 2, no. 4, pp. 210–219, Apr. 2021, Publisher: American Chemical Society. DOI: 10.1021/accountsmr.0c00111.

[268] L.-y. Huang, "Electronic band structure trends of perovskite halides: Beyond Pb and Sn to Ge and Si," *Phys. Rev. B*, vol. 93, no. 19, 2016. DOI: 10.1103/PhysRevB.93.195211.

[269] E. A. Nyiekaa, T. A. Aika, P. E. Orukpe, C. E. Akhabue, and E. Danladi, "Development on inverted perovskite solar cells: A review," *Heliyon*, vol. 10, no. 2, e24689, Jan. 2024, ISSN: 2405-8440. DOI: 10.1016/j.heliyon.2024.e24689.

[270] Z. Hongwei, L. Pan, F. Eickemeyer, *et al.*, "Efficient and Stable Large Bandgap MAPbBr 3 Perovskite Solar Cell Attaining an Open Circuit Voltage of 1.65 V," *ACS Energy Letters*, vol. 7, pp. 1112–1119, Feb. 2022. DOI: 10.1021/acsenergylett.1c02431.

[271] J. Liang, J. Liu, and Z. Jin, "All-Inorganic Halide Perovskites for Optoelectronics: Progress and Prospects," en, *Solar RRL*, vol. 1, no. 10, p. 1 700 086, 2017, _eprint: https://onlinelibrary.wiley.com/doi/pdf/10.1002/solr.201700086, ISSN: 2367-198X. DOI: 10.1002/solr.201700086.

[272] S. De Wolf, J. Holovsky, S.-J. Moon, *et al.*, "Organometallic Halide Perovskites: Sharp Optical Absorption Edge and Its Relation to Photovoltaic Performance," en, *J. Phys. Chem. Lett.*, vol. 5, no. 6, pp. 1035–1039, Mar. 2014, ISSN: 1948-7185, 1948-7185. DOI: 10.1021/jz500279b.

[273] M. U. Rothmann, J. S. Kim, J. Borchert, *et al.*, "Atomic-scale microstructure of metal halide perovskite," *Science*, vol. 370, no. 6516, eabb5940, Oct. 2020, Publisher: American Association for the Advancement of Science. DOI: 10.1126/science.abb5940.

[274] Y. Zhou, O. S. Game, S. Pang, and N. P. Padture, "Microstructures of Organometal Trihalide Perovskites for Solar Cells: Their Evolution from Solutions and Characterization," eng, *J Phys Chem Lett*, vol. 6, no. 23, pp. 4827–4839, Dec. 2015, ISSN: 1948-7185. DOI: 10.1021/acs.jpclett.5b01843.

[275] J. S. Yun, J. Kim, T. Young, *et al.*, "Humidity-Induced Degradation via Grain Boundaries of HC(NH2)2PbI3 Planar Perovskite Solar Cells," en, *Advanced Functional Materials*, vol. 28, no. 11, p. 1 705 363, 2018, _eprint: https://advanced.onlinelibrary.wiley.c ISSN: 1616-3028. DOI: 10.1002/adfm.201705363.

[276] Y. Zong, Y. Zhou, Y. Zhang, *et al.*, "Continuous Grain-Boundary Functionalization for High-Efficiency Perovskite Solar Cells with Exceptional Stability," *Chem*, vol. 4, no. 6, pp. 1404–1415, Jun. 2018, ISSN: 2451-9294. DOI: 10.1016/j.chempr.2018.03.005.

[277] M. Hao, T. Duan, Z. Ma, *et al.*, "Flattening Grain-Boundary Grooves for Perovskite Solar Cells with High Optomechanical Reliability," en, *Advanced Materials*, vol. 35, no. 15, p. 2 211 155, 2023, _eprint: https://advanced.onlinelibrary.wiley.com/doi/pdf/10.1002/ad ISSN: 1521-4095. DOI: 10.1002/adma.202211155.

[278] T. Xiao, M. Hao, T. Duan, *et al.*, "Elimination of grain surface concavities for improved perovskite thin-film interfaces," *Nature Energy*, vol. 9, pp. 1–12, Jul. 2024. DOI: 10.1038/s41560-024-01567-x.

[279] X. Xiao, W. Li, Y. Fang, *et al.*, "Benign ferroelastic twin boundaries in halide perovskites for charge carrier transport and recombination," en, *Nat Commun*, vol. 11, no. 1, p. 2215, May 2020, Publisher: Nature Publishing Group, ISSN: 2041-1723. DOI: 10.1038/s41467-020-16075-1.

[280] G. Y. Kim, S. H. Oh, B. P. Nguyen, *et al.*, "Efficient carrier separation and intriguing switching of bound charges in inorganic-organic lead halide solar cells," *Journal of Physical Chemistry Letters*, vol. 6, no. 12, pp. 2355–2362, Jun. 2015, ISSN: 1948-7185. DOI: 10.1021/acs.jpclett.5b00967.

[281] J. S. Yun, A. Ho-Baillie, S. Huang, *et al.*, "Benefit of Grain Boundaries in Organic–Inorganic Halide Planar Perovskite Solar Cells," *J. Phys. Chem. Lett.*, vol. 6, no. 5, pp. 875–880, Mar. 2015, Publisher: American Chemical Society. DOI: 10.1021/acs.jpclett.5b00182.

[282] J. Li, Q. Dong, N. Li, and L. Wang, "Direct Evidence of Ion Diffusion for the Silver-Electrode-Induced Thermal Degradation of Inverted Perovskite Solar Cells," en, *Advanced Energy Materials*, vol. 7, no. 14, p. 1 602 922, 2017, _eprint: https://advanced.onlinelibr ISSN: 1614-6840. DOI: 10.1002/aenm.201602922.

[283] J. Chen, X. Wang, T. Wang, *et al.*, "Determining the bonding–degradation trade-off at heterointerfaces for increased efficiency and stability of perovskite solar cells," *Nature Energy*, vol. 10, pp. 181–190, Dec. 2024. DOI: 10.1038/s41560-024-01680-x.

[284] *Chiral-structured heterointerfaces enable durable perovskite solar cells | Science.* [Online]. Available: https://www.science.org/doi/10.1126/science.ado5172 (visited on 09/16/2025).

[285] Y. Yang, Q. Xiong, J. Wu, *et al.*, "Poly(3-hexylthiophene)/perovskite Heterointerface by Spinodal Decomposition Enabling Efficient and Stable Perovskite Solar Cells," en, *Advanced Materials*, vol. 36, no. 7, p. 2 310 800, 2024, _eprint: https://advanced.onlinelibrary.wiley.com/doi/pdf/10.1002/adma.202310800, ISSN: 1521-4095. DOI: 10.1002/adma.202310800.

[286] L. Xie and Y. Zhou, "Microstructural disorder in perovskite photovoltaics," en, *Front. Chem. Sci. Eng.*, vol. 19, no. 9, p. 87, Jul. 2025, ISSN: 2095-0187. DOI: 10.1007/s11705-025-2600-z.

[287] Y. Li, Z. Li, F. Liu, and J. Wei, "Defects and passivation in perovskite solar cells," *Surface Innovations*, vol. 10, pp. 3–20, Jan. 2022. DOI: 10.1680/jsuin.21.00058.

[288] Z. Wang, H. Gao, D. Wu, J. Meng, J. Deng, and M. Cui, "Defects and Defect Passivation in Perovskite Solar Cells," en, *Molecules*, vol. 29, no. 9, p. 2104, Jan. 2024, Publisher: Multidisciplinary Digital Publishing Institute, ISSN: 1420-3049. DOI: 10.3390/molecules29092104.

[289] N. Yadav and A. Khare, "Resolving interfacial challenges in perovskite solar cells: From defect control to energy band optimization," *Surfaces and Interfaces*, vol. 56, p. 105 593, Jan. 2025, ISSN: 2468-0230. DOI: 10.1016/j.surfin.2024.105593.

[290] H. Zheng, Y. Wang, B. Niu, *et al.*, "Controlling the Defect Density of Perovskite Films by MXene/SnO2 Hybrid Electron Transport Layers for Efficient and Stable Photovoltaics," *J. Phys. Chem. C*, vol. 125, no. 28, pp. 15 210–15 222, Jul. 2021, Publisher: American Chemical Society, ISSN: 1932-7447. DOI: 10.1021/acs.jpcc.1c04361.

[291] A. A. Abdelghafar, A. Mdallal, M. A. Allam, *et al.*, "Passivation strategies in lead-free perovskite solar cells: Towards efficient and stable photovoltaic devices," *Energy Nexus*, vol. 19, p. 100 487, Sep. 2025, ISSN: 2772-4271. DOI: 10.1016/j.nexus.2025.100487.

[292] J. S. Manser, J. A. Christians, and P. V. Kamat, "Intriguing Optoelectronic Properties of Metal Halide Perovskites," *Chem. Rev.*, vol. 116, no. 21, pp. 12 956–13 008, Nov. 2016, Publisher: American Chemical Society, ISSN: 0009-2665. DOI: 10.1021/acs.chemrev.6b00136.

[293] Y. Xiang, R. Zheng, C. Li, *et al.*, "Multistep optimization for the electrodeposited mixed perovskite FA1-y Cs y PbBr x I3-x solar cells," *Nanotechnology*, vol. 35, Oct. 2023. DOI: 10.1088/1361-6528/acff77.

[294] Q. Lin, D. J. Kubicki, M. Omrani, F. Alam, and M. Abdi-Jalebi, "The race between complicated multiple cation/anion compositions and stabilization of FAPbI3 for halide perovskite solar cells," en, *J. Mater. Chem. C*, vol. 11, no. 7, pp. 2449–2468, Feb. 2023, Publisher: The Royal Society of Chemistry, ISSN: 2050-7534. DOI: 10.1039/D2TC04529J.

[295] A. M. Ntouga Abena, A. Teyou Ngoupo, and J. M. B. Ndjaka, "Computational analysis of mixed cation mixed halide-based perovskite solar cell using SCAPS-1D software," *Heliyon*, vol. 8, no. 11, e11428, Nov. 2022, ISSN: 2405-8440. DOI: 10.1016/j.heliyon.2022.e11428.

[296] M. M. Byranvand, C. Otero-Martínez, J. Ye, *et al.*, "Recent Progress in Mixed A-Site Cation Halide Perovskite Thin-Films and Nanocrystals for Solar Cells and Light-Emitting Diodes," en, *Advanced Optical Materials*, vol. 10, no. 14, p. 2 200 423, 2022, _eprint: https://advanced.onlinelibrary.wiley.com/doi/pdf/10.1002/adom.202200423, ISSN: 2195-1071. DOI: 10.1002/adom.202200423.

[297] S. Mondal, N. Eguchi, N. Nishimura, *et al.*, "Mixed 2D-cation passivation towards improved durability of perovskite solar cells and dynamics of 2D-perovskites under light irradiation and at high temperature," en, *Sustainable Energy Fuels*, vol. 9, no. 1, pp. 247–255, Dec. 2024, Publisher: The Royal Society of Chemistry, ISSN: 2398-4902. DOI: 10.1039/D4SE01227E.

[298] N. Filipoiu, T. L. Mitran, D. V. Anghel, *et al.*, "Investigation of Opto-Electronic Properties and Stability of Mixed-Cation Mixed-Halide Perovskite Materials with Machine-Learning Implementation," en, *Energies*, vol. 14, no. 17, p. 5431, Jan. 2021, Publisher: Multidisciplinary Digital Publishing Institute, ISSN: 1996-1073. DOI: 10.3390/en14175431.

[299] A. Azhari, F. Then, D. S. Che Halin, S. Sepeai, and N. Ludin, "Tin and germanium substitution in lead free perovskite solar cell: Current status and future trends," *IOP Conference Series: Materials Science and Engineering*, vol. 957, p. 012 057, Nov. 2020. DOI: 10.1088/1757-899X/957/1/012057.

[300] C. Huang, E. Gajewiak, A. Wright, W. Rodriguez-Kazeem, D. Heift, and J. C. Bear, "A comparative meta-analysis of gains in efficiency in Pb- and Sn-based perovskite solar cells over the last decade," en, *Zeitschrift für anorganische und allgemeine Chemie*, vol. 649, no. 13, e202300045, 2023, _eprint: https://onlinelibrary.wiley.com/doi/p ISSN: 1521-3749. DOI: 10.1002/zaac.202300045.

[301] A. Sheikh and K. K. Sharma, "Dimensional Engineering of 2D/3D Perovskite Halides for Efficient and Stable Solar Cells," in Nov. 2023, pp. 431–456, ISBN: 978-981-99-7145-9 978-981-99-7144-2. DOI: 10.1007/978-981-99-7145-9_15.

[302] X. Yan, S. Hu, Y. Zhang, H. Li, and C. Sheng, "Methylammonium acetate as an additive to improve performance and eliminate J-V hysteresis in 2D homologous organic-inorganic perovskite solar cells," *Solar Energy Materials and Solar Cells*, vol. 191, pp. 283–289, Mar. 2019, ISSN: 0927-0248. DOI: 10.1016/j.solmat.2018.11.030.

[303] H. Rafique, G. Abbas, M. J. Mendes, *et al.*, "Recent Advancements and Perspectives of Low-Dimensional Halide Perovskites for Visual Perception and Optoelectronic Applications," en, *Nano-Micro Lett.*, vol. 18, no. 1, p. 44, Aug. 2025, ISSN: 2150-5551. DOI: 10.1007/s40820-025-01823-z.

[304] T. Yang, F. Li, C.-H. Lin, *et al.*, "One-pot solution synthesis of 2D-3D mixed-dimensional perovskite crystalline lateral heterostructures," *Cell Reports Physical Science*, vol. 4, no. 6, p. 101 447, Jun. 2023, ISSN: 2666-3864. DOI: 10.1016/j.xcrp.2023.101447.

[305] C. Yan, K. Lin, J. Lu, and Z. Wei, "Composition engineering to obtain efficient hybrid perovskite light-emitting diodes," en, *Front. Optoelectron.*, vol. 13, no. 3, pp. 282–290, Sep. 2020, ISSN: 2095-2767. DOI: 10.1007/s12200-020-1046-7.

[306] Q. Cao, H. Liu, J. Xing, *et al.*, "Optimal Methylammounium Chloride Additive for High-Performance Perovskite Solar Cells," en, *Nanomaterials*, vol. 15, no. 4, p. 292, Jan. 2025, Publisher: Multidisciplinary Digital Publishing Institute, ISSN: 2079-4991. DOI: 10.3390/nano15040292.

[307] Z. Wang, L. Liu, X. Liu, *et al.*, "Uncovering synergistic effect of chloride additives for efficient quasi-2D perovskite solar cells," *Chemical Engineering Journal*, vol. 432, p. 134 367, Mar. 2022, ISSN: 1385-8947. DOI: 10.1016/j.cej.2021.134367.

[308] R. Swartwout, M. Hoerantner, and V. Bulovic, "Scalable Deposition Methods for Large-Area Production of Perovskite Thin Films," *Energy & Environmental Materials*, vol. 2, pp. 119–143, Jun. 2019. DOI: 10.1002/eem2.12043.

[309] C. Huang, N. Fu, F. Liu, L. Jiang, X. Hao, and H. Huang, "Highly efficient perovskite solar cells with precursor composition-dependent morphology," *Solar Energy Materials and Solar Cells*, vol. 145, pp. 231–237, Feb. 2016, ISSN: 0927-0248. DOI: 10.1016/j.solmat.2015.10.032.

[310] R. Yin, Y. Wu, Z. Huang, A. S. Vasenko, S. Xu, and H. Zhou, "Fabricating Perovskite Films for Solar Modules from Small to Large Scale," en, *Advanced Functional Materials*, vol. 35, no. 24, p. 2 419 184, 2025, _eprint: https://advanced.onlinelibrary.wiley.c ISSN: 1616-3028. DOI: 10.1002/adfm.202419184.

[311] J. L. Starger, A. E. Louks, K. Schutt, *et al.*, "Formation trajectories of solution-processed perovskite thin films from mixed solvents," *Cell Reports Physical Science*, vol. 6, no. 7, p. 102 655, Jul. 2025, ISSN: 2666-3864. DOI: 10.1016/j.xcrp.2025.102655.

[312] M. Jamal, M. Bashar, A. M. Hasan, *et al.*, "Fabrication techniques and morphological analysis of perovskite absorber layer for high-efficiency perovskite solar cell: A review," en, *Renewable and Sustainable Energy Reviews*, vol. 98, pp. 469–488, Dec. 2018, ISSN: 13640321. DOI: 10.1016/j.rser.2018.09.016.

[313] N. J. Jeon, J. H. Noh, Y. C. Kim, W. S. Yang, S. Ryu, and S. I. Seok, "Solvent engineering for high-performance inorganic–organic hybrid perovskite solar cells," en, *Nature Mater*, vol. 13, no. 9, pp. 897–903, Sep. 2014, Publisher: Nature Publishing Group, ISSN: 1476-4660. DOI: 10.1038/nmat4014.

[314] D. Wang, Z. Liu, Z. Zhou, *et al.*, "Reproducible One-Step Fabrication of Compact MAPbI3–xClx Thin Films Derived from Mixed-Lead-Halide Precursors," *Chem. Mater.*, vol. 26, no. 24, pp. 7145–7150, Dec. 2014, Publisher: American Chemical Society, ISSN: 0897-4756. DOI: 10.1021/cm5037869.

[315] J.-H. Im, H.-S. Kim, and N.-G. Park, "Morphology-photovoltaic property correlation in perovskite solar cells: One-step versus two-step deposition of CH3NH3PbI3," *APL Mater.*, vol. 2, no. 8, p. 081 510, Jul. 2014, ISSN: 2166-532X. DOI: 10.1063/1.4891275.

[316] M. Abueid, M. Jafar, H. Hodali, B. Bulos, M. H. Saleh, and T. Aldaraghmeh, "Structural and Optical Properties of Two-Step Dip-Coated CH3NH3PbI3 Films Based on Underlying Dip-Coated PbI2 Films," *Journal of Electronic Materials*, vol. 51, Apr. 2022. DOI: 10.1007/s11664-022-09637-0.

[317] Z. Song, S. Watthage, A. Phillips, and M. Heben, "Pathways toward high-performance perovskite solar cells: Review of recent advances in organo-metal halide perovskites for photovoltaic applications," *Journal of Photonics for Energy*, vol. 6, p. 022 001, Apr. 2016. DOI: 10.1117/1.JPE.6.022001.

[318] X. Yang, Y. Zhu, S. Yan, H. Hu, C. Chen, and J. Tang, "Blade-Coating Perovskites for Tandem Devices: Liquid Mechanism, Film Formation, and Performance," en, *Solar RRL*, vol. 9, no. 10, p. 2 500 149, 2025, _eprint: https://onlinelibrary.wiley.com/doi/pdf/10. ISSN: 2367-198X. DOI: 10.1002/solr.202500149.

[319] W. Nie, H. Tsai, R. Asadpour, *et al.*, "Solar cells. High-efficiency solution-processed perovskite solar cells with millimeter-scale grains," *Science*, vol. 347, p. 522, Jan. 2015. DOI: 10.1126/science.aaa0472.

[320] F. U. Kosasih, E. Erdenebileg, N. Mathews, S. G. Mhaisalkar, and A. Bruno, "Thermal evaporation and hybrid deposition of perovskite solar cells and mini-modules," *Joule*, vol. 6, no. 12, pp. 2692–2734, Dec. 2022, ISSN: 2542-4351. DOI: 10.1016/j.joule.2022.11.004.

[321] M. Liu, M. Johnston, and H. Snaith, "Efficient planar heterojunction perovskite solar cells by vapour deposition," *Nature*, vol. 501, Sep. 2013. DOI: 10.1038/nature12509.

[322] P. Du, L. Wang, J. Li, *et al.*, "Thermal Evaporation for Halide Perovskite Optoelectronics: Fundamentals, Progress, and Outlook," en, *Advanced Optical Materials*, vol. 10, no. 4, p. 2 101 770, 2022, _eprint: https://advanced.onlinelibrary.wiley.com/doi/pdf/10.10 ISSN: 2195-1071. DOI: 10.1002/adom.202101770.

[323] P. Pandey and D.-W. Kang, "Vapor-Deposited Inorganic Perovskite Solar Cells from Fundamentals to Scalable Commercial Pathways," *Electronics*, vol. 14, p. 3171, Aug. 2025. DOI: 10.3390/electronics14163171.

[324] R. Ji, A. Mallick, B. Rivkin, H. Yuce-Cakir, O. D. Jurchescu, and Y. Vaynzof, "Solvent-Free Fabrication Methods of Metal Halide Perovskites," en, *Advanced Materials*, vol. n/a, no. n/a, p. 2 416 604, _eprint: https://advanced.onlinelibrary.wiley.com/doi/pdf/ ISSN: 1521-4095. DOI: 10.1002/adma.202416604.

[325] C.-H. Tien, J.-Y. Fang, and L.-C. Chen, "Hybrid spin coating and evaporation techniques for fabricating double-layer stacked dual-color perovskite LEDs," en, *Sci Rep*, vol. 15, no. 1, p. 1215, Jan. 2025, Publisher: Nature Publishing Group, ISSN: 2045-2322. DOI: 10.1038/s41598-025-85713-9.

[326] S. Xiao, Y. Li, S. Zheng, and S. Yang, "Post-treatment techniques for high-performance perovskite solar cells," en, *MRS Bull.*, vol. 45, no. 6, pp. 431–438, Jun. 2020, ISSN: 0883-7694, 1938-1425. DOI: 10.1557/mrs.2020.141.

[327] K. Lochhead, E. Johlin, D. Yang, K. Lochhead, E. Johlin, and D. Yang, "Encapsulation of Perovskite Solar Cells with Thin Barrier Films," en, in *Thin Films - Deposition Methods and Applications*, IntechOpen, Sep. 2022, ISBN: 978-1-80356-456-2. DOI: 10.5772/intechopen.107189.

[328] Y. Wang, I. Ahmad, T. Leung, *et al.*, "Encapsulation and Stability Testing of Perovskite Solar Cells for Real Life Applications," en, *ACS Mater. Au*, vol. 2, no. 3, pp. 215–236, May 2022, ISSN: 2694-2461, 2694-2461. DOI: 10.1021/acsmaterialsau.1c00045.

[329] W. Yang, Y. Zhang, C. Xiao, J. Yang, and T. Shi, "A review of encapsulation methods and geometric improvements of perovskite solar cells and modules for mass production and commercialization," *Nano Materials Science*, Mar. 2025, ISSN: 2589-9651. DOI: 10.1016/j.nanoms.2025.02.005.

[330] Z. Du, J. Wen, T. Li, X. Wang, H. Zhang, and Y. Chen, "Nature-Inspired Structure Design for Robust and Efficient Flexible Perovskite Solar Cells," en, *Small*, vol. n/a, no. n/a, e08389, _eprint: https://onlinelibrary.wiley.com/doi/pdf/10.1002/smll.202508389, ISSN: 1613-6829. DOI: 10.1002/smll.202508389.

[331] P. Tonui, S. O. Oseni, G. Sharma, Q. Yan, and G. Tessema Mola, "Perovskites photovoltaic solar cells: An overview of current status," *Renewable and Sustainable Energy Reviews*, vol. 91, pp. 1025–1044, Aug. 2018, ISSN: 1364-0321. DOI: 10.1016/j.rser.2018.04.069.

[332] A. S. Yusuf, A. A. Abubakar, I. K. Mohammed, U. Ahmadu, and K. U. Isah, "A review of coating tin oxide electron transport layer for optimizing the performance of perovskite solar cells," *Chemistry of Inorganic Materials*, vol. 6, p. 100 100, Aug. 2025, ISSN: 2949-7469. DOI: 10.1016/j.cinorg.2025.100100.

[333] S. B. Almahsen and G. A. Al-Dahash, "High-efficiency lead-free all-perovskite tandem solar cells achieving 28.22 % power conversion efficiency: A Cs2AgBi0.75Sb0.25Br6/FASnI3 heterostructure design," *Results in Optics*, vol. 21, p. 100 882, Dec. 2025, ISSN: 2666-9501. DOI: 10.1016/j.rio.2025.100882.

[334] L. Liu, D. Zheng, M. Du, *et al.*, "Advancements and Challenges in Wide-Bandgap Perovskite Solar Cells: From Single Junction to Tandem Solar Cells," en, *Solar RRL*, vol. 8, no. 17, p. 2 400 359, 2024, _eprint: https://onlinelibrary.wiley.com/doi/pdf/10.1002/ ISSN: 2367-198X. DOI: 10.1002/solr.202400359.

[335] S. Tammireddy, M. N. Lintangpradipto, O. Telschow, *et al.*, "Hysteresis and Its Correlation to Ionic Defects in Perovskite Solar Cells," *J. Phys. Chem. Lett.*, vol. 15, no. 5, pp. 1363–1372, Feb. 2024, Publisher: American Chemical Society. DOI: 10.1021/acs.jpclett.3c03146.

[336] I. Hussain, H. P. Tran, J. Jaksik, J. Moore, N. Islam, and M. J. Uddin, "Functional materials, device architecture, and flexibility of perovskite solar cell," en, *emergent mater.*, vol. 1, no. 3, pp. 133–154, Dec. 2018, ISSN: 2522-574X. DOI: 10.1007/s42247-018-0013-1.

[337] N. K. Elangovan, R. Kannadasan, B. B. Beenarani, M. H. Alsharif, M.-K. Kim, and Z. Hasan Inamul, "Recent developments in perovskite materials, fabrication techniques, band gap engineering, and the stability of perovskite solar cells," *Energy Reports*, vol. 11, pp. 1171–1190, Jun. 2024, ISSN: 2352-4847. DOI: 10.1016/j.egyr.2023.12.068.

[338] A. Sharma, R. Sharma, S. Agarwal, and M. S. Dhaka, "Role of transport layers in efficiency enhancement of perovskite solar cells," *Renewable and Sustainable Energy Reviews*, vol. 222, p. 115 795, Oct. 2025, ISSN: 1364-0321. DOI: 10.1016/j.rser.2025.115795.

[339] W. Ke, G. Fang, Q. Liu, *et al.*, "Low-Temperature Solution Processed Tin Oxide as an Alternative Electron Transporting Layer for Efficient Perovskite Solar Cells," *Journal of the American Chemical Society*, vol. 137, May 2015. DOI: 10.1021/jacs.5b01994.

[340] X. Wang, L.-L. Deng, W. Luyao, *et al.*, "Cerium oxide standing out as electron transport layer for efficient and stable perovskite solar cells processed in low-temperature," *J. Mater. Chem. A*, vol. 5, Jan. 2016. DOI: 10.1039/C6TA07541J.

[341] A. Yella, L.-P. Heiniger, P. Gao, M. K. Nazeeruddin, and M. Grätzel, "Nanocrystalline Rutile Electron Extraction Layer Enables Low-Temperature Solution Processed Perovskite Photovoltaics with 13.7% Efficiency," *Nano Lett.*, vol. 14, no. 5, pp. 2591–2596, May 2014, Publisher: American Chemical Society, ISSN: 1530-6984. DOI: 10.1021/nl500399m.

[342] Q. Wang, Y. Shao, Q. Dong, Z. Xiao, Y. Yuan, and J. Huang, "Large fill-factor bilayer iodine perovskite solar cells fabricated by a low-temperature solution-process," en, *Energy Environ. Sci.*, vol. 7, no. 7, pp. 2359–2365, Jun. 2014, Publisher: The Royal Society of Chemistry, ISSN: 1754-5706. DOI: 10.1039/C4EE00233D.

[343] H. Xi, S. Tang, X. Ma, *et al.*, "Performance Enhancement of Planar Heterojunction Perovskite Solar Cells through Tuning the Doping Properties of Hole-Transporting Materials," *ACS Omega*, vol. 2, no. 1, pp. 326–336, Jan. 2017, Publisher: American Chemical Society. DOI: 10.1021/acsomega.6b00465.

[344] J. H. Heo, S. H. Im, J. H. Noh, *et al.*, "Efficient inorganic-organic hybrid heterojunction solar cells containing perovskite compound and polymeric hole conductors," *Nature Photonics*, vol. 7, pp. 486–491, Jun. 2013, ADS Bibcode: 2013NaPho...7..486H, ISSN: 1749-4885. DOI: 10.1038/nphoton.2013.80.

[345] H. A. Abbas, R. Kottokkaran, B. Ganapathy, *et al.*, "High efficiency sequentially vapor grown n-i-p CH3NH3PbI3 perovskite solar cells with undoped P3HT as p-type heterojunction layer," *APL Mater.*, vol. 3, no. 1, p. 016 105, Jan. 2015, ISSN: 2166-532X. DOI: 10.1063/1.4905932.

[346] L. Calió, S. Kazim, M. Grätzel, and S. Ahmad, "Hole-Transport Materials for Perovskite Solar Cells," en, *Angewandte Chemie International Edition*, vol. 55, no. 47, pp. 14 522–14 545, 2016, _eprint: https://onlinelibrary.wiley.com/doi/pdf/10.1002/anie.201601757, ISSN: 1521-3773. DOI: 10.1002/anie.201601757.

[347] J. Cameron and P. J. Skabara, "The damaging effects of the acidity in PEDOT:PSS on semiconductor device performance and solutions based on non-acidic alternatives," en, *Materials Horizons*, vol. 7, no. 7, pp. 1759–1772, 2020, Publisher: Royal Society of Chemistry. DOI: 10.1039/C9MH01978B.

[348] Z. Yu and L. Sun, "Inorganic Hole-Transporting Materials for Perovskite Solar Cells," *Small Methods*, vol. 2, p. 1 700 280, Dec. 2017. DOI: 10.1002/smtd.201700280.

[349] M. Althumayri, R. Das, R. Banavath, L. Beker, A. M. Achim, and H. Ceylan Koydemir, "Recent Advances in Transparent Electrodes and Their Multimodal Sensing Applications," en, *Advanced Science*, vol. 11, no. 38, p. 2 405 099, 2024, _eprint: https://advanced.onlinelibrary.wiley.com/doi/pdf/10.1002/advs.202405099, ISSN: 2198-3844. DOI: 10.1002/advs.202405099.

[350] J. Príncipe, V. C. M. Duarte, A. M. V. M. Pereira, A. Mendes, and L. Andrade, "Highly efficient and cost-effective carbon paper electrode for inverted perovskite solar cells," *Carbon*, vol. 245, p. 120 830, Oct. 2025, ISSN: 0008-6223. DOI: 10.1016/j.carbon.2025.120830.

[351] T. Du, S. Qiu, X. Zhou, *et al.*, "Efficient, stable, and fully printed carbon-electrode perovskite solar cells enabled by hole-transporting bilayers," *Joule*, vol. 7, no. 8, pp. 1920–1937, Aug. 2023, ISSN: 2542-4351. DOI: 10.1016/j.joule.2023.06.005.

[352] G. G. Njema, J. K. Kibet, and S. M. Ngari, "A review of interface engineering characteristics for high performance perovskite solar cells," *Measurement: Energy*, vol. 2, p. 100 005, Jun. 2024, ISSN: 2950-3450. DOI: 10.1016/j.meaene.2024.100005.

[353] T. Ibn-Mohammed, S. C. L. Koh, I. M. Reaney, *et al.*, "Perovskite solar cells: An integrated hybrid lifecycle assessment and review in comparison with other photovoltaic technologies," *Renewable and Sustainable Energy Reviews*, vol. 80, pp. 1321–1344, Dec. 2017, ISSN: 1364-0321. DOI: 10.1016/j.rser.2017.05.095.

[354] F. Di Giacomo, V. Zardetto, G. Lucarelli, *et al.*, "Mesoporous perovskite solar cells and the role of nanoscale compact layers for remarkable all-round high efficiency under both indoor and outdoor illumination," *Nano Energy*, vol. 30, pp. 460–469, Dec. 2016, ISSN: 2211-2855. DOI: 10.1016/j.nanoen.2016.10.030.

[355] Y. Ming, Y. Jiang, J. Li, *et al.*, "Design and upgrade of mesoporous perovskite solar cells," *Chemistry of Inorganic Materials*, vol. 3, p. 100 050, Aug. 2024, ISSN: 2949-7469. DOI: 10.1016/j.cinorg.2024.100050.

[356] M. Abdi-Jalebi, M. I. Dar, A. Sadhanala, *et al.*, "Impact of a Mesoporous Titania–Perovskite Interface on the Performance of Hybrid Organic–Inorganic Perovskite Solar Cells," *J. Phys. Chem. Lett.*, vol. 7, no. 16, pp. 3264–3269, Aug. 2016, Publisher: American Chemical Society. DOI: 10.1021/acs.jpclett.6b01617.

[357] B. Feleki, G. Bex, R. Andriessen, Y. Galagan, and F. Di Giacomo, "Rapid and low temperature processing of mesoporous TiO 2 for perovskite solar cells on flexible and rigid substrates," *Materials Today Communications*, vol. 13, Sep. 2017. DOI: 10.1016/j.mtcomm.2017.09.007.

[358] Y. Huang, L. Zhao, Y. Li, W. Li, and S. Wang, "Comparison of mesoporous materials based on mixed-organic-cation hole-conductor-free perovskite solar cells," *Applied Surface Science*, vol. 493, pp. 975–981, Nov. 2019, ISSN: 0169-4332. DOI: 10.1016/j.apsusc.2019.07.099.

[359] H. D. Pham, T. C.-J. Yang, S. M. Jain, G. J. Wilson, and P. Sonar, "Development of Dopant-Free Organic Hole Transporting Materials for Perovskite Solar Cells," en, *Advanced Energy Materials*, vol. 10, no. 13, p. 1 903 326, 2020, _eprint: https://advanced.onlinelibrary.wiley.com/doi/pdf/10.1002/aenm.201903326, ISSN: 1614-6840. DOI: 10.1002/aenm.201903326.

[360] S. S. Mali and C. K. Hong, "P-i-n/n-i-p type planar hybrid structure of highly efficient perovskite solar cells towards improved air stability: Synthetic strategies and the role of p-type hole transport layer (HTL) and n-type electron transport layer (ETL) metal oxides," en, *Nanoscale*, vol. 8, no. 20, pp. 10 528–10 540, May 2016, Publisher: The Royal Society of Chemistry, ISSN: 2040-3372. DOI: 10.1039/C6NR02276F.

[361] Q. Fatima, A. A. Haidry, H. Zhang, A. El Jery, and M. Aldrdery, "A critical review on advancement and challenges in using TiO2 as electron transport layer for perovskite solar cell," *Materials Today Sustainability*, vol. 27, p. 100 857, Sep. 2024, ISSN: 2589-2347. DOI: 10.1016/j.mtsust.2024.100857.

[362] Y. Zhao, Q. Ye, Z. Chu, F. Gao, X. Zhang, and J. You, "Recent Progress in High-efficiency Planar-structure Perovskite Solar Cells," en, *ENERGY & ENVIRONMENTAL MATERIALS*, vol. 2, no. 2, pp. 93–106, 2019, _eprint: https://onlinelibrary.wiley.com/ ISSN: 2575-0356. DOI: 10.1002/eem2.12042.

[363] A. Ashina, R. K. Battula, E. Ramasamy, N. Chundi, S. Sakthivel, and G. Veerappan, "Dip coated SnO2 film as electron transport layer for low temperature processed planar perovskite solar cells," *Applied Surface Science Advances*, vol. 4, p. 100 066, Jun. 2021, ISSN: 2666-5239. DOI: 10.1016/j.apsadv.2021.100066.

[364] Z. Chen, Z. Lin, Y. Wu, and X. Ouyang, "Polymers for perovskite solar cells: Advances and perspectives," en, *J. Mater. Chem. A*, vol. 13, no. 32, pp. 26 067–26 109, Aug. 2025, Publisher: The Royal Society of Chemistry, ISSN: 2050-7496. DOI: 10.1039/D5TA02970H.

[365] Y. Liu, Y. Xiao, J. Jia, H. Wang, W. Yan, and M. Zhu, "Perovskite solar cells: From planar designs to fiber-based innovations," *Wearable Electronics*, vol. 1, pp. 150–159, Dec. 2024, ISSN: 2950-2357. DOI: 10.1016/j.wees.2024.07.004.

[366] Y.-E. Lye, K.-Y. Chan, and Z.-N. Ng, "A Review on the Progress, Challenges, and Performances of Tin-Based Perovskite Solar Cells," en, *Nanomaterials*, vol. 13, no. 3, p. 585, Jan. 2023, Publisher: Multidisciplinary Digital Publishing Institute, ISSN: 2079-4991. DOI: 10.3390/nano13030585.

[367] S. Li, P. Liu, L. Pan, *et al.*, "The investigation of inverted p-i-n planar perovskite solar cells based on FASnI3 films," *Solar Energy Materials and Solar Cells*, vol. 199, pp. 75–82, Sep. 2019, ISSN: 0927-0248. DOI: 10.1016/j.solmat.2019.04.023.

[368] T. Lemercier, L. Perrin, E. Planes, S. Berson, and L. Flandin, "A Comparison of the Structure and Properties of Opaque and Semi-Transparent NIP/PIN-Type Scalable Perovskite Solar Cells," *Energies*, vol. 13, p. 3794, Jul. 2020. DOI: 10.3390/en13153794.

[369] F. Fu, T. Feurer, T. Weiss, *et al.*, "High-efficiency inverted semi-transparent planar perovskite solar cells in substrate configuration," *Nature Energy*, vol. 2, Dec. 2016. DOI: 10.1038/nenergy.2016.190.

[370] Z. Zhou, X. Li, M. Cai, *et al.*, "Stable Inverted Planar Perovskite Solar Cells with Low-Temperature-Processed Hole-Transport Bilayer," *Advanced Energy Materials*, vol. 7, Aug. 2017. DOI: 10.1002/aenm.201700763.

[371] M. I. Asghar, J. Zhang, H. Wang, and P. D. Lund, "Device stability of perovskite solar cells – A review," en, *Renewable and Sustainable Energy Reviews*, vol. 77, no. C, pp. 131–146, 2017, Publisher: Elsevier.

[372] J. Chen and N.-G. Park, "Inorganic Hole Transporting Materials for Stable and High Efficiency Perovskite Solar Cells," *J. Phys. Chem. C*, vol. 122, no. 25, pp. 14 039–14 063, Jun. 2018, Publisher: American Chemical Society, ISSN: 1932-7447. DOI: 10.1021/acs.jpcc.8b01177.

[373] X. Qi, Y. Hu, L. Chen, *et al.*, "Performance research of perovskite solar cell with light conversion electron transport layer utilizing prism scattered lights," *Optical Materials*, vol. 141, p. 113 987, Jul. 2023, ISSN: 0925-3467. DOI: 10.1016/j.optmat.2023.113987.

[374] O. O. Moyofola and M. E. Emetere, "Improving the performance conversion efficiency of perovskite solar cells through optimization of charge transport layers: A review," *Renewable and Sustainable Energy Reviews*, vol. 222, p. 115 943, Oct. 2025, ISSN: 1364-0321. DOI: 10.1016/j.rser.2025.115943.

[375] M. S. Hasan, J. Alom, M. Asaduzzaman, *et al.*, "Recent Criterion on Stability Enhancement of Perovskite Solar Cells," en, *Processes*, vol. 10, no. 7, p. 1408, Jul. 2022, Publisher: Multidisciplinary Digital Publishing Institute, ISSN: 2227-9717. DOI: 10.3390/pr10071408.

[376] F. Wu, R. Pathak, K. Chen, *et al.*, "Inverted Current–Voltage Hysteresis in Perovskite Solar Cells," *ACS Energy Lett.*, vol. 3, no. 10, pp. 2457–2460, Oct. 2018, Publisher: American Chemical Society. DOI: 10.1021/acsenergylett.8b01606.

[377] C. Yang, X. Shan, and T. Xie, "Insights of Hysteresis Behaviors in Perovskite Solar Cells from a Mixed Drift-Diffusion Model Coupled with Recombination," en, *Photonics*, vol. 7, no. 3, p. 47, Sep. 2020, Publisher: Multidisciplinary Digital Publishing Institute, ISSN: 2304-6732. DOI: 10.3390/photonics7030047.

[378] H. Zai, Y. Ma, Q. Chen, and H. Zhou, "Ion migration in halide perovskite solar cells: Mechanism, characterization, impact and suppression," *Journal of Energy Chemistry*, In Celebration of the 100th anniversary of Chemisry at Nankai University, vol. 63, pp. 528–549, Dec. 2021, ISSN: 2095-4956. DOI: 10.1016/j.jechem.2021.08.006.

[379] "Fundamentals of Hysteresis in Perovskite Solar Cells: From Structure-Property Relationship to Neoteric Breakthroughs," en, DOI: 10.1002/tcr.202100150.

[380] X. Shen, K. Kang, Z. Yu, *et al.*, "Passivation strategies for mitigating defect challenges in halide perovskite light-emitting diodes," *Joule*, vol. 7, no. 2, pp. 272–308, Feb. 2023, ISSN: 2542-4351. DOI: 10.1016/j.joule.2023.01.008.

[381] L. Fu, H. Li, L. Wang, R. Yin, B. Li, and L. Yin, "Defect passivation strategies in perovskites for an enhanced photovoltaic performance," en, *Energy Environ. Sci.*, vol. 13, no. 11, pp. 4017–4056, Nov. 2020, Publisher: The Royal Society of Chemistry, ISSN: 1754-5706. DOI: 10.1039/D0EE01767A.

[382] R. Liu, R. Yu, and Z. Tan, "Photostability of Perovskite Solar Cells: Challenges and Strategies," en, *Nanomaterials*, vol. 15, no. 11, p. 786, Jan. 2025, Publisher: Multidisciplinary Digital Publishing Institute, ISSN: 2079-4991. DOI: 10.3390/nano15110786.

[383] F. Wang, Y. Han, D. Duan, C. Ge, H. Hu, and G. Li, "Recent progress of scalable perovskite solar cells and modules," *Energy Reviews*, vol. 1, no. 2, p. 100 010, Dec. 2022, ISSN: 2772-9702. DOI: 10.1016/j.enrev.2022.100010.

[384] H. Nikbakht, P. Mariani, L. Vesce, *et al.*, "Upscaling Perovskite Photovoltaics: From 156 cm2 Modules to 0.73 M2 Panels," en, *Advanced Science*, vol. 12, no. 22, p. 2 416 316, 2025, _eprint: https://advanced.onlinelibrary.wiley.com/doi/pdf/10.1002/advs.2024 ISSN: 2198-3844. DOI: 10.1002/advs.202416316.

[385] Z. Yang, S. Zhang, L. Li, and W. Chen, "Research progress on large-area perovskite thin films and solar modules," *Journal of Materiomics*, vol. 3, no. 4, pp. 231–244, Dec. 2017, ISSN: 2352-8478. DOI: 10.1016/j.jmat.2017.09.002.

[386] G. E. Eperon, S. D. Stranks, C. Menelaou, M. B. Johnston, L. M. Herz, and H. J. Snaith, "Formamidinium lead trihalide: A broadly tunable perovskite for efficient planar heterojunction solar cells," en, *Energy Environ. Sci.*, vol. 7, no. 3, pp. 982–988, Feb. 2014, Publisher: The Royal Society of Chemistry, ISSN: 1754-5706. DOI: 10.1039/C3EE43822H.

[387] R. Wang, M. Mujahid, Y. Duan, Z.-K. Wang, J. Xue, and Y. Yang, "A Review of Perovskites Solar Cell Stability," en, *Advanced Functional Materials*, vol. 29, no. 47, p. 1 808 843, 2019, _eprint: https://advanced.onlinelibrary.wiley.com/doi/pdf/10.1002/adfm.2018 ISSN: 1616-3028. DOI: 10.1002/adfm.201808843.

[388] T. Seyisi, B. G. Fouda-Mbanga, J. I. Mnyango, *et al.*, "Major challenges for commercialization of perovskite solar cells: A critical review," *Energy Reports*, vol. 13, pp. 1400–1415, Jun. 2025, ISSN: 2352-4847. DOI: 10.1016/j.egyr.2025.01.019.

[389] K. O. Ogunniran and N. T. Martins, "Humidity and Moisture Degradation of Perovskite Material in Solar Cells: Effects on Efficiency," en, *IOP Conf. Ser.: Earth Environ. Sci.*, vol. 655, no. 1, p. 012 049, Feb. 2021, Publisher: IOP Publishing, ISSN: 1755-1315. DOI: 10.1088/1755-1315/655/1/012049.

[390] B. P. Kore, M. Jamshidi, and J. M. Gardner, "The impact of moisture on the stability and degradation of perovskites in solar cells," en, *Mater. Adv.*, vol. 5, no. 6, pp. 2200–2217, Mar. 2024, Publisher: RSC, ISSN: 2633-5409. DOI: 10.1039/D3MA00828B.

[391] D. Bryant, N. Aristidou, S. Pont, *et al.*, "Light and oxygen induced degradation limits the operational stability of methylammonium lead triiodide perovskite solar cells," en, *Energy Environ. Sci.*, vol. 9, no. 5, pp. 1655–1660, May 2016, Publisher: The Royal Society of Chemistry, ISSN: 1754-5706. DOI: 10.1039/C6EE00409A.

[392] Z. Zhang, X. Tian, C. Wang, *et al.*, "Revealing superoxide-induced degradation in lead-free tin perovskite solar cells," *Energy & Environmental Science*, Oct. 2022. DOI: 10.1039/D2EE02796H.

[393] X. Li, M. Ibrahim Dar, C. Yi, *et al.*, "Improved performance and stability of perovskite solar cells by crystal crosslinking with alkylphosphonic acid $\omega$-ammonium chlorides," en, *Nature Chem*, vol. 7, no. 9, pp. 703–711, Sep. 2015, Publisher: Nature Publishing Group, ISSN: 1755-4349. DOI: 10.1038/nchem.2324.

[394] M. Helal Miah, M. Bulu Rahman, M. Nur-E-Alam, *et al.*, "Key degradation mechanisms of perovskite solar cells and strategies for enhanced stability: Issues and prospects," en, *RSC Advances*, vol. 15, no. 1, pp. 628–654, 2025, Publisher: Royal Society of Chemistry. DOI: 10.1039/D4RA07942F.

[395] T. Webb, S. J. Sweeney, and W. Zhang, "Device Architecture Engineering: Progress toward Next Generation Perovskite Solar Cells," en, *Advanced Functional Materials*, vol. 31, no. 35, p. 2 103 121, 2021, _eprint: https://advanced.onlinelibrary.wiley.com/doi/pdf/ ISSN: 1616-3028. DOI: 10.1002/adfm.202103121.

[396] C.-H. Lin, L. Hu, X. Guan, *et al.*, "Electrode Engineering in Halide Perovskite Electronics: Plenty of Room at the Interfaces," en, *Advanced Materials*, vol. 34, no. 18, p. 2 108 616, 2022, _eprint: https://advanced.onlinelibrary.wiley.com/doi/pdf/10.1002/adma.202 ISSN: 1521-4095. DOI: 10.1002/adma.202108616.

[397] K. Datta, B. T. van Gorkom, Z. Chen, *et al.*, "Effect of Light-Induced Halide Segregation on the Performance of Mixed-Halide Perovskite Solar Cells," *ACS Appl. Energy Mater.*, vol. 4, no. 7, pp. 6650–6658, Jul. 2021, Publisher: American Chemical Society. DOI: 10.1021/acsaem.1c00707.

[398] Y. Guo, X. Yin, D. Liu, *et al.*, "Photoinduced Self-healing of Halide Segregation in Mixed-halide Perovskites," *ACS Energy Letters*, vol. 6, pp. 2502–2511, Jun. 2021. DOI: 10.1021/acsenergylett.1c01040.

[399] N. K. Tailor, "Influence of the A-site cation on hysteresis and ion migration in lead-free perovskite single crystals," *Phys. Rev. Mater.*, vol. 6, no. 4, 2022. DOI: 10.1103/PhysRevMaterials.6.045401.

[400] E. Bi, Z. Song, C. Li, Z. Wu, and Y. Yan, "Mitigating ion migration in perovskite solar cells," en, *Trends in Chemistry*, vol. 3, no. 7, pp. 575–588, Jul. 2021, ISSN: 25895974. DOI: 10.1016/j.trechm.2021.04.004.

[401] L. Zuo, Z. Li, and H. Chen, "Ion Migration and Accumulation in Halide Perovskite Solar Cells," en, *Chinese Journal of Chemistry*, vol. 41, no. 7, pp. 861–876, 2023, _eprint: https://onlinelibrary.wiley.com/doi/pdf/10.1002/cjoc.202200505, ISSN: 1614-7065. DOI: 10.1002/cjoc.202200505.

[402] A. E. Magdalin, P. D. Nixon, E. Jayaseelan, *et al.*, "Development of lead-free perovskite solar cells: Opportunities, challenges, and future technologies," *Results in Engineering*, vol. 20, p. 101 438, Dec. 2023, ISSN: 2590-1230. DOI: 10.1016/j.rineng.2023.101438.

[403] M. Ren, X. Qian, Y. Chen, T. Wang, and Y. Zhao, "Potential lead toxicity and leakage issues on lead halide perovskite photovoltaics," *Journal of Hazardous Materials*, vol. 426, p. 127 848, Mar. 2022, ISSN: 0304-3894. DOI: 10.1016/j.jhazmat.2021.127848.

[404] N. Balagowtham, K. R. Acchutharaman, M. S. Pandian, M. Kumar, J.-H. Chang, and P. Ramasamy, "Challenges in commercializing perovskite solar cells with focus on sustainability, stability, and cost efficiency," *Solar Energy*, vol. 301, p. 113 892, Nov. 2025, ISSN: 0038-092X. DOI: 10.1016/j.solener.2025.113892.

[405] B. Ehrler, E. Alarcón-Lladó, S. W. Tabernig, T. Veeken, E. C. Garnett, and A. Polman, "Photovoltaics Reaching for the Shockley–Queisser Limit," en, *ACS Energy Lett.*, vol. 5, no. 9, pp. 3029–3033, Sep. 2020, ISSN: 2380-8195, 2380-8195. DOI: 10.1021/acsenergylett.0c01790.

[406] S.-B. Wen and A. Bhaskar, "The Shockley–Queisser Efficiency Limit of Solar Thermophotovoltaic (STPV) Cells Using Different Photovoltaic Cells and a Radiation Shield Considering the étendue of Solar Radiation," en, *Energies*, vol. 16, no. 20, p. 7085, Jan. 2023, Publisher: Multidisciplinary Digital Publishing Institute, ISSN: 1996-1073. DOI: 10.3390/en16207085.

[407] E. Raza and Z. Ahmad, "Review on two-terminal and four-terminal crystalline-silicon/perovskite tandem solar cells; progress, challenges, and future perspectives," *Energy Reports*, vol. 8, pp. 5820–5851, Nov. 2022, ISSN: 2352-4847. DOI: 10.1016/j.egyr.2022.04.028.

[408] K. Alberi, J. J. Berry, J. J. Cordell, *et al.*, "A roadmap for tandem photovoltaics," *Joule*, vol. 8, no. 3, pp. 658–692, Mar. 2024, ISSN: 2542-4351. DOI: 10.1016/j.joule.2024.01.017.

[409] J. Huang and L. Mao, "A Review on Perovskite/Silicon Tandem Solar Cells: Current Status and Future Challenges," en, *Energies*, vol. 18, no. 16, p. 4327, Jan. 2025, Publisher: Multidisciplinary Digital Publishing Institute, ISSN: 1996-1073. DOI: 10.3390/en18164327.

[410] P. Kumar, S. Thokala, S. P. Singh, and R. Singh, "Research progress and challenges in extending the infra-red absorption of perovskite tandem solar cells," *Nano Energy*, vol. 121, p. 109 175, Mar. 2024, ISSN: 2211-2855. DOI: 10.1016/j.nanoen.2023.109175.

[411] P. Kumar, G. Shankar, A. Kumar, A. Najar, and B. Pradhan, "Recent progress in all-perovskite tandem solar cells and modules: Redefining limits," *Progress in Materials Science*, vol. 156, p. 101 560, Feb. 2026, ISSN: 0079-6425. DOI: 10.1016/j.pmatsci.2025.101560.

[412] T. Leijtens, K. A. Bush, R. Prasanna, and M. D. McGehee, "Opportunities and challenges for tandem solar cells using metal halide perovskite semiconductors," en, *Nat Energy*, vol. 3, no. 10, pp. 828–838, Jul. 2018, ISSN: 2058-7546. DOI: 10.1038/s41560-018-0190-4.

[413] M. Simmonds, K. Xu, S. Albrecht, L. Korte, and I. Levine, "Monitoring Charge Separation of Individual Cells in Perovskite/Silicon Tandems via Transient Surface Photovoltage Spectroscopy," *Solar RRL*, vol. 9, Jul. 2025. DOI: 10.1002/solr.202500321.

[414] M. H. Futscher and B. Ehrler, "Efficiency Limit of Perovskite/Si Tandem Solar Cells," en, *ACS Energy Lett.*, vol. 1, no. 4, pp. 863–868, Oct. 2016, ISSN: 2380-8195, 2380-8195. DOI: 10.1021/acsenergylett.6b00405.

[415] M. Jošt, L. Kegelmann, L. Korte, and S. Albrecht, "Monolithic Perovskite Tandem Solar Cells: A Review of the Present Status and Advanced Characterization Methods Toward 30% Efficiency," en, *Advanced Energy Materials*, vol. 10, no. 26, p. 1 904 102, 2020, _eprint: https://advanced.onlinelibrary.wiley.com/doi/pdf/10.1002/aenm.201 ISSN: 1614-6840. DOI: 10.1002/aenm.201904102.

[416] J. Werner, C.-H. Weng, A. Walter, *et al.*, "Efficient Monolithic Perovskite/Silicon Tandem Solar Cell with Cell Area >1 cm2," *J. Phys. Chem. Lett.*, vol. 7, no. 1, pp. 161–166, Jan. 2016, Publisher: American Chemical Society. DOI: 10.1021/acs.jpclett.5b02686.

[417] Y. Cheng and L. Ding, "Perovskite/Si tandem solar cells: Fundamentals, advances, challenges, and novel applications," en, *SusMat*, vol. 1, no. 3, pp. 324–344, 2021, _eprint: https://onlinelibrary.wiley.com/doi/pdf/10.1002/sus2.25, ISSN: 2692-4552. DOI: 10.1002/sus2.25.

[418] J. Wei, D. Zhang, R. Li, *et al.*, "Operationally Stable Perovskite/Silicon Tandem Solar Cells via Suppression of Lead Iodide-Mediated Phase Segregation in Wide-Bandgap Perovskites," en, *Advanced Energy Materials*, vol. 15, no. 34, p. 2 502 696, 2025, _eprint: https://advanced.onlinelibrary.wiley.com/doi/pdf/10.1002/aenm.202502696, ISSN: 1614-6840. DOI: 10.1002/aenm.202502696.

[419] F. Khan, B. D. Rezgui, M. T. Khan, and F. Al-Sulaiman, "Perovskite-based tandem solar cells: Device architecture, stability, and economic perspectives," *Renewable and Sustainable Energy Reviews*, vol. 165, p. 112 553, Sep. 2022, ISSN: 1364-0321. DOI: 10.1016/j.rser.2022.112553.

[420] J. H. Park, S. G. Ji, I. J. Park, S. K. Hwang, H. W. Lim, and J. Y. Kim, "Subcell characterization of two-terminal perovskite/silicon tandem solar cells," *Cell Reports Physical Science*, vol. 3, no. 10, p. 101 076, Oct. 2022, ISSN: 2666-3864. DOI: 10.1016/j.xcrp.2022.101076.

[421] Y. Lin, W. Yang, H. Gu, *et al.*, "Transparent Recombination Layers Design and Rational Characterizations for Efficient Two-Terminal Perovskite-Based Tandem Solar Cells," *Advanced Materials*, vol. 36, e2405684, May 2024. DOI: 10.1002/adma.202405684.

[422] M. Zhang and Z. Lin, "Efficient interconnecting layers in monolithic all-perovskite tandem solar cells," en, *Energy Environ. Sci.*, vol. 15, no. 8, pp. 3152–3170, Aug. 2022, Publisher: The Royal Society of Chemistry, ISSN: 1754-5706. DOI: 10.1039/D2EE00731B.

[423] J. P. Mailoa, C. D. Bailie, E. C. Johlin, *et al.*, "A 2-terminal perovskite/silicon multijunction solar cell enabled by a silicon tunnel junction," *Appl. Phys. Lett.*, vol. 106, no. 12, p. 121 105, Mar. 2015, ISSN: 0003-6951. DOI: 10.1063/1.4914179.

[424] C. Li, Y. Chen, Y. Li, *et al.*, "Achieving 32% Efficiency in Perovskite/Silicon Tandem Solar Cells with Bidentate-Anchored Superwetting Self-Assembled Molecular Layers," *Angewandte Chemie International Edition*, vol. 64, Apr. 2025. DOI: 10.1002/anie.202502730.

[425] A. S. R. Bati, Y. L. Zhong, P. L. Burn, M. K. Nazeeruddin, P. E. Shaw, and M. Batmunkh, "Next-generation applications for integrated perovskite solar cells," en, *Commun Mater*, vol. 4, no. 1, p. 2, Jan. 2023, Publisher: Nature Publishing Group, ISSN: 2662-4443. DOI: 10.1038/s43246-022-00325-4.

[426] Z. Shokrollahi, M. Piralaee, and A. Asgari, "Performance and optimization study of selected 4-terminal tandem solar cells," en, *Sci Rep*, vol. 14, no. 1, p. 11 515, May 2024, Publisher: Nature Publishing Group, ISSN: 2045-2322. DOI: 10.1038/s41598-024-62085-0.

[427] N. N. Lal, Y. Dkhissi, W. Li, Q. Hou, Y.-B. Cheng, and U. Bach, "Perovskite Tandem Solar Cells," en, *Advanced Energy Materials*, vol. 7, no. 18, p. 1 602 761, 2017, _eprint: https://advanced.onlinelibrary.wiley.com/doi/pdf/10.1002/aenm.201602761, ISSN: 1614-6840. DOI: 10.1002/aenm.201602761.

[428] S. Ašmontas and M. Mujahid, "Recent Progress in Perovskite Tandem Solar Cells," en, *Nanomaterials*, vol. 13, no. 12, p. 1886, Jan. 2023, Publisher: Multidisciplinary Digital Publishing Institute, ISSN: 2079-4991. DOI: 10.3390/nano13121886.

[429] E. Raza, Z. Ahmad, F. Aziz, *et al.*, "Design and optimization of four-terminal mechanically stacked and optically coupled silicon/perovskite tandem solar cells with over 28% efficiency," *Heliyon*, vol. 9, no. 2, e13477, Feb. 2023, ISSN: 2405-8440. DOI: 10.1016/j.heliyon.2023.e13477.

[430] N. E. I. Boukortt, C. Triolo, S. Santangelo, and S. Patanè, "All-Perovskite Tandem Solar Cells: From Certified 25% and Beyond," en, *Energies*, vol. 16, no. 8, p. 3519, Jan. 2023, Publisher: Multidisciplinary Digital Publishing Institute, ISSN: 1996-1073. DOI: 10.3390/en16083519.

[431] S. P. Bremner, M. Y. Levy, and C. B. Honsberg, "Analysis of tandem solar cell efficiencies under AM1.5G spectrum using a rapid flux calculation method," en, *Progress in Photovoltaics: Research and Applications*, vol. 16, no. 3, pp. 225–233, 2008, _eprint: https://onlinelibrary.wiley.com/doi/pdf/10.1002/pip.799, ISSN: 1099-159X. DOI: 10.1002/pip.799.

[432] M. I. Hossain, W. Qarony, S. Ma, L. Zeng, D. Knipp, and Y. H. Tsang, "Perovskite/Silicon Tandem Solar Cells: From Detailed Balance Limit Calculations to Photon Management," en, *Nano-Micro Lett.*, vol. 11, no. 1, p. 58, Jul. 2019, ISSN: 2150-5551. DOI: 10.1007/s40820-019-0287-8.

[433] Z. Liu, R. Lin, M. Wei, *et al.*, "All-perovskite tandem solar cells achieving >29% efficiency with improved (100) orientation in wide-bandgap perovskites," en, *Nat. Mater.*, vol. 24, no. 2, pp. 252–259, Feb. 2025, Publisher: Nature Publishing Group, ISSN: 1476-4660. DOI: 10.1038/s41563-024-02073-x.

[434] D. Zhao, C. Chen, C. Wang, *et al.*, "Efficient two-terminal all-perovskite tandem solar cells enabled by high-quality low-bandgap absorber layers," en, *Nat Energy*, vol. 3, no. 12, pp. 1093–1100, Dec. 2018, Publisher: Nature Publishing Group, ISSN: 2058-7546. DOI: 10.1038/s41560-018-0278-x.

[435] D. Forgács, L. Gil-Escrig, D. Pérez-Del-Rey, *et al.*, "Efficient Monolithic Perovskite/Perovskite Tandem Solar Cells," *Advanced Energy Materials*, vol. 7, no. 8, p. 1 602 121, 2017, _eprint: https://advanced.onlinelibrary.wiley.com/doi/pdf/10.1002/aenm.201 ISSN: 1614-6840. DOI: 10.1002/aenm.201602121.

[436] M. I. Hossain, A. M. Saleque, S. Ahmed, *et al.*, "Perovskite/perovskite planar tandem solar cells: A comprehensive guideline for reaching energy conversion efficiency beyond 30%," en, *Nano Energy*, vol. 79, p. 105 400, Jan. 2021, ISSN: 22112855. DOI: 10.1016/j.nanoen.2020.105400.

[437] Y. Bai, Y. Meng, M. Yang, *et al.*, "Lattice stabilization and strain homogenization in Sn-Pb bottom subcells enable stable all-perovskite tandems solar cells," en, *Nat Commun*, vol. 16, no. 1, p. 7344, Aug. 2025, Publisher: Nature Publishing Group, ISSN: 2041-1723. DOI: 10.1038/s41467-025-62661-6.

[438] A. Onno, N. Rodkey, A. Asgharzadeh, *et al.*, "Predicted Power Output of Silicon-Based Bifacial Tandem Photovoltaic Systems," English, *Joule*, vol. 4, no. 3, pp. 580–596, Mar. 2020, Publisher: Elsevier, ISSN: 2542-4785, 2542-4351. DOI: 10.1016/j.joule.2019.12.017.

[439] M. A. Alam and M. R. Khan, "Thermodynamic efficiency limits of classical and bifacial multi-junction tandem solar cells: An analytical approach," *Appl. Phys. Lett.*, vol. 109, no. 17, p. 173 504, Oct. 2016, ISSN: 0003-6951. DOI: 10.1063/1.4966137.

[440] M. M. Salah, A. Zekry, A. Shaker, M. Abouelatta, M. Mousa, and A. Saeed, "Investigation of Electron Transport Material-Free Perovskite/CIGS Tandem Solar Cell," en, *Energies*, vol. 15, no. 17, p. 6326, Jan. 2022, Publisher: Multidisciplinary Digital Publishing Institute, ISSN: 1996-1073. DOI: 10.3390/en15176326.

[441] R. K. Kothandaraman, H. Lai, A. Aribia, *et al.*, "Laser Patterned Flexible 4T Perovskite-Cu(In,Ga)Se2 Tandem Mini-module with Over 18% Efficiency," en, *Solar RRL*, vol. 6, no. 9, p. 2 200 392, 2022, _eprint: https://onlinelibrary.wiley.com/doi/pdf/10.100 ISSN: 2367-198X. DOI: 10.1002/solr.202200392.

[442] T. Todorov, T. Gershon, O. Gunawan, *et al.*, "Monolithic Perovskite-CIGS Tandem Solar Cells via In Situ Band Gap Engineering," *Advanced Energy Materials*, vol. 5, no. 23, p. 1 500 799, 2015, _eprint: https://advanced.onlinelibrary.wiley.com/doi/pdf/10.1002/aer ISSN: 1614-6840. DOI: 10.1002/aenm.201500799.

[443] M. Jošt, E. Köhnen, A. Al-Ashouri, *et al.*, "Perovskite/CIGS Tandem Solar Cells: From Certified 24.2% toward 30% and Beyond," *ACS Energy Lett.*, vol. 7, no. 4, pp. 1298–1307, Apr. 2022, Publisher: American Chemical Society. DOI: 10.1021/acsenergylett.2c00274.

[444] M. Nakamura, C. C. Lin, C. Nishiyama, K. Tada, T. Bessho, and H. Segawa, "Semi-transparent Perovskite Solar Cells for Four-Terminal Perovskite/CIGS Tandem Solar Cells," *ACS Appl. Energy Mater.*, vol. 5, no. 7, pp. 8103–8111, Jul. 2022, Publisher: American Chemical Society. DOI: 10.1021/acsaem.2c00620.

[445] D. H. Kim, C. P. Muzzillo, J. Tong, *et al.*, "Bimolecular Additives Improve Wide-Band-Gap Perovskites for Efficient Tandem Solar Cells with CIGS," *Joule*, vol. 3, no. 7, pp. 1734–1745, Jul. 2019, ISSN: 2542-4351. DOI: 10.1016/j.joule.2019.04.012.

[446] J. F. Benitez Rodriguez, D. Chen, M. Gao, and R. Caruso, "Roll-to-Roll Processes for the Fabrication of Perovskite Solar Cells under Ambient Conditions," *Solar RRL*, vol. 5, Aug. 2021. DOI: 10.1002/solr.202100341.

[447] J. Luo, L. Tang, S. Wang, *et al.*, "Manipulating Ga growth profile enables all-flexible high-performance single-junction CIGS and 4 T perovskite/CIGS tandem solar cells," *Chemical Engineering Journal*, vol. 455, p. 140 960, Jan. 2023, ISSN: 1385-8947. DOI: 10.1016/j.cej.2022.140960.

[448] L. Tang, H. Yan, L. Zeng, *et al.*, "Record-Efficient Flexible Monolithic Perovskite–CIGS Tandem Solar Cell with VOC Exceeding 1.8 V on Polymer Substrate," en, *Advanced Energy Materials*, vol. 15, no. 23, p. 2 403 682, 2025, _eprint: https://advanced.onlinelib ISSN: 1614-6840. DOI: 10.1002/aenm.202403682.

[449] J. X. Zhai, L. Xie, and S. Shafian, "Advancements in perovskite/CIGS tandem solar cells: Material synergies, device configurations, and economic viability for sustainable energy," en, *Nanotechnology Reviews*, vol. 14, no. 1, Jan. 2025, Publisher: De Gruyter, ISSN: 2191-9097. DOI: 10.1515/ntrev-2025-0196.

[450] E.-B. Kim, M. S. Akhtar, C. Liu, Y. Wang, and S. Ameen, "Possibility of highly efficient 2D–3D perovskite/CIGS tandem solar cells with over 30% efficiency," en, *J. Mater. Chem. A*, vol. 12, no. 20, pp. 12 262–12 273, May 2024, Publisher: The Royal Society of Chemistry, ISSN: 2050-7496. DOI: 10.1039/D3TA07628H.

[451] W. Chi, S. K. Banerjee, K. G. D. I. Jayawardena, S. R. P. Silva, and S. I. Seok, "Perovskite/Silicon Tandem Solar Cells: Choice of Bottom Devices and Recombination Layers," *ACS Energy Lett.*, vol. 8, no. 3, pp. 1535–1550, Mar. 2023, Publisher: American Chemical Society. DOI: 10.1021/acsenergylett.2c02725.

[452] C. Marchant and R. M. Williams, "Perovskite/silicon tandem solar cells–compositions for improved stability and power conversion efficiency," en, *Photochem Photobiol Sci*, vol. 23, no. 1, pp. 1–22, Jan. 2024, ISSN: 1474-9092. DOI: 10.1007/s43630-023-00500-7.

[453] A. K. Abbasi and J. P. Tiwari, "Silicon–Perovskite Tandem Solar Cells: An Alternative to the Market-Dominated Silicon-Based Solar Cell Technology," *ACS Appl. Mater. Interfaces*, vol. 17, no. 37, pp. 51 552–51 577, Sep. 2025, Publisher: American Chemical Society, ISSN: 1944-8244. DOI: 10.1021/acsami.5c09599.

[454] M. He, M. Zhang, Z. Li, *et al.*, "Top Cells for Silicon-Based Tandem Photovoltaics," en, *Advanced Materials*, vol. n/a, no. n/a, p. 2 411 858, _eprint: https://advanced.onlinelibrary.wi ISSN: 1521-4095. DOI: 10.1002/adma.202411858.

[455] Y. Yao, S. Liu, C. D. Rodríguez-Gallegos, C. A. Rodríguez-Gallegos, Z. Wang, and Y. Hou, "Perovskite-based multi-junction solar cells," en, *Nat. Rev. Clean Technol.*, pp. 1–17, Sep. 2025, Publisher: Nature Publishing Group, ISSN: 3005-0685. DOI: 10.1038/s44359-025-00103-8.

[456] C. D. Bailie, M. G. Christoforo, J. P. Mailoa, *et al.*, "Semi-transparent perovskite solar cells for tandems with silicon and CIGS," en, *Energy Environ. Sci.*, vol. 8, no. 3, pp. 956–963, Mar. 2015, Publisher: The Royal Society of Chemistry, ISSN: 1754-5706. DOI: 10.1039/C4EE03322A.

[457] *Oxford PV*. [Online]. Available: https://www.oxfordpv.com/press-releases/oxford-pv-solar-energy-innovation (visited on 09/17/2025).

[458] N. Liu, L. Wang, F. Xu, J. Wu, T. Song, and Q. Chen, "Recent Progress in Developing Monolithic Perovskite/Si Tandem Solar Cells," English, *Front. Chem.*, vol. 8, Dec. 2020, Publisher: Frontiers, ISSN: 2296-2646. DOI: 10.3389/fchem.2020.603375.

[459] D. Turkay, K. Artuk, X.-Y. Chin, *et al.*, "Synergetic substrate and additive engineering for over 30%-efficient perovskite-Si tandem solar cells," *Joule*, vol. 8, no. 6, pp. 1735–1753, Jun. 2024, ISSN: 2542-4351. DOI: 10.1016/j.joule.2024.04.015.

[460] L. Duan, D. Walter, N. Chang, *et al.*, "Stability challenges for the commercialization of perovskite–silicon tandem solar cells," *Nature Reviews Materials*, vol. 8, pp. 1–21, Jan. 2023. DOI: 10.1038/s41578-022-00521-1.

[461] O. Er-raji, M. A. A. Mahmoud, O. Fischer, *et al.*, "Tailoring perovskite crystallization and interfacial passivation in efficient, fully textured perovskite silicon tandem solar cells," *Joule*, vol. 8, no. 10, pp. 2811–2833, Oct. 2024, ISSN: 2542-4351. DOI: 10.1016/j.joule.2024.06.018.

[462] K. K. Shin Thant, C. Seriwattanachai, T. Jittham, N. Thamangraksat, P. Sakata, and P. Kanjanaboos, "Comprehensive Review on Slot-Die-Based Perovskite Photovoltaics: Mechanisms, Materials, Methods, and Marketability," en, *Advanced Energy Materials*, vol. 15, no. 5, p. 2 403 088, 2025, _eprint: https://advanced.onlinelibrary.wiley.com ISSN: 1614-6840. DOI: 10.1002/aenm.202403088.

[463] F. E. Ikuemonisan, Y. O. Kayode, and O. B. Odubote, "A comparative analysis of numerical and experimental optimization of $CuSbS_2$ absorber layer thickness for improved solar cell performance," *Next Materials*, vol. 8, p. 100 870, Jul. 2025, ISSN: 2949-8228. DOI: 10.1016/j.nxmate.2025.100870.

[464] F. Cherif and H. Sammouda, "Strategies for high performance perovskite/c-Si tandem solar cells: Effects of bandgap engineering, solar concentration and device temperature," *Optical Materials*, vol. 106, p. 109 935, Apr. 2020. DOI: 10.1016/j.optmat.2020.109935.

[465] H. Zhang, Y. Luo, T. A. Dela Peña, *et al.*, "Latest Strategies Promoting Stable and Efficient Perovskite, Organic, and Perovskite-Organic Tandem Solar Cells," en, *Advanced Materials Interfaces*, vol. 12, no. 13, p. 2 500 204, 2025, _eprint: https://advanced.onlinelibrary.wiley.com/doi/pdf/10.1002/admi.202500204, ISSN: 2196-7350. DOI: 10.1002/admi.202500204.

[466] *GCL reaches 29.51% efficiency of perovskite-silicon tandem module | Perovskite-Info*. [Online]. Available: https://www.perovskite-info.com/gcl-reaches-2951-efficiency-perovskite-silicon-tandem-module (visited on 09/17/2025).

[467] J. Li, E. Alvianto, and Y. Hou, "Developing the Next-Generation Perovskite/Si Tandems: Toward Efficient, Stable, and Commercially Viable Photovoltaics," *ACS Appl. Mater. Interfaces*, vol. 14, no. 30, pp. 34 262–34 268, Aug. 2022, Publisher: American Chemical Society, ISSN: 1944-8244. DOI: 10.1021/acsami.2c01191.

[468] Z. S. Ismail, E. F. Sawires, F. Z. Amer, and S. O. Abdellatif, "Experimentally verified analytical models for the dynamic response of perovskite solar cells using measured I–V and C–V characteristics," en, *Opt Quant Electron*, vol. 55, no. 14, p. 1272, Dec. 2023, ISSN: 0306-8919, 1572-817X. DOI: 10.1007/s11082-023-05304-8.

[469] C.-J. Yu, "Advances in modelling and simulation of halide perovskites for solar cell applications," en, *J. Phys. Energy*, vol. 1, no. 2, p. 022 001, Jan. 2019, ISSN: 2515-7655. DOI: 10.1088/2515-7655/aaf143.

[470] D. Sharma, R. Mehra, and B. Raj, *Mathematical Modelling And Simulation of CH3NH3Pb(I1-Xbrx)3 Based Perovskite Solar Cells For High Efficiency*, en, Jan. 2022. DOI: 10.21203/rs.3.rs-1133949/v1. [Online]. Available: https://www.researchsquare.com/article/rs-1133949/v1 (visited on 11/27/2024).

[471] H. Xue, K. Fu, L. H. Wong, E. Birgersson, and R. Stangl, "Modelling and loss analysis of meso-structured perovskite solar cells," en, *Journal of Applied Physics*, vol. 122, no. 8, p. 083 105, Aug. 2017, ISSN: 0021-8979, 1089-7550. DOI: 10.1063/1.4986115.

[472] A. Rismanchi, V. Mottaghitalab, and H. Rahimpour Soleimani, "The modelling and simulation of perovskite solar cell consisting textile-based electrodes," en, *Results in Surfaces and Interfaces*, vol. 10, p. 100 095, Feb. 2023, ISSN: 26668459. DOI: 10.1016/j.rsurfi.2022.100095.

[473] M. Z. Kabir, "A Physics-Based Analytical Model for Current–Voltage Characteristics of Perovskite Solar Cells Incorporating Bulk Recombination," en, *Energies*, vol. 14, no. 13, p. 3868, Jun. 2021, ISSN: 1996-1073. DOI: 10.3390/en14133868.

[474] M. Z. Kabir, "Analytical Model for Current–Voltage Characteristics in Perovskite Solar Cells Incorporating Bulk and Surface Recombination," en, *Micromachines*, vol. 15, no. 8, p. 972, Jul. 2024, ISSN: 2072-666X. DOI: 10.3390/mi15080972.

[475] I. Montoya De Los Santos, H. J. Cortina-Marrero, M. Ruíz-Sánchez, *et al.*, "Optimization of CH3NH3PbI3 perovskite solar cells: A theoretical and experimental study," en, *Solar Energy*, vol. 199, pp. 198–205, Mar. 2020, ISSN: 0038092X. DOI: 10.1016/j.solener.2020.02.026.

[476] Robert F. Pierret, *Semiconductor Device Fundamentals*.

[477] B. G. Streetman and S. K. Banerjee, *Solid state electronic devices*, en, 7. ed., global ed, ser. Always learning. Boston Munich: Pearson, 2016, ISBN: 978-0-13-335603-8 978-1-292-06055-2.

[478] S. D. Stranks, G. E. Eperon, G. Grancini, *et al.*, "Electron-Hole Diffusion Lengths Exceeding 1 Micrometer in an Organometal Trihalide Perovskite Absorber," en, *Science*, vol. 342, no. 6156, pp. 341–344, Oct. 2013, ISSN: 0036-8075, 1095-9203. DOI: 10.1126/science.1243982.

[479] V. Gonzalez-Pedro, E. J. Juarez-Perez, W.-S. Arsyad, *et al.*, "General Working Principles of $CH_3$ $NH_3$ $PbX_3$ Perovskite Solar Cells," en, *Nano Lett.*, vol. 14, no. 2, pp. 888–893, Feb. 2014, ISSN: 1530-6984, 1530-6992. DOI: 10.1021/nl404252e.

[480] Q. Dong, Y. Fang, Y. Shao, *et al.*, "Electron-hole diffusion lengths $> 175$ $\mu$m in solution-grown $CH_3$ $NH_3$ $PbI_3$ single crystals," en, *Science*, vol. 347, no. 6225, pp. 967–970, Feb. 2015, ISSN: 0036-8075, 1095-9203. DOI: 10.1126/science.aaa5760.

[481] L. M. Herz, "Charge-Carrier Dynamics in Organic-Inorganic Metal Halide Perovskites," en, *Annu. Rev. Phys. Chem.*, vol. 67, no. 1, pp. 65–89, May 2016, ISSN: 0066-426X, 1545-1593. DOI: 10.1146/annurev-physchem-040215-112222.

[482] C. C. Stoumpos, C. D. Malliakas, and M. G. Kanatzidis, "Semiconducting Tin and Lead Iodide Perovskites with Organic Cations: Phase Transitions, High Mobilities, and Near-Infrared Photoluminescent Properties," en, *Inorg. Chem.*, vol. 52, no. 15, pp. 9019–9038, Aug. 2013, ISSN: 0020-1669, 1520-510X. DOI: 10.1021/ic401215x.

[483] H. Oga, A. Saeki, Y. Ogomi, S. Hayase, and S. Seki, "Improved Understanding of the Electronic and Energetic Landscapes of Perovskite Solar Cells: High Local Charge Carrier Mobility, Reduced Recombination, and Extremely Shallow Traps," en, *J. Am. Chem. Soc.*, vol. 136, no. 39, pp. 13 818–13 825, Oct. 2014, ISSN: 0002-7863, 1520-5126. DOI: 10.1021/ja506936f.

[484] C. Wehrenfennig, G. E. Eperon, M. B. Johnston, H. J. Snaith, and L. M. Herz, "High Charge Carrier Mobilities and Lifetimes in Organolead Trihalide Perovskites," en, *Advanced Materials*, vol. 26, no. 10, pp. 1584–1589, Mar. 2014, ISSN: 0935-9648, 1521-4095. DOI: 10.1002/adma.201305172.

[485] M. B. Johnston and L. M. Herz, "Hybrid Perovskites for Photovoltaics: Charge-Carrier Recombination, Diffusion, and Radiative Efficiencies," en, *Acc. Chem. Res.*, vol. 49, no. 1, pp. 146–154, Jan. 2016, ISSN: 0001-4842, 1520-4898. DOI: 10.1021/acs.accounts.5b00411.

[486] G. Xing, N. Mathews, S. Sun, *et al.*, "Long-Range Balanced Electron- and Hole-Transport Lengths in Organic-Inorganic CH3NH3PbI3," *Science (New York, N.Y.)*, vol. 342, pp. 344–7, Oct. 2013. DOI: 10.1126/science.1243167.

[487] Y. Li, W. Yan, Y. Li, *et al.*, "Direct Observation of Long Electron-Hole Diffusion Distance in CH3NH3PbI3 Perovskite Thin Film," en, *Sci Rep*, vol. 5, no. 1, p. 14 485, Sep. 2015, Publisher: Nature Publishing Group, ISSN: 2045-2322. DOI: 10.1038/srep14485.

[488] X. Ziang, L. Shifeng, Q. Laixiang, *et al.*, "Refractive index and extinction coefficient of CH_3nh_3pbi_3 studied by spectroscopic ellipsometry," en, *Opt. Mater. Express*, vol. 5, no. 1, p. 29, Jan. 2015, ISSN: 2159-3930. DOI: 10.1364/OME.5.000029.

[489] D. Song, P. Cui, T. Wang, *et al.*, "Managing Carrier Lifetime and Doping Property of Lead Halide Perovskite by Postannealing Processes for Highly Efficient Perovskite Solar Cells," *J. Phys. Chem. C*, vol. 119, no. 40, pp. 22 812–22 819, Oct. 2015, Publisher: American Chemical Society, ISSN: 1932-7447. DOI: 10.1021/acs.jpcc.5b06859.

[490] C. Ponseca, T. Savenije, M. Abdellah, *et al.*, "Organometal Halide Perovskite Solar Cell Materials Rationalized: Ultrafast Charge Generation, High and Microsecond-Long Balanced Mobilities, and Slow Recombination," *Journal of the American Chemical Society*, vol. 136, Mar. 2014. DOI: 10.1021/ja412583t.

[491] F. Deschler, M. Price, S. Pathak, *et al.*, "High Photoluminescence Efficiency and Optically Pumped Lasing in Solution-Processed Mixed Halide Perovskite Semiconductors," *J. Phys. Chem. Lett.*, vol. 5, no. 8, pp. 1421–1426, Apr. 2014, Publisher: American Chemical Society. DOI: 10.1021/jz5005285.

[492] W.-J. Yin, T. Shi, and Y. Yan, "Unusual defect physics in CH3NH3PbI3 perovskite solar cell absorber," en, *Applied Physics Letters*, vol. 104, no. 6, p. 063 903, Feb. 2014, ISSN: 0003-6951, 1077-3118. DOI: 10.1063/1.4864778.

[493] J. Kim, S.-H. Lee, J. H. Lee, and K.-H. Hong, "The Role of Intrinsic Defects in Methylammonium Lead Iodide Perovskite," en, *J. Phys. Chem. Lett.*, vol. 5, no. 8, pp. 1312–1317, Apr. 2014, ISSN: 1948-7185, 1948-7185. DOI: 10.1021/jz500370k.

[494] P. Würfel, *Physics of Solar Cells: From Principles to New Concepts*, en, 1st ed. Wiley, Jan. 2005, ISBN: 978-3-527-40428-5 978-3-527-61854-5. DOI: 10.1002/9783527618545.

[495] Z. Molenda, "N-type substitutional doping of halide perovskite using metastable ions," These de doctorat, Bordeaux, Dec. 2022.

[496] F. Peña-Camargo, J. Thiesbrummel, H. Hempel, *et al.*, "Revealing the doping density in perovskite solar cells and its impact on device performance," en,

[497] Y. Liang, F. Li, X. Cui, *et al.*, "Multiple B-site doping suppresses ion migration in halide perovskites," en, *Sci. Adv.*, vol. 11, no. 11, eads7054, Mar. 2025, ISSN: 2375-2548. DOI: 10.1126/sciadv.ads7054.

[498] S. Wahid, M. Islam, M. S. S. Rahman, and M. K. Alam, "Transfer Matrix Formalism-Based Analytical Modeling and Performance Evaluation of Perovskite Solar Cells," en, *IEEE Trans. Electron Devices*, vol. 64, no. 12, pp. 5034–5041, Dec. 2017, ISSN: 0018-9383, 1557-9646. DOI: 10.1109/TED.2017.2763091.

[499] S. M. Sze and K. K. Ng, *Physics of semiconductor devices*, en, 3. ed, ser. Wiley-Interscience online books. Hoboken, N.J: Wiley-Interscience, 2007, ISBN: 9780471143239 9780470068328 9780470068304 9780585315508 9786610721498. DOI: 10.1002/0470068329.

[500] S. J. Fonash, *Solar cell device physics*, en, 2nd ed. Burlington, MA: Academic Press/Elsevier, 2010, ISBN: 978-0-12-374774-7.

[501] O. J. Sandberg, J. Kurpiers, M. Stolterfoht, *et al.*, "On the Question of the Need for a Built-In Potential in Perovskite Solar Cells," en, *Adv Materials Inter*, vol. 7, no. 10, p. 2 000 041, May 2020, ISSN: 2196-7350, 2196-7350. DOI: 10.1002/admi.202000041.

[502] E. A. Luque, S. Hegedus, and J. Wiley, "Handbook of Photovoltaic Science and Engineering," en,

[503] W. Tress, "Metal Halide Perovskites as Mixed Electronic–Ionic Conductors: Challenges and Opportunities—From Hysteresis to Memristivity," *J. Phys. Chem. Lett.*, vol. 8, no. 13, pp. 3106–3114, Jul. 2017, Publisher: American Chemical Society. DOI: 10.1021/acs.jpclett.7b00975.

[504] C. Ahläng, M. Nyman, and R. Österbacka, "Influence of the Electric Potential on Charge Extraction and Interface Recombination in Perovskite Solar Cells," *Phys. Rev. Appl.*, vol. 16, no. 1, p. 014 041, Jul. 2021, Publisher: American Physical Society. DOI: 10.1103/PhysRevApplied.16.014041.

[505] D. Glowienka and Y. Galagan, "Light Intensity Analysis of Photovoltaic Parameters for Perovskite Solar Cells," en, *Advanced Materials*, vol. 34, no. 2, p. 2 105 920, 2022, _eprint: https://onlinelibrary.wiley.com/doi/pdf/10.1002/adma.202105920, ISSN: 1521-4095. DOI: 10.1002/adma.202105920.

[506] T. Xu, Z.-S. Wang, X.-H. Li, and W. E. I. Sha, "Loss Mechanism Analyses of Perovskite Solar Cells with an Equivalent Circuit Model," *Acta Phys. Sin.*, vol. 70, no. 9, p. 098 801, 2021, arXiv:2103.11141 [cond-mat], ISSN: 1000-3290, 1000-3290. DOI: 10.7498/aps.70.20201975.

[507] N. Mundhaas, Z. J. Yu, K. A. Bush, *et al.*, "Series Resistance Measurements of Perovskite Solar Cells Using $J_{sc}$ – $V_{oc}$ Measurements," en, *Solar RRL*, vol. 3, no. 4, p. 1 800 378, Apr. 2019, ISSN: 2367-198X, 2367-198X. DOI: 10.1002/solr.201800378.

[508] S. Selberherr, *Analysis and Simulation of Semiconductor Devices*, eng. Vienna: Springer Wien, 1984, ISBN: 978-3-7091-8752-4.

[509] R. N. Hall, "RECOMBINATION PROCESSES IN SEMICONDUCTORS," en,

[510] G. Namkoong, P. Boland, K. Lee, and J. Dean, "Design of organic tandem solar cells using PCPDTBT:PC61BM and P3HT:PC71BM," en, *Journal of Applied Physics*, vol. 107, no. 12, p. 124 515, Jun. 2010, ISSN: 0021-8979, 1089-7550. DOI: 10.1063/1.3448271.

[511] A. P. Singh, R. K. Baghel, and S. Tirkey, "Device Simulation Process on TCAD," in *Advanced Field-Effect Transistors*, Num Pages: 27, CRC Press, 2023.

[512] S. Tripathi, "STUDY OF SiC-BASED NEUTRON DETECTOR FOR APPLICATIONS IN THE HARSH ENVIRONMENT OF FAST REACTORS," en,

[513] O. Demchenko, D. Zykov, and N. Kurbanova, "Research possibilities of Silvaco TCAD for physical simulation of gallium nitride power transistor," en, Tomsk, Russia, 2016, p. 060 007. DOI: 10.1063/1.4964587.

[514] A. F. Bouhdjar, "Etude et simulation numérique des cellules solaires à hétérojonction (a-Si:H/µc-Si:H)," en,

[515] *ATLAS User's Manual Copyright 2004 SILVACO International 4701 Patrick Henry Drive, Building 1 Santa Clara, CA 95054*.

[516] S. Hamady, "Nouveaux concepts de transistors de puissance à haute mobilité électronique (HEMT) en nitrure de gallium (GaN)," fr, thesis, Toulouse 3, Jan. 2014.

[517] S. Z. Haider, H. Anwar, and M. Wang, "A comprehensive device modelling of perovskite solar cell with inorganic copper iodide as hole transport material," en, *Semicond. Sci. Technol.*, vol. 33, no. 3, p. 035 001, Jan. 2018, Publisher: IOP Publishing, ISSN: 0268-1242. DOI: 10.1088/1361-6641/aaa596.

[518] A. Hima, N. Lakhdar, B. Benhaoua, A. Saadoune, I. Kemerchou, and F. Rogti, "An optimized perovskite solar cell designs for high conversion efficiency," *Superlattices and Microstructures*, vol. 129, pp. 240–246, May 2019, ISSN: 0749-6036. DOI: 10.1016/j.spmi.2019.04.007.

[519] M. Houshmand, H. Esmaili, M. Hossein Zandi, and N. E. Gorji, "Degradation and device physics modeling of TiO2/CZTS ultrathin film photovoltaics," *Materials Letters*, vol. 157, pp. 123–126, Oct. 2015, ISSN: 0167-577X. DOI: 10.1016/j.matlet.2015.05.055.

[520] D. Liu, M. K. Gangishetty, and T. L. Kelly, "Effect of CH3NH3PbI3 thickness on device efficiency in planar heterojunction perovskite solar cells," en, *J. Mater. Chem. A*, vol. 2, no. 46, pp. 19 873–19 881, Nov. 2014, Publisher: The Royal Society of Chemistry, ISSN: 2050-7496. DOI: 10.1039/C4TA02637C.

[521] F. Azri, A. Meftah, N. Sengouga, and A. Meftah, "Electron and hole transport layers optimization by numerical simulation of a perovskite solar cell," *Solar Energy*, vol. 181, pp. 372–378, Mar. 2019, ISSN: 0038-092X. DOI: 10.1016/j.solener.2019.02.017.

[522] L. Huang, X. Sun, C. Li, *et al.*, "Electron transport layer-free planar perovskite solar cells: Further performance enhancement perspective from device simulation," *Solar Energy Materials and Solar Cells*, vol. 157, pp. 1038–1047, Dec. 2016, ISSN: 0927-0248. DOI: 10.1016/j.solmat.2016.08.025.

[523] T. Minemoto and M. Murata, "Impact of work function of back contact of perovskite solar cells without hole transport material analyzed by device simulation," *Current Applied Physics*, vol. 14, no. 11, pp. 1428–1433, Nov. 2014, ISSN: 1567-1739. DOI: 10.1016/j.cap.2014.08.002.

[524] Y. Raoui, H. Ez-Zahraouy, N. Tahiri, O. El Bounagui, S. Ahmad, and S. Kazim, "Performance analysis of MAPbI3 based perovskite solar cells employing diverse charge selective contacts: Simulation study," *Solar Energy*, vol. 193, pp. 948–955, Nov. 2019, ISSN: 0038-092X. DOI: 10.1016/j.solener.2019.10.009.

[525] A.-A. Kanoun, M. B. Kanoun, A. E. Merad, and S. Goumri-Said, "Toward development of high-performance perovskite solar cells based on CH3NH3GeI3 using computational approach," *Solar Energy*, vol. 182, pp. 237–244, Apr. 2019, ISSN: 0038-092X. DOI: 10.1016/j.solener.2019.02.041.

[526] H. Rouigueb, M. Khaouani, S. Kerai, A. Z. Djennati, and M. A. Belbachir, "Comprehensive analytical modeling of perovskite (MAPbI3) solar cells: A rigorous validation via simulations and experiments," *Solar Energy*, vol. 302, p. 113 996, Dec. 2025, ISSN: 0038-092X. DOI: 10.1016/j.solener.2025.113996.

[527] M. A. Belbachir, A. Z. Djennati, S. Kerai, M. Khaouani, and H. Rouigueb, "Simulation Validation and Performance Optimization of Tandem Perovskite/Silicon Solar Cells Based on Experimental Single-Junction Perovskite Solar Cell," en, *J. Electron. Mater.*, Jul. 2025, ISSN: 1543-186X. DOI: 10.1007/s11664-025-12173-2.

[528] Z. Qin, S. Dai, C. C. Gajjela, *et al.*, "Spontaneous Formation of 2D/3D Heterostructures on the Edges of 2D Ruddlesden–Popper Hybrid Perovskite Crystals," en, *Chem. Mater.*, vol. 32, no. 12, pp. 5009–5015, Jun. 2020, ISSN: 0897-4756, 1520-5002. DOI: 10.1021/acs.chemmater.0c00419.

[529] A. Mathieson, M. Rahil, Y. Zhang, *et al.*, "Ruddlesden Popper 2D perovskites as Li-ion battery electrodes," en, *Mater. Adv.*, vol. 2, no. 10, pp. 3370–3377, May 2021, Publisher: RSC, ISSN: 2633-5409. DOI: 10.1039/D1MA00020A.

[530] B. Song, J. Hou, H. Wang, *et al.*, "Determination of Dielectric Functions and Exciton Oscillator Strength of Two-Dimensional Hybrid Perovskites," en, *ACS Materials Lett.*, vol. 3, no. 1, pp. 148–159, Jan. 2021, ISSN: 2639-4979, 2639-4979. DOI: 10.1021/acsmaterialslett.0c00505.

[531] P. Peksa, A. Maufort, M. Baranowski, *et al.*, "Engineering the Effective Mass in 2D Perovskites via Octahedral Distortion," en, *J. Phys. Chem. C*, vol. 128, no. 42, pp. 17 984–17 989, Oct. 2024, ISSN: 1932-7447, 1932-7455. DOI: 10.1021/acs.jpcc.4c05300.

[532] H. Rouigueb, M. Khaouani, S. Kerai, A. Z. Djennati, and M. A. Belbachir, "Numerical optimization of hybrid 2D/3D and tandem perovskite/silicon HTJ solar cells, based on an experimentally validated $MAPbI_3$ cell: Influence of HTL doping and temperature," *Semiconductor Science and Technology*, vol. 41, no. 2, p. 025 020, Feb. 2026, ISSN: 0268-1242, 1361-6641. DOI: 10.1088/1361-6641/ae44c4.

[533] D. H. Cao, C. C. Stoumpos, O. K. Farha, J. T. Hupp, and M. G. Kanatzidis, "2D Homologous Perovskites as Light-Absorbing Materials for Solar Cell Applications," en, *J. Am. Chem. Soc.*, vol. 137, no. 24, pp. 7843–7850, Jun. 2015, ISSN: 0002-7863, 1520-5126. DOI: 10.1021/jacs.5b03796.

[534] R. Liu, C. Lan, M. Zeng, *et al.*, "Precisely Tuning 3D/Quasi-2D Perovskite Heterojunctions in Wide-Bandgap Perovskites for High-Performance Tandem Solar Cells," en, *Advanced Materials*, vol. n/a, no. n/a, p. 2 504 321, _eprint: https://advanced.onlinelib ISSN: 1521-4095. DOI: 10.1002/adma.202504321.

[535] S. Ali, K. Ahmad, R. A. Khan, and P. Kumar, "Simulation-Based Studies on FAGeI3-Based Lead (Pb2+)-Free Perovskite Solar Cells," en, *Crystals*, vol. 15, no. 2, p. 135, Feb. 2025, Number: 2 Publisher: Multidisciplinary Digital Publishing Institute, ISSN: 2073-4352. DOI: 10.3390/cryst15020135.

[536] C. Song, H. Du, M. Xu, *et al.*, "Improving the performance of perovskite solar cells using a dual-hole transport layer," en, *Dalton Trans.*, vol. 53, no. 2, pp. 484–492, Jan. 2024, Publisher: The Royal Society of Chemistry, ISSN: 1477-9234. DOI: 10.1039/D3DT03501H.

[537] H. Alipour and A. Ghadimi, "Optimization of lead-free perovskite solar cells in normal-structure with WO 3 and water-free PEDOT: PSS composite for hole transport layer by SCAPS-1D simulation," en, *Optical Materials*, vol. 120, p. 111 432, Oct. 2021, ISSN: 09253467. DOI: 10.1016/j.optmat.2021.111432.

[538] J. Sun, N. Zhang, J. Wu, *et al.*, "Additive Engineering of the CuSCN Hole Transport Layer for High-Performance Perovskite Semitransparent Solar Cells," *ACS Appl. Mater. Interfaces*, vol. 14, no. 46, pp. 52 223–52 232, Nov. 2022, Publisher: American Chemical Society, ISSN: 1944-8244. DOI: 10.1021/acsami.2c18120.

[539] T. Wang, D. Ding, X. Wang, R. Zeng, H. Liu, and W. Shen, "High-Performance Inverted Perovskite Solar Cells with Mesoporous NiOx Hole Transport Layer by Electrochemical Deposition," *ACS Omega*, vol. 3, no. 12, pp. 18 434–18 443, Dec. 2018, Publisher: American Chemical Society. DOI: 10.1021/acsomega.8b02612.

# Appendices

# .1 Detailed Pseudocode

**Start of the program**

1. **Physical constants:**
   - $q \leftarrow 1.602 \times 10^{-19}$ C (elementary charge)
   - $k \leftarrow 1.381 \times 10^{-23}$ J/K (Boltzmann constant)
   - $T \leftarrow 300$ K (ambient temperature)
   - $h \leftarrow 6.626 \times 10^{-34}$ J·s (Planck's constant)
   - $c \leftarrow 3 \times 10^{8}$ m/s (speed of light)
   - $P_{\text{inc}} \leftarrow$ incident power (W/cm$^2$)
2. **Device parameters:**
   - $t_0 \leftarrow$ active layer thickness (in cm)
   - $\lambda_{\text{ave}} \leftarrow$ average absorption wavelength (in cm)
   - $V_{\text{bi}} \leftarrow$ built-in voltage (in volts)
   - $G_{\text{max}} \leftarrow$ maximum carrier generation rate (cm$^{-3}\cdot$ s$^{-1}$)
3. **Carrier transport parameters:**
   - $\mu_n \leftarrow$ electron mobility (cm$^2$/V·s)
   - $\mu_p \leftarrow$ hole mobility (cm$^2$/V·s)
   - $D_n \leftarrow \mu_n \cdot \frac{kT}{q}$ (electron diffusivity)
   - $D_p \leftarrow \mu_p \cdot \frac{kT}{q}$ (hole diffusivity)
4. **Carrier concentrations and recombination velocities:**
   - $n_i \leftarrow$ intrinsic carrier concentration (cm$^{-3}$)
   - $N_{D,\text{eff}} \leftarrow$ effective donor doping concentration (cm$^{-3}$)
   - $N_{A,\text{eff}} \leftarrow$ effective acceptor doping concentration (cm$^{-3}$)
   - $s_n \leftarrow$ electron surface recombination velocity
   - $s_p \leftarrow$ hole surface recombination velocity
5. **Voltage vector:**
   - A vector $V$ from 0 to 1.5 V with a step of 0.01 V
6. **Calculate Dark current density $J_{\text{dark}}$ for each $V$:**

$$J_{\text{dark}} \leftarrow q\frac{(V - V_{\text{bi}})}{t_p}\left[\mu_n\left(N_{\text{D,eff}} + \frac{s_n KT t_p\left(n_i - \frac{n_i^2}{N_{\text{A,eff}}}\right)}{D_n q(V - V_{\text{bi}})e^{-\frac{q(V-V_{\text{bi}})}{KT}}}\right) + \mu_p\left(N_{\text{A,eff}} + \frac{s_p KT t_p\left(n_i - \frac{n_i^2}{N_{\text{D,eff}}}\right)e^{\frac{q(V-V_{\text{bi}})}{KT}}}{q(V - V_{\text{bi}})D_p}\right)\right]$$

7. **Calculate Photocurrent density $J_{\text{phot}}$ for each $V$:**

$$J_{\text{phot}} \leftarrow \frac{q(V - V_{\text{bi}})G_{\max}}{t_0} \cdot \left[ \frac{\mu_n}{D_n \left( \frac{q(V-V_{\text{bi}})\lambda_{\text{ave}}}{kTt_0} - 1 \right)} \cdot \left( \frac{e^{-t_0/\lambda_{\text{ave}}}}{\frac{q(V-V_{\text{bi}})e^{-q(V-V_{\text{bi}})/(kT)}}{kTt_0}} - \lambda_{\text{ave}} \right) + \frac{\mu_p}{D_p \left( \frac{q(V-V_{\text{bi}})\lambda_{\text{ave}}}{kTt_0} + 1 \right)} \cdot \left( \frac{e^{q(V-V_{\text{bi}})/(kT)}}{\frac{q(V-V_{\text{bi}})}{kTt_0}} + \lambda_{\text{ave}} e^{-t_0/\lambda_{\text{ave}}} \right) \right]$$

8. **Calculate total current density:**
   - $J_{\text{total}} \leftarrow J_{\text{dark}} + J_{\text{phot}}$
9. **Extract main photovoltaic parameters:**
   - $J_{\text{sc}} \leftarrow J_{\text{total}}$ at $V = 0$ (short-circuit current)
   - $V_{\text{oc}} \leftarrow$ value of $V$ for which $J_{\text{total}} \approx 0$ (open-circuit voltage)
10. **Plot the J-V curve:**
    - Plot $J_{\text{total}}$ as a function of $V$
    - Add axes labels, title, and grid
11. **Calculate EQE (External Quantum Efficiency):**
    - Define a wavelength vector $\lambda$ from 0.3 µm to 1 µm with step 0.01 µm
    - Convert to cm: $\lambda_{\text{cm}} \leftarrow \lambda \cdot 10^{-4}$
    - EQE $\leftarrow \frac{J_{\text{phot}} \cdot h \cdot c}{q \cdot P_{\text{inc}} \cdot \lambda_{\text{ave}}}$
    - Plot EQE as a function of $\lambda$
12. **Calculate IQE (Internal Quantum Efficiency):**
    - Define reflection and transmission coefficients
    - IQE $\leftarrow \frac{\text{EQE}}{1 - \text{reflection} - \text{transmission}}$
    - Plot IQE as a function of $\lambda$

**End of program**